

---

# On the role of stochasticity in biochemical systems far from thermal equilibrium

How fluctuations affect phenomenology

Patrick Wilke

---



München 2020



---

**On the role of stochasticity in biochemical  
systems far from thermal equilibrium**  
**How fluctuations affect phenomenology**

Patrick Wilke

---

Dissertation  
der Fakultät für Physik  
der Ludwig-Maximilians-Universität  
München

vorgelegt von  
Patrick Wilke  
aus Kassel

München, den 26.05.2020

Erstgutachter: Prof. Dr. Erwin Frey

Zweitgutachter: Prof. Dr. Ulrich Schollwöck

Tag der mündlichen Prüfung: 07.07.2020

# Zusammenfassung

Auf zellulärer Ebene ist Leben ein kollektives Phänomen unbelebter Makromoleküle. Dieser Übergang von biochemischen Wechselwirkungen zu belebten Organismen stellt ein zentrales Forschungsgebiet der interdisziplinären Wissenschaft dar. Bei der zugrunde liegenden Problematik, die kollektive Dynamik einer Vielzahl von Komponenten aus ihren individuellen Eigenschaften abzuleiten, handelt es sich um die charakteristische Fragestellung der statistischen Mechanik. Bedingt durch das weitreichende Interaktionsspektrum der Basiscomponenten bestehen allerdings signifikante Unterschiede im Vergleich zur unbelebten Materie.

Während einzelne Atome und kleine Moleküle auf einfache Elektrostatik beschränkt sind, weisen Proteine und andere Makromoleküle komplexe biochemische Wechselwirkungen auf. Da diese oftmals mit der Umwandlung chemischer Energie einhergehen, ist eine Beschreibung mittels des thermischen Gleichgewichts von Natur aus unzureichend, um die sich ergebende Dynamik zu erfassen. Hinzu kommt, dass auf zellulären Skalen kollektives Verhalten zwar von großer Relevanz ist, Komponenten aber in geringerer Zahl vorhanden und ihre Längenskalen von denen ihrer Umgebung nicht derart verschieden sind, wie dies in makroskopischen Systemen der Fall ist. Dies führt dazu, dass stochastische Fluktuationen eine zentrale Rolle bei der Beschreibung einnehmen.

Diese Dissertation befasst sich mit der Frage, wie stochastische Fluktuationen die kollektive Phänomenologie in verschiedenen biochemisch motivierten Systemen beeinflussen. In meinem ersten Projekt beschäftigte ich mich gemeinsam mit Emanuel Reithmann und Erwin Frey mit den Folgen der Interaktion verschiedener Arten molekularer Motoren für den intrazellulären Transport entlang von Mikrotubuli. Hierbei zeigten wir auf, dass eine resultierende langreichweitige Kopplung dazu führt, dass Stauprozesse von weitaus größerer Bedeutung sind als erwartet. In einem zweiten Projekt untersuchte ich in Zusammenarbeit mit Florian Gartner, Isabella Graf, Philipp Geiger und Erwin Frey die Selbstassemblierung komplexer Makromoleküle. Wir erarbeiteten Kriterien für die Robustheit dieses Vorgangs und machten deutlich, wie stochastische Effekte gängige Konzepte zur Optimierung der Produktionsausbeute in Frage stellen. Das Thema meines dritten Projekts war der Phasenübergang des diffusiven epidemischen Prozesses. Basierend auf umfassenden stochastischen Simulationen gelang es mir gemeinsam mit Borislav Polovnikov und Erwin Frey bisher ungeklärte Diskrepanzen zwischen störungstheoretischer Renormierungsgruppentheorie und numerischen Untersuchungen aufzuklären.

Allen genannten Arbeiten ist gemein, dass durch die Gegenüberstellung der Resultate aus deterministischen Näherungen, analytischen Berechnungen und exakten stochastischen Simulationen die Ursprünge der stochastischen Effekte sowie deren Stärke bestimmende Faktoren identifiziert werden konnten. Um diesen Ansatz über die von mir untersuchten Systeme hinaus zu verallgemeinern, entwickelte ich in meinem letzten Projekt eine modular erweiterbare Umgebung zur exakten stochastischen Simulation allgemeiner Reaktionsdiffusionssysteme in unterschiedlichen Geometrien.



# Summary

At the cellular level, life is a collective phenomenon of inanimate macromolecules. This transition from biochemical interactions to living organisms represents a central research area of modern interdisciplinary science. The underlying problem of deriving the collective dynamics of a large number of agents from their microscopic behavior is the characterizing research question of statistical mechanics. However, due to the broad range of interactions of the basic components, there are significant differences compared to inanimate matter.

While single atoms and small molecules are limited to simple electrostatics, proteins and other macromolecules admit complex biochemical interactions. Since these often include the conversion of chemical energy, descriptions based on the thermal equilibrium are inherently inadequate to grasp the resulting dynamics. In addition, collective behavior plays an important role on the cellular level, but there are fewer components and their length scales are not as different from those of the entire system as in typical macroscopic setups. As a consequence, stochastic fluctuations are essential for the description of such systems.

This dissertation deals with the question of how stochastic fluctuations affect the collective phenomenology in different biochemically motivated systems. In my first project, together with Emanuel Reithmann and Erwin Frey, I analyzed the effects of the interaction of different types of molecular motors on intracellular transport along microtubules. We showed that a resulting long-range coupling leads to overcrowding being of far greater relevance than expected. In a second project, I studied the self-assembly of complex macromolecules in collaboration with Florian Gartner, Isabella Graf, Philipp Geiger and Erwin Frey. We developed criteria for its robustness and showed how stochastic effects question common concepts for optimizing production yield. The research topic of my third project was the phase transition of the diffusive epidemic process. Based on extensive stochastic simulations, Borislav Polovnikov, Erwin Frey and I, succeeded in resolving previously unexplained discrepancies between perturbative renormalization group methods and numerical investigations.

All my research projects have in common that by comparing the results from deterministic approximations, analytical calculations and exact stochastic simulations, we were able to identify the origins of the stochastic effects and their determining factors. In order to generalize this approach beyond the systems I investigated, in my last project I developed a modularly expandable framework for exact stochastic simulations of general reaction-diffusion systems in different geometries.



# Contents

<b>Zusammenfassung</b>	<b>iii</b>
<b>Summary</b>	<b>iv</b>
<b>1 Abstracts of the projects</b>	<b>1</b>
<b>2 Geometry and arrangement: Molecular transport along microtubules</b>	<b>11</b>
2.1 Biological background . . . . .	11
2.2 The totally asymmetric simple exclusion process . . . . .	13
2.3 Modelling active transport by molecular motors . . . . .	16
2.4 Spiralling motion of motors and modelling . . . . .	17
2.5 Failure of mean-field . . . . .	19
2.6 Particle arrangement and fluctuations . . . . .	22
2.7 Quantifying the impact on transport . . . . .	30
2.8 Control parameters and phase diagram . . . . .	33
2.9 Conclusion . . . . .	38
<b>3 Reaction paths and depletion traps: Macromolecular self-assembly</b>	<b>43</b>
3.1 Biochemical background . . . . .	43
3.2 General principles and modelling . . . . .	46
3.3 Deterministic theory . . . . .	48
3.4 Stochastic effects . . . . .	55
3.5 Conclusion . . . . .	59
<b>4 Reaction kinetics and absorbing states: The diffusive epidemic process</b>	<b>63</b>
4.1 The diffusive epidemic process . . . . .	64
4.2 Renormalization group methods and stochastic simulations . . . . .	67
4.3 Scaling relations . . . . .	68
4.4 Critical exponents in one dimension . . . . .	69
4.5 Spreading behavior for different diffusion ratios . . . . .	77
4.6 Conclusion . . . . .	79

<b>5</b>	<b>Exact stochastic simulations of general reaction-diffusion systems</b>	<b>83</b>
5.1	Basics . . . . .	84
5.2	Program structure . . . . .	87
5.3	Spatially extended systems . . . . .	90
5.4	Measurement of critical exponents . . . . .	94
5.5	Conclusion . . . . .	98
<b>6</b>	<b>Conclusion</b>	<b>99</b>
<b>A</b>	<b>Optimization methods</b>	<b>103</b>
A.1	TASEP-like systems . . . . .	104
A.2	Heterogeneous self-assembly . . . . .	107
A.3	Reaction-diffusion systems on lattices . . . . .	110
<b>B</b>	<b>Supplementary calculations</b>	<b>115</b>
B.1	Cramming density for arbitrary species ratios . . . . .	115
B.2	Derivatives of the hindrance function . . . . .	118
B.3	General low-density theory . . . . .	120
<b>C</b>	<b>Supplementary figures</b>	<b>123</b>
<b>D</b>	<b>Reprint: Supplementary information for stochastic yield catastrophes and robustness in self-assembly</b>	<b>131</b>
D.1	Chemical reaction equations and the equivalence of models with different numbers of species . . . . .	135
D.2	Effective description of the evolution of the polymer size distribution as an advection-diffusion equation . . . . .	137
D.3	Threshold values for the activation and dimerization rate . . . . .	140
D.4	Impact of the implementation of sub-nucleation reactions . . . . .	147
D.5	Time evolution of the yield in the activation and dimerization scenario . .	149
D.6	Standard deviation of the yield . . . . .	151
D.7	Influence of the heterogeneity of the target structure for fixed number of particles per species . . . . .	153
D.8	Dependence of the maximal yield $y_{\max}$ in the activation scenario on $N$ and $L$	155
	<b>Bibliography</b>	<b>157</b>
	<b>Acknowledgments</b>	<b>171</b>

# Chapter 1

## Abstracts of the projects

How to derive the collective behavior of a multitude of agents based on their individual interactions has been a long-standing research question in physics. Most prominently, the attempt to describe macroscopic systems using only incomplete information about their microscopic states gave rise to the theory of statistical mechanics; Without exact knowledge of the considered configurations, *randomness* is introduced to a theory, which is hence subject to the laws of statistics. Based on the minimal assumptions of equal probabilities for all possible states and sufficiently large particle numbers to neglect stochastic fluctuations the—until then phenomenological—theory of thermodynamics was rigorously derived [1]. This connection between microscopics and macroscopics has been one of the major breakthroughs in modern physics. Remarkably, it is completely independent of the material considered as long as the system is in thermal equilibrium [2]. So, in one sense the range of application is very broad and in another very limited. In essence, every object can be described, but only in one well-defined state.

For systems far from thermal equilibrium no unifying theory was discovered so far and it is still unknown whether it could be [3]. While the existence of thermodynamics made it clear that general principles, which are independent of the considered systems, have to exist before knowledge of the underlying microscopic details was available, for systems far from thermal equilibrium we do not have such universal phenomenological principles—not to speak of a general theory connecting them to the microscopic interactions. On the other hand, it is exactly what makes those systems so complicated to describe that makes them so versatile and interesting to study. Strong non-linear effects and stochastic fluctuations, which amplify each other, create far richer and often times unexpected behavior. In this context, biological systems are of particular interest since a constant consumption of energy in exchange for local entropy reduction can be seen as one of the defining features of living organisms [4, 5]. Consequently, their theoretical understanding is closely connected to physics far from thermal equilibrium. In addition, on the smallest possible, the cellular level, life starts as a collective phenomenon caused by biochemical interactions of inanimate macromolecules. But in contrast to macroscopic systems, components are not as abundant and the length scales of environment and agents are not as different. The description hence takes place on an intermediate (*mesoscopic*) scale, which means stochastic fluctuations may

significantly affect the collective dynamics [6].

In this thesis, I investigate how stochastic fluctuations in biochemically motivated systems give rise to new phenomenology. Because of the lack of a general theoretical framework to do so, explicit systems are studied to give proofs of concepts for central mechanisms and their origins. I show how seemingly minor changes to well understood systems can drastically alter the collective behavior in a way that cannot be captured using deterministic approaches. Comparing analytic calculations, mean-field approximations and exact stochastic simulations, the sources of stochastic effects are identified and means for their quantification are derived. To allow for the application of the employed methods beyond the systems studied in this thesis, as a last step I created a simulation framework which can be used for the investigation of stochastic effects and critical phenomena in general spatially extended reaction-diffusion systems in different geometries.

---

## Active two-species transport along cylindrical structures

with *Emanuel Reithmann and Erwin Frey*.

Published in “Two-Species Active Transport along Cylindrical Biofilaments is Limited by Emergent Topological Hindrance” (*Phys. Rev. X*, **8**(3) 031063, 2018) to which I contributed as shared first author.

### Summary

In the first project, which is discussed in Chapter 2, we investigate the effects of geometry and particle arrangement on active intracellular transport by kinesin motors along microtubules. We study an experimentally motivated two-dimensional lattice gas model that constitutes an extension of the totally asymmetric simple exclusion process (TASEP). This paradigmatic system has been used as a minimal model for a plethora of transport phenomena [3, 7–12].

Despite its very simple microscopic dynamics the TASEP admits complex collective behavior in the form of boundary induced phase transitions. Interestingly, these can be well described using a mean-field approximation that neglects stochastic fluctuations [13]. Including Langmuir kinetics, the model was successfully applied to describe intracellular transport along microtubules [14, 15], making predictions that have been verified experimentally [16]. However, both theory and experiment are based on a single motor species which only follows a one-dimensional pathway such that the cylindrical structure of microtubules does not matter.

In recent years, single motor experiments showed, that different kinesin motor families admit different modes of motion along the cylindrical microtubule. In particular, members of the kinesin-2 and kinesin-8 families have been reported to follow helical pathways [18–20]. This naturally raises the question whether a reduction to one dimension is still possible in the presence of more than one motor species since the entire system may become coupled. To investigate the effect of multi-species interactions on collective active transport, we created an extended model that features two motor species with different gaits move along a cylindrical lattice.

The central new aspects which come into play are the arrangement of molecular motors and a second length scale in the form of the cylinder circumference which is much shorter than the individual filaments. Those two at first glance minor changes in our model cause a complete failure of the previously so successful mean-field theory and give rise to unexpected phenomena. Since the original TASEP does not exhibit relevant fluctuations, the source of this behavior has to be solely based on arrangement and geometry. By comparing mean-field approximations, refined analytic calculations and exact stochastic simulations, we provide a detailed picture of the underlying mechanics and discuss their implications for molecular transport along microtubules.

## Research questions

How does the presence of a second molecular motor species with a different gait affect collective molecular transport along microtubules? Does a mapping exist which allows us to treat our model as effectively one-dimensional? If not, what are the fundamental differences compared to the TASEP?

## Key findings

*Mean-field approximations fail to describe the collective behavior on a qualitative level.*

Applying the same approximation steps, that work successfully for the TASEP, to our model the resulting equations predict identical behavior. However, all phenomenology discussed in the following is not captured by this prediction. In fact, the notion of a particle density itself turns out to be incompatible with the observed behavior.

*Jamming is not only driven by crowding but also by arrangement.*

The most evident difference compared to one-dimensional transport is that total jamming occurs at densities far below full occupation. If two species with different gaits are present, their arrangement causes a new type of hindrance to their motion. For a lattice site to be able to contribute to transport it is not sufficient for it to be empty, it also needs to be accessible. What seems to be a minor effect drastically amplifies the relevance of stochastic fluctuations and becomes the most dominant limitation for transport.

*The number of lanes and the species ratio have significant impact on transport efficiency.*

Increasing the number of lanes of the cylindrical lattice increases the impact of hindrance driven by arrangement. Simulations even suggest the paradoxical limit of complete arrest on an empty lattice since no lower bound other than zero has been found for the jamming density. Furthermore, just small fractions of a second motor species with different gait are sufficient to cause the described effects. Already at values around 5%, transport is completely dominated by the limitation in accessible lattice sites.

*Long-range correlations result in self-organization and pattern formation.*

The reason that the impact of particle arrangement becomes stronger for higher numbers of lanes is an increase in the correlation length. When the cylindrical lattice is sufficiently short such that both height and circumference are of the same order in size, a new phenomenon emerges. Wave-like density patterns form in the longitudinal direction with the wave-length being identical to the number of lanes representing the transversal extension. This form of stochasticity driven self-organization is strictly prohibited in a density-based description as it violates current conservation.

*Overcrowding may play a more significant role in molecular transport than expected*

Using generalized models, we showed that our findings are robust against biochemically motivated model extensions that allow us to make experimentally verifiable predictions. For example, gradually adding a second motor species causes significantly stronger crowding effects than members of the same species do. This effect can induce phase coexistence in an otherwise sparsely populated system; Which addresses the major criticism for the *in vivo* relevance of crowding phenomena.

---

## Effects of stochastic fluctuations in macromolecular self-assembly

with *Florian Gartner, Isabella Graf, Philipp Geiger and Erwin Frey.*

Published in “Stochastic yield catastrophes and robustness in self-assembly,” (*Elife* 8 e51020, 2020) to which I contributed as shared first author.

### Summary

Motivated by the fact that functional macromolecules such as microtubules and molecular motors, whose existence is taken for granted in Chapter 2, need to be created from simpler subunits without external control, Chapter 3 deals with the problem of reliable self-assembly. A general principle in this context is that the nucleation of new structures has to be significantly slower than their growth to achieve high production yield [21–26]. Otherwise, resources may get depleted before all initiated polymers can be finished. This effect is called a depletion trap and how to circumvent it is one of the central research questions in the field of self-assembly.

Employing conceptual mathematical models, we study systems in which several structures of higher complexity are produced simultaneously from a finite number of components in a well-mixed environment. To avoid having any distinguished subunits, the target structure is a ring. Despite the existence of several strikingly similar experimental setups [27,28] it is not our intention to model any of them specifically. They are simply one possible implementation of the characterizing features we are interested in: finite size target structures built from subunits with equivalent binding properties.

In order to study the influence of the heterogeneity of a structure on its assembly process, we treat ring size and number of species as independent parameters. In detail, this means a ring of size 12 can be assembled from just one or up to 12 different species which all bind to specific neighbors. This way, our model can be seen as an interpolation between DNA origami and virus capsid assembly. In the first case, complex artificial structures are designed using highly specialized building blocks [22, 23, 29]. The assembly of capsids in contrast is a naturally occurring phenomenon in which identical small proteins form a spherical shell to encapsulate the genetic material of a virus [30, 31]. In both these cases, self-assembly has been shown to be a nucleation phenomenon [22–24, 32–34]. Slowing down the creation of new polymers compared to structure growth increases production yield by reducing depletion traps irrespective of the underlying mechanism or the heterogeneity of the structure.

Using different mechanisms such as the introduction of an activation step or a reduced dimerization rate to slow down nucleation, we demonstrate that approaches which are equally successful on a macroscopic level show severe differences in their susceptibility to stochastic fluctuations when particle numbers are reduced. A combination of deterministic approximations and stochastic simulations allows us to identify criteria for robust self-assembly and understand their limitations. In a biological context, the implications of our results are that cells require sophisticated mechanisms to counteract strong fluctuations and ensure reliable supply of functioning macromolecules.

## Research questions

What are conditions that ensure robust and efficient self-assembly of macromolecules? Is it sufficient to slow down nucleation to avoid depletion traps or does the mechanism itself matter? How does the heterogeneity of a structure affect its self-assembly process?

## Key findings

*In the limit of abundant resources, assembly is independent of the number of different species and yield can be maximized by slowing down nucleation irrespective of the underlying mechanism.*

If the total number of particles in a system is sufficiently high, fluctuations can be neglected and its state is well described by a mean-field approximation in terms of continuous densities. Since the assembled target structure is a ring, no distinguished species exists and all densities of polymers of equal size have to be identical. Accordingly, the system can always be mapped to a homogeneous assembly process irrespective of the number of species using symmetry arguments. Stochastic simulations and analytic solutions both confirm that for such a system yield is only limited by depletion traps that can be avoided by reducing nucleation speed.

*Heterogeneous systems are susceptible to stochastic fluctuations which limit the maximally achievable yield.*

Reducing the number of initial monomers in the system, the equivalence between homogeneous and heterogeneous systems breaks down. If particles undergo an activation step, yield saturates at an imperfect value irrespective of how much the nucleation speed is lowered. This effect can be reduced by decreasing the number of different species and it vanished completely in a homogeneous system.

*The existence of a transition from deterministic to stochastic dynamics results in non-monotonic yield curves.*

Since stochastic fluctuations become more relevant for slower supply of constituents in the heterogeneous system and deterministically decreasing nucleation speed always improves yield a transition between the two regimes exists. First, a reduction in deterministic depletion traps causes the yield to increase. But at some point, an increase in fluctuations limits and even reduces the maximally achievable yield. This results in non-monotonic yield curves and turns self-assembly of heterogeneous structures into a fine-tuning problem instead of being solved by a simple "more is always better" solution.

---

## Dynamic spreading of activity in the diffusive epidemic process

with *Borislav Polovnikov and Erwin Frey*.

In preparation for publication in “Strong Coupling Behavior in the Diffusive Epidemic Process” to which I contribute as shared first author.

### Summary

Following the influence of particle arrangement in Chapter 2 and structure heterogeneity in Chapter 3, Chapter 4 focuses on reaction kinetics. We study the diffusive epidemic process (DEP), a mass-conserving extension of the paradigmatic directed percolation model, in one dimension. Despite its simple structure the model has resisted classification for decades and hence constitutes a major challenge in the field of interacting lattice gases.

The diffusive epidemic process models the spreading of an infectious disease [35, 36]. Two freely diffusing particle species which are referred to as "healthy" and "infected" populate a  $d$ -dimensional lattice. Sick particles infect healthy ones with a fixed rate but turn themselves healthy again after some time. Ignoring stochastic fluctuations, the DEP can easily be described using methods of non-linear dynamics that predict the existence of a continuous phase transition which is controlled by the particle density. What makes this system so interesting is the fact that even for parameter sets for which coexistence of infected and healthy particles constitutes a stable fixed point, the unstable extinction fixed point is an absorbing state. This means, deterministically the system never approaches it but if fluctuations bring the particle number of the infected species to zero it will remain extinct. Consequently, stochasticity plays a significant role and a more complex analysis is required to characterize the corresponding absorbing-state phase transition [37, 38].

Renormalization group methods predict the existence of three different regimes based on the ratio of the diffusion rates [36]. While the cases of identical diffusion speed and slower diffusion of the healthy particles are phenomenologically understood and universally considered to be continuous, the phase transition in systems with slower diffusion of the infected species has resisted classification for more than 20 years. Perturbative [36] and non-perturbative [39] renormalization group methods have been applied but did not yield any fixed point leading to the conclusion that the phase transition has to be discontinuous. This, however, is inconsistent with stochastic simulations that reported scaling behavior in lower dimensions, which implies a continuous phase transition [37, 40–46]. Unfortunately, these simulations, which rely on different approximation methods, are in turn partially inconsistent among each other.

Using our experiences with exact stochastic simulations [47–49] gathered throughout previous projects, in combination with measurements of dynamic spreading of activity [38, 50–52], we elucidate the ambiguities of the phase transition of the diffusive epidemic process in one dimension. By performing reliable data collapses, we prove the existence of a continuous phase transition. Furthermore, comparing the dynamics of the system for identical diffusion rates with our finding for slower diffusion of the infected species, we identify a mass-redistribution mechanism as a possible source of strong coupling behavior,

which explains the failure of perturbative mean-field methods. Finally, we argue that a homogeneous initial state represents a metastable configuration that does not allow for the correct measurement of all critical exponents, causing the differences compared to previous numerical studies.

## Research questions

Is the absorbing-state phase transition of the diffusive epidemic process always continuous? If the transition is indeed continuous what are the critical exponents? What is the reason for the discrepancies between renormalization group methods and previous numerical studies?

## Key findings

*The phase transition of the diffusive epidemic process is always continuous.*

Based on extensive stochastic simulations, we showed that a critical density exists close to which all data can be collapsed onto universal curves irrespective of the ratio of the diffusion constants. This allowed us to provide estimates of the critical exponents necessary to characterize the system. The existence of universal scaling contradicts a discontinuous phase transition.

*Activity spreads sub-diffusively in case of faster diffusion of the healthy species.*

One particularly interesting exponent is the dynamical exponent  $z = \nu_{\parallel}/\nu_{\perp} = 3$  for faster diffusion of healthy particles. On the one hand, its existence contradicts a discontinuous phase transition as predicted by perturbative renormalization group methods but also on the other hand previous numerical measurements imply  $z = 2$  in one dimension.  $z = 3$  can be interpreted as activity spreading sub-diffusively instead of diffusively at the phase transition, which shows that slower diffusion of infected particles indeed constitutes a special case.

*Mass redistribution is responsible for the anomalous behavior in the case of faster diffusion of healthy particles in one dimension.*

Resolving the temporal evolution of a cluster of infected particles over time, we found that the sub-diffusive spreading of activity indicated by  $z = 3$  is caused by mass redistribution. Because particles outside of the cluster are mainly healthy and are assumed to move at higher speed while infected particles inside the cluster have a reduced diffusion rate, a net flux of total mass into the cluster is created. This depletes the surroundings of the cluster such that it hampers its own expansion, resulting in the critical exponent  $z = 3$ . In a more general context, the effect is probably related to the cause of the strong coupling behavior that prohibits perturbative treatment.

---

## Exact stochastic simulations of reaction-diffusion systems in different geometries

Each of the systems analyzed in this thesis exhibits a different type of fluctuation-driven phenomenology. In contrast, the approximation methods that can be applied to derive a deterministic solution are comparably similar. Densities are used for the description of states instead of particle numbers and discrete lattice sites are replaced by continuous space. However, whether those approximations are indeed justified and under which conditions they break down is different for each system. In the end, the only tool that can be applied reliably without making any prior assumptions are exact stochastic simulations [47–49].

In my last project, which is discussed in Chapter 5, I provide means to study the effects of stochastic fluctuations beyond the systems investigated in this thesis. To this end, I created a framework which can be used to perform exact stochastic simulations of general reaction-diffusion activation-inhibition systems in different geometries. It provides a simple user interface in the form of a script language based on chemical equations. This enables usage without any need for a deeper understanding of the underlying program structures written in C++. Still, to allow for more flexibility, the framework is constructed in a modular form such that it can be easily extended in case additional functionality is needed for future research. Furthermore, since measurements of the dynamic spreading of activity [38, 50–52] in combination with exact stochastic simulations have proven very successful for the study of phase transitions of reaction-diffusion systems in Chapter 4, it has been integrated into the program as a native feature. Using the general framework, the diffusive epidemic process, for example, could now immediately be studied using a simple 7 lines script:

```
A + B -> 2B : 1
B -> A : 0.2
D: A = 1
D: B = *1
A = *2
B = 10
Ensemble1D(8192,1000000,250,False,results,*3,50000,B)
```

Chapter 5 serves as an introduction to the program itself as well as the script language and the usage of its features.

It is important to emphasize that this project is not intended to answer a particular research question but can be used for a systematic study of the role of stochastic effects in a broad class of systems. Its purpose is to find overarching patterns which further a general understanding.



# Chapter 2

## Geometry and arrangement: Molecular transport along microtubules

This chapter deals with the theoretical study of two-species transport of molecular motors along microtubules. It is based on research results I published as first author in the manuscript *Two-Species Active Transport along Cylindrical Biofilaments is Limited by Emergent Topological Hindrance* [53], in the journal *Physical Review X* 8(3), 031063 in 2018 (doi: 10.1103/PhysRevX.8.031063) under the CC BY 4.0 license together with Emanuel Reithmann [54] (who contributed equally) and Erwin Frey. In particular, simulation data and the graphical presentation thereof have been partially adopted.

The goal of the research project is to investigate and quantify how collective transport along a cylindrical structure is affected by the existence of different agents which are distinguished by their gaits. To this end, we created a minimal lattice gas model that can be used to study the emerging phenomenology in isolation. We do so by combining exact stochastic simulations with analytical results and mean-field approximation methods. Deviations between the different approaches are used to determine the relevance of stochastic effects and find their central determinants. Finally, we compare our results to previous research performed in the absence of a second species and discuss the implications of the differences in the context of the biological system. As a start, we give an introduction to molecular motors and their mathematical modelling as well as the experimental findings that motivated this project.

### 2.1 Biological background

The cytoskeleton provides eukaryotic cells with rigidity and plays a central role for their internal organization as well as their movement [55–58]. It consists of polar microtubules and actin filaments<sup>1</sup> which serve as tracks for molecular motors [59]. While actin filaments are comparably small and flexible, microtubules, on which we are focusing in this work,

---

<sup>1</sup>In addition, intermediate filaments exist which we ignore here because of their minor relevance in this context.

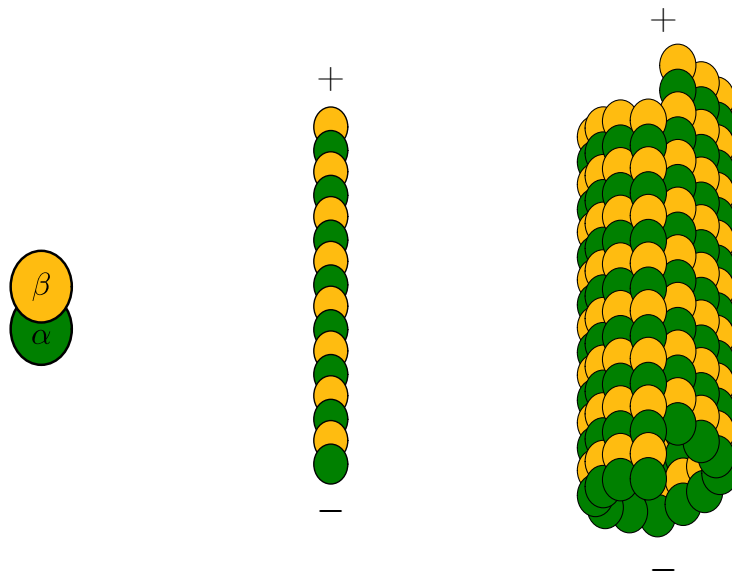


Figure 2.1: **Illustration of the microtubule structure.** Dimers which consist of alpha and beta tubulin serve as the fundamental building block (left panel). They bind and form rod-like structures called protofilaments (middle panel). Typically, 13 protofilaments compose the cylindrical microtubule (right panel). Because the tubulin dimers are a polar structures, so are the protofilaments and the final microtubule, which is indicated by the plus and minus signs.

constitute long and stiff cylindrical structures [57]. Their basic building block is the tubulin dimer which consists of alpha and beta tubulin. Due to their polar structure, those dimers bind linearly to each other and form long protofilaments. The filaments in turn (usually 13 [60]) bind laterally amongst each other and form the final microtubule, as illustrated in Fig. 2.1. Because of the polarity the filaments inherit from the tubulin dimers, the microtubule itself has a polar structure providing it with an orientation. This feature is used by different molecular motor families to perform directed transport along the microtubule via ATP consumption [58, 61, 62].

While motors of the kinesin family walk from the minus to the plus end [63, 64], members of the dynein family move in the opposite direction [65]. In this project, we are interested in the derivation of collective transport properties of different types of kinesin motors based on their individual behavior. For that reason, the motion of motors of the kinesin-1 family is discussed in more detail in the following.

Kinesin-1 motors have two head domains that bind to neighboring tubulin dimers [66, 67]. Via ATP consumption they perform unidirectional hand-over-hand motion towards the plus end of the microtubule [68–70]. Because of the two heads, kinesin-1 motors have a low detachment rate and walk processively over several micrometers along a single protofilament of the microtubule [61, 63, 71–73]. Furthermore, this mode of motion results in a constant step size with the length of a tubulin dimer. The motion of kinesin-1 motors is illustrated in Fig. 2.2.

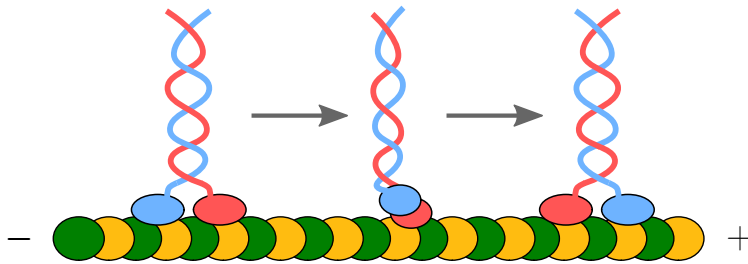


Figure 2.2: **Illustration of kinesin-1 type motor proteins.** Motor proteins of the kinesin-1 family feature two head structures that bind to the tubulin dimers of a microtubule. Using energy from the conversion of ATP to ADP they walk along a single protofilament in a hand-over-hand fashion from the minus end to the plus end.

In summary, kinesin-1 motors walk unidirectionally along a single protofilament with a fixed steps size. It is for this reason, that modelling of their collective behavior is based in particular on the totally asymmetric exclusion process, a one-dimensional lattice gas model for active transport. The next section provides an introduction to this fundamental far from equilibrium system.

## 2.2 The totally asymmetric simple exclusion process

*The totally asymmetric simple exclusion process* (TASEP) is a one-dimensional lattice gas model that was originally introduced in a biological context to describe the kinetics of biopolymerization [74]. However, because of its boundary induced phase transitions [13] it has turned into an extensively studied paradigmatic system in the field of non-equilibrium physics [75–79]. Furthermore, it has been applied to model transport phenomena in various different contexts ranging from ion channels to mRNA translation [3, 7–12].

Fig. 2.3 shows a schematic illustration of the model. Particles populate a one-dimensional lattice. Movement only takes place in the form of stochastic hopping events to the right next lattice site. Because the particles obey steric exclusion such an event is prohibited if the respective site is already occupied. Typically, open boundary conditions are applied. Particles enter the system on the left at an in rate  $\alpha$  — while obeying exclusion — and leave it on the right at an exit rate  $\beta$ . Using particle occupation numbers  $n_\mu \in \{0, 1\}$  to describe the current state of the  $\mu$ -th lattice site, the dynamics of the TASEP can be mathematically represented by a differential difference equation

$$\frac{d}{dt}n_\mu = \nu n_{\mu-1}(1 - n_\mu) - \nu n_\mu(1 - n_{\mu+1}). \quad (2.1)$$

Despite the simple appearance of this equation, solving it, in general, constitutes a significant challenge and was only achieved decades after the original introduction of the model [75, 76]. Interestingly, the TASEP can be studied very successfully by employing mean-field approximation methods [13, 80]. Because we are going to make extensive use

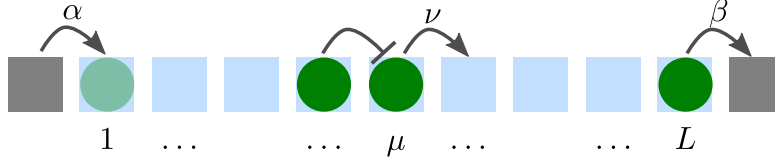


Figure 2.3: **Illustration of the totally asymmetric simple exclusion process.** Particles populate a one-dimensional lattice. They enter the system on the left at rate  $\alpha$  and leave it on the right at rate  $\beta$ . Movement takes place in the form of stochastic hopping events to the right at rate  $\nu$ . Because particles obey steric exclusion they are only allowed to enter the system or perform hopping events if the respective site is empty.

of these methods in this and the subsequent chapters, they are discussed in detail in the following.

Instead of the actual micro-states, the evolution of the macroscopic observables in the form ensemble averages are considered. In particular, according to Eq. 2.1 the time evolution of the particle density  $\rho_\mu := \langle n_\mu \rangle$  is given by

$$\frac{d}{dt}\rho_\mu = \nu\langle n_{\mu-1}(1 - n_\mu) \rangle - \nu\langle n_\mu(1 - n_{\mu+1}) \rangle =: J_\mu - J_{\mu+1}, \quad (2.2)$$

where  $J_\mu$  denotes the particle current towards the  $\mu$ -th lattice site. This corresponds to a discrete form of the continuity equation. Making the mean-field approximation  $\langle n_\mu n_\xi \rangle = \langle n_\mu \rangle \langle n_\xi \rangle$ , which amounts to the absence of correlations, the hierarchic of equations initiated by Eq. 2.2 can be brought into a closed form. If the system is further assumed to be in the stationary state for which  $d\langle n_\mu \rangle/dt = 0$  holds, Eq. 2.2 is reduced to

$$0 = \langle n_{\mu-1} \rangle (1 - \langle n_\mu \rangle) - \langle n_\mu \rangle (1 - \langle n_{\mu+1} \rangle) = \rho_{\mu-1}(1 - \rho_\mu) - \rho_\mu(1 - \rho_{\mu+1}), \quad (2.3)$$

which can simply be interpreted as current conservation. To further reduce the complexity of the problem, a continuous approximation can be performed. The discrete variable  $\mu$  is replaced by a continuous one  $\frac{\mu}{L} =: x \in (0, 1]$ . In this way, the density can be expanded in a Taylor series in terms of the lattice spacing  $\frac{1}{L} =: \epsilon$

$$\rho_{\mu+1} = \rho(x + \epsilon) = \rho(x) + \frac{d}{dx}\rho(x)\epsilon + \mathcal{O}(\epsilon^2). \quad (2.4)$$

Plugging the expanded density into the mean-field equation Eq. 2.3 a simple differential equation for the stationary density can be obtained

$$\begin{aligned} 0 &= \left( \rho(x) - \frac{d}{dx}\rho(x)\epsilon \right) (1 - \rho(x)) - \rho(x) \left( 1 - \rho(x) - \frac{d}{dx}\rho(x)\epsilon \right) + \mathcal{O}(\epsilon^2) \\ &= 2\rho(x)\frac{d}{dx}\rho(x)\epsilon - \frac{d}{dx}\rho(x)\epsilon + \mathcal{O}(\epsilon^2) \\ &= -\frac{d}{dx}\rho(x)(1 - \rho(x))\epsilon + \mathcal{O}(\epsilon^2) \\ &= -\frac{d}{dx}J(x)\epsilon + \mathcal{O}(\epsilon^2). \end{aligned} \quad (2.5)$$

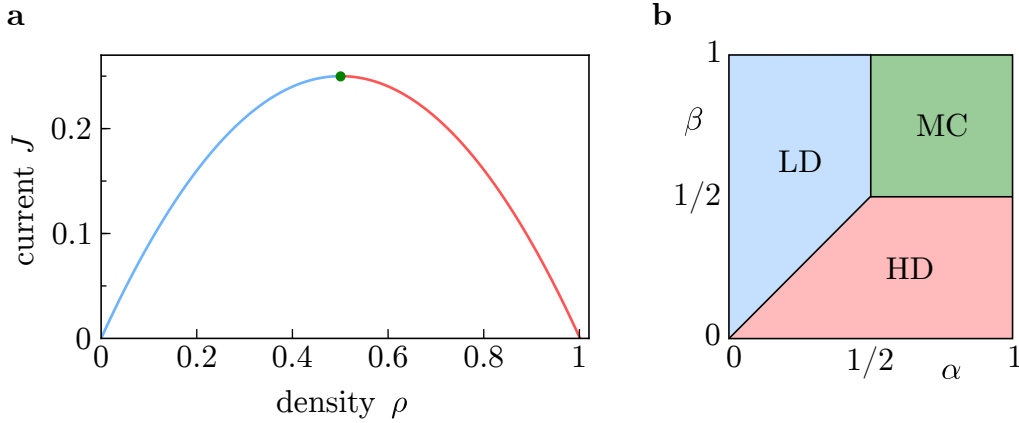


Figure 2.4: **Current-density relation and phase diagram of the TASEP.** Current and density have a strict relation. As shown in panel (a), for each density  $\rho$  there exists only one corresponding current  $J$ . Depending on the response of the current to a change in density different phases are characterized which are depicted in the phase diagram (b). For each combination of values of control parameters  $\alpha$  and  $\beta$  a specific density  $\rho$  and a specific current  $J$  are realized. The colors in (a) and (b) illustrate this correspondence.

Dividing by  $\epsilon$  and taking the number of lattice sites to infinity  $L \rightarrow \infty$  the lattice spacing vanishes  $\epsilon \rightarrow 0$  and the final approximation reads

$$J(\rho) = \rho(1 - \rho) = \text{const.} \quad (2.6)$$

This simple looking current conservation equation is known as the *current-density relation* and it is at the center of the TASEPs phenomenology. Importantly, on an infinite lattice the approximated solution Eq. 2.6 does not differ from the exact result [75–77]. The intuitive interpretation of its form is that movement from one site to the next can only take place if a particle is present—reflected by the factor  $\rho$ —and the site in front of it is empty, which is accounted for by the factor  $(1 - \rho)$ . This immediately implies that correlations are negligible in the stationary state for transport scenarios described by the TASEP.

The existence of a unique current-density relation can finally be used to derive the phase behavior of a system [13]. This phenomenological approach goes back to the work of Lighthill and Whitham [81]. Beyond the TASEP, it has since been applied to many different transport models [17, 82, 83].

In the context of the current-density relation Eq. 2.6 the in rate  $\alpha$  can be interpreted as a reservoir on the left end which causes a constant particle flux  $J_\alpha = \alpha(1 - \rho)$  into the system. Accordingly, the boundary condition at the right end can be realized by a density  $1 - \beta$  that corresponds to the current  $J_\beta = \rho\beta$ . The different currents at the two boundaries are actually a major discrepancy in general. Because the differential equation Eq. 2.5 is of first order, only a single free parameter in the form of the density exists. Either the left ( $\rho = \alpha$ ) or the right ( $\rho = 1 - \beta$ ) boundary condition can be fulfilled. The phenomenological

solution to this paradox situation provides the *extremal current principle* [13, 82, 84, 85]

$$J = \begin{cases} \max_{\rho \in [\rho_R, \rho_L]} J(\rho) & \text{if } \rho_L > \rho_R \\ \min_{\rho \in [\rho_L, \rho_R]} J(\rho) & \text{if } \rho_L < \rho_R \end{cases}. \quad (2.7)$$

Intuitively, it states that the boundary which is limiting the current dictates the behavior of the system. The current-density relation and the phase diagram according to the extremal current principle [13] are depicted in Fig. 2.4. Three different phases exist which are named according to their transport features. In the low-density phase (LD) the current is limited by a lack of particles in the system. Correspondingly, the high density-phase (HD) is controlled by the right boundary at which an abundance of particles limits transport. Finally, in the maximal current phase (MC) a density of  $\rho = 1/2$  is realized and neither of the boundaries but the particle exclusion itself is the most relevant factor. An important consequence of this phenomenological derivation that did not rely on any microscopic details is that every system that has the same current-density relation as the TASEP should have the same phase diagram structure.

One of the central reasons the TASEP has gained so much importance is its rich phenomenology which can be understood using the very intuitive arguments reviewed above. Furthermore, it has been extended in various ways to describe a plethora of transport phenomena ranging from different species [83, 86–91] to connected systems [9, 10, 85, 92–100] and entire networks [101–105]. One particularly successful application is the molecular transport along microtubules which is discussed in more detail in the next section.

### 2.3 Modelling active transport by molecular motors

As discussed in Sec. 2.1, molecular motors of the kinesin-1 family walk unidirectional from the microtubule’s minus to its plus end. Because of the hand-over-hand motion they perform using their two head domains which are attached to consecutive tubulin dimers, kinesin motors have a fixed step size. Adding the fact that they are extended objects which cannot circumvent each other or be bound at the same dimers at the same time, the TASEP appears to be a natural choice for the modelling of collective transport by such molecular motors. However, depending on the exact research question, several extensions may have to be made.

The arguably most successful model for collective transport by kinesin motors is the *TASEP with Langmuir kinetics* (TASEP LK) [14, 15]. In addition to the basic TASEP dynamics, random attachment and detach at all lattice sites is included. This mimics the interaction of molecular motor with the surrounding cytosol. To facilitate a competition between boundary effects and Langmuir kinetics in the bulk of the system a mesoscopic limit is assumed. The local attachment and detachment rates  $\omega_a := \Omega_a/L$  and  $\omega_d := \Omega_d/L$  scale with the inverse of the system length preventing complete domination of the bulk for large systems. The predictions made by the model, such as phase coexistence, have been confirmed by *in vitro* experiments [16]. Despite these astonishing results the application

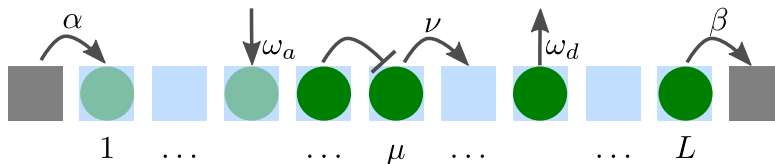


Figure 2.5: **Illustration of the TASEP with Langmuir kinetics.** In addition to the normal TASEP dynamics, particles can randomly attach and detach at arbitrary lattice sites. To facilitate actual competition between bulk and boundary effects, a mesoscopic limit is considered. The attachment rate  $\omega_a$  and the detachment rate  $\omega_d$  are assumed to scale with the inverse system length  $L$ .

to *in vivo* scenarios is still debated because motor concentrations in cells are considered too low to cause overcrowding. So, despite the model making correct predictions *in vitro*, the interesting physics may simply be not relevant *in vivo*.

Beyond the TASEP LK, models accounting for rare lane switching [10], internal states [9], extended or dimeric particles [106], finite resources [107], confined spaces [108] and microtubule length regulation [109, 110] have been developed to deepen the knowledge about the central determinants in molecular transport along microtubules. In particular, it has been shown that for single-species transport, even if switching events between protofilaments take place regularly, the transport behavior can still effectively be reduced to one dimension [17]. This finding nicely complements our results for multi-species transport that are explained in following.

## 2.4 Spiralling motion of motors and modelling

Despite kinesin-1 tracking only a single protofilament [73], members of other kinesin families have been shown to produce torsional forces while moving along the microtubule [111–114]. In fact, such behavior is observed for all super-families of molecular motors [115, 116]. This has important implications for the modelling of collective transport. While all results obtained are still valid for kinesin-1 they are in question for the other families. For kinesin-2 and kinesin-8 in particular, regular biased switching of protofilaments causing them to move on a handed spiral along the microtubule has been reported [18–20]. Transport performed according to this single molecule behavior exactly corresponds to the one theoretically studied by Curatolo et al. [17] which showed that the collective dynamics are basically unaffected—apart from the existence of transversal currents which do not contribute to the transport along the microtubule.

At this point, we face the question whether transport phenomena along microtubules are always well described using mean-field methods and can be reduced to one-dimensional continuous models. Because this thesis is concerned with the modification of phenomenology by stochastic fluctuations the general absence of those makes the respective systems unsuited for our purposes. This, however, changes drastically when we move from the study of the collective behavior of a single motor species to the interaction of multiple

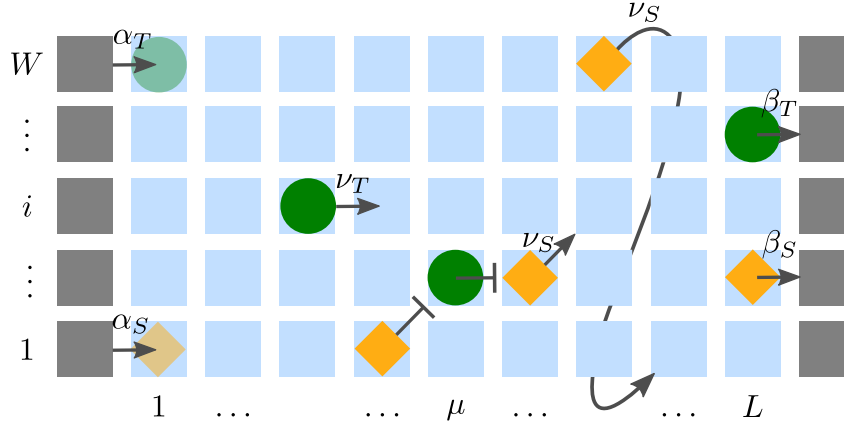


Figure 2.6: **Model for two-species molecular transport along microtubules.** Two different particle species  $S$  and  $T$  populate a two-dimensional lattice. They enter the system at respective rate  $\alpha_S$  and  $\alpha_T$  on the left and leave it at rates  $\beta_S$  and  $\beta_T$  on the right. Both species perform stochastic hopping events to the right at rates  $\nu_S$  and  $\nu_T$ . While the  $T$  species follows a single lane of the lattice, the  $S$  species, in addition to moving forward, jumps up one lane. At the top of the lattice periodic boundary conditions are applied. All particles obey steric exclusion with respect to both species which prohibits access to an occupied lattice site.

ones. Kinesin-1 is known to processively track single protofilaments while kinesin-2 or kinesin-8 motors walk along helical pathways. So, a natural question to ask is whether a system containing motors with different gaits that walk along a cylindrical structure can be reduced to one dimension via mean-field methods.

To study the effect of a second motor species with a different gait, we employ the extended model shown in Fig. 2.6. Two species populate a two-dimensional lattice consisting of  $W$  lanes with  $L$  lattice sites each. One species, called the lane tracking species  $T$ , follows the normal TASEP dynamics on each lane. The respective particles enter the lattice on the left at rate  $\alpha_T$  and leave it on the right at rate  $\beta_T$ . In the bulk,  $T$  particles hop at rate  $\nu_T$  to the right most lattice site on the same lane  $i \rightarrow i, \mu \rightarrow \mu + 1$ . The second species performs lane switching while walking across the lattice. For that reason, it is referred as the switching species  $S$ . At each hopping event a particle moves to the right next site on the upper next lane  $i \rightarrow i + 1, \mu \rightarrow \mu + 1$ . At the top of the lattice periodic boundary conditions are applied such that the  $S$  species walks in spirals from the left to the right end mimicking the behavior of kinesin-2 or kinesin-8 type molecular motors. Apart from its stepping behavior, the  $S$  species behaves in the same way the  $T$  species does. It interacts at rates  $\alpha_S$  and  $\beta_S$  with the right and left boundaries and all particles obey exclusion with respect to all other species irrespective of their type. As for the TASEP, the entire dynamics is considered to be stochastic. At this point, it is important to note that, because depending on the labelling of lattice sites each species can be considered the straight walking one, a corresponding symmetry exists. The system has to be invariant under  $T \leftrightarrow S$

transformations. We will refer to this as the *species exchange symmetry*. Using occupation numbers  $n_{i,\mu}^T, n_{i,\mu}^S \in \{0, 1\}$  to describe the current state of a lattice site, the corresponding time evolution of the system is given by a set of coupled differential difference equations

$$\begin{aligned} \frac{d}{dt}n_{i,\mu}^T &= \nu_T n_{i,\mu-1}^T (1 - n_{i,\mu}) - \nu_T n_{i,\mu}^T (1 - n_{i,\mu+1}), \\ \frac{d}{dt}n_{i,\mu}^S &= \nu_S n_{i-1,\mu-1}^S (1 - n_{i,\mu}) - \nu_S n_{i,\mu}^S (1 - n_{i+1,\mu+1}). \end{aligned} \quad (2.8)$$

In analogy to the TASEP, the currents for the individual species can be defined as  $J_{i,\mu}^S := \nu_S \langle n_{i-1,\mu-1}^S (1 - n_{i,\mu}^T - n_{i,\mu}^S) \rangle$  and  $J_{i,\mu}^T := \nu_T \langle n_{i,\mu-1}^T (1 - n_{i,\mu}^T - n_{i,\mu}^S) \rangle$ . Furthermore, the density of a species at a given lattice site reads  $\rho_{i,\mu}^T := \langle n_{i,\mu}^T \rangle$  and  $\rho_{i,\mu}^S := \langle n_{i,\mu}^S \rangle$ , respectively. Because of the similarities, two important conclusions can be drawn. First, finding an exact solution to this problem seems futile for now since already the solution to the TASEP admits an enormous complexity. Second, it might not be necessary to obtain an exact solution to understand and quantify the model in detail. So far, mean-field methods have been very successful in describing such systems. Accordingly, we may expect the same for this one.

## 2.5 Failure of mean-field

A central feature for the analytical study of our system to recognize is that it has a unique stationary state (if any). It is trivially ergodic since the lattice can be emptied completely and filled with any desired configuration. Because we are considering a continuous time Markov process this is sufficient to prove that the stationary state is unique [117]. As a consequence, each macroscopic observable has to adopt the rotational symmetry of the system in the stationary state, which we are interested in. A spontaneous symmetry breaking is not possible. Hence, when considering the stationary state all indices  $i$  referring to a specific lane can be dropped e.g.,  $J_{i,\mu}^S = J_\mu^S$ .

To facilitate the comparison with the TASEP, it is convenient to define a different set of control variables. The total in rate  $\alpha := \alpha_T + \alpha_S$  accounts for the total flux of particles into the system. Correspondingly,  $\delta = \alpha_S/\alpha \in [0, 1]$  denotes the ratio of  $S$  type particles<sup>2</sup>. For  $\delta = 0$  only  $T$  type particles are present. Similarly, for  $\delta = 1$  the entire system is populated by  $S$  particles. In both cases, the system is reduced to  $W$  independent TASEPs and all known results have to be recovered. In that sense,  $\delta$  is a measure for how much the system differs from the TASEP whereas  $\alpha$  keeps the original meaning. Another important realization to make is that, at the last lattice site, particle species are indistinguishable from each other apart from the rate at which they leave the system. Their gait does not matter anymore. However, because of particle conservation, we know that the ratio of particles of the respective types at the last lattice sites has to be  $\delta$ . This allows us to

<sup>2</sup>The species ratio  $\delta$  actually describes the ratio of currents  $J^S/(J^S + J^T)$  in the stationary state. In case of non-vanishing correlations, the density ratio  $\rho^S/(\rho^S + \rho^T)$  does not need to be identical. The effect is illustrated in Fig. C.2 of the Appendix.

calculate the time the last lattice site is on average occupied by an unknown particle. It is given by  $T := \delta/\beta_S + (1 - \delta)/\beta_T$ . This corresponds to an effective exit rate

$$\beta := T^{-1} = \frac{\beta_T \beta_S}{\delta \beta_T + (1 - \delta) \beta_S}. \quad (2.9)$$

The new control parameter fixes the total particle flux out of the system. Because of the definition of  $\delta$  the variables  $\beta_T$  and  $\beta_S$  combined contain redundant information that can be removed using only  $\beta$ . Fig. C.1 in the Appendix illustrates this effect. Finally, to reduce complexity we focus on the case of identical hopping rates  $\nu = \nu_T = \nu_S$ . Choosing an appropriate measure of time, we may assume  $\nu_T = \nu_S = 1$  without loss of generality in this case.

Using  $(\alpha, \delta, \beta)$  as our set of control parameters we find that the species exchange symmetry simply amounts to an invariance under  $\delta \rightarrow 1 - \delta$  transformations. This realization will be very useful for later considerations. Finally, defining the joint stationary state particle density  $\rho_\mu := \rho_\mu^T + \rho_\mu^S$  and current  $J_\mu := J_\mu^T + J_\mu^S$  we find that the total current into the system  $J_1 = \alpha(1 - \rho_1)$  and out of it  $J_{L+1} = \beta\rho_L$  are identical in structure and meaning to the TASEP. The boundary conditions are the same and all deviations have to be captured by  $\delta$ .

Going back to our original intention of deriving a mean-field approximation for Eq. 2.8 we find that in the stationary state the equations

$$\begin{aligned} 0 &= \langle n_{i,\mu-1}^T (1 - n_{i,\mu}) \rangle - \langle n_{i,\mu}^T (1 - n_{i,\mu+1}) \rangle \\ &= J_{i,\mu}^T - J_{i,\mu+1}^T \\ 0 &= \langle n_{i-1,\mu-1}^S (1 - n_{i,\mu}) \rangle - \langle n_{i,\mu}^S (1 - n_{i+1,\mu+1}) \rangle \\ &= J_{i,\mu}^S - J_{i+1,\mu+1}^S. \end{aligned} \quad (2.10)$$

have to hold. Employing the rotational invariance of the stationary state and making the mean-field assumption  $\langle n_{i,\mu}^X n_{j,\nu}^Y \rangle = \langle n_{i,\mu}^X \rangle \langle n_{j,\nu}^Y \rangle$ ,  $X, Y \in \{T, S\}$  we are left with two current conservation equations

$$\begin{aligned} J_\mu^T &= \rho_{\mu-1}^T (1 - \rho_\mu^T - \rho_\mu^S), \\ J_\mu^S &= \rho_{\mu-1}^S (1 - \rho_\mu^T - \rho_\mu^S). \end{aligned} \quad (2.11)$$

Summing both up, we find for the total current

$$J_\mu = \rho_{\mu-1}^T (1 - \rho_\mu^T - \rho_\mu^S) + \rho_{\mu-1}^S (1 - \rho_\mu^T - \rho_\mu^S) = \rho_{\mu-1} (1 - \rho_\mu). \quad (2.12)$$

This means, under the mean-field assumption—which was the only approximation made everything else only relied on stationary state properties—the system is reduced to  $W$  uncoupled TASEPs irrespective of the species fraction  $\delta$ .  $\alpha$  and  $\beta$  even have the same meaning as before. From here on we can apply exactly the same reasoning as in Sec. 2.2 to arrive at the current density relation

$$J = \rho(1 - \rho). \quad (2.13)$$

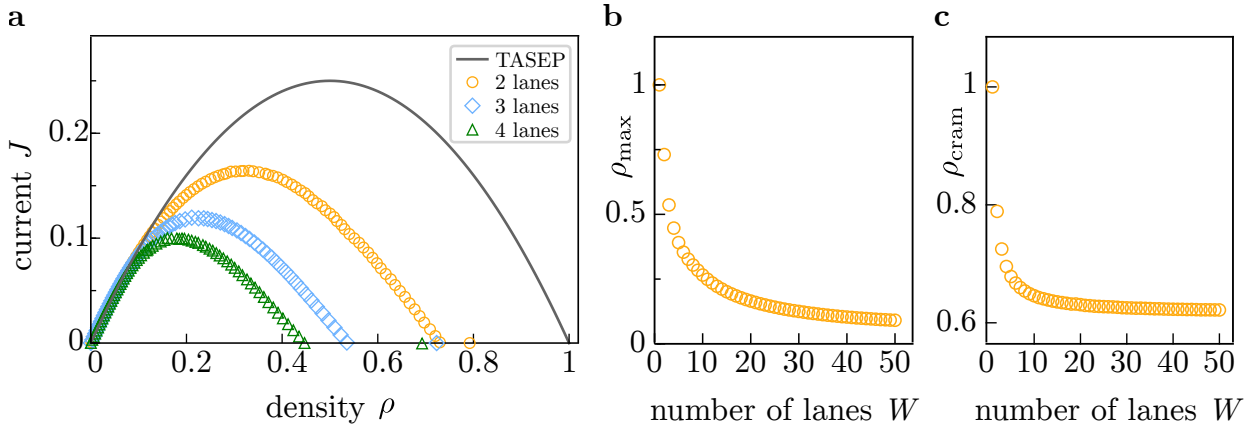


Figure 2.7: **Stochastic simulations of the current-density relation for  $\delta = 1/2$ .** In the same way as the TASEP, our model possess a current-density relation which is shown in panel (a). However, it strongly depends on the numbers of lanes  $W$ . Most importantly, for  $\beta \rightarrow 0$  and  $\beta = 0$  different densities are realized. The dependencies of  $\rho_{\max}$  ( $\beta \rightarrow 0$ ) and  $\rho_{\text{cram}}$  ( $\beta = 0$ ) on the number of lanes are shown in panels (b) and (c). [Parameters:  $L = 16384$ , (b)  $\alpha = 0.1$ ,  $\beta = 0.001$ , (c)  $\alpha = 0.001$ ,  $\beta = 0$ ; partially adapted from [53]]

So, if mean-field holds true there should be absolutely no difference between the TASEP and our system. In particular, the species ratio  $\delta$  should be irrelevant for the system and its phase behavior.

Fig. 2.7.a shows the current-density relation obtained for different numbers of lanes  $W$  using exact stochastic simulations according to the methods described in Appendix A.1. It becomes immediately evident that the basic mean-field approximation fails. Most prominently, a strong dependence on the number of lanes can be observed—a parameter that does not even exists in the mean-field theory. But still, all curves show the same characteristic shape. A unique current maximum that separates two regimes of different responses to a change in density. So, qualitatively the systems seem similar to the TASEP at first glance despite some apparent flaws in the mean-field argument. However, as it turns out the observed results are incompatible with a description purely based on a notion of density. The current vanishes for densities far below one and, as illustrated in Fig. 2.7.b, this maximal density  $\rho_{\max}$  which can be realized while still observing a finite current in the system monotonically decreases with the number of lanes. Furthermore, a discontinuity in the current-density relation exists indicating an additional phase transition. The density realized for vanishing current  $\rho_{\max}$  is actually different from the one right at zero, which we denote as  $\rho_{\text{cram}}$ . Both even show different convergence with respect to high lane numbers  $W$ . Whereas for  $\rho_{\max}$  no finite bound different from zero exists, the cramming density  $\rho_{\text{cram}}$  converges to a value close to 0.6 as illustrated in Fig. 2.7.c.

Summing up the results of this section, numerical findings show that standard mean-field methods and in particular the one used for the TASEP fail drastically when applied

to our system<sup>3</sup>. Whenever a density is used to describe the flow of a system complete arrest can only take place at maximum occupation because otherwise a finite chance for movement always exists. It is important to stress that, here the current does not just get very low or undetectable. Actually, a phase transition takes place when reducing the current to zero and it still does not cause the system to reach full occupation. To describe those effects, we need a modified theory that takes the previously neglected fluctuations into account that have to be the source of this behavior.

From the greater perspective of this thesis, the deviations found are exactly what we were looking for. We made a simple change to a well understood system that resulted in fluctuations that cause a significant change in phenomenology. Since this is most evident by the existence of the cramming and jamming densities and their discontinuous transition, a deeper study of them seems to be a good starting point for our analysis.

## 2.6 Particle arrangement and fluctuations

The best way to identify the cause of the abnormal behavior for low or zero exit rates  $\beta$  is to take an explicit look at the respective micro-configurations. Those are shown in Fig. 2.8 panels (a) and (b). As can be seen, despite no particle being able to move in both configurations there still exist empty lattice sites. Because of the particle arrangement none of those can be accessed by either species; It causes the system to arrest below full occupation for both systems. However, there are apparent differences between the two configurations. While the crammed system ( $\beta = 0$ ) looks more like a random surface growth process, the jammed state ( $\beta \rightarrow 0$ ) appears to be ordered. Transitioning from zero current to an infinitesimally small one apparently makes the system self-organize into sorted structures. How this happens and why is the central question of this section.

As shown in Fig. 2.8.c, two major new types of *indirect* interactions have been introduced to our system compared to the TASEP. The more intuitive configuration 1 is based on one particle blocking two others. This effectively couples different lanes and leads to a dependence of the systems dynamics on the explicit particle arrangement. Such an effect cannot be captured using densities for the description. Effect 2 is slightly subtler but plays a central role as well. Even if two neighboring particles are in front of two empty lattice sites it does not necessary imply that both hop at their normal rates. For different species sequential hopping is enforced leading to further current reduction.

If the in rate  $\alpha$  is sufficiently small, particles do not interact before they reach their right most possible position. In case of a crammed state this is their final position as well since nothing can leave the system to induce further movement. Only configurations of type 1 are relevant in this scenario. For the jammed state this is not the case. No matter how small the exit rate, particles will leave the system and hence cause rearrangement in

---

<sup>3</sup>A finite segment mean-field method as successfully applied to similar models [10] does not seem to be promising either. The strong dependence on the number of lanes indicates the presence of very long-ranged correlations which cannot be contained in a small subset of lattice sites.

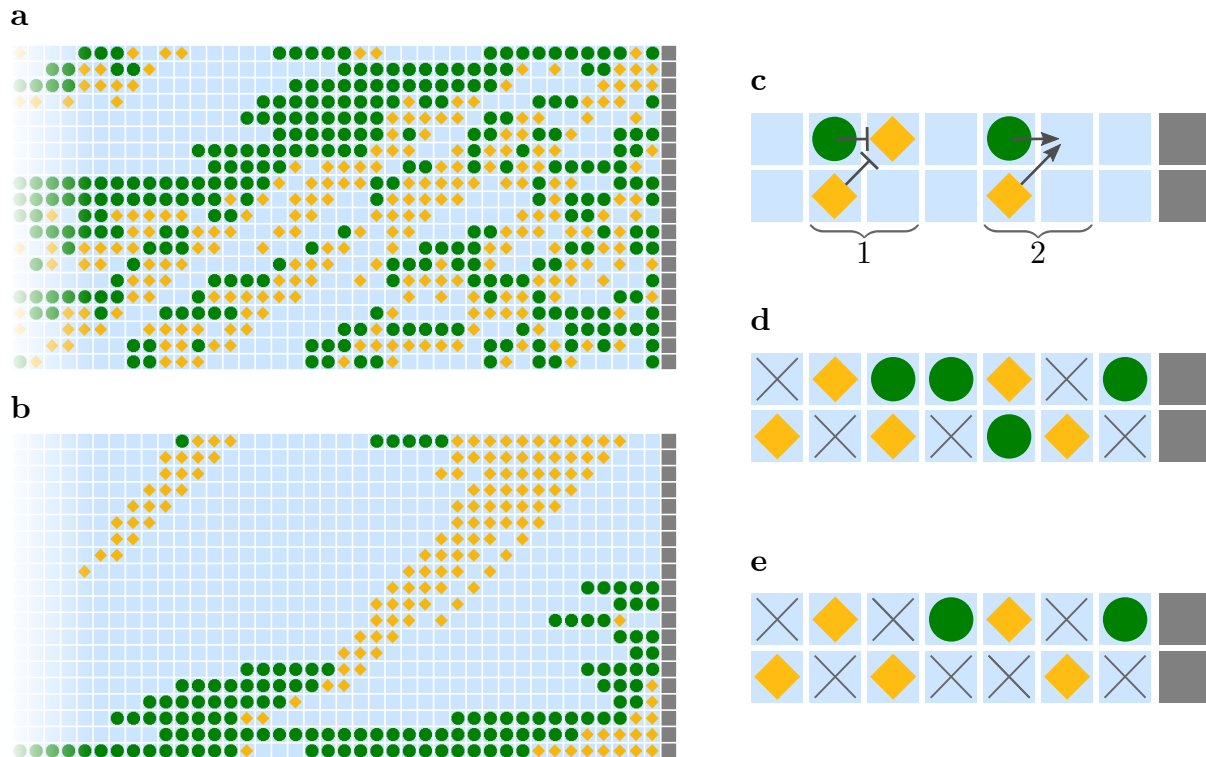


Figure 2.8: **Illustration of the phenomenological differences between jamming and cramming.** The panels (a) and (b) show configurations obtained in the cramming ( $\beta = 0$ ) and jamming ( $\beta \rightarrow 0$ ) parameter regime respectively. While the cramming configuration appears to be completely random the jamming configuration shows strong sorting. In both systems many empty lattice sites exist which cannot be accessed by any of the two species. Panel (c) depicts the particle configurations which cause the failure of mean-field. The more intuitive configuration 1 is one particle blocking the movement of two others. This is the static scenario. Configuration 2 is in contrast dynamic. Despite having two particles in front of two empty sites, an interaction exists because both are forced to hop sequentially. Only the static part 1 is relevant for the crammed state shown in panel (a). It is characterized by a random configuration whose density reduction is only caused by random double-blocking-configurations as illustrated in (d). Because in a stationary state with finite current each particle that leaves the system has to be replaced by a another one entering the system, overhead present for the cramming density is removed as shown in panel (e). This effect couples to the dynamic interaction 2 shown in part (c) and causes the sorting seen in panel (b).

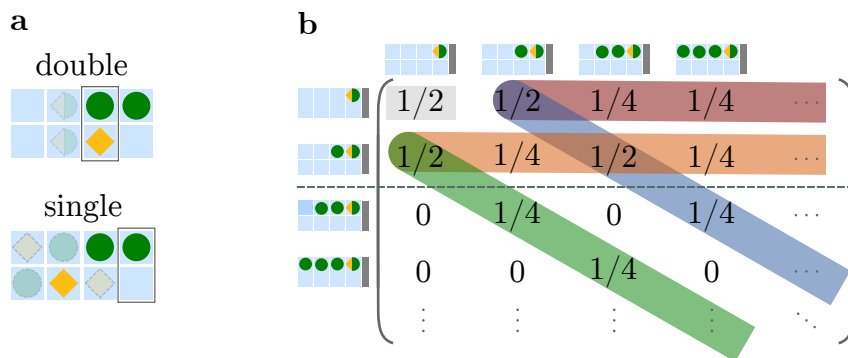


Figure 2.9: **Illustration of the state-reduction scheme.** Because of the existence of lane and species exchange symmetry, w.l.o.g. it is sufficient to only consider a sequence of  $T$  particles on the upper lane. If a particle of the  $S$  species enters the system a barrier is created that can no longer be passed. Depending on the lane, it is either a two-particle barrier at the front or a single particle barrier two lattice sites behind it, as shown in panel (a). This allows for a state reduction by only taking the part of the system into account that can still be subject to change. The transition rates between those sub-configurations at the front are given by the matrix shown in panel (b). The green line indicates particle sequence growth, the blue line shrinking. Red and orange correspond to a double or single closing of the state. The dashed line marks the region in which the matrix is completely regular. [partially adapted from [53]]

the system resulting in a contribution of both scenarios 1 and 2. This makes crammed state the better one to study.

To get an understanding of the central determinants of the cramming density we are going to derive an exact analytic solution for the totally symmetric case  $\delta = 1/2$  in a two-lane system. As the first step, we create a new stochastic process solely based on the surface-growth dynamics called the *filling process*. For  $\alpha \rightarrow 0$  and  $\beta = 0$  time in the previous form becomes meaningless. Whenever a particle enters it will pass through the system until it reaches a position which is stable and remains there. A second particle enters at a random time afterwards but how much later exactly is irrelevant. The same is true for all hopping events before reaching the final position. The most natural measure of "time" passing in this case is simply the number of particles entering the system. The according states are the stable particle configurations starting from the right end. This way, the corresponding state space we are confronted with is still infinite but as illustrated in Fig. 2.9.a can be made very regular.

The key idea is that certain configurations exist which make everything to their right irrelevant for the future evolution of the system. Any state can be decomposed into a sequence of sub-states ending with such a closing configuration. Only the last one decides on the further evolution of the system. This means the entire dynamics can be reduced to a discrete time Markov process characterized by the transition matrix that acts on the sub-configurations shown in Fig. 2.9.b. The configurations in the end are just sequence

of identical particles on the same lane with the other lane remaining empty. Whenever a particle of the other species enters the system a closure is created and the length of the front-state is reduced.

To actually calculate the cramming density, we first need the stationary sub-configuration probability vector  $P^{\text{st.}}$  the system converges to. It describes how the front of the surface-growth process looks on average. As the transition matrix in Fig. 2.9.b has a very regular structure, we write the vector in the form

$$P^{\text{st.}} = \begin{pmatrix} a \\ b_0 \\ b_1 \\ b_2 \\ \vdots \end{pmatrix}, \quad (2.14)$$

anticipating the final result. The first and second state differ from the other ones as a transition to one of those is always possible (red and orange lines). For all other states however, just two scenarios exist. Either a large sequence shrinks by one element (blue line) or a smaller one increases by one (green line). This observation can be turned into a recursion equation

$$b_n = \frac{1}{4} (b_{n-1} + b_{n+1}), \quad n \geq 1. \quad (2.15)$$

Equations of this type have a well-defined general solution

$$b_n = c_1 (2 + \sqrt{3})^n + c_2 (2 - \sqrt{3})^n, \quad n \geq 1. \quad (2.16)$$

Because a probability vector needs to be normalizable and  $(2 + \sqrt{3})^n$  diverges as  $n \rightarrow \infty$ ,  $c_1 = 0$  follows immediately. The second constant can be found using the equation obtained for the first element  $b_1 = \frac{1}{4} (b_0 + b_2)$  which implies  $b_0 = c_2 (2 - \sqrt{3})^0 = c_2$ . In this way, we find that the solution to the recursion equation reads

$$b_n = b_0 (2 - \sqrt{3})^n. \quad (2.17)$$

It retroactively explains the choice to name the second vector component  $b_0$  despite being different from the others. For later progress it is useful to note that

$$\sum_{n=0}^{\infty} b_n = b_0 \sum_{n=0}^{\infty} (2 - \sqrt{3})^n = \frac{b_0}{\sqrt{3} - 1}, \quad (2.18)$$

which is the geometric series of all sequence elements. Using this relation in combination with the state transitions rates given in Fig. 2.9.b, we obtain a simple expression for the first vector component

$$a \stackrel{!}{=} \frac{b_0}{2} + \frac{1}{2} \sum_{n=0}^{\infty} b_n = \frac{b_0}{2} \left( 1 + \frac{1}{\sqrt{3} - 1} \right), \quad (2.19)$$

which depends only on the second vector component  $b_0$ . The value of  $b_0$  itself can finally be fixed by demanding that the probability vector has to be normalized<sup>4</sup>

$$1 \stackrel{!}{=} \|P^{\text{st.}}\|_1 = a + \sum_{n=0}^{\infty} b_n = b_0 \left( \frac{1}{2} + \frac{3}{2\sqrt{3}-2} \right). \quad (2.20)$$

Taking all information together the stationary probability vector reads

$$P^{\text{st.}} = \begin{pmatrix} 2\sqrt{3}-3 \\ 6\sqrt{3}-10 \\ (6\sqrt{3}-10)(2-\sqrt{3}) \\ (6\sqrt{3}-10)(2-\sqrt{3})^2 \\ \vdots \end{pmatrix}. \quad (2.21)$$

Unfortunately, it is still not sufficient to calculate the final density. A naive approach would be to just weight the densities of the respective states by their probability to obtain an expectation value but this is a misinterpretation. A state being at the front of the surface with a given probability in discrete time does not imply that it occurs that often in the actual configuration of the system. A particle sequence of length three may just grow into a sequence of length four and hence simply vanish. In fact, the states themselves are not as relevant as the transitions between them. Only if a sub-configuration stops growing, at the right end a permanent contribution to stationary state of the system as a whole is created. As illustrated in Fig. 2.10, there are four equally likely transition scenarios for each state. Depending on the length of the considered sequence  $l$  the contribution of particles to the stationary state of the system per unit time  $N_l$  can be calculated. It is the probability of having the respective configuration at the front of the system  $P_l^{\text{st.}}$  times the expected number of contributed particles

$$N_l = \frac{1}{4} P_l^{\text{st.}} \sum_{k=1}^4 p_{lk} = \frac{1}{4} P_l^{\text{st.}} (2l+2). \quad (2.22)$$

Here,  $p_{lk}$  denotes the number of particles a sequence of length  $l$  contributes during the  $k$ -th transition according to Fig. 2.10. From the length dependent particle contributions  $N_l$ , the total number of particles contributed to the stationary state of the whole system per unit time  $N$  can be calculated

$$N = \sum_{l=1}^{\infty} N_l = a + \sum_{n=0}^{\infty} b_n \left( \frac{1}{2}n + \frac{3}{2} \right). \quad (2.23)$$

For this equation we used  $P_1^{\text{st.}} = a$  and the fact that the length of a particle sequence  $l$  is directly related to the  $b_n$ -sequence index via  $l = n + 2$ . In the same way, it is possible to

---

<sup>4</sup>Since we are solving an eigenvalue problem and we know by now that  $P^{\text{st.}} = b_0 \hat{P}^{\text{st.}}$ ,  $b_0$  cannot be determined using the remaining second equation. It has to be linear dependent by construction.

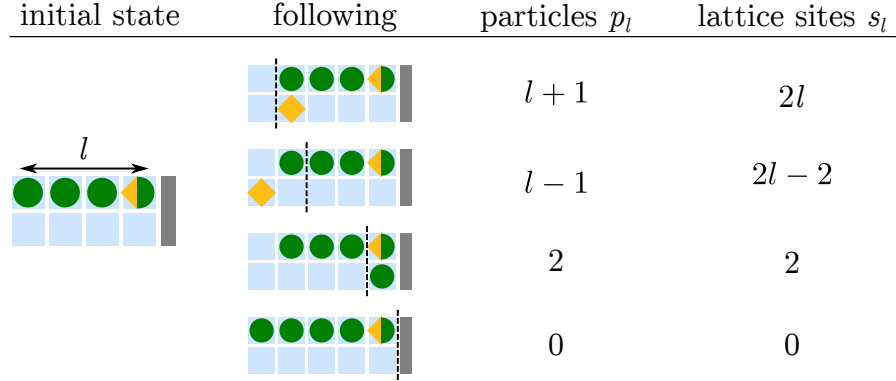


Figure 2.10: **Contributions to the stationary state by the different transition types.** Depending on the state a particle sequence transitions to, another sub-configuration of the stationary state is fixated. For each case four different scenarios are possible which are all equally likely.

derive  $Z$ , the total number of lattice sites contributed per unit time

$$Z_l = \frac{1}{4} P_l^{\text{st.}} \sum_{k=1}^4 s_{lk} = \frac{1}{4} P_l^{\text{st.}} (4l), \quad (2.24)$$

$$\Rightarrow Z = \sum_{l=1}^{\infty} Z_l = a + \sum_{n=0}^{\infty} b_n (n + 2),$$

where  $s_{lk}$  denotes the number of lattice sites a sequence of length  $l$  contributes during the  $k$ -th transition. To actually calculate  $N$  and  $Z$ , we need in addition to the geometric series Eq. 2.18 a second series which is closely related

$$\sum_{n=0}^{\infty} n b_n = b_0 \sum_{n=0}^{\infty} n (2 - \sqrt{3})^n = \frac{b_0(2 - \sqrt{3})}{(\sqrt{3} - 1)^2} = \frac{b_0}{2}. \quad (2.25)$$

Finally, to obtain the cramming density which is the average particle occupation of the filling process' stationary state we need to divide the total particle contribution per unit time  $N$  by the lattice site contribution  $Z$ . This results in

$$\rho_{\text{cram}} = \frac{N}{Z} = \frac{\frac{1}{2} \left( 1 + \frac{1}{\sqrt{3} - 1} \right) + \frac{1}{4} + \frac{3}{2\sqrt{3} - 2}}{\frac{1}{2} \left( 1 + \frac{1}{\sqrt{3} - 1} \right) + \frac{1}{2} + \frac{2}{\sqrt{3} - 1}} \approx 0.789, \quad (2.26)$$

which is exactly the numerical value given in Fig. 2.7. As discussed in detail in Appendix B.1 the applied method can be generalized to arbitrary species ratios  $\delta$ . All main steps and ideas are identical but the computational effort is significantly higher. The final result

$$\rho_{\text{cram}}(\delta) = \frac{\sqrt{\frac{1}{(1-\delta)^2} - 1} - 1 - \delta \left( \sqrt{\frac{1}{(1-\delta)^2} - 1} + \sqrt{\frac{1}{\delta^2} - 1} - 2 \right)}{4\delta - 2}, \quad (2.27)$$

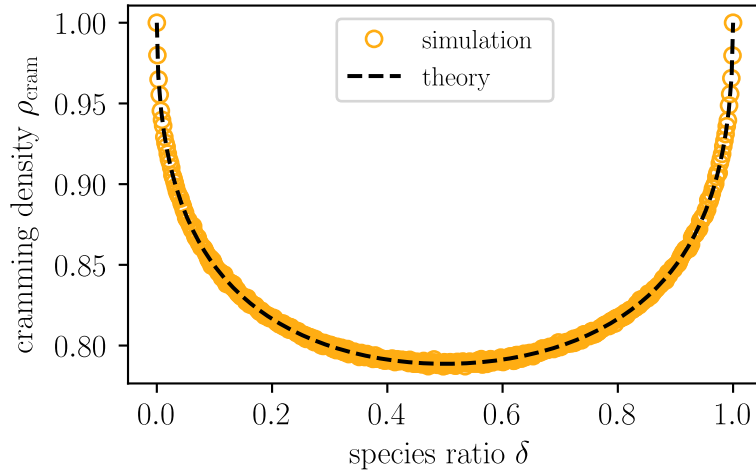


Figure 2.11: **Cramming density plotted against the species ratios  $\delta$  for two lanes.** The analytic theory (dashed line) and the exact stochastic simulations (yellow circles) are in perfect agreement. The shape of the curve nicely illustrates the species exchange symmetry  $\delta \rightarrow 1 - \delta$ . [Parameters:  $L = 131072$ ,  $\alpha \rightarrow 0$  (special simulation),  $\beta = 0$ ]

is shown in Fig. 2.11 together with data obtained from exact stochastic simulations. Both are in perfect agreement. Since for the filling process actual time and hence hopping rates are irrelevant, the solution applies to different hopping rates  $\nu_T$  and  $\nu_S$  as well. So, for the two-lane system we derived the most general solution possible.

At this point, it is important to emphasize that, absolutely no approximations have been made in the above derivation. Just all symmetries of the two-lane system have been exploited. This has two central implications. First of all, we have given a proof of principle showing that our qualitative understanding of the mechanics of our model is correct and can be quantified. However, secondly, we have seen that all symmetries possible have been used but still a complex solution had to be specifically tailored to the problem. Hence, an extension of the method to higher lane numbers seems futile. Already for three lanes a comparable state reduction is out of the question. Maybe a solution for an infinite lane number could be approximately derived using method employed in the field of surface growth. But so far, no suitable mapping could be found.

All previous considerations with regard to an exact quantification of the systems behavior only addressed the zero-current case  $\beta = 0$ . Adding correlation effects caused by dynamical particle interactions make the chance for an analytic solution even lower. The phase transition for infinitesimal  $\beta$  is a peculiarity of this. From the perspective of this thesis, one of the central goals was already achieved. The considered system shows a strong change in phenomenology because of a minor modification which we managed to understand and, at least to small extend, quantify. With respect to the biological motivation however, approximative solutions to the dynamical case are more relevant because that is where molecular transport operates. The first step in this direction is to understand how

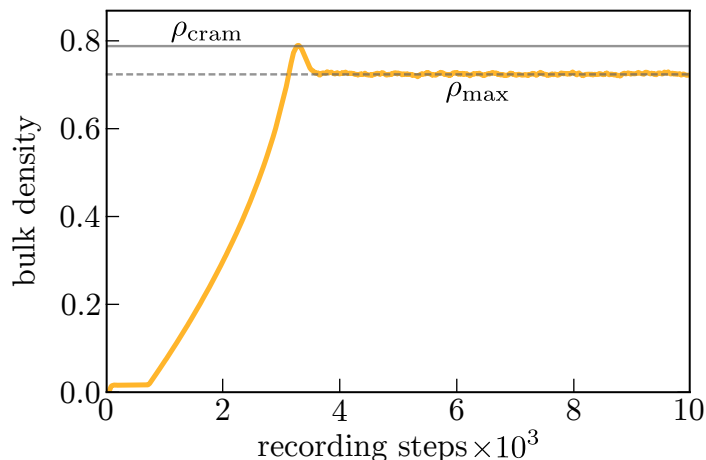


Figure 2.12: **Cramming to jamming transition.** In the limit  $1 \gg \alpha \gg \beta$  a separation of time scales exists. First, the system is filled with particles up to the cramming density on a time scale controlled by  $\alpha^{-1}$ . Afterwards, on a time scale  $\beta^{-1}$  the system approaches its true stationary state which is characterized by the maximal density  $\rho_{\max}$ . To resolve both processes, progression is measured in events instead of physical time. [Parameters:  $W = 2$ ,  $L = 16384$ ,  $\delta = 1/2$ ,  $\alpha = 0.02$ ,  $\beta = 0.0001$ ; adapted from [53]]

the sorted jammed states of the maximum density  $\rho_{\max}$  differ from the disordered crammed states we managed to quantify.

Both densities correspond to stationary states of different processes. The crammed state is a growth process in an infinite system; Once a particle reaches its position it remains there. In contrast, the jammed stationary state is caused by constant rearrangement in a restricted area. No matter how small the exit rate, each particle leaving the system has to be replaced by a new one entering. This thins out the number of particles drastically and causes the discontinuity in the system (Fig. 2.8 (d) and (e)). Furthermore, the dynamic interactions result in self organized sorting. This intuition is actually confirmed by Fig. 2.12. A system with very low exit rate first fills up completely before on a second time scale the rearrangement takes place because of particles leaving the system. An empty system approaches the jammed state via a crammed configuration that sorts itself.

Finding a solution for the maximal density for arbitrary numbers of lanes appears to be a hopeless task. The system cannot be reduced as for the cramming density because the interactions throughout the entire movement across the lattice have to be considered. But at this point, it is actually of minor importance. We understand the mechanism behind it and managed to form an understanding of the mechanics which have been confirmed by proofs of principle. The relation between particle arrangement, fluctuations and those singular densities has gotten clear. Extending those ideas to higher lane numbers would be a nice mathematical result but it would not further the overall understanding too much. The more interesting question remaining now is: How do all those additional fluctuations affect actual transport instead of jammed states? Taking the existence of  $\rho_{\max}$  and  $\rho_{\text{cram}}$

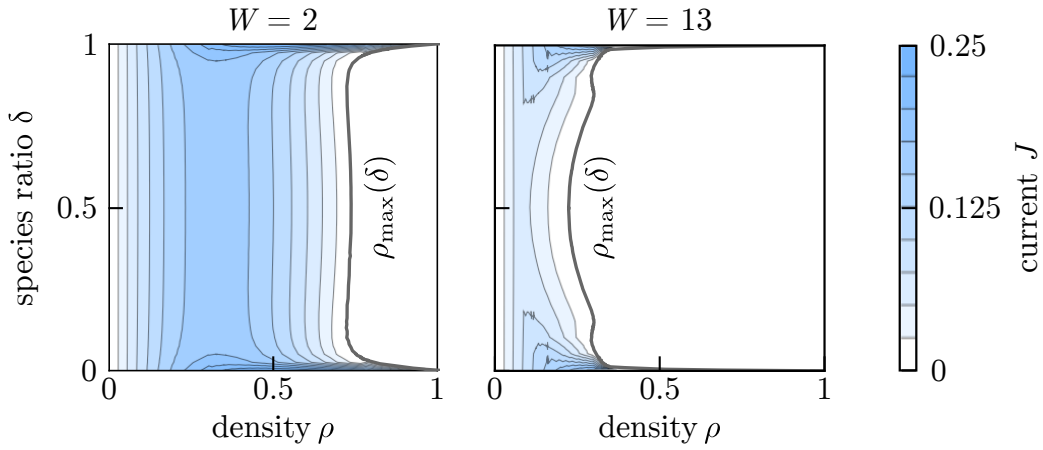


Figure 2.13: **Extended current-density relation.** In addition to the density, the current depends on the number of lanes  $W$  and species ratio  $\delta$ . Densities above  $\rho_{\max}$  are never realized in a stationary state. For high enough numbers of lanes this effect dominates the entire transport process. [Parameters:  $L = 16384$ ; adapted from [53]]

for granted the next section deals with the extrapolation of their impact on transport.

## 2.7 Quantifying the impact on transport

As a consequence of describing our system in terms of the total density  $\rho$  instead of the species specific ones  $\rho^S$  and  $\rho^T$ , the current-density relation depends on the species ratio  $\delta$ . Furthermore, because of long-ranged correlations, the number of lanes  $W$  has also to be taken into account. However, as can be seen in Fig. 2.13 the qualitative behavior remains similar to the TASEP. The major difference only lies in the value of  $\rho_{\max}$  that limits the overall transport potential. For a fixed value of  $\delta$  we still find a normal current-density relation. It is just shrunk to the interval  $[0, \rho_{\max}]$ . Based on the approach by Lighthill and Whitham and the extremal current principle as discussed in Sec. 2.2 we can at least expect a similar phase behavior in this region despite mean-field failing. Anticipating the desired outcome, it is hence possible to create an effective theory around a regular current-density relation which however manages to incorporate the significance of stochastic fluctuations.

We start by rewriting the particle currents as

$$\begin{aligned} J_{\mu}^S &= \rho_{\mu-1}^S(1 - \rho_{\mu}) - \text{cov}(n_{i-1,\mu-1}^S, n_{i,\mu}), \\ J_{\mu}^T &= \rho_{\mu-1}^T(1 - \rho_{\mu}) - \text{cov}(n_{i,\mu-1}^T, n_{i,\mu}), \end{aligned} \quad (2.28)$$

with  $\text{cov}(n_{i,\mu}^X, n_{l,\nu}^Y) = \langle n_{i,\mu}^X n_{l,\nu}^Y \rangle - \langle n_{i,\mu}^X \rangle \langle n_{l,\nu}^Y \rangle$  denoting the covariances. This form facilitates a comparison to the current-density relation of the mean-field solution. Because of the rotational invariance of the stationary state we can drop the lane index  $i$  in general—it only appears inside the covariances to indicate relative lane positions. Summing up both

currents we arrive at a joined current-density relation which we know has to reproduce the TASEP results for  $\delta = 0$  and  $\delta = 1$

$$\begin{aligned} J &= \rho_{\mu-1}(1 - \rho_{\mu}) - \text{cov}(n_{i-1,\mu-1}^S, n_{i,\mu}) - \text{cov}(n_{i,\mu-1}^T, n_{i,\mu}) \\ &= \text{const.} \end{aligned} \quad (2.29)$$

For reasons which become clear later, we define the hindrance function at lattice column  $\mu$

$$H_{\mu} := \frac{\text{cov}(n_{i-1,\mu-1}^S, n_{i,\mu}) + \text{cov}(n_{i,\mu-1}^T, n_{i,\mu})}{\rho_{\mu-1}}. \quad (2.30)$$

This allows us to rewrite the—so far still exact—current-density relation

$$J = \rho_{\mu-1} (1 - H_{\mu} - \rho_{\mu}). \quad (2.31)$$

In this form it is easy to see under which conditions the current may vanish. Either for an empty lattice with  $\rho = 0$  or for  $\rho = 1 - H_{\mu}$ . Comparing this to the TASEP we find an intuitive interpretation for the hindrance function. Normally, all lattice sites may contribute to transport and only if they are fully occupied transport stops. This is reflected by the factor of  $1 - \rho$ . In contrast, because of particle arrangement, not all lattice sites can contribute to transport at all times. The availability is reduced by  $H_{\mu}$ . This means understanding  $H$  is the key to quantifying the impact of arrangement effects. Unfortunately, because of the covariances used to define  $H_{\mu}$ , Eq. 2.31 still defines an unclosed set of equations and we have to rely on approximation methods to make further progress.

Assuming a slowly varying density profile in space, we can perform a continuous approximation as explained in Sec. 2.2

$$J = \rho(x) [1 - H(x) - \rho(x)]. \quad (2.32)$$

This assumption is actually the most severe simplification we make as will be discussed later. Now, realizing that the system has to obey current conservation, this directly implies that the hindrance function can only depend on the local density and not explicitly on the respective location

$$J = \rho [1 - H(\rho) - \rho]. \quad (2.33)$$

At this point, we have reduced the problem to the derivation of the hindrance function in dependence of the local density  $\rho$ . In the following, we will do so by expanding the function based on the physical properties we are expecting based on physical arguments. To make our lives easier, we split the hindrance function into two regimes.  $H_{\text{LD}}$  corresponds to the regime in which the current increases if the density increases and  $H_{\text{HD}}$  corresponds to the opposite case. We now use extremal density limits in the respective regimes  $\rho \rightarrow 0$  and  $\rho \rightarrow \rho_{\text{max}}$  to derive the linear order coefficients of a Taylor series.

For the low-density regime two major properties can be found

$$H_{\text{LD}}(0) = 0, \quad (2.34)$$

$$\left. \frac{d}{d\rho} H_{\text{LD}}(\rho) \right|_{\rho=0} = \delta(1 - \delta). \quad (2.35)$$

The first one simply accounts for the fact that on an empty lattice, particles do not interact and hence no correlations are formed. The second equation is an exact analytic result that is derived by requiring mean-field to hold in the limit  $\rho \rightarrow 0$  because particle interactions vanish. The detailed calculations are given in Appendix B.2.

In a similar way, in the high-density regime the equations

$$1 - H_{\text{HD}}(\rho_{\text{max}}) \stackrel{!}{=} \rho_{\text{max}}, \quad (2.36)$$

$$\left. \frac{d}{d\rho} H_{\text{HD}}(\rho) \right|_{\rho=\rho_{\text{max}}} = -\delta(1 - \delta)\rho_{\text{max}}, \quad (2.37)$$

are required to hold. The first is true by the definition of the maximal density as it corresponds to the point at which the current vanishes. The second the equation is the only approximative one. It is derived by calculating the effect of removing a single particle from a completely jammed system assuming a mean-field distribution of species. The details are provided in Appendix B.2.

Since the linearly approximated hindrance functions do not intersect in the relevant interval  $[0, \rho_{\text{max}}]$  additional equations are needed to define a physically meaningful result. Interestingly, a reason for this problem lies in the negative derivative of the hindrance function  $H_{\text{HD}}$  at maximum density. Later on, we will find that the prediction is actually correct despite being counterintuitive in the beginning. More density causes less inaccessible lattice sites. The explanation goes back to the different kinds of interactions shown in Fig .2.8. A dynamical and a static component exist but in a completely jammed system the dynamical one cannot contribute. Close to the maximum density the reduction of dynamical effects is larger than the increase by the static interaction. Despite being just a small detail, this nicely connects to the understanding we built up initially.

The final needed conditions are obtained by taking the transition between both phases into account<sup>5</sup>. As it has to be the point where neither a lack of particles nor an abundance limits transport it has to take place at the maximal current. Accordingly, the derivatives of both functions have to vanish

$$H_{\text{LD}}(\rho_{\text{MC}}) = H_{\text{HD}}(\rho_{\text{MC}}), \quad (2.38)$$

$$\left. \frac{d}{d\rho} \rho(1 - H_{\text{LD}}(\rho) - \rho) \right|_{\rho=\rho_{\text{MC}}} = 0, \quad (2.39)$$

$$\left. \frac{d}{d\rho} \rho(1 - H_{\text{HD}}(\rho) - \rho) \right|_{\rho=\rho_{\text{MC}}} = 0. \quad (2.40)$$

Using the set of seven equations, for a fixed number of lattice sites  $W$  the hindrance

---

<sup>5</sup>It is important to emphasize that, we do not postulate the hindrance function to be of second order. It is just the lowest expansion which yields a physically meaningful result. In fact, it would be possible to predict higher order derivatives for further approximation. But in the end, this does not improve our understanding of the mechanism itself; It just makes the approximation slightly better. However, we can get as precise estimates as we want from the stochastic simulations. The analytic part just validates our phenomenological understanding.

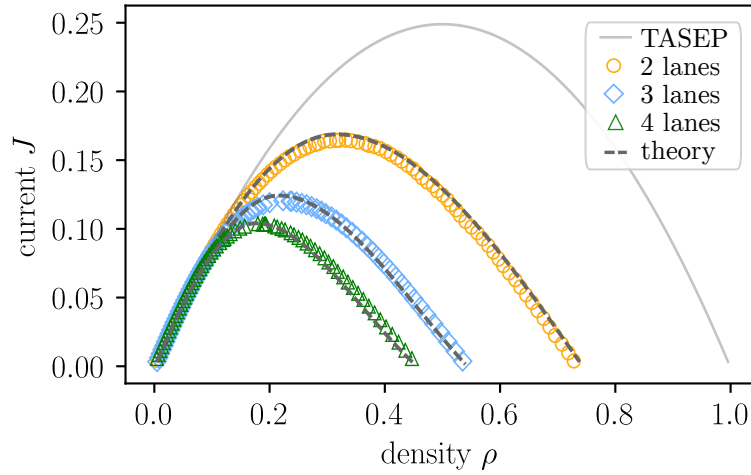


Figure 2.14: **Comparison of the current-density relations derived using the hindrance function with stochastic simulations.** The theory (dashed lines) and stochastic simulations (symbols) are in good agreement. [Parameters:  $L = 16384$ ,  $\delta = 1/2$ ; adapted from [53]]

function can be approximated up to second order in the density assuming knowledge of the respective maximal density. The results for different numbers of lanes are shown in Fig. 2.14. The good agreement between theory and simulations confirms our effective approach. In essence, it interpolates the influence of particle arrangement and fluctuations between the two extremal cases of an empty and a completely jammed system. The first case can be handled exactly the second one can be well approximated using the understanding gained in the previous section.

As a final proof of concept, we can use Eq. 2.30 to derive an expression for the covariances in terms of the hindrance function

$$\text{cov}(n_{i-1,\mu-1}^S + n_{i,\mu-1}^T, n_{i,\mu}) \approx \rho H(\delta, W; \rho), \quad (2.41)$$

To be more explicit, we included the dependencies on the control parameters  $\delta$  and  $W$ . As shown in Fig. 2.15 the correct covariances are indeed recovered. This again confirms our understanding of the system's dynamics. The last thing that is now left is the derivation of the dependencies on the control parameters  $\alpha$  and  $\beta$  and hence the phase diagram.

## 2.8 Control parameters and phase diagram

After deriving the effective current-density relation in the previous section, the final step to the full characterization of our model is to find the actual phase diagram. We know by the extremal current principle that the topology will be similar to the TASEP. Furthermore, the behavior in the respective phases will be controlled by one of the boundaries or the

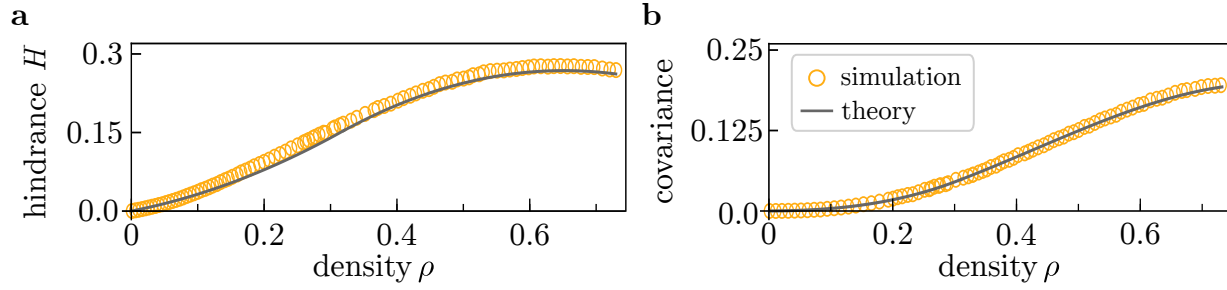


Figure 2.15: **Derivation of the covariances from the hindrance function.** Panel (a) shows the hindrance function derived for a two-lane system with symmetric species ratio  $\delta = 1/2$ . Employing Eq. 2.30, it can be translated into the respective covariances hampering transport. The corresponding result (line) is shown in panel (b) and is in good agreement with the stochastic simulations (symbols). [Parameters:  $W = 2$ ,  $L = 16384$ ; adapted from [53]]

exclusion in the bulk. Hence, we need to calculate the dependencies of the current on the control parameters first.

The simplest phase to consider is the high-density phase. By current conservation we know that

$$\beta\rho_L = \rho(1 - H(\rho) - \rho), \quad (2.42)$$

has to hold. Here,  $\rho_L$  denotes the density of a lattice site in the last lattice column. For the TASEP, it is simply given by  $\rho_L = 1 - \beta$ . Since, jamming in our system takes place at densities far below one, this cannot be the case. However, because particles have to traverse the entire bulk to reach the right boundary a reasonable and simple assumption to make is that the density at the last lattice site is identical to the one in the bulk. Accordingly, the dependency of the density and consequently the current can be found as the solution to the equation

$$\beta = 1 - H(\rho) - \rho. \quad (2.43)$$

This expression cannot further be simplified in general because it depends on the hindrance function that is approximated for each configuration of species ratio  $\delta$  and number of lanes  $W$  separately. Nonetheless, the approximation works sufficiently well as can be seen in Fig. C.3 of the appendix.

In contrast to the high-density phase, we cannot use any features of the bulk to determine the density at the left end in the low-density phase. Particles enter the system uncorrelated and only while passing through the system they reach the spatially stationary values used for the hindrance function. The first lattice site may behave completely different. For that reason, we need to find a separate theory that approximates the behavior at the first lattice site to find the dependencies on the in rate  $\alpha$ . The presented approach is based on the phenomenological understanding of the system we derived up to this point. Its validity is only confirmed *posteriori* and is not clear from the start.

Particles enter the system uncorrelated without previous interactions. Members of the own species on the second lattice site a particle at the first lattice site could interact with afterwards must have entered the system before it because bypassing is not possible. However, a particle of the respective other species enters the system on a different lane and hence always may hop in front; In a one-dimensional description, effectively, one particle of each species occupies the first lattice site at the same time. In contrast to the TASEP, this breaks the balance between positive and negative correlations with respect to the occupation of neighboring sites that was the reason for mean-field to work.

In our system, the other species serves as a randomly appearing obstacle that cannot directly be affected (at the first lattice site); It can be seen as a simple modification to the hopping rate. To account for this effect, we start from the normal mean-field solution and iteratively correct the density until we arrive at a result consistent with the hopping rate reduction picture. The first part of the idea can be expressed in the following form

$$\begin{aligned}\rho^T (1 - \rho^T - \rho^S) &\stackrel{!}{=} \rho^T (1 - \rho^T) \nu_T, \\ \rho^S (1 - \rho^T - \rho^S) &\stackrel{!}{=} \rho^S (1 - \rho^S) \nu_S.\end{aligned}\tag{2.44}$$

To reduce the amount of technical calculations we restrict the further derivation to the symmetrical case  $\delta = 1/2$  which already contains all major ideas. The general ansatz is discussed in Appendix B.3.

The reduced hopping rate now in turn causes the density to increase. For an independent TASEP with hopping rate different from one we can simply rescale time to find the corresponding reaction to the given in rate  $\alpha$

$$\rho(\alpha, \nu) = \frac{\alpha}{\nu}.\tag{2.45}$$

So, in the described scenario, both species would slightly increase the density of the respective other at the first lattice site by randomly hopping in front. What was not taken into account at this point is the feedback that is created because the additional density will as well contribute to the blocking. This argument can be repeated iteratively creating a sequence of hopping reductions

$$\nu^{N+1} = \frac{1 - \rho(\alpha, \nu^N)}{1 - \frac{1}{2}\rho(\alpha, \nu^N)}.\tag{2.46}$$

The final density at the first lattice site is the one obtained as the limit of this sequence  $\nu^N \rightarrow \nu$  which takes all feedback between the different species into account. It should not create any additional modification of the density and hence has to mapped towards itself. This can be expressed in the form of a self-consistency equation

$$\nu = \frac{1 - \rho(\alpha, \nu)}{1 - \frac{1}{2}\rho(\alpha, \nu)}.\tag{2.47}$$

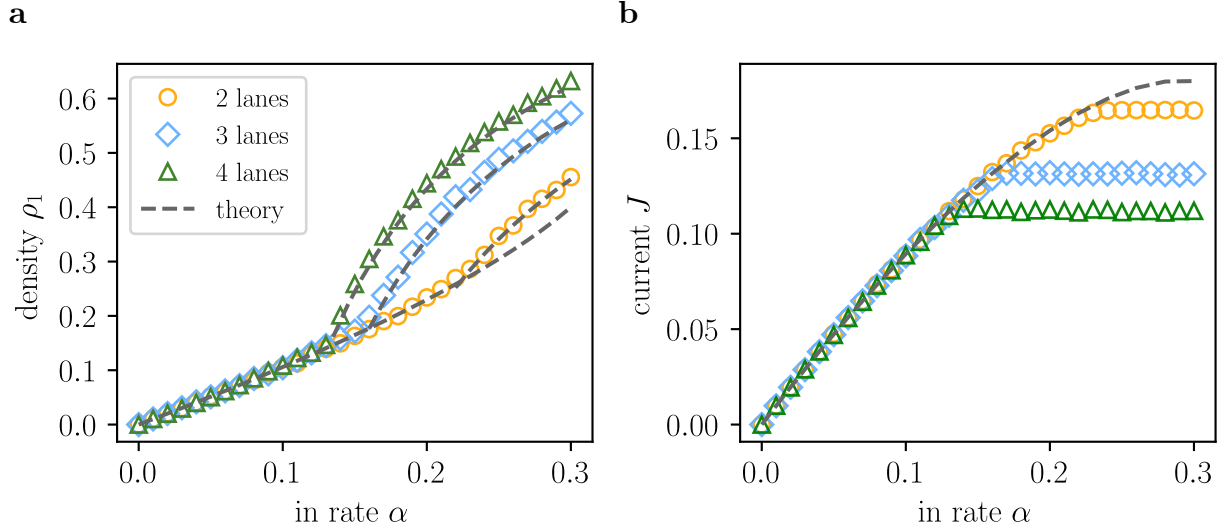


Figure 2.16: **Comparison of the low-density theory with stochastic simulations.** Up to the transition to the maximal current phase simulations (symbols) and theory (dashed line) are in good agreement. A lane dependency only enters because the maximal current decreases with the number of lanes and hence the phase transition is triggered earlier. After that point, the density at the first lattice site is determined by current conservation. [Parameters:  $L = 16384$ ,  $\delta = 1/2$ ,  $\beta = 0.8$ ; adapted from [53]]

Plugging in the relation for independent TASEPs with modified hopping rates (Eq. 2.45) one obtains

$$\nu = \frac{1 - \frac{\alpha}{2\nu}}{1 - \frac{\nu}{\alpha}}. \quad (2.48)$$

Two possible solutions exist to this equation

$$\nu^* = \frac{1}{2} \left( 1 + \alpha \pm \sqrt{1 - 6\alpha + \alpha^2} \right), \quad (2.49)$$

of which only one is stable and can be the attractor of an iteration scheme. Having found the effective hopping rate we can directly calculate density according to Eq. 2.45 and the corresponding current  $J = \alpha(1 - \rho)$ . The equation for the current actually is exact and has always to be fulfilled. The final results for the symmetric case read

$$\rho = \frac{4\alpha}{2 + \alpha + \sqrt{4 + (-12 + \alpha)\alpha}}, \quad (2.50)$$

$$J = \frac{\alpha}{4} \left( 2 - \alpha + \sqrt{4 + (\alpha - 12)\alpha} \right). \quad (2.51)$$

Notably, those are independent from the number of lanes. In the low-density regime no long-ranged coupling occurs which would cause this dependency. All systems follow the

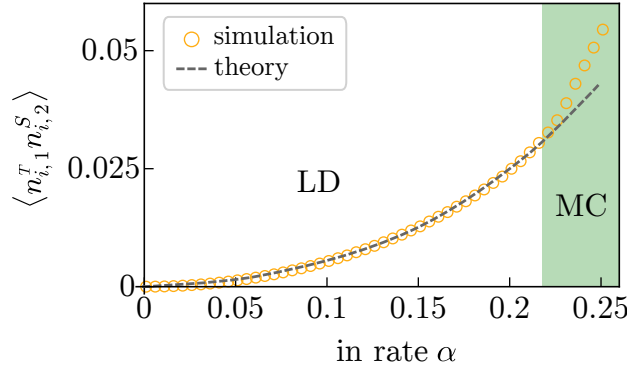


Figure 2.17: **Two-point function at the first two lattice sites in the LD phase.** Up to the transition to the maximal current phase the low-density theory (line) and stochastic simulations (symbols) are in good agreement. Afterwards, long-ranged coupling takes place which is absent for low densities. [Parameters:  $W = 2$ ,  $L = 16384$ ,  $\delta = 1/2$ ,  $\beta = 0.8$ ; adapted from [53]]

same initial curve irrespective of the number of lanes. However, at some point the transition to the maximal current phase is triggered. When this takes place in turn depends on the number of lanes. For higher in rates the density at the first lattice site is simply given by current conservation

$$\rho_1 = 1 - \frac{J_{\max}}{\alpha}. \quad (2.52)$$

In contrast, the bulk density, which is shown in Fig. C.4 of the Appendix, takes a fixed value which corresponds to the maximal current according to the current-density relation. The comparison with stochastic simulations shown in Fig.2.16 retrospectively confirms our approach. In addition, the initial equations Eqs. 2.44 can be rewritten in the following way

$$\begin{aligned} \rho^T (1 - \rho^T - \rho^S) &\stackrel{!}{=} \alpha_T (1 - \rho^T), \\ \rho^S (1 - \rho^T - \rho^S) &\stackrel{!}{=} \alpha_S (1 - \rho^S), \end{aligned} \quad (2.53)$$

which exactly corresponds to the initial intuitions we used. The current into the system on the right behaves like an independent TASEP for the respective species but needs to be balanced with an additional hindrance in the form of the second species inside the system which is represented by the left side.

A final interesting realization to make is that, since we have successfully calculated the behavior of the system using a phenomenological approach, we can now use the exact equations that were unclosed to actually calculate the corresponding strength of stochastic fluctuations

$$\begin{aligned} (1 - \delta)J = J^T &= \langle n_{i,1}^T \rangle - \langle n_{i,1}^T n_{i,2}^T \rangle - \langle n_{i,1}^T n_{i,2}^S \rangle \\ &\approx \rho^T (1 - \rho^T) - \langle n_{i,1}^T n_{i,2}^S \rangle. \end{aligned} \quad (2.54)$$

Here, we again used the argument that in the low density regime a species interacts with itself as a uncoupled TASEP would do, meaning  $\langle n_{i,1}^T n_{i,2}^T \rangle = \rho^T \rho^T$ , whereas the interaction

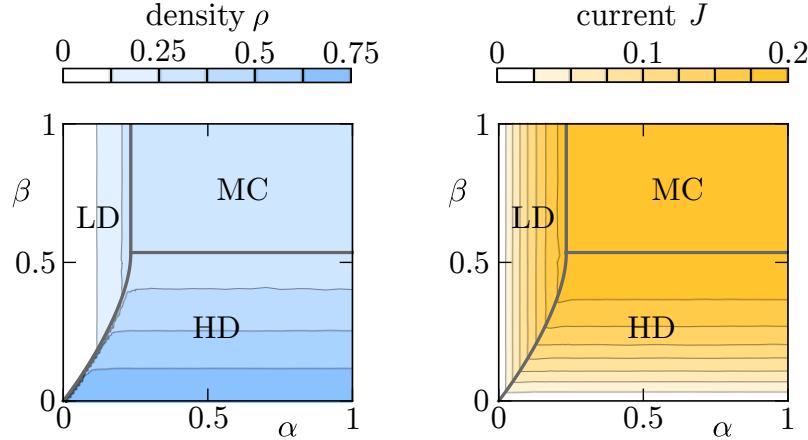


Figure 2.18: **Phase diagram for the symmetric two-lane system.** The topology of the phase diagram is identical to the TASEP. Based on the extremal current principle the phase boundaries can be derived from the theoretical results. Stochastic simulations (colors) and predictions (thick lines) are in good agreement. [Parameters:  $W = 2$ ,  $L = 16384$ ,  $\delta = 1/2$ ; adapted from [53]]

with the respective other species causes the deviations. The according equation reads

$$\langle n_{i,1}^T n_{i,2}^S \rangle = \rho^T (1 - \rho^T) - (1 - \delta)J. \quad (2.55)$$

The result is in great agreement with the stochastic simulations as shown in Fig. 2.17. Starting with the beginning of the maximal current phase correlations start to increase faster as the coupling of lanes comes into play.

Having derived the dependencies on the control parameters, the phase diagram can be obtained by looking at the current. As soon as the boundary currents  $J_\alpha$  and  $J_\beta$  reach the maximal current value which is already calculated as a side effect of finding the hindrance function, the transition between the phases takes place. Furthermore, at the line  $J_\alpha = J_\beta$  the discontinuous transition between HD and LD regime occurs. The resulting phase diagram is shown in Fig. 2.18.

Being able to obtain an approximated phase diagram which is in good agreement with the stochastic simulations and being able to recover the underlying correlations confirms our final understanding of the system. It may not be possible to give additional exact analytic results but at this point there is no real need for it either. The final step left is to make the way back from our findings for the model to the original motivations for creating it.

## 2.9 Conclusion

To properly analyze the implications of our results, it is important to consider which assumptions and approximations have been made and what their limitations are. We begin with the methods employed to study our model before turning to the model itself.

The starting point of our quantitative discussion was the cramming density. In case of a two-lane system, we managed to derive an exact analytical solution. Because of the complexity of the problem and the drastic increase in the numbers of states a generalization to higher lane numbers appears to be impossible at this point. In addition, the cramming density constitutes a rather pathological case. It is very unlikely to occur if a system is not explicitly tuned towards this behavior. However, the cramming density and its calculation serve as proof of principle of our overall understanding and was successfully used to elucidate the origin of the maximal density. By demanding that every particle that leaves the system has to be replaced by a new one entering, "dead weight" is removed from the crammed state. In combination with self-organized particle sorting this effect is at the heart of the existence of the maximal density. Attempts to quantify this effect have remained unsuccessful so far due to the lack of a suitable mapping or reduction scheme.

To extrapolate the results found for completely jammed states to actual transport phenomena, we introduced the hindrance function which accounts for the inaccessibility of lattice sites due to particle arrangement; This in itself is not an approximation. The first and most severe one that was made in this context was the continuous approximation. It heavily relies on a slowly varying density profile. In fact, based on our experiences with the TASEP we assumed the density to be constant in the bulk of the system most of the time. But it is actually unclear whether this is always the case. Looking further into this aspect, it turns out that it is not only not always true but a completely unexpected new phenomenology can be found. As illustrated in Fig. 2.19 for large lane sizes compared to the number of lanes, a flat density profile is realized and our assumptions are justified. If the number of lanes and lattice sites do not differ by a significant magnitude the density profile starts to develop wave-like density patterns. Such an effect is absolutely impossible to understand using a density-based mean-field picture; It is prohibited by current conservation. The length of an oscillation in the longitudinal direction actually corresponds to the transversal extension in the form of the number of lanes. This is caused by the fact that if two particles of different species block each other the next time they can do so again is after the  $S$  species has walked once around the cylinder which corresponds to  $W$  steps. Beyond this phenomenological understand no further progress could be achieved so far. An analytical analysis probably requires an exact solution to the system, which is far out of reach if possible at all. Similar behavior as in our system was observed in the Biham-Middleton-Levine model [118] for traffic flow which showed emerging patterns in case of deterministic movement. The model has been investigated for more than 15 years and its jamming transition is still considered to be an open mathematical problem [119–121]. From this perspective, that our system self-organizes in a way that allows for proper distance measurements using only *stochastic* local interactions is impressive in its own right, and the fact that we partially found exact approaches to the system is a significant accomplishment.

Apart from the continuous approximation no other major simplifications beyond mean-field reasoning have been employed. The basic message obtained is that if the number of lanes is increased, long-ranged coupling hinders transport and decreases the maximal current. This results in an expansion of the parameter regime in which the maximal current

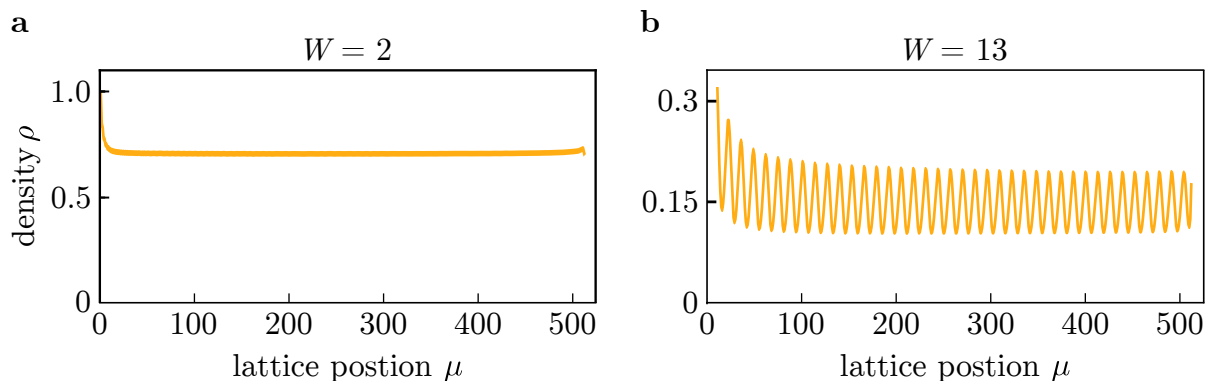


Figure 2.19: **Pattern formation for large aspect ratios.** If the number of lanes is small compared to the length of a system a constant density profile as for the TASEP is realized, which is shown in panel (a). In contrast, oscillatory density patterns occur for large numbers of lanes which are depicted in panel (b). [Parameters:  $\delta = 1/2$ ,  $\alpha = 0.6$ ,  $\beta = 0.2$ ; adapted from [53]]

is reached (but still with less efficient transport). This quite general finding does not rely on any of the model assumptions in particular and can hence be seen as a robust result.

Going back to the model itself and the original question of how species interaction changes transport we can give a very direct answer. It is always worse than single species transport. At least as long as our model applies. Since particles walk from one site of the lattice to the other without detaching, the central feature molecular motors have to fulfil to be properly described is to be very processive. This is true for kinesin-1 and in parts for other motor families as well. In the end, it depends on the explicit conditions. It is for the same reason, that Langmuir kinetics has been added to the TASEP to study transport by a single motor species. The random attachment and detachment real molecular motors perform might have a significant impact on the overall phenomenology. In particular since the effects in our system are arrangement driven which is undermined by particle rearrangement via random attachment and detachment. However, as illustrated Fig. 2.20 an effect can be found making them more relevant instead of less when Langmuir kinetics is incorporated in our model. The normal criticism of TASEP LK based models of cellular transport is that concentrations are actually too low to cause overcrowding. But as our results show, combining motor species with different modes of motion can lower the maximum current sufficiently to cause jamming at lower attachment rates. Furthermore, the position of the shock between different regimes along the lattice can be controlled. This is a prediction that could be tested experimentally as well as an interesting direction for future research. Because Langmuir kinetics destroys correlations an extended model might be even more accessible for analytic methods and appears to be a promising direction for the continuation of this project.

Taking another step back from the project level to the original question of this thesis, we achieved our goal. We found a basic system that is well described by mean-field methods and caused them to fail via a small change to the systems dynamics. The source of this

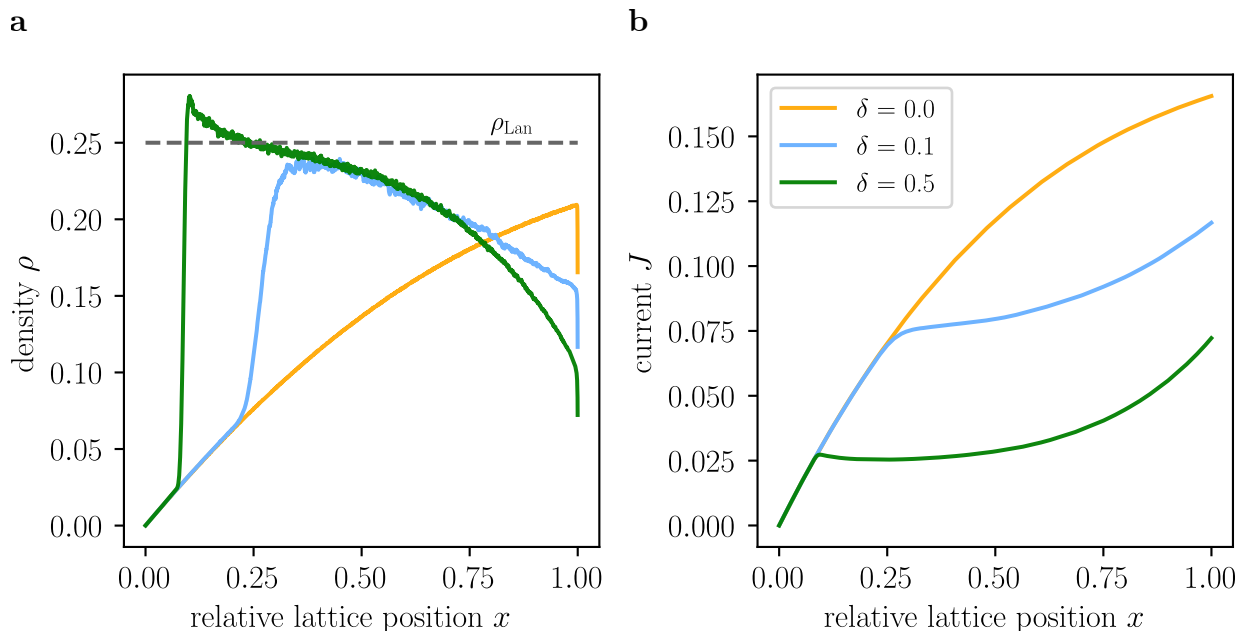


Figure 2.20: **Langmuir kinetics in combination with different species ratios.** A parameter configuration that corresponds to a system in the low-density phase may be heavily affected by an increase in the species ratio  $\delta = \omega_a^S / (\omega_a^T + \omega_a^S)$ ; Which in this case is defined via the ratio of attachment rates. Without increasing the total attachment rate  $\omega_a = \omega_a^T + \omega_a^S$ , just by lowering the maximal density due to lane coupling (panel (b)) a rapid spatial transition in the density can be achieved (panel (a)). On the one hand, this is a simple prediction by our model that can be verified experimentally. On the other hand, it shows that jamming phenomena could be more relevant for *in vivo* systems than currently expected. [Parameters:  $W = 13$ ,  $L = 4096$ ,  $\alpha = 0$ ,  $\beta = 1.0$ ,  $\omega_a = 1/3$ ,  $\omega_d = 1.0$ ]

effect was identified as the introduction of particle arrangement as a new determinant for the transport properties. We created a basic understanding of the key mechanisms at work and managed to in parts turn it into a quantitative description.



# Chapter 3

## Reaction paths and depletion traps: Macromolecular self-assembly

This chapter deals with the theoretical analysis of general principles for efficient self-assembly of macromolecules. It is based on research results I published as first author in the manuscript *Stochastic Yield Catastrophes and Robustness in Self-Assembly* [122] in the journal *eLife*, 9:e51020 in 2020 (DOI: <https://doi.org/10.7554/eLife.51020>) under the CC BY 4.0 license together with Florian Gartner (who contributed equally), Isabella Graf [123] (who contributed equally), Philipp Geiger and Erwin Frey. In particular, Philipp Geiger is credited for the original graphics design and Isabella Graf and Florian Gartner are credited for the in-depth analysis of the threshold values presented in Appendix D.3. Research data and the graphical presentation thereof have been adapted from the manuscript.

The goal of this research project is to find general principles in different fields of self-assembly such as virus capsid assembly and DNA-brick-based assembly. To this end, we built a mathematical model that combines features from various self-assembly fields. Employing deterministic approximation methods, we derive a unifying theory for information rich and homogeneous structures. Comparing our results to exact stochastic simulations we uncover the limitations of the deterministic behavior and provide insight into how stochasticity differently affects assembly processes depending on the complexity of the target structure. We give a phenomenological explanation of the origin of stochastic fluctuations in our system along with methods how they can be mitigated.

### 3.1 Biochemical background

Reliable self-assembly of macromolecules is a vital feature for self-reproducing organisms [124, 125]. Examples range from the creation of simple virus capsids [34, 126, 127] to complex flagella motors [128, 129] and ribosomes [130–132] of living cells. Furthermore, great potential for artificial self-assembly exists in the production of designed nanostructures [133–135]. The goal of this project is to find abstract unifying concepts that connect all these different fields of application and to investigate how stochasticity comes

into play on a mesoscopic scale. To this end, we are going to give a review of the biochemical background of the considered systems first.

## Virus capsids

Virus capsids are regular structures made of proteins that surround the genome of a virus. Because the genome has to be encapsulated by proteins created from it, the capsid cannot consist of only a single protein but has to be assembled from multiple, sufficiently small, subunits [30]. The exact realization may greatly differ among species. Small homogeneous capsids exist as well as significantly large and complex ones which have several different types of components [136–138]. However, the latter ones seem to be rather an exception since a large proportion of the genome has to be dedicated only to the creation of the capsid, which may constitute an evolutionary disadvantage [31].

Overarching principles in the self-assembly of virus capsids have been found over the years. A commonly used picture to describe the conceptual steps is the assembly line model, which has been studied extensively in this context [21, 26, 33, 34, 126, 139, 140]. It can be summarized as a nucleation process of identical particles followed by subsequent growth until the target structure is reached. Several important predictions are made. First, a sigmoidal curve describes the dependence of the relative number of finished capsids on the initial concentration of subunits. Second, weak and hence reversible interactions favor the creation of finished capsids by avoiding depletion of resources in an early stage. Third, at a given subunit concentration the yield can be improved by slowing down the nucleation speed compared to growth. Various comparisons with experimental studies and computer simulations confirmed the assembly line picture but also led to extensions of the model [32, 127, 141, 142]. One extension which we mention specifically because it will be relevant later on is the inclusion of an activation step [32]. Before being actually able to take part in the capsid formation, for some viruses subunits may have to perform a conformational change first as suggested by short time scale experiments. The same experiments also estimated the corresponding nucleation size to be around three.

## Artificial DNA-based assembly

In a way, DNA-based assembly is the exact opposite of virus capsid assembly. Complex nano-structures are realized using specifically designed building blocks [143]. The basic idea for the artificial creation of small-scale objects using DNA strains traces back to work by Seeman in the early 80's [144] and was realized in the form of DNA origami by Rothmund in 2006 [145]. A single strand of DNA is combined with several short staples which bind to specific parts causing it to fold in a pre-defined way to form the desired structure [146]; hence the name origami. The method has been extended in multiple ways to allow for the creation of a plethora of different structures ranging from (almost) arbitrary two-dimensional objects to three-dimensional structures and entire nano-particles or crystals [133, 147, 148]. A major source of work using this method is, however, that for

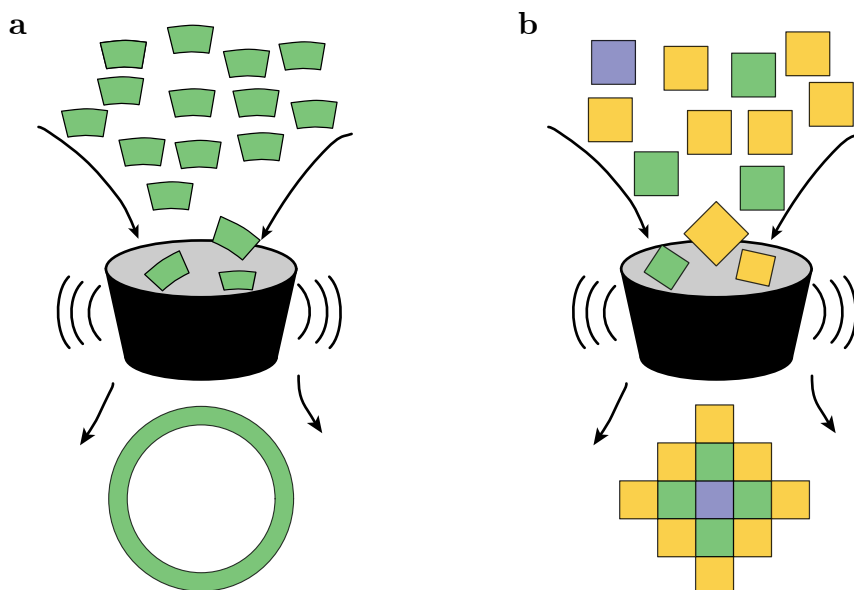


Figure 3.1: **Conceptual illustration of homogeneous and heterogeneous self-assembly.** Depending on the complexity of the target structure, constituents need higher specificity. The simple ring structure (a) can be assembled using identical components with suitable curvature. Because no microscopic control is possible during the assembly process the more complex structure (b) can only be realized reliably using different species with specific binding partners and tuned binding rates that favor a certain assembly path.

each new creation a suitable origami has to be found which may involve a significant time and resource investment.

An approach developed to allow for modularity in the creation of artificial nanostructures is DNA-brick-based assembly [22, 23, 29]. It is not based on folding a single DNA strand but uses a set of short artificially created DNAs. This allows for the assembly of different three-dimensional structures by choosing the correct combination of pieces from an existing set. Put together the sub-units self-assemble into their final structure in a similar way virus capsids do. The only major difference between the two is the specificity of components and hence the achievable complexity. A conceptual comparison is shown in Fig. 3.1. The similarity of the dynamics of the two processes hints at the existence of similar weaknesses and strategies to account for them. Indeed, brick-based assembly is affected by the same type of depletion traps implied by the assembly line model. Furthermore, it has been observed experimentally as well as by computational simulations that nucleation plays a central role for the assembly process [22–24, 27]. Accordingly, the reduction in nucleation speed leads to a similar improvement in yield as for virus capsids. In addition, the variability between sub-units allows for strategies like the creation of hierarchical assembly paths or strongly favor seeds centered around a specific component [149–151]. Which methods can be used to reliably improve yield in general is an open research question that is also the basis of our project.

## 3.2 General principles and modelling

In this work, we focus on the simultaneous assembly of identical structures into finite sized target structures. Examples are the assembly of virus capsid or DNA-brick-based creation of artificial nano-structures as discussed above. Despite occurring in many different biochemical contexts such self-assembly processes seem to follow the same basic principles (see Fig. 3.1). In a first step, resources need to be made available or enabled to perform their respective task. This may happen via simple addition to a solution by an experimentalist or more complex biological mechanisms like gene expression or conformational changes [32, 152]. In the next step, an initial nucleus has to form [22–24, 32–34]. As was observed experimentally as well as in theoretical studies, a free energy barrier exists that has to be overcome to enter the actual growth phase [26, 153–155]. In this stage, the initiated structures become stable and grow, mainly by monomer attachment, into their final form [32, 156, 157]. Depending on the time scales considered the growth process may be assumed to be irreversible. If resources are limited, this may result in the depletion of all resources with many structures being stuck in intermediate configurations. A universally observed method to avoid depletion traps is to make structure nucleation significantly slower than growth [21–26]. The goal of this research project is to study whether this is indeed the case, particularly when stochastic effects come into play on mesoscopic scales. To this end, we introduce a conceptual mathematical model that captures the characteristics of a generic self-assembly process and study it employing analytical methods in combination with stochastic simulations. How those two methods compare to each other provides insight into the relevance of fluctuations and hence directly links to the research question of this thesis.

An illustration of the model is shown in Fig. 3.2. It extends and combines previous work in the fields of virus capsids assembly [32, 156], linear filament assembly [158–160] and assembly of information rich structures [151, 161, 162].  $S$  particle species denoted by the indices  $1, \dots, S$  populate a well-mixed environment. The target structure they assemble into is a ring of size  $L$ . Each species binds to particles with periodically neighboring indices e.g., 3 to 2 and 4 or 1 to 2 and  $S$ . Apart from that, no species is distinguished from the others. In the special case  $S = 1$  the ring is completely *homogeneous* and an assembly-line-like model is obtained. Systems with  $1 < S \leq L$  are called (fully) heterogeneous and describe the assembly of information rich structures. Note that because miss binding is not allowed,  $L$  has to be an integer multiple of  $S$ . Once a dimer is formed via the combination of two monomers it can only grow via monomer attachment. A generalized model including polymer-polymer binding is discussed in the outlook in Section 3.5 in combination with a second model extension relaxing the linear binding assumption. Both generalizations are, however, assumed to be of minor importance for our purposes [21, 32, 151, 163–165].

Monomers of all species start in an inactive state and become activated at identical per capita rate  $\alpha$ . Afterwards, they can perform any binding event available to their species. In the beginning the system contains  $N$  particles of each species allowing for the creation of  $NS/L$  ring structures. The yield of the process is measured relative to this

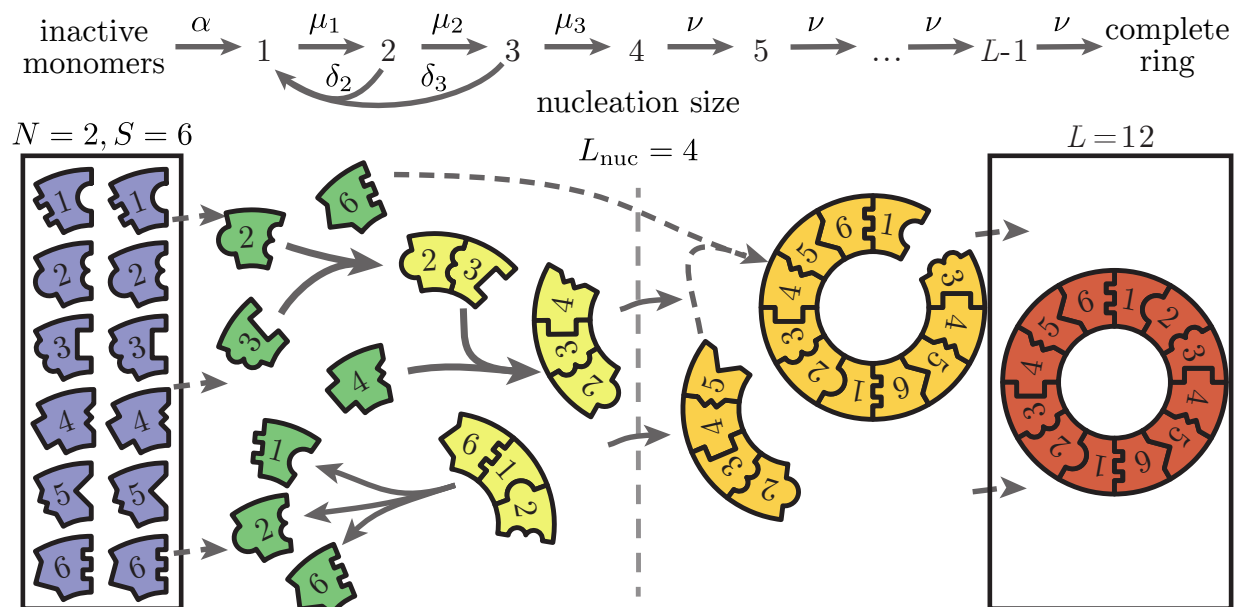


Figure 3.2: **Illustration of the assembly model.**  $S$  particle species form a ring of size  $L$  via circular binding e.g., species 1 may bind to 2 or  $S$ . If the size of the ring is larger than the number of species each species appears  $L/S$  times in the final structure. To have a unique production yield and well-defined absorbing state,  $L/S$  is only allowed to take integer values. Initially,  $N$  particles of each species are in an inactive state. Only after the activation step, which happens at rate  $\alpha$ , the monomers are able to bind to each other. Structures grow via monomer attachment. A nucleation size  $L_{\text{nuc}}$  exist. Above, growth is irreversible and takes place with identical rates  $\nu$ . Below, binding is size dependent and happens at rates  $\mu_\ell$ . Furthermore, polymers may decay into monomers at size dependent rates  $\delta_\ell$ . As soon as a ring is finished it can neither grow nor shrink but remains stable for the rest of the assembly process. [Adapted from [122]]

number. If  $NS/L$  rings are created the yield equals one. The existence of a free energy barrier is explicitly included in the form of a nucleation size  $L_{\text{nuc}}$  corresponding to the position of its maximum [22–24, 32, 140, 151, 155, 158]. Decay of polymers is only possible below and happens at size dependent rates  $\delta_\ell$ . Monomer attachment in the nucleation regime has size dependent rates  $\mu_\ell$ . In contrast, the growth process taking place above is irreversible [32, 140, 151] and has constant monomer binding rate  $\nu$ . Once a ring structure is finished it is completely stable and does not affect other reactions. This way, the system reaches an absorbing state that marks the well-defined end of the assembly process. The yield obtained at this point is an upper bound for the best achievable results at finite times. From an experimental perspective, time in general is another important aspect to be considered but it introduces a certain level of arbitrariness. When to evaluate or alternatively which yield should be achieved at compared times is a matter of pure choice. A more detailed discussion of this topic is given in Appendix D and will also be part of a follow-up research project [166]. Finally, because of the limited resources in combination

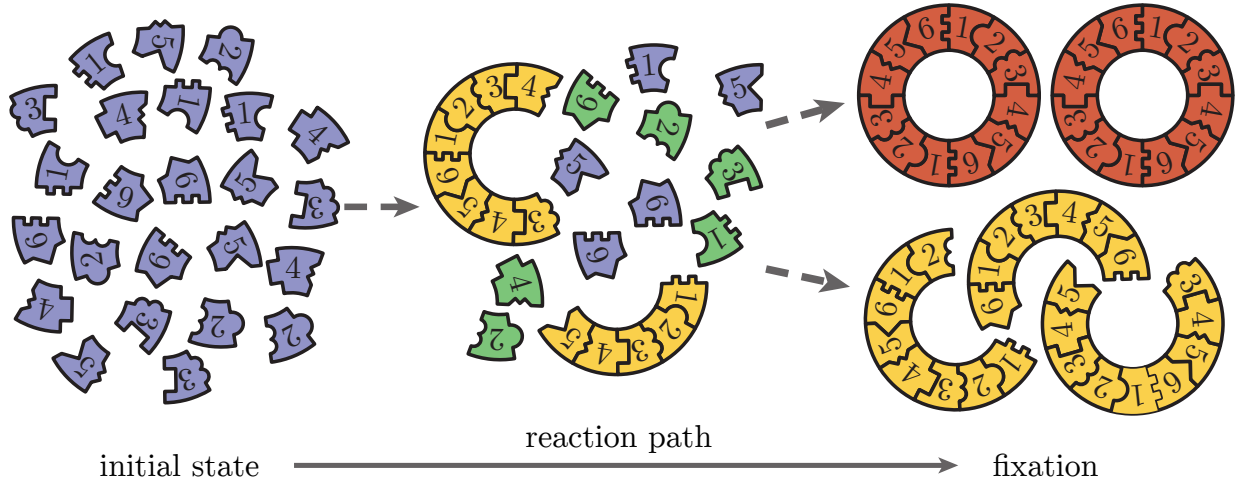


Figure 3.3: **Illustration of kinetic trapping.** Because resources are finite not all initiated ring structures might get finished. If several are assembled simultaneously they may take required monomers from each other. The resources get depleted and the system becomes trapped in an unfavorable configuration. This can be avoided if structure growth is sufficiently favored compared to nucleation events. [Adapted from [122]]

with irreversible binding depletion traps may randomly occur as illustrated in Fig. 3.3. The yield obtained hence depends on the exact assembly path of the system. To study how this is related to the existence of significant stochastic fluctuations is what makes the investigation conceptually interesting beyond its implications for the field of self-assembly itself. We start our analysis by discussing the derivation of an analytic theory based on a deterministic approximation.

### 3.3 Deterministic theory

To allow for a more concise notation, we start by introducing the general binding rates  $\xi_\ell$  and decay rates  $\Delta_\ell$  which apply to structures above and below the nucleation size

$$\xi_\ell := \begin{cases} \mu_\ell, & \text{if } \ell < L_{\text{nuc}} \\ \nu, & \text{if } \ell \geq L_{\text{nuc}} \end{cases}, \quad (3.1a)$$

$$\Delta_\ell := \begin{cases} \delta_\ell, & \text{if } \ell < L_{\text{nuc}} \\ 0, & \text{if } \ell \geq L_{\text{nuc}} \end{cases}. \quad (3.1b)$$

Similar to the approach employed for TASEP like systems in Chapter 2 particle numbers  $n_\ell^s \in \{0, \dots, N\}$  are used to describe the state of the system. The upper index  $s$  denotes the species at the left end of the considered structure and the lower index  $0 \leq \ell \leq L$  its size with  $\ell = 0$  referring to the inactive state. So, the major difference compared to Chapter 2

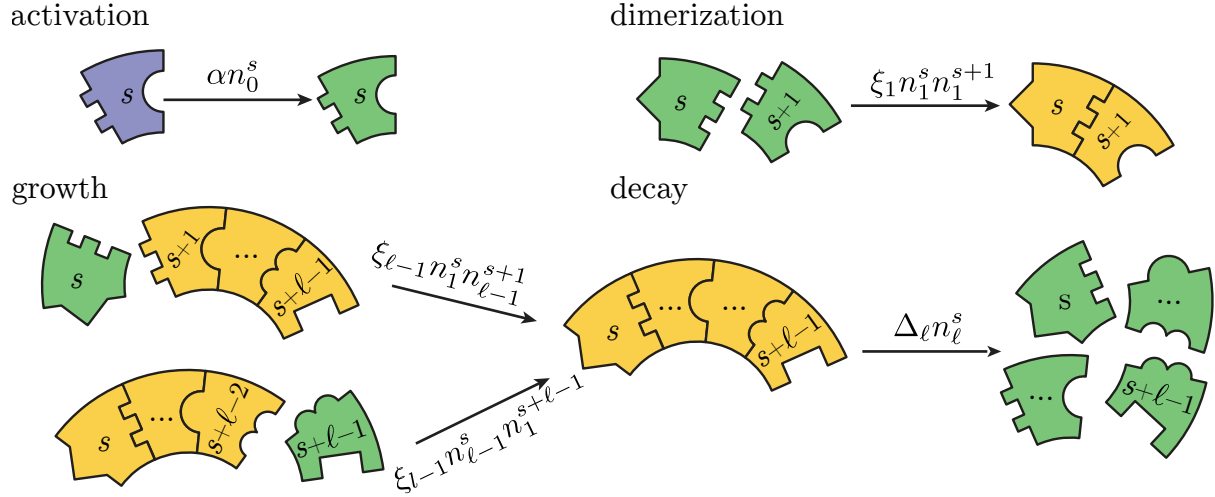


Figure 3.4: **Conceptual illustration of the master equation terms.** Four possible types of events may take place. Monomers get activated independently. Two active monomers can form a dimer. A monomer can bind to either end of a polymer. Finally, a polymer which is below the nucleation size may decay into monomers. [Adapted from [122]]

is that more than two states and species exist<sup>1</sup>. The lattice site index  $\mu$  and the polymer index  $\ell$  do not differ conceptually. Accordingly, we can describe the time evolution of our system by a set of differential difference equations

$$\frac{d}{dt} n_0^s = -\alpha n_0^s, \quad (3.2a)$$

$$\frac{d}{dt} n_1^s = \alpha n_0^s - \sum_{\ell=1}^{L-1} \xi_\ell (n_1^s n_\ell^{s+1} + n_1^s n_\ell^{s-\ell}) + \sum_{\ell=2}^{L_{\text{muc}}-1} \sum_{k=s+1-\ell}^s \Delta_\ell n_\ell^k, \quad (3.2b)$$

$$\frac{d}{dt} n_2^s = \xi_1 n_1^s n_1^{s+1} - \xi_2 n_2^s n_1^{s+2} - \xi_2 n_2^s n_1^{s-1} - \Delta_2 n_2^s, \quad (3.2c)$$

$$\frac{d}{dt} n_\ell^s = \xi_{\ell-1} n_{\ell-1}^s n_1^{\ell+s-1} + \xi_{\ell-1} n_{\ell-1}^{s+1} n_1^s - \xi_\ell n_\ell^s n_1^{s+\ell} - \xi_\ell n_\ell^s n_1^{s-1} - \Delta_\ell n_\ell^s, \quad (3.2d)$$

$$\frac{d}{dt} n_L^s = \xi_{L-1} n_{L-1}^s n_1^{L+s-1} + \xi_{L-1} n_{L-1}^{s+1} n_1^s. \quad (3.2e)$$

Four different types of terms appear corresponding to the events of activation, dimerization, structure growth and decay. An illustration of the origin of the respective expressions is shown in Fig. 3.4. Again, finding an exact solution to these equations is out of scope and we focus on the analysis of macroscopic observables given in the form of expectation values  $\langle n_\ell^s \rangle$ . At this point it is important to note that, while our system studied in Chapter 2 was trivially ergodic this one trivially is not. The assembly process by construction always ends up in an absorbing state after a finite number of reaction steps. Afterwards no other state

<sup>1</sup>In fact, the species index  $s$  is in analogy to the lane index  $i$  of the lattice gas model. The species  $S$  and  $D$  do not have a counterpart in the assembly model.

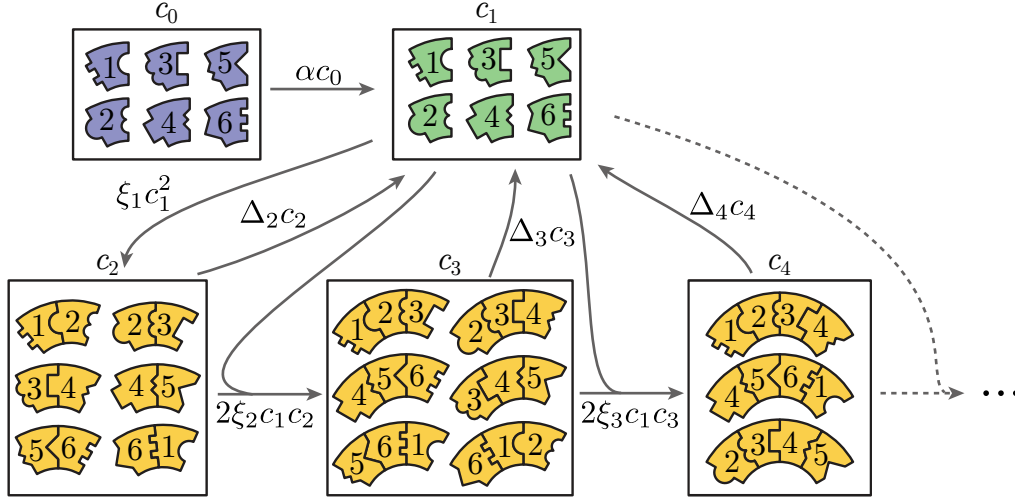


Figure 3.5: **Illustration of the mean-field assumption.** Because of the rotational symmetry of the assembled ring, species are not distinguishable in the ensemble average. Factorizing correlations, the system is effectively always treated as being homogeneous, irrespective of the number of species  $S$ . Accordingly, polymers of the same size can be grouped and are referred to by a single density  $c_\ell$ . [Adapted from [122]]

can be reached at all. This directly implies that a time average is not suited to describe our system and terms of the form  $\langle n_\ell^s \rangle$  have always to be treated as ensemble averages. As a consequence, we cannot study the stationary state configuration but have to keep time as an important factor for the current state. Fortunately, since by construction of the model all species are interchangeable via cyclic relabeling a symmetry breaking between them cannot occur in the ensemble average, meaning  $\langle n_\ell^s \rangle = \langle n_\ell^k \rangle \forall s, k$ . So, as for the lane index  $i$  of the extended TASEP model, we can drop the species index  $s$  in the macroscopic description. To emphasize the similarity to chemical rate equations we use concentrations

$$c_\ell := \frac{\langle n_\ell^s \rangle}{V}, \quad (3.3)$$

to describe the current state of the system. As before, no approximations have been made so far but now become necessary to obtain a closed set of equations. Neglecting stochastic fluctuations, we make the mean-field assumption

$$\langle n_i^s n_j^k \rangle = \langle n_i^s \rangle \langle n_j^k \rangle \quad \forall s, k. \quad (3.4)$$

Any major differences between theory and stochastic simulations must be assumed to have their origin in this approximation. The corresponding effective model that is studied

is illustrated in Fig. 3.5 and is described by the differential difference equations

$$\frac{d}{dt}c_0 = -\alpha c_0, \quad (3.5a)$$

$$\frac{d}{dt}c_1 = \alpha c_0 - 2c_1 \sum_{\ell=1}^{L-1} \xi_\ell c_\ell + \sum_{\ell=2}^{L_{\text{nuc}}-1} l \Delta_\ell c_\ell, \quad (3.5b)$$

$$\frac{d}{dt}c_2 = \xi_1 c_1^2 - 2\xi_2 c_1 c_2 - \Delta_2 c_2, \quad (3.5c)$$

$$\frac{d}{dt}c_\ell = 2\xi_{\ell-1} c_1 c_{\ell-1} - 2\xi_\ell c_1 c_\ell - \Delta_\ell c_\ell, \quad \text{for } 3 \leq \ell < L, \quad (3.5d)$$

$$\frac{d}{dt}c_L = 2\xi_{L-1} c_1 c_{L-1}. \quad (3.5e)$$

The associated yield is given by

$$\text{yield}(t) = \frac{c_L(t)VL}{SN}. \quad (3.6)$$

Eq. 3.5 is closely related to the Becker-Döring equation used to describe crystallization phenomena [167]. Furthermore, it has been used to generally describe the assembly process of virus capsids previously [32, 156, 158–160]. In particular, the case  $L_{\text{nuc}} = 2$  in the absence of an activation steps was studied analytically [140] using a continuous limit similar to the one discussed for the TASEP in Chapter 2. The difference in this case is that the process is not assumed to be stationary. To stress this point, we will explicitly include the time dependence  $c_\ell = c_\ell(t)$  from here on. In the following we are going to extend the results existing for virus capsid assembly [140] to derive an analytic theory describing our model.

In the simplified case  $L_{\text{nuc}} = 2$  the generalized binding and detachment rates reduce to  $\xi_1 =: \mu$ ,  $\xi_{\ell \geq 2} =: \nu$  and  $\Delta_i = 0$ . This allows to write Eqs. 3.5 for structures with  $\ell > 2$  in a simple form

$$\partial_t c_\ell(t) = 2\nu c_1(t) [c_{\ell-1}(t) - c_\ell(t)]. \quad (3.7)$$

Now, similar to the previous chapter we assume  $\ell$  to be a continuous variable  $x$  and  $c$  to vary slowly in space such that it can be approximated via a Taylor series expansion

$$c(x-1, t) = c(x, t) - \partial_x c(x, t) + \frac{1}{2} \partial_x^2 c(x, t). \quad (3.8)$$

Plugging the expanded concentration into Eq. 3.7 yields a partial differential equation of the form

$$\partial_t c(x, t) = -2\nu A(t) \partial_x c(x, t) + \nu A(t) \partial_x^2 c(x, t), \quad (3.9)$$

where  $A := c_1$  denotes the concentration of active monomers. Eq. 3.9 can be interpreted as a continuity equation  $\partial_t c(x, t) = -\partial_x J(x, t)$  with current  $J(x, t) = 2\nu A(t) c(x, t) - \nu A(t) \partial_x c(x, t)$ . The particle flux into the system takes place in the form of dimerization which happens at  $x = 2$  with the rate  $\mu A^2(t)$  resulting in the boundary condition

$$2\nu A(t) c(2, t) - \nu A(t) \partial_x c(2, t) = \mu A^2(t). \quad (3.10)$$

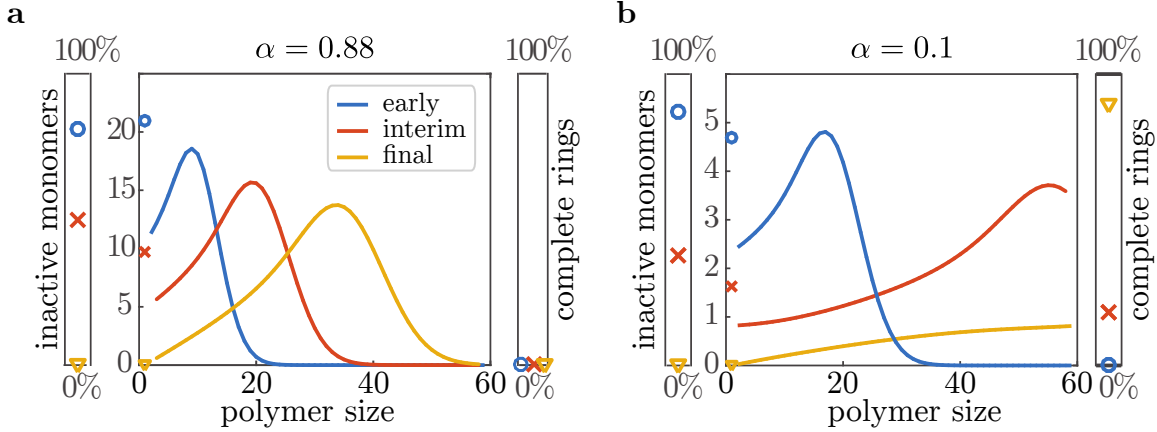


Figure 3.6: **Travelling wave picture.** The system's dynamics can be approximated as a travelling wave in the space of polymer sizes. It starts at the left and moves to the right via monomer consumption. The right boundary corresponds to the absorbing state. Two scenarios exist: (a) All monomers may be bound in intermediate configurations and the wave gets stuck on its way. (b) Alternatively, it reaches the right boundary which marks the onset of yield. Active and inactive monomers as well as finished ring structures have to be treated separately and are not part of the continuous description (symbols). [Parameters:  $L = 60$ ,  $L_{\text{nuc}} = 2$ ,  $N = 10000$ ,  $\mu = \nu = 1$ ; adapted from [122]]

Because finished ring structures do not interact with the rest of the system they can be treated as leaving the system. This picture corresponds to an absorbing boundary condition at the right end of the system  $c(L, t) = 0$ . Finally, the monomer concentration has to fulfil the differential-integral equation

$$\partial_t A(t) = \alpha C e^{-\alpha t} - 2\mu A^2(t) - 2\nu A(t) \int_2^L c(x, t) dx, \quad (3.11)$$

with  $C$  being the initial inactive monomer concentration  $C = NS/V$ . The integral accounts for the possible binding of an inactive monomer to any unfinished polymer.

The physical interpretation of Eq. 3.9 in combination with Eq. 3.11 is that the assembly of rings can be seen as a travelling wave whose movement is fueled by the consumption of monomers. Yield is produced as soon as the wave reaches the right boundary. In this picture, a depletion trap corresponds to the wave getting stuck because it ran out of monomers to consume for movement. Fig. 3.6 shows the numerical solution of Eqs. 3.5 confirming the physical interpretation.

The intuitive picture can now be turned into a mathematical condition for the onset of yield. Two aspects contribute to the travel distance of the right end of the wave. The center of mass movement  $d_{\text{adv}} = 2\nu \int_0^\infty A(t) dt$  and the spreading of particles around it due to fluctuations  $d_{\text{diff}} = \sqrt{2\nu \int_0^\infty A(t) dt}$ . The sum of both must be large enough to reach the

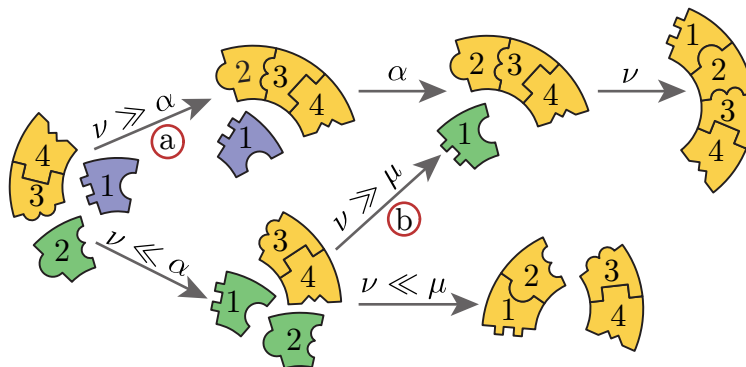


Figure 3.7: **Illustration of the yield improvement strategies.** Two possible scenarios exist that favor structure growth over nucleation. Either the activation step **a** has to be slow to ensure limited resources such that an existing structure is finished before a new one can be started. Alternatively, the nucleation of new structures can be slowed down directly. In this dimerization limited scenario step **b** is enforced which suppresses nucleation. [Adapted from [122]]

right boundary

$$d_{\text{adv}} + d_{\text{diff}} \geq L - 2. \quad (3.12)$$

The corresponding equation for the monomer concentration reads

$$\int_0^{\infty} A(t) dt \stackrel{!}{=} \frac{1}{8\nu} \left( \sqrt{1 + 4(L - 2)} - 1 \right)^2 \approx \frac{L - \sqrt{L}}{2\nu}. \quad (3.13)$$

This equation has a very intuitive interpretation as well. The left side corresponds to the availability of monomers over time. A small value means fast depletion of resources while a large one signals continuous long-time usage. The larger the assembled ring is—represented by the factor  $L$  on the right side—the more control during the assembly is needed. In contrast, faster growth represented by a higher rate  $\nu$  makes higher yield easier to achieve. This is reminiscent of the idea that structure nucleation should be slow compared to growth. In our model two rates exist which can slow down nucleation if they are small compared to  $\nu$ , the activation rate  $\alpha$  and the dimerization rate  $\mu$ . Both are included only implicitly in Eq. 3.13 via the solution for  $A$  based on Eq. 3.11. The respective mechanisms are illustrated in Fig. 3.7. Two extremal cases exist in which only one of them is responsible for the limitation of nucleation events. We will study both isolated at first to separate their individual effects. The first one  $\alpha \rightarrow \infty$  which is controlled by  $\mu$  we refer to as the *dimerization scenario*. The second one  $\mu = \nu$  controlled by  $\alpha$  is called the *activation scenario* in the following. For both, threshold values of the respective parameters below

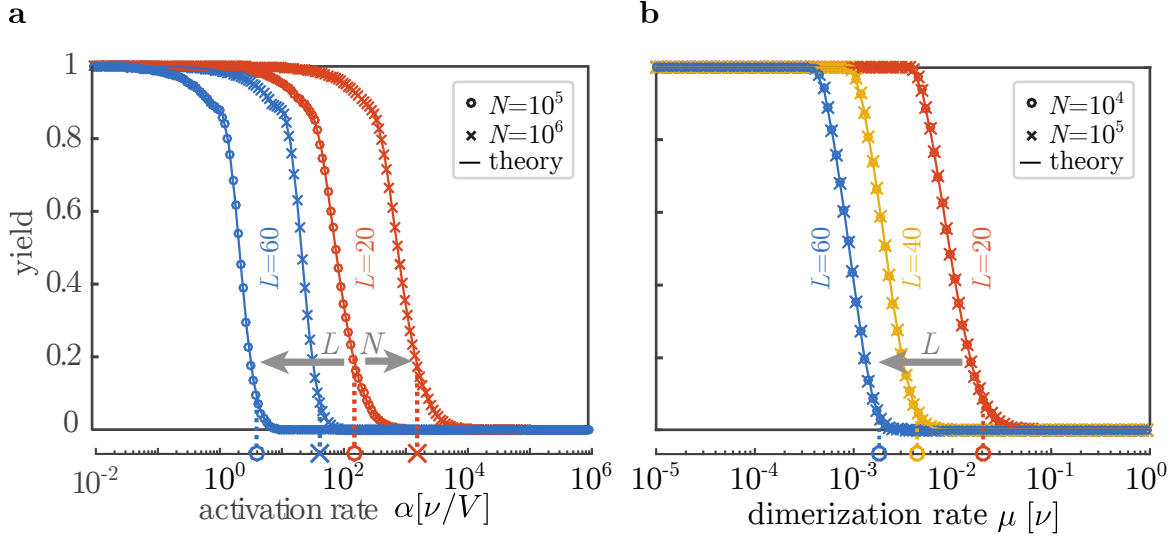


Figure 3.8: **Deterministic yield curves.** Slowing down nucleation either via reduction of the activation rate  $\alpha$  or the dimerization rate  $\mu$  increases the yield from zero to up to one. Increasing the size of the ring  $L$  shifts the curves towards slower nucleation. While the activation scenario  $\mu = \nu$  (a) depends on the number of particles, the dimerization scenario  $\alpha \rightarrow \infty$  (b) does not, as emphasized by the overlapping data points. The theoretical description based on chemical rate equations (lines) and stochastic simulations (symbols) are in perfect agreement. The symbols on the lower axis and dashed lines indicate the threshold activation rate  $\alpha_{\text{th}}$  and dimerization rate  $\mu_{\text{th}}$ . Those become more accurate with increasing ring size  $L$ . [Parameters:  $\text{ens.} = 16$ ,  $S = L$ ,  $L_{\text{nuc}} = 2$ ,  $\nu = 1$ ; adapted from [122]]

which finite yield is observed can be derived

$$\alpha < \alpha_{\text{th}} := \frac{\nu}{\mu} \left( \frac{\sqrt{\pi} \frac{\Gamma(2/3)}{\Gamma(7/6)}}{3} \right)^3 \frac{\nu C}{(L - \sqrt{L})^3} \quad (3.14)$$

$$\mu < \mu_{\text{th}} := \frac{\pi^2 \nu}{2(L - \sqrt{L})^2}. \quad (3.15)$$

The detailed derivation of the results is presented in the supplemental material of our research paper [122] which is reprinted in Appendix D to provide a complete picture. They constitute a generalization of the previous results in the field of virus capsid assembly [140]

Eqs. 3.15 have several interesting implications for the comparison of both mechanisms. In contrast to the dimerization mechanism, the yield of the activation mechanism depends on the initial particle number. In addition, it depends cubically on the ring size  $L$  while the dimerization threshold decreases quadratically. A comparison between exact stochastic simulations, numerical solutions of the original mean-field differential difference equation Eq. 3.2 and the threshold values in the limit of large particle numbers is shown in Fig. 3.8 for a completely heterogeneous system. As can be seen, the deterministic approximation for the final yield based on concentrations perfectly agrees with the exact results confirming

the validity of the performed mean-field approximation. Because the simulations were performed for a fully heterogeneous system while the deterministic ansatz indirectly assumes a homogeneous system it is implied that the existence of different species actually is irrelevant. The threshold values adequately describe the onset of yield with an improvement in accuracy for larger ring sizes  $L$  as expected since  $L \gg 1$  was assumed for the derivation. Furthermore, the qualitative predictions are confirmed. The activation scenario depends on the initial particle number  $N$  and shows more sensitivity towards the ring size. Both mechanisms can be used for yield improvement. Increasing either  $\alpha$  or  $\mu$  sufficiently always results in perfect yield at some point.

Taking together, in this section we analytically derived an approximation for the yield realized in the absorbing state in terms of particle concentrations. Further analysis resulted in explicit conditions for the onset of finite yield in the form of the threshold values Eq. 3.15. Finally, all results were confirmed in the limit of large particle numbers by stochastic simulations implying an equivalence between heterogeneous and homogeneous system. This now serves as the starting point for the study of the impact of stochastic fluctuations. We have found a system that is well described by an analytic theory based on mean-field assumptions. Comparing the analytic theory to the stochastic simulations we now investigate what the limitations are and which parameters are responsible for controlling the strength of stochastic fluctuations.

### 3.4 Stochastic effects

The most natural variable to start the analysis of stochastic effects with is the initial particle number  $N$ . Because the system is assumed to be well-mixed no length scale exists that can be controlled in the system as for the two-dimensional lattice gas model in the previous chapter. Fig. 3.9 shows how in a completely heterogeneous system the yield changes for both scenarios if the particle number is lowered while keeping all other parameters constant. The effects are significantly different for both scenarios.

Irrespective of how low the particle number is, by reducing the dimerization rate  $\mu$  sufficiently, perfect yield can always be achieved. Even in the most extreme case of a single particle per species the curve is just slightly spread out. The inflection point remains in the same position. Consequently, the dimerization scenario can generally be described by the deterministic theory which ultimately leads to the conclusion that stochastic fluctuations are of minor relevance.

While for the activation scenario the activation rate at which yield first can be observed does not significantly change either, the story drastically changes with respect to the yield optimization potential. For limited resources the yield saturates below one which is in sharp contrast to the deterministic theory. Already for 100 particles per species, or 6000 in total, production of successfully assembled rings is completely suppressed. The difference between the deterministic approximation and the actual system is as large as possible there. We thus found the best parameter regime for the investigation of stochastic effects: The activation scenario with a mesoscopic number of particles in the limit of vanishing

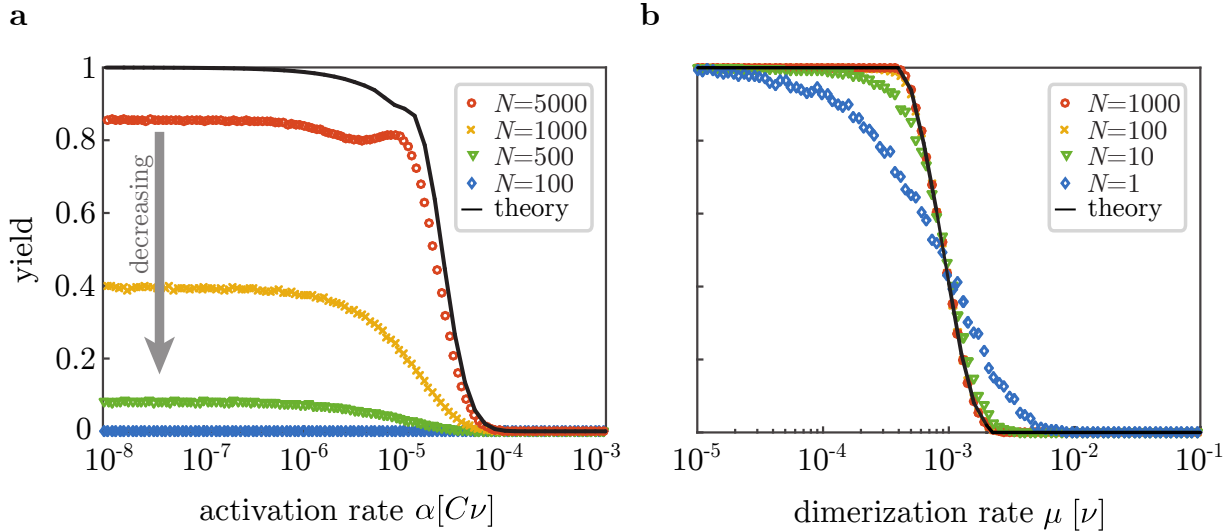


Figure 3.9: **Yield curves for reduced particle numbers.** For the activation scenario  $\mu = \nu$  (a) strong deviations between deterministic theory (line) and stochastic simulations (symbols) exist. Most prominently, the yield curves saturate below one. Depending on the initial numbers of particles, perfect yield might be expected theoretically while no yield is achieved at all. Because the activation rate  $\alpha$  is rescaled, deterministically all curves are expected to collapse onto the same master curve. In contrast to the activation scenario, the dimerization scenario  $\alpha \rightarrow \infty$  (b) is barely affected by fluctuations. Even for the lowest possible number of particles the curve is just flattened and the characteristics like maximum possible yield and the position of the inflection point do not change. [Parameters:  $\text{ens.} = 1024$ ,  $L = 60$ ,  $S = L$ ,  $L_{\text{nuc}} = 2$ ,  $\nu = 1$ ; adapted from [122]]

activation rate.

To find the source of the drastic deviations between actual dynamics and the deterministic theory we compare the stochastic simulations to the travelling wave ansatz. As can be seen in Fig. 3.10.a the number of structures in unfinished configurations is heavily underestimated. This causes the wave to get stuck significantly earlier than expected according to the deterministic theory. Apparently, there exists a lower limit to the number of actively built structures that cannot be overcome by reducing the activation rate. The investigation can further be systematized by taking the effects of nucleation size  $L_{\text{nuc}}$  and number of species  $S$  into account<sup>2</sup>. The dependency of the maximal possible yield in the activation scenario is shown in Fig. 3.10.b. The strength of the stochastic fluctuations, manifesting in the reduction of the maximum yield, increases with the number of species composing the ring. While a homogeneous system is not affected at all heterogeneity strengthens deviations from the mean-field behavior. Furthermore, increasing the nucleation size weakens the yield reduction until perfect yield is always achieved independent of the number of

<sup>2</sup>In the main text we only focus on constant sub-critical rates  $\mu_\ell = \mu$  and  $\delta_\ell = \delta$ . The more general case is discussed in the Appendix D

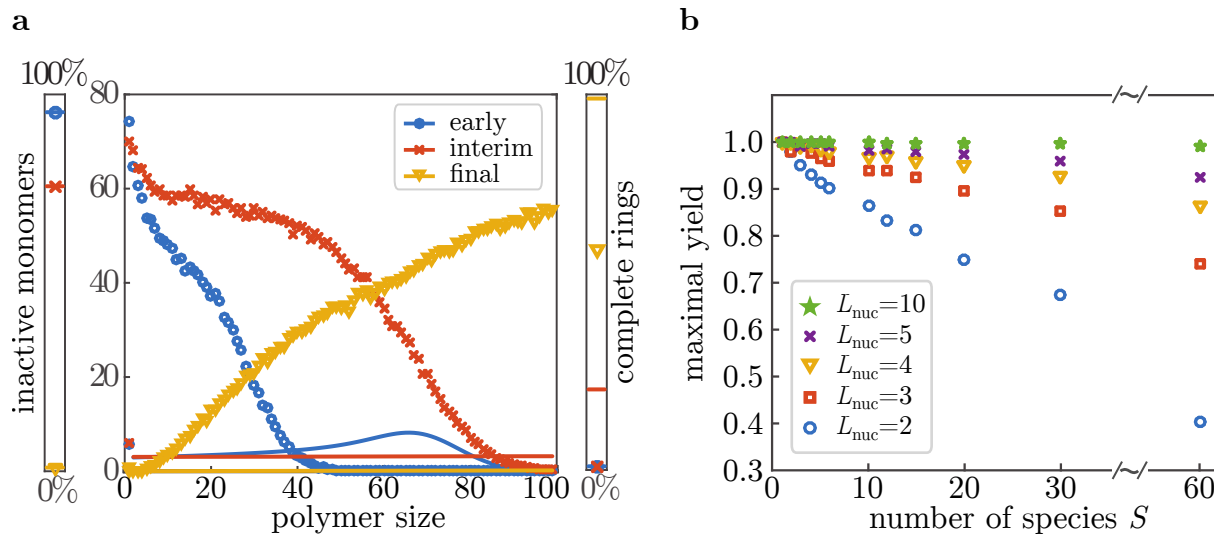


Figure 3.10: **Sources of the stochastic yield reduction.** (a) As soon as particle numbers get low, significant deviations between the deterministic travelling wave solution and the stochastic simulations can be observed. The height of the wave and accordingly the number of simultaneously assembled structures becomes much larger. This results in a faster monomer depletion which causes the wave to freeze further to the left. The maximum yield limitation can hence be interpreted as a limitation in the travel distance by too many nucleation events. (b) The strength of the stochastic effects depends on the number of species composing a ring  $S$  and the nucleation size  $L_{\text{nuc}}$ . A completely homogeneous structure ( $S = 1$ ) is not affected at all. The strength of the stochastic effects increases with  $S$  because more potential for fluctuations among species exists. In contrast, increasing the nucleation size allows larger structures to disassemble and thereby reduces the susceptibility to early stage fluctuations. [Parameters:  $\text{ens.} = 1024$ ,  $\mu = \nu = 1$ , (a)  $S = L = 100$ ,  $L_{\text{nuc}} = 2$ ,  $N = 1000$ , (b)  $L = 60$ ,  $SN = 60000$ ; adapted from [122]]

species. Taking all observations together, the maximum yield decreases with the number of particles and the nucleation size but most critically the effect depends on the chosen mechanism and the number of species.

The reason why heterogeneous systems containing few particles saturate at low yield can be understood in terms of Fig. 3.11. Considering the limit of vanishing activation rate, time becomes irrelevant since all binding events possible take place before the next particle is made available. The entire dynamics of the system is determined solely by the order in which particles are activated. Interestingly, this is fairly similar to the mechanism causing the extended TASEP model to exhibit a cramming density below one. Everything is simply reduced to a random sequence of particle species—or species and lanes in the last chapter. This established combinatorics as the central determinant of the system which brings along fluctuations that cannot be neglected. Here, those are fluctuations between the particle numbers of different species. To put it simple, just because the number of particles of each species at a given time are identical in the ensemble average does not imply they are

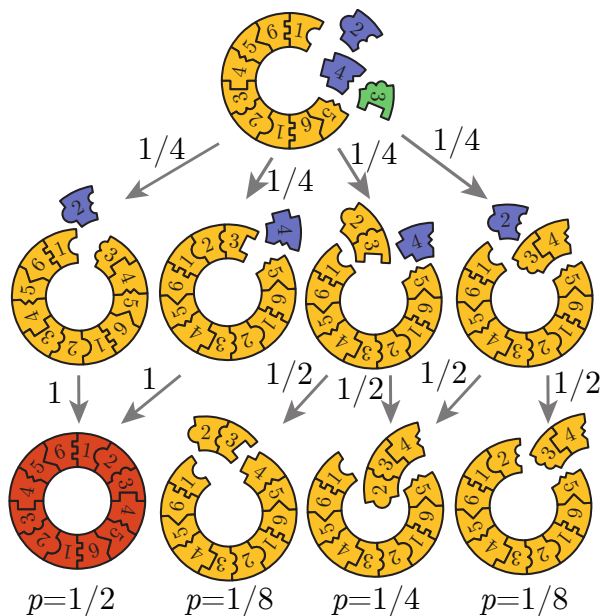


Figure 3.11: **Illustration of the combinatorics origin of the maximum yield.** In the limit of infinitely small activation rate  $\alpha$ , all possible reactions take place before the next monomer becomes available for binding. Effectively, the system's dynamics can be reduced to a random sequence of particles. The assembly process is purely limited by combinatorics that cannot be affected by any of the other control parameters. [Adapted from [122]]

in each run. This invalidates the mean-field assumption  $\langle n_i^s n_j^k \rangle = \langle n_i^s \rangle \langle n_j^k \rangle$ . Increasing the nucleation size relaxes the strict dependence on the particle sequences. Only after the respective size is reached particles are permanently bound to a single structure. Furthermore, if fewer species are present in the system the potential for large deviations between them is smaller with the extreme of just a single species without any. A quantification of this qualitative arguing is the topic of a follow-up research project [168].

Since we have found that our system possesses deterministic mechanisms that increase the yield by reducing the nucleation rate and stochastic effects that limit the maximum yield by combinatorics if the activation becomes too low, a natural question to ask is whether competition between those two effects exists. And indeed, if the activation and dimerization scenario are combined, a transition between two regimes dominated by either the deterministic or the stochastic dynamics can be observed as illustrated in Fig. 3.12. This is possible since the inverse dependence of  $\alpha_{\text{th}}$  on the dimerization rate  $\mu$  causes a shift of the curves to the right. Yield is achieved deterministically in a regime which is not already dominated by fluctuation. As a result, the yield does not only saturate at some point but may even decrease again for smaller activation rates. Such a non-monotonic dependency of the yield is in clear contradiction to the assumption of a sigmoidal shape and turns yield maximization into a fine-tuning problem. This nicely proves that our basic

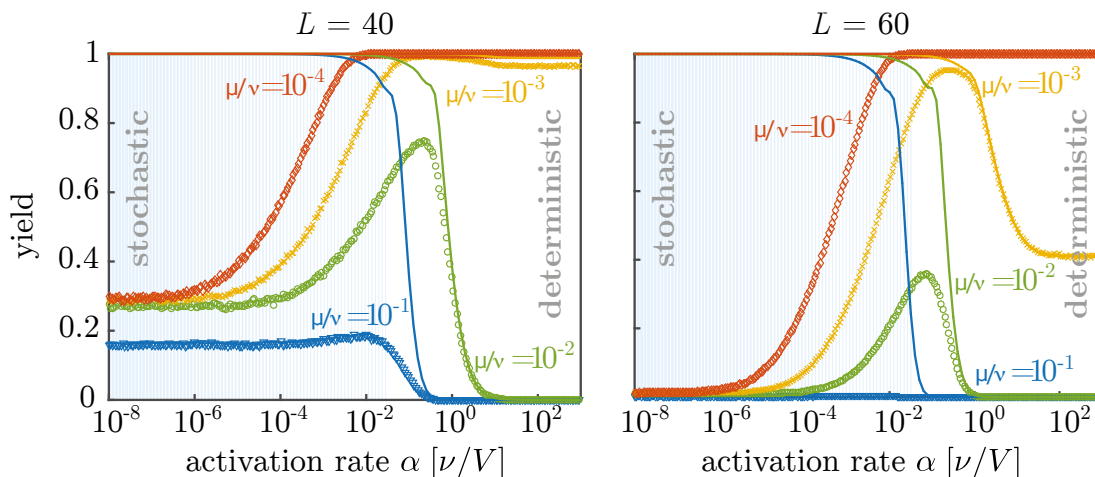


Figure 3.12: **Transition between deterministic and stochastic regime.** In case activation and dimerization reduction are combined, a strongly non-monotonic yield curve can be achieved. Initially, reducing the activation rate causes the deterministically expected increase in yield. But at some point, fluctuations become dominant in the system which triggers a yield reduction. The optimum is achieved not by the slowest possible activation rate but on an intermediate scale. This turns optimization into a fine-tuning problem. [Parameters:  $\text{ens.} = 1024$ ,  $S = L$ ,  $L_{\text{nuc}} = 2$ ,  $\nu = 1$ ; adapted from [122]]

understanding of the mechanism relevant for the final yield are indeed correct and we can now conceptually discuss their implications for the field of self-assembly and beyond that in the context of this thesis.

### 3.5 Conclusion

We found that in our system two sources for a reduction in yield exist. First, depletion traps which are present already at a deterministic level and affect the yield irrespective of the number of species  $S$ . They can fully be captured using a mean-field approximation to derive chemical rate equations that describe the dynamics in terms of concentrations. A travelling wave fueled by monomer consumption transports mass from smaller to larger structure sizes in the configuration space. Maximization of yield can be achieved by slowing down activation or dimerization sufficiently to ensure a lasting supply. In this way, perfect yield can always be realized. An equivalence between homogeneous and heterogeneous systems exists because of the symmetry between species in the deterministic limit. The simple idea of slowing down nucleation compared to growth in an arbitrary way to improve yield is generally confirmed.

The story drastically changes as soon as resources are no longer abundant. While the dimerization scenario is still well described using the deterministic theory, significant deviations can be observed in the activation scenario. Most prominently, the yield saturates

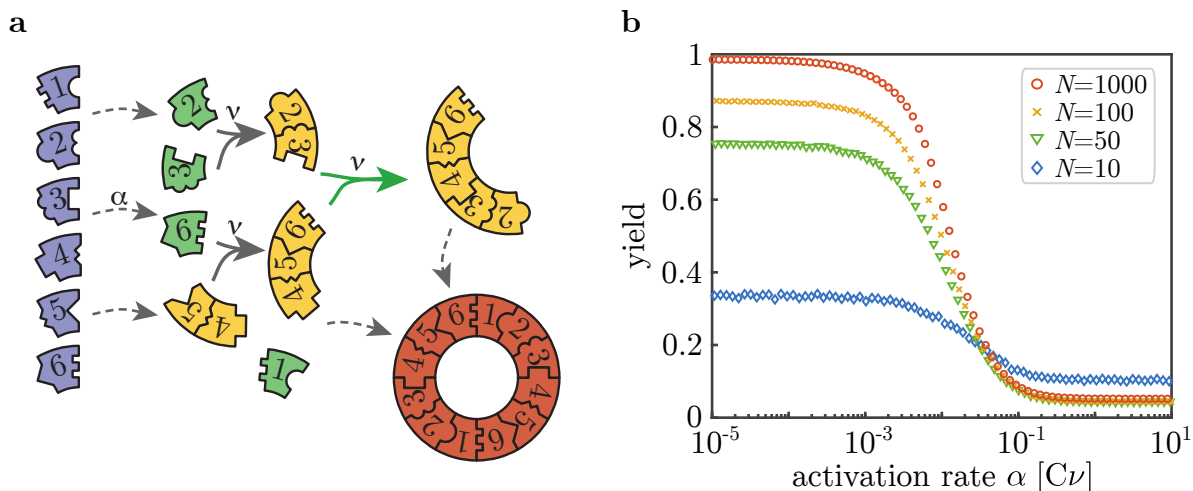


Figure 3.13: **Polymer-polymer binding model.** The original model assumed structure growth to take place only via monomer attachment. In an extended model, we also include the possibility of polymer-polymer binding as illustrated in panel (a). Since the extended model shows the same kind of stochasticity induced yield limitation (panel (b)), we can conclude that it is not just an artefact of the original model assumptions. [Parameters:  $\text{ens.} = 1024$ ,  $S = L = 100$ ,  $L_{\text{nuc}} = 2$ ,  $\mu = \nu = 1$ ; adapted from [122]]

at an imperfect value for heterogeneous systems. This cannot be explained via mean-field approximations and reveals fundamental differences between homogeneous and heterogeneous assembly on the stochastic level. Increasing the nucleation size mitigates this effect because reversibility allows for the correction of stochastically occurring unfavorable nucleation events. Finally, if both mechanisms are combined a transition from a deterministic to a stochastic-dynamics-dominated regime can be observed. This results in non-monotonic yield curves that are not possible for homogeneous systems; Maximization of the yield turns into a complex fine-tuning problem and cannot be reduced to a simple reduction of a single rate.

An important question to ask at this point is how much the observed effects rely on our model assumptions. Particularly, polymer-polymer binding appears to fully resolve the yield limitation as illustrated in Fig. 3.11. To test the robustness of our results we simulated the extended dynamics shown in Fig. 3.13.a. Binding is possible as long as no overlap between two polymers is created ( $l_1 + l_2 \leq L$ ). As can be seen in Fig. 3.13.b the stochastic yield reduction still exists. The reason is that irreversible binding results in the creation of polymers that permanently cannot bind to each other because of the partial overlap. Interestingly, for the assembly of a single ring structure this cannot be the case and yield has to be always one. Accordingly, the yield does not monotonically depend on the number of particles as can be seen from the comparison of the 10-particle system to the others. This is a curiosity for which reducing the number of particles reduces the relevance of fluctuations. Beyond that, the extended model confirms our findings for the main model.

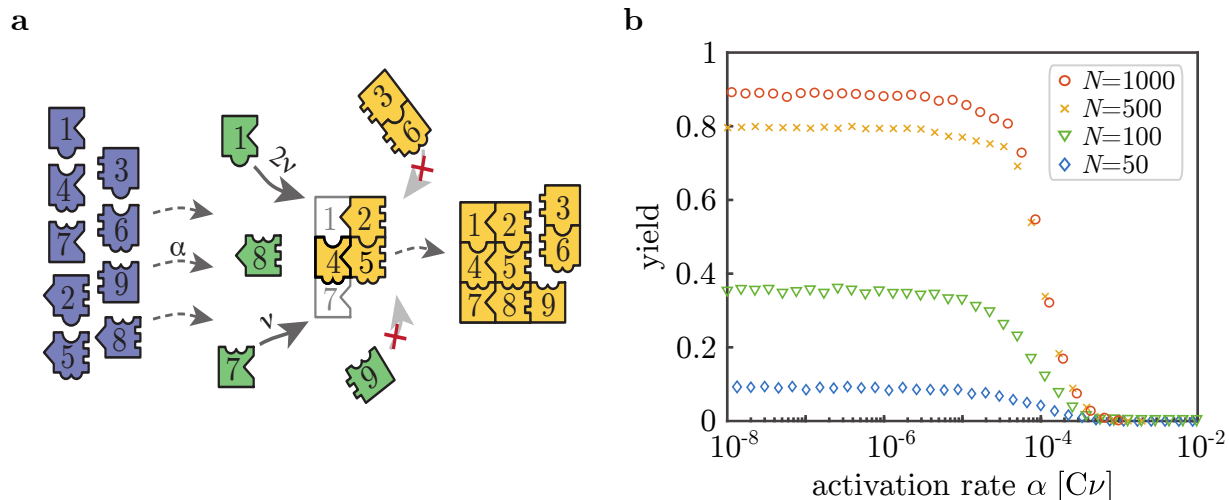


Figure 3.14: **Non-linear assembly path model.** (a) In a second extended model, we study the assembly of a fully heterogeneous square of size  $\sqrt{L} \times \sqrt{L}$ . This model does neither exhibit a complete symmetry between the different species nor a linear assembly path. In this way, we relaxed all major assumption of the original model. The binding rate of a monomer to the square is proportional to the numbers of contacts created. As shown in panel (b), still a reduction of the maximum yield due to stochastic fluctuations exists, which shows the same characteristics. This confirms that the overall effect is not caused by a particular model assumption. [Parameters:  $\text{ens.} = 256$ ,  $S = L = 100$ ,  $L_{\text{nuc}} = 2$ ,  $\mu = \nu = 1$ ; adapted from [122]]

Another simplifying assumption made is the existence of a linear assembly path. To ensure validity of our results, we studied the additional model shown in Fig. 3.14.a. A square is assembled using similar dynamics as in the original model. But because of its two-dimensional structure it is not limited to a unique assembly path. Note that this model is only well-defined in the fully heterogeneous case. It is not possible to define a homogeneous analogue because no limitations in the size could exist. As can be seen in Fig. 3.14.b the same effects are present as for the ring models. Accordingly, our results do not rely on the linear assembly path either and hence are robust against this modification.

Our analysis shows that while being deterministically similar, differences between virus capsid assembly and information rich structures exist when stochastic fluctuations are taken into account. Capsid assembly is well described by concentration-based models and favoring growth over nucleation in any way can improve the yield. For DNA-brick-like assembly processes reducing the dimerization are theoretically preferred if resources are not abundant. In practice, the experimental realization may not be as easy as for the activation scenario which only requires gradual provision of components. For a reduced dimerization rate a sophisticated design causing cooperative or allosteric effects is required. Alternatively, homogeneity of the components or an increased nucleation size can be employed to improve yield. But those two options reduce achievable complexity or require

more specific design. Mechanisms which reliably and efficiently can be used to optimize yield for information rich structures remain an interesting open question that is the topic of follow-up research to this project [166,168]. This is particularly true since demographic noise as caused by the activation mechanism is not the only possible source of fluctuations. Spatio-temporal fluctuations induced by reactions or diffusion are another example and are the topic of the next chapter.

From a more general perspective, despite the differences of the system studied in Chapter 2 and this model, conceptually many similarities exist: While one system is a spatially extended driven lattice gas model with exclusion in the stationary state, the other exhibits an absorbing state and describes well-mixed assembly of large macromolecules. These do not seem to have an overlap at all. But on an abstract level the number of lanes plays a similar role as the number of species and, because of irreversible binding, assembly of a structure can be interpreted as unidirectional motion in a one-dimensional configuration space. Furthermore, the ultimate source of stochasticity is given by a combinatorics problem that manifests in the limit of infinitely slow particle addition. The scale controlling the strength of fluctuations is in one case the number of lanes and in the other it is the number of species. If either of the two is increased, stochastic effects become stronger. For a value equal to one no fluctuations are observed at all.

# Chapter 4

## Reaction kinetics and absorbing states: The diffusive epidemic process

This chapter deals with the numerical investigation of the absorbing-state phase transition in the diffusive epidemic process. The results presented will be part of the manuscript *Strong Coupling Behavior in the Diffusive Epidemic Process* [169] which I prepare for publication<sup>1</sup> together with Borislav Polovnikov [170] (who contributes equally) and Erwin Frey.

Despite its simple structure, the diffusive epidemic process admits a very rich phenomenology which has resisted rigorous classification for several decades. A parameter regime exists for which neither perturbatively nor non-perturbatively renormalization group methods found a stable fixed point. This was interpreted as an indication for the existence of a discontinuous phase transition. However, several numerical studies reported the phase transition to be continuous in lower dimensions. Unfortunately, all these studies relied on different approximation methods and are partially inconsistent among each other such that still no definitive answer is available. The goal of this research project is to provide a concise picture of the one-dimensional diffusive epidemic process' phase transition. Since close to a critical point, systems exhibit very strong stochastic fluctuations, we use exact stochastic simulations to obtain unambiguous numerical data. To avoid finite size effects and similar artefacts, we employ measurements of dynamic spreading of activity to show that the phase transition is always continuous and determine the corresponding critical exponents. Based on our findings, we provide an explanation for the existing deviations between different previous approaches to study this system, and unravel the underlying mechanisms. To put our results into perspective, we start with an introduction to the diffusive epidemic process and methods employed for its quantification.

---

<sup>1</sup>Title may change in the process.

## 4.1 The diffusive epidemic process

The *diffusive epidemic process* (DEP) was introduced in 1989 to model the spreading of an infectious disease [35]. Nine years later it was generalized and reformulated in the form of a reaction-diffusion system [36]. Alternatively, the DEP can also be interpreted as a minimal model for cell polarity [171]. An illustration of the system in one dimension is shown in Fig. 4.1. The diffusive epidemic process consists of two particle species that populate a  $d$ -dimensional lattice. One species, denoted by  $A$ , represents "healthy" individuals while the second species, denoted as  $B$ , corresponds to "infected" members of the population. The interactions between the two are given via the reactions



The first reaction 4.1a represents the infection of healthy particles that happens at rate  $\lambda$ . Recovery of infected particles takes place on a characteristic time scale  $\tau$ , which manifests in the form of the second reaction 4.1b. No immunity after recovery exists such that a particle can immediately be reinfected. Both species move via diffusion at respective rates  $D_A$  and  $D_B$ . In this form, the system constitutes a mass-conserving extension of the paradigmatic *directed percolation* model [38]. Because particles only reallocate or switch between the species, the total number of particles  $N$  and the average particle density in the system  $\rho$  are conserved. Accordingly, the *global* state of the system is well-defined by the total number of infected particles  $N_B$ .

As for the systems discussed in Chapters 2 and 3, the stochastic dynamics of the occupation numbers  $n_i^A$  and  $n_i^B$  at a given lattice site  $i$  can be represented by coupled differential difference equations. In one dimension they read

$$\begin{aligned} \frac{d}{dt}n_i^A &= D_A n_{i-1}^A + D_A n_{i+1}^A + n_i^B/\tau - 2D_A n_i^A - \lambda n_i^A n_i^B, \\ \frac{d}{dt}n_i^B &= D_B n_{i-1}^B + D_B n_{i+1}^B - n_i^B/\tau - 2D_B n_i^B + \lambda n_i^A n_i^B, \end{aligned} \quad (4.2)$$

which can be generalized to higher dimensions by including the possibility of diffusion events in additional directions. Eqs. 4.2 appear to be fairly simple at first sight, but the non-linear coupling  $n_i^A n_i^B$  is sufficient to prohibit an exact solution. Consequently, as a start the same methods as in the previous chapters are applied to derive a deterministic approximation. To emphasize the connection to mass-conserving reaction-diffusion systems, we use the notation  $a_i := \langle n_i^A \rangle$  and  $b_i := \langle n_i^B \rangle$ . This way, the mean-field approximation takes the form

$$\lambda \langle n_i^A n_i^B \rangle = \lambda a_i b_i. \quad (4.3)$$

As for the self-assembly model in Chapter 3, it is important to realize that the DEP is not ergodic.  $B$  particles can only be created by other  $B$  particles. Once the infected species goes extinct the system is trapped in an absorbing state; Irreversibility exists in the system.

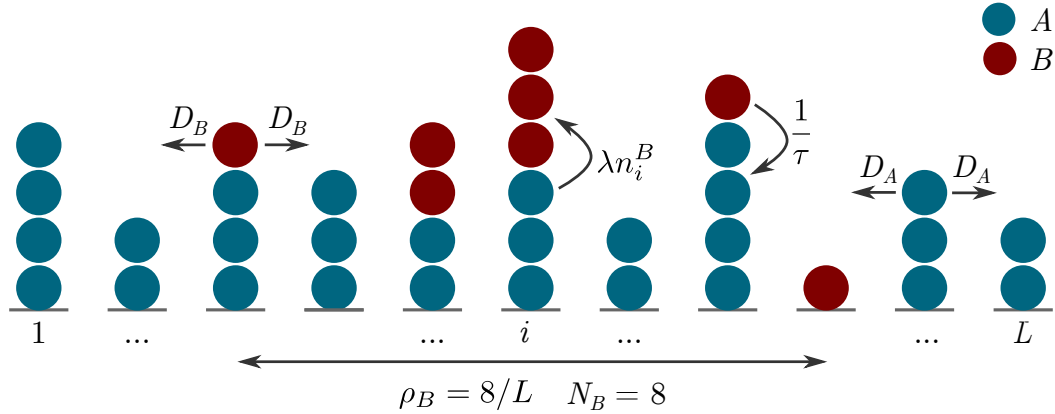


Figure 4.1: **Illustration of the diffusive epidemic process in one dimension.** Two particle species populate a one-dimensional lattice. Each particle of the infected species  $B$  may infect any particle of the healthy species  $A$  at the same lattice site at rate  $\lambda$ . In turn, an infected  $B$  particle turns healthy again at rate  $1/\tau$ . Both species randomly diffuse at fixed rates  $D_A$  and  $D_B$ . Because of mass conservation, the *global* state of the system can be fully characterized using the total number of  $B$  particles  $N_B$ .

However, this time it is not an explicit part of the model definition but a consequence of the postulated dynamics. In contrast to Chapter 2, all simulation averages hence have to be performed as ensemble averages. To emphasize the difference to a stationary state average, we will include the time dependency explicitly from here on. Assuming the absence of strong correlations between the species, the set of equations to solve then reads

$$\begin{aligned} \frac{d}{dt} a_i(t) &= D_A \Delta a_i(t) + b_i(t)/\tau - \lambda a_i(t) b_i(t), \\ \frac{d}{dt} b_i(t) &= D_B \Delta b_i(t) - b_i(t)/\tau + \lambda a_i(t) b_i(t), \end{aligned} \quad (4.4)$$

where  $\Delta$  denotes the discrete Laplacian. Despite being derived for the one-dimensional system, in this form the equations can be used to describe the DEP in arbitrary dimensions. The central question now is, what stationary state the deterministic system approaches for sufficiently long evolution times. A direct solution to Eqs. 4.4 are spatially constant densities

$$\begin{aligned} a_i(t) &=: \rho_A(t), \\ b_i(t) &=: \rho_B(t). \end{aligned} \quad (4.5)$$

The stationary state condition then simply is given by

$$0 = -\lambda \rho_A(t) \rho_B(t) + \rho_B(t)/\tau. \quad (4.6)$$

Because of the mass conservation, which requires  $\rho_A(t) + \rho_B(t) = \rho = \text{const}$ , two possible phase space structures exist in dependence on the initial condition. Fig. 4.2 (a) and (b)

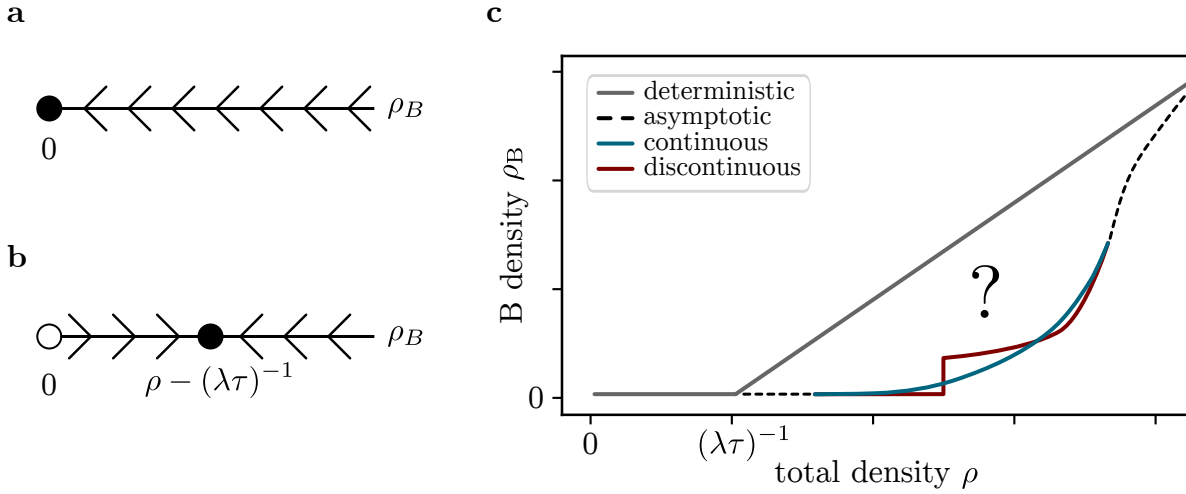


Figure 4.2: **Illustration of the deterministic homogeneous solution of the DEP.** Depending on the total particle density  $\rho$  coexistence between infected and healthy species may be possible. If it is too low (a), only one stable fixed point exists at zero  $B$  species density. When increasing the total density (b), this fixed point becomes unstable while a stable fixed point at finite  $\rho_B$  is created. (c) Deterministically, a transition between extinction and coexistence is predicted at  $(\lambda\tau)^{-1}$ . Because fluctuations can drive the system into the unstable but absorbing extinction fixed point, the actual system shows different behavior; Coexistence has to require higher total densities. In the limit of infinite density, the deterministic behavior has to be recovered. How the transition between extinction and coexistence takes place is an open question. In particular, it is unclear whether the transition can be discontinuous or is continuous in general.

illustrate the respective scenarios. Either a stable fixed point of Eqs. 4.4 exists at  $\rho_B = 0$  or this fixed point becomes unstable and a second, stable one occurs at  $\rho_B = \rho - (\lambda\tau)^{-1}$ . This can be summarized by [38, 51, 52]

$$\rho_B = \begin{cases} \rho - (\lambda\tau)^{-1} & \text{if } \rho > (\lambda\tau)^{-1} \\ 0 & \text{if } \rho \leq (\lambda\tau)^{-1} \end{cases} \quad (4.7)$$

Deterministically, the system undergoes a continuous phase transition between coexistence and extinction of the infected species as shown in Fig. 4.2.c. This, however, makes one important simplification that does not hold true as soon as stochasticity is considered. Fluctuations may drive the system into the unstable fixed point, trapping it permanently.

The diffusive epidemic process exhibits an *absorbing-state phase transition* [37, 38] that leads to significant deviations from the mean-field result (which does not even depend on the dimensionality or diffusion rates). Still, it allows us to draw some important conclusions. The transition towards coexistence will be shifted to higher densities since fluctuations favor extinction such that  $(\lambda\tau)^{-1}$  is a lower bound for the critical density. Furthermore, in the macroscopic limit  $\rho \rightarrow \infty$  the actual behavior of the system should approach the

mean-field result. Whether the transition that takes place in between is continuous or discontinuous is at this point an open question and a refined analysis or suitable stochastic simulations are necessary to obtain accurate predictions. The next sections provide an overview of the respective approaches.

## 4.2 Renormalization group methods and stochastic simulations

To analytically study Eqs. 4.2 without using the rather drastic mean-field approximation  $\langle n_i^A n_i^B \rangle = a_i b_i$ , the diffusive epidemic process can be mapped onto a continuous field theory; This allows for the use of renormalization group methods [172–175]. As was already shown in 1998 [36], the DEP has three different parameter regimes that depend on the ratio of the diffusion constants  $D_A$  and  $D_B$ . For the cases  $D_A = D_B$  and  $D_A < D_B$  perturbative renormalization predicts the existence of fixed points and hence suggests a second order phase transition. In contrast, for  $D_A > D_B$  neither using perturbative [36] nor non-perturbative methods [39] a stable fixed point has been found. This led to the conclusion that the transition has to be discontinuous in this case [176]. Based on the renormalization group analysis it seems, both scenarios illustrated in Fig. 4.2.c may occur depending on the diffusion constants.

Inconsistencies in the understanding of the diffusive epidemic process became evident when several numerical studies on the one hand confirmed the existence of the three different regimes, but on the other hand reported that all of them show a continuous phase transition (up to dimension three) [37, 40–46]. In addition, the actual values of the critical exponents associated with the transitions vary among the studies which all used different numerical approximation methods. Because of the contradictory results, a debate about the validity of the analytic predictions in dimensions one and two exist [40, 41, 177, 178].

A possible source of the deviations between simulations and analytic calculations in lower dimensions is that the perturbative renormalization is performed assuming the system to be close to four dimensions, with only a small deviation  $\epsilon := 4 - d$ . Recent theoretical studies suggest that terms in the action which can be neglected close to the critical dimension  $d_c = 4$  may play a significant role in dimensions below two [39]. Whether this is indeed the case has to be confirmed numerically. As a first step, the inconsistencies between the different studies have to be resolved first. We do so by employing exact stochastic simulations that yield unambiguous results for the behavior of the system and combine them with measurements of the dynamic spreading of activity [179–187]. The advantage of this method is that finite-size effects are only relevant as soon as the front reaches the system’s boundaries [38, 50–52].

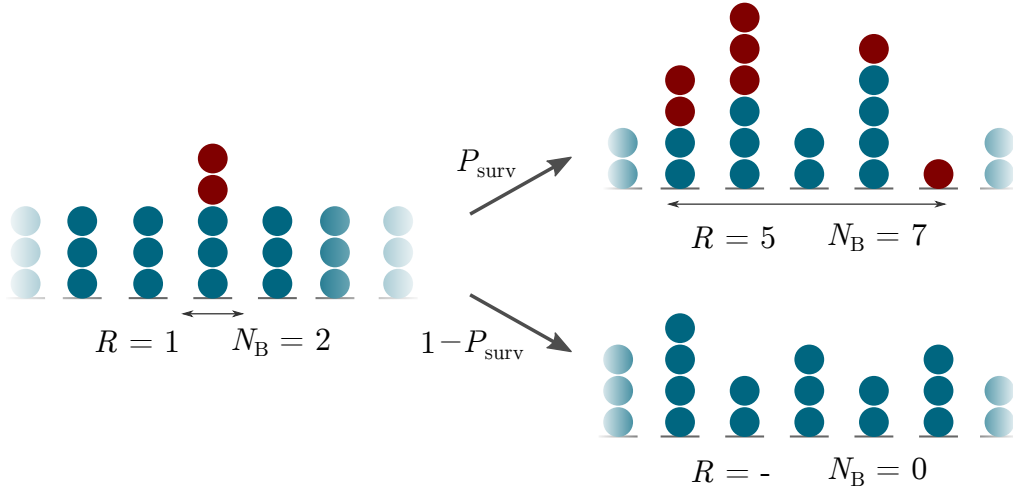


Figure 4.3: **Illustration of the dynamic spreading measurements.** The system is initialized with a small cluster of infected particles at its center. Three observables are tracked: First, the total number of  $B$  particles in the system  $N_B$ ; Second, the ratio of systems that still have a  $B$  particle population at a given time  $P_{\text{surv}}$ ; And third, the size of the  $B$  particle cluster in the *surviving* systems  $R$ . For the respective averages extinct systems are disregarded and do not contribute with the value zero.

### 4.3 Scaling relations

Instead of measuring observables only in homogeneous systems of different sizes [37, 40–46], we use *dynamic spreading of activity* [38, 50–52] to determine the critical exponents. The approach is conceptually illustrated in Fig. 4.3. In the initial state, a cluster of infected  $B$  particles is positioned at the center of the system. Afterwards, the temporal evolution of the number of  $B$  particles in the system  $N_B$ , the ratio of systems having a surviving  $B$  particle population  $P_{\text{surv}}$  and the cluster size squared  $R^2$  in the *surviving* system is recorded. If the absorbing-state phase transition of the DEP is indeed continuous, the scaling relations

$$\langle N_B(\rho, t) \rangle = t^\theta \widehat{N}_B((\rho - \rho_c)^{\nu_\parallel} t), \quad (4.8a)$$

$$P_{\text{surv}}(\rho, t) = t^{-\delta} \widehat{P}_{\text{surv}}((\rho - \rho_c)^{\nu_\parallel} t), \quad (4.8b)$$

$$\langle R^2(\rho, t) \rangle = t^{2/z} \widehat{R}^2((\rho - \rho_c)^{\nu_\parallel} t), \quad (4.8c)$$

have to hold close to it [51, 52]. Here  $\rho_c$  denotes the critical density and  $\widehat{N}_B$ ,  $\widehat{P}_{\text{surv}}$  and  $\widehat{R}^2$  are universal functions. Furthermore,  $\theta$ ,  $\nu_\parallel$ ,  $\delta$  and  $z$  are four independent critical exponents — note that  $\nu_\parallel = z\nu_\perp$  and  $\delta := \beta'/\nu_\parallel$  in the usual notation. In addition, to directly compare our results to previous work and hyperscaling relations, we also measure the decay of the order parameter  $\rho_B$  when initializing the system in a homogeneous state. In this case, the

scaling form reads [38, 52]

$$\langle \rho_B(\rho, t) \rangle = t^{-\beta/\nu_{\parallel}} \widehat{\rho}_B\left((\rho - \rho_c)^{\nu_{\parallel}} t\right). \quad (4.8d)$$

Altogether, Eqs. 4.8 define four observables and five independent critical exponents that characterize the absorbing-state phase transition [38, 52]. For both types of measurements long simulation times in combination with sufficiently large ensemble sizes are required. The respective results, obtained via the simulation methods explained in Appendix A.3, are discussed in the next section.

## 4.4 Critical exponents in one dimension

The parameter regime of main interest is the one of faster  $A$  particle diffusion ( $D_A > D_B$ ). However, we start by analyzing the case of equal diffusion rates ( $D_A = D_B$ ) which is best understood. It will serve as a reference for our results obtained for the controversial phase transition for  $D_A > D_B$ . We choose  $(\lambda\tau)^{-1} = 5$  which represents an intermediate deterministic critical density; Fluctuations are not too strong such that all systems die out immediately but the behavior is not fully deterministic either. Furthermore, by rescaling time the  $A$  particle diffusion rate is set to one (w.l.o.g.  $D_A = 1$ ).

Fig. 4.4.a shows the time evolution of the average  $B$  particle density  $\rho_B$  for systems initialized homogeneously without any  $A$  particle present in the beginning. The large system size  $L = 4096$  in combination with periodic boundary conditions allows for the assumption of weak finite size effects. According to Eq. 4.8d it is possible to collapse all data onto one universal curve  $\widehat{\rho}_B$  using the correct critical exponents  $\nu_{\parallel}$  and  $\beta/\nu_{\parallel}$  as well as critical density  $\rho_c$ . The best achievable result is depicted in Fig. 4.4.b. After rather long initial transients all curves align onto two branches — one below and one above the critical density. The estimated critical quantities<sup>2</sup> are  $\rho_c = 7.0 \pm 0.05$ ,  $\beta/\nu_{\parallel} = 0.078 \pm 0.003$  and  $\nu_{\parallel} \approx 4$ .

In a next step, we employ the estimated critical density obtained from the homogeneous initial state to derive the remaining critical exponents using dynamic activity spreading. Fig. 4.5 displays the time evolution of all four observables given in Eqs. 4.8. Panels (a–c) were obtained for systems of size  $L = 8192$  initialized with a cluster of ten  $B$  particles in the center<sup>3</sup>. For comparison, panel (d) shows the density evolution of the homogeneous initial state as used for the collapse in Fig. 4.4. All four curves converge towards straight lines in the loglog-plots, with corresponding estimates for the critical exponents<sup>4</sup> of  $z = 2.01 \pm 0.05$ ,  $\theta = 0.333 \pm 0.003$ ,  $\delta = 0.072 \pm 0.005$  and  $\beta/\nu_{\parallel} = 0.075 \pm 0.005$ . This agrees with the value  $\beta/\nu_{\parallel} = 0.078 \pm 0.003$  obtained from the data collapse. Two more consistency checks exist.

<sup>2</sup>The collapse is comparably insensitive to  $\nu_{\parallel}$ . The value  $\nu_{\parallel} \approx 4$  is consistent with theoretical predictions and hence the natural choice.

<sup>3</sup>The large system size  $L = 8192$  is actually the smallest one possible to ensure that the cluster does not reach the boundary in the considered time and hence avoid corruption of data.

<sup>4</sup>The estimates were obtained performing least square fits starting at  $t=1000$ .

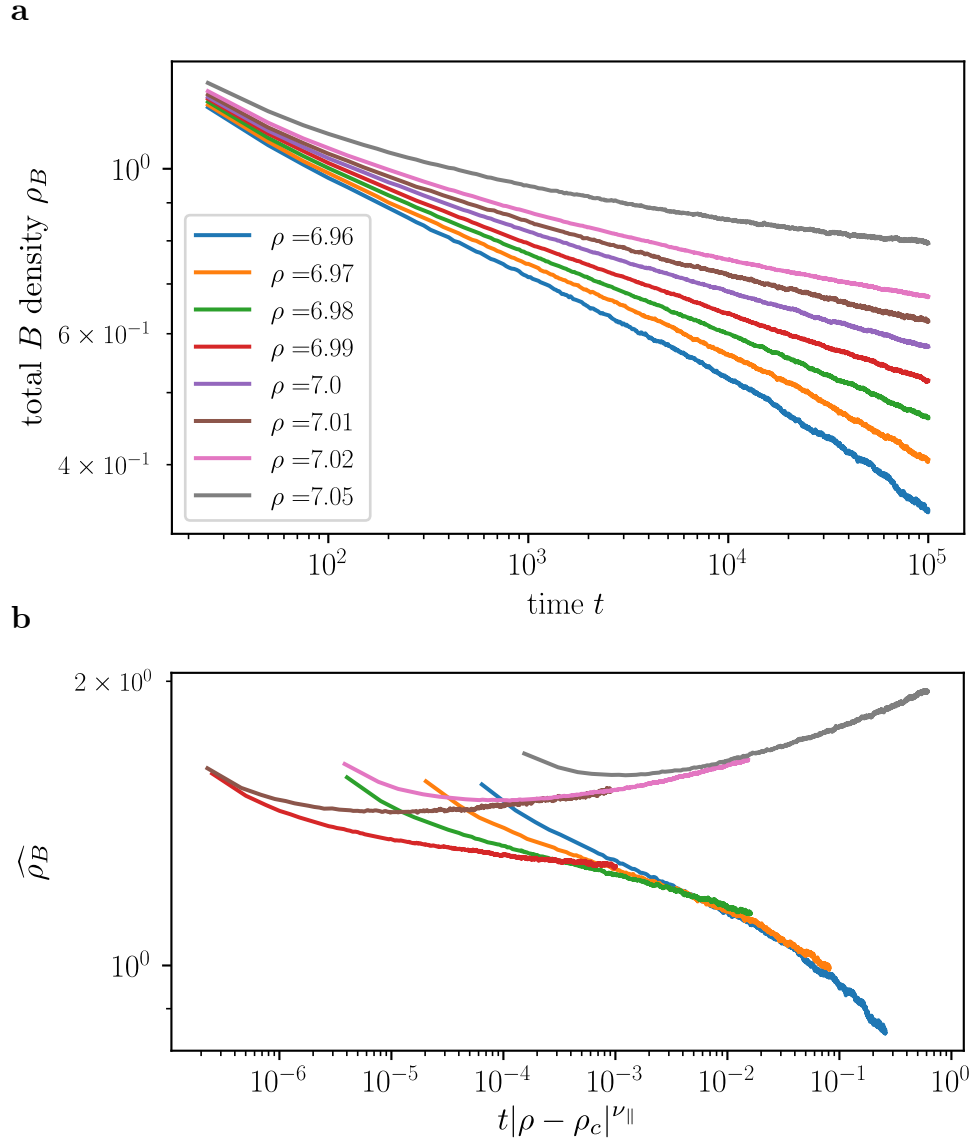


Figure 4.4: **Data collapse of the  $B$  particle density for  $D_A = D_B$  and a homogeneous initial state.** All curves can be collapsed assuming  $\rho_c = 7.0$ ,  $\nu_{\parallel} = 4.0$  and  $\beta/\nu_{\parallel} = 0.078$ . Long initial transients exist for all densities before the universal curve is reached. [Parameters:  $\text{ens.} = 5000$ ,  $L = 4096$ ,  $D_A = 1$ ,  $\lambda = 0.2$ ,  $1/\tau = 1$ ]

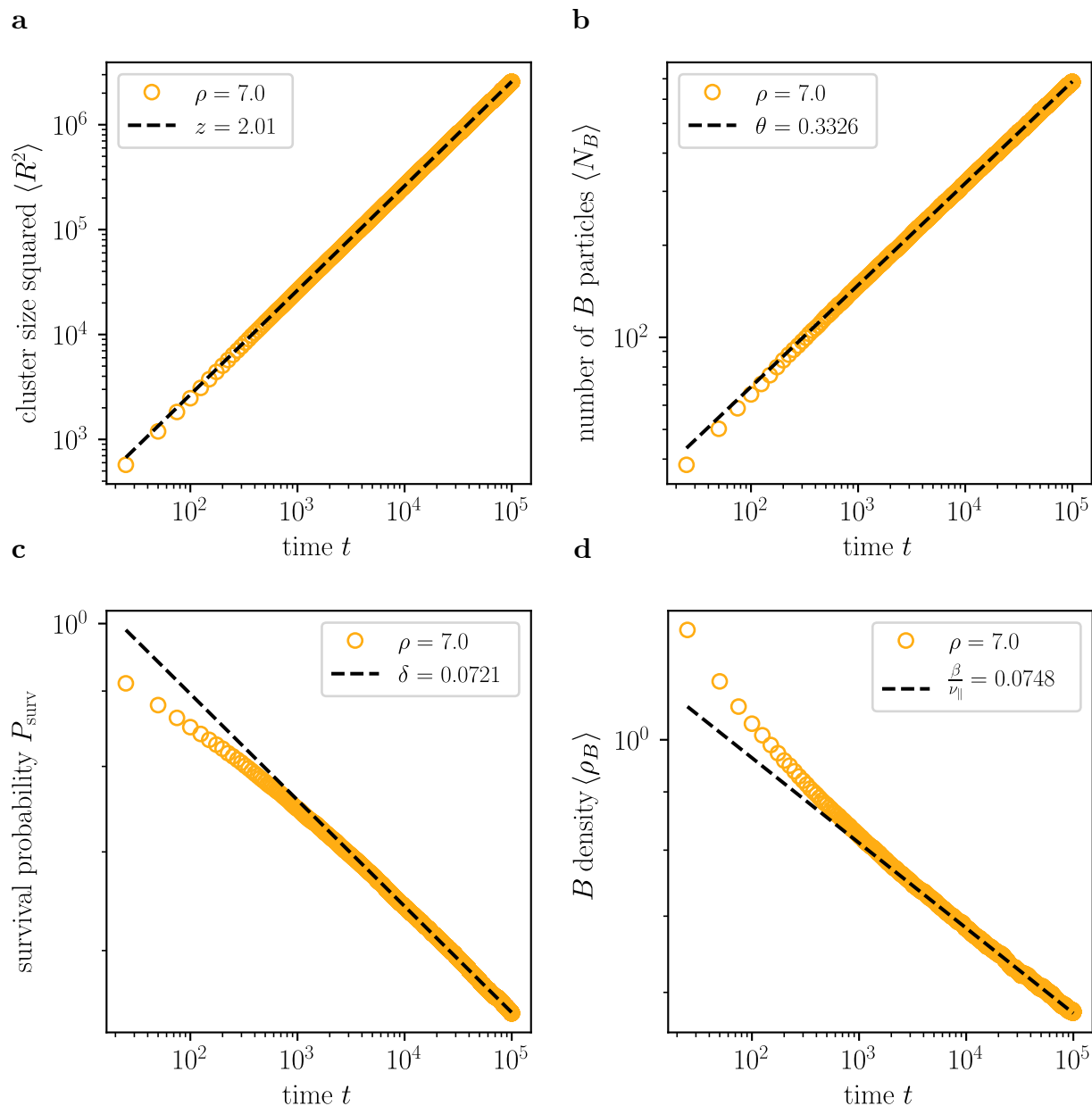


Figure 4.5: **Scaling behavior for  $D_A = D_B$ .** Panels (a–c) show the power law fits for systems initialized with a seed of ten  $B$  particles in the center. No deviations from the stochastic simulations can be observed after the initial transients. (d) The particle density for a system initialized with homogeneously distributed  $B$  particles follows a power law as well. As expected from the scaling theory, we find  $\delta = \beta/\nu_{\parallel}$  within the numerical error margins. [Parameters:  $\text{ens.} = 20000$ ,  $L = 8192$ ,  $D_A = 1$ ,  $\lambda = 0.2$ ,  $1/\tau = 1$ , (d) as in Fig. 4.4]

Time-reversal symmetry of the DEP-action enforces  $\beta = \beta'$ , resulting in the condition  $\delta = \beta/\nu_{\parallel}$  and the hyperscaling relation [36, 52, 188]

$$\theta = \frac{1}{z} - 2\frac{\beta}{\nu_{\parallel}}. \quad (4.9)$$

Both are confirmed within reasonable error margins. The difference between  $\delta$  and  $\beta/\nu_{\parallel}$  is only 0.003 and the expected value for  $\theta$  of 0.348 based on the hyperscaling relation differs by 0.014 from our measurement. In addition, our results for  $z$  and  $\nu_{\parallel}$  are compatible with previous reports using finite-size scaling methods and the existing theoretical predictions [36, 37, 45]. After the confirmation of our approach by the performed consistency checks, we now investigate the ambiguous parameter regime  $D_A > D_B$ .

In the following, we choose  $D_B = D_A/2 = 1/2$  for the diffusion rate of the  $B$  species. As before, we start by measuring and collapsing the data obtained for the time evolution of the total  $B$  particle density  $\rho_B$  in a system with homogeneous initial state. We find that all data can be collapsed close to the critical density  $\rho_c = 6.76 \pm 0.05$  assuming critical exponents  $\beta/\nu_{\parallel} = 0.51 \pm 0.03$  and  $\nu_{\parallel} = 3.8 \pm 0.3$ . Note that the maximum time had to be increased by a factor of ten to ensure that the system has overcome the initial transients. The scaling behavior confirms the existence of a continuous phase transition which agrees with previous numerical studies but contradicts the analytic prediction based on perturbative renormalization group methods [36, 37, 41, 45].

Next, we again use dynamic spreading of activity to derive the remaining critical exponents. In the  $D_A > D_B$  regime, we find  $z = 3.02 \pm 0.05$ ,  $\theta = -0.41 \pm 0.03$  and  $\delta = 0.72 \pm 0.02$  at the critical density  $\rho_c = 6.76$ . All curves approach straight lines in the loglog-plot except for the total particle number  $\langle N_B \rangle$  which shows deviations towards later times. This indicates a slightly higher critical density compared to the measurements performed in homogeneously initiated systems. To test and refine our results, we collapse our data according to Eqs. 4.8. As shown in Fig. 4.8 and Fig. 4.9, despite the existence of very long initial transients all curves approach universal functions and we can estimate <sup>5</sup> the critical exponents  $z = 3 \pm 0.02$ ,  $\theta = -0.38 \pm 0.02$  and  $\delta = 0.68 \pm 0.05$  and  $\nu_{\parallel} \approx 4$  at the critical density  $\rho_c = 6.765 \pm 0.05$ . Unfortunately, we cannot apply the same consistency checks as before. Because of the different diffusion rates, the symmetry between  $\beta$  and  $\beta'$  no longer exists and hence  $\delta \neq \beta/\nu_{\parallel}$  is to be expected. The hyperscaling relation in this case reads [36, 52, 188]

$$\theta = \frac{1}{z} - \frac{\beta}{\nu_{\parallel}} - \delta. \quad (4.10)$$

---

<sup>5</sup>Note that, we do not show the collapse for the cluster size squared in the main text but in Fig. C.5 of the Appendix. Since the effective ensemble size is drastically reduced by the condition on survival, strong fluctuations result in noisy curves. However, a collapse is still possible assuming  $z = 3$ ,  $\rho_c = 6.765$  and  $\nu_{\parallel} = 4$  which is consistent with our other results. Furthermore, the shown data implies that  $z$  only weakly changes for densities between 6.73 and 6.81 making a collapse not as necessary for a precise estimate as for the fast-changing particle number and survival probability.

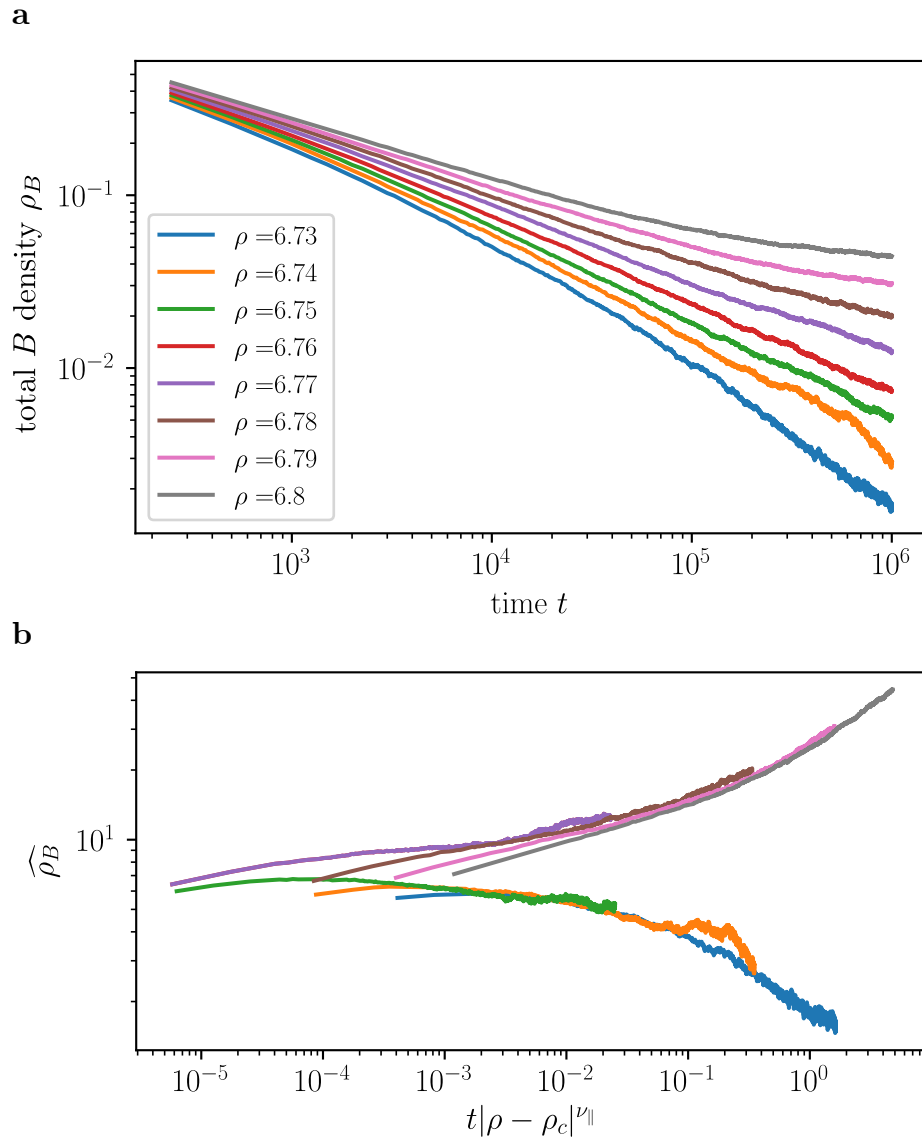


Figure 4.6: **Data collapse of the  $B$  particle density for  $D_A = 2D_B$  starting from a homogeneous state.** All curves can be collapsed assuming  $\rho_c = 6.76$ ,  $\beta/\nu_{||} = 0.51$  and  $\nu_{||} = 3.8$ . Strong fluctuations exist at later times because of the higher extinction rate compared to equal diffusion rates. [Parameters: ens. = 5000,  $L = 4096$ ,  $D_A = 1$ ,  $\lambda = 0.2$ ,  $1/\tau = 1$ ]

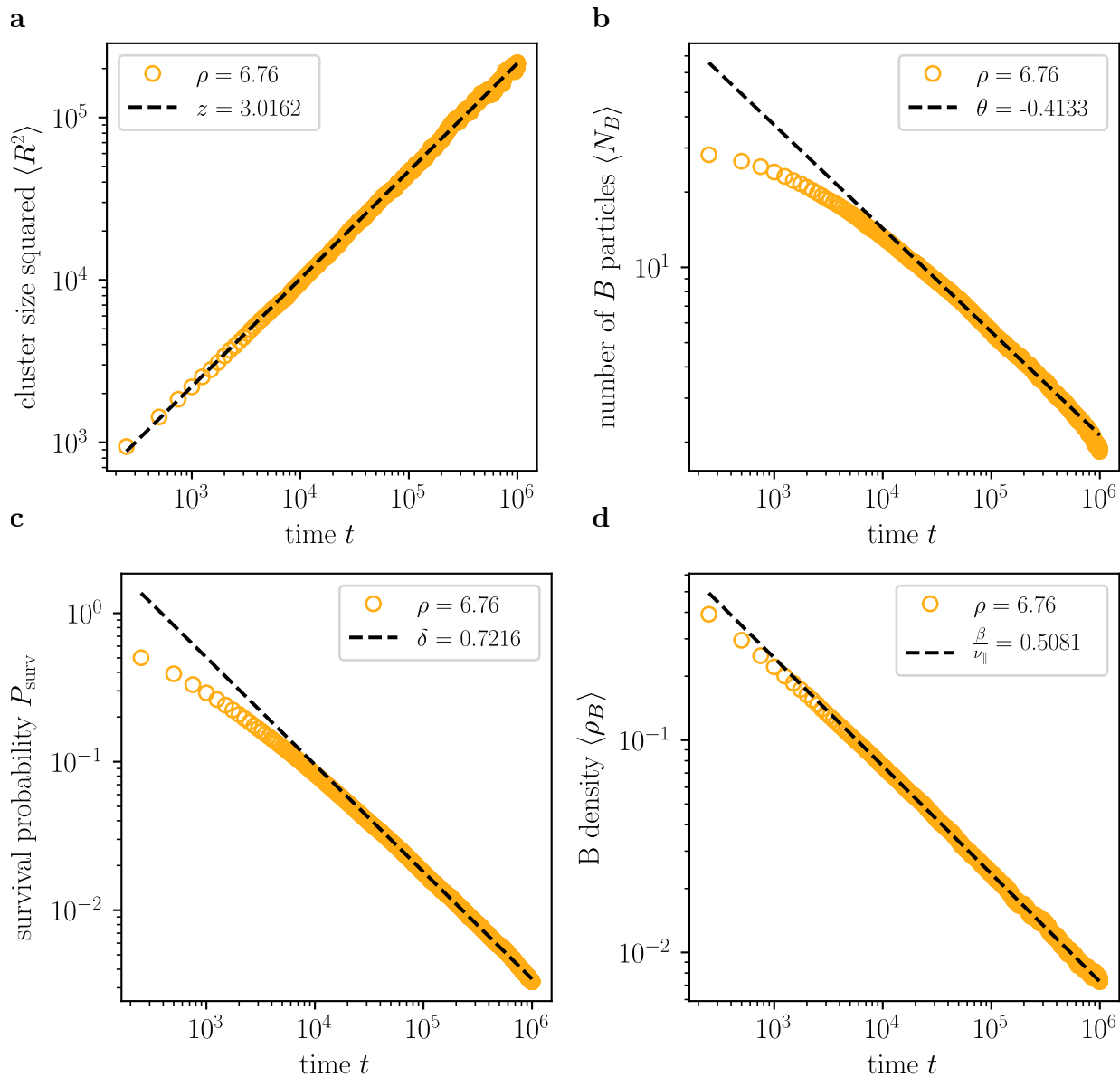


Figure 4.7: **Scaling behavior for  $D_A = 2D_B$ .** Panels (a–c) show the power law fits for systems initialized with a seed of ten  $B$  particles in the center. The deviations of the number of particles for larger times shown in panel (b) indicates that 6.76 is actually slightly below the critical density. (d) The particle density for a system initialized with homogeneously distributed  $B$  particles follows a strict power law. [Parameters:  $\text{ens.} = 15 \times 10^4$ ,  $L = 8192$ ,  $D_A = 1$ ,  $\lambda = 0.2$ ,  $1/\tau = 1$ ; (d) as in Fig. 4.6]

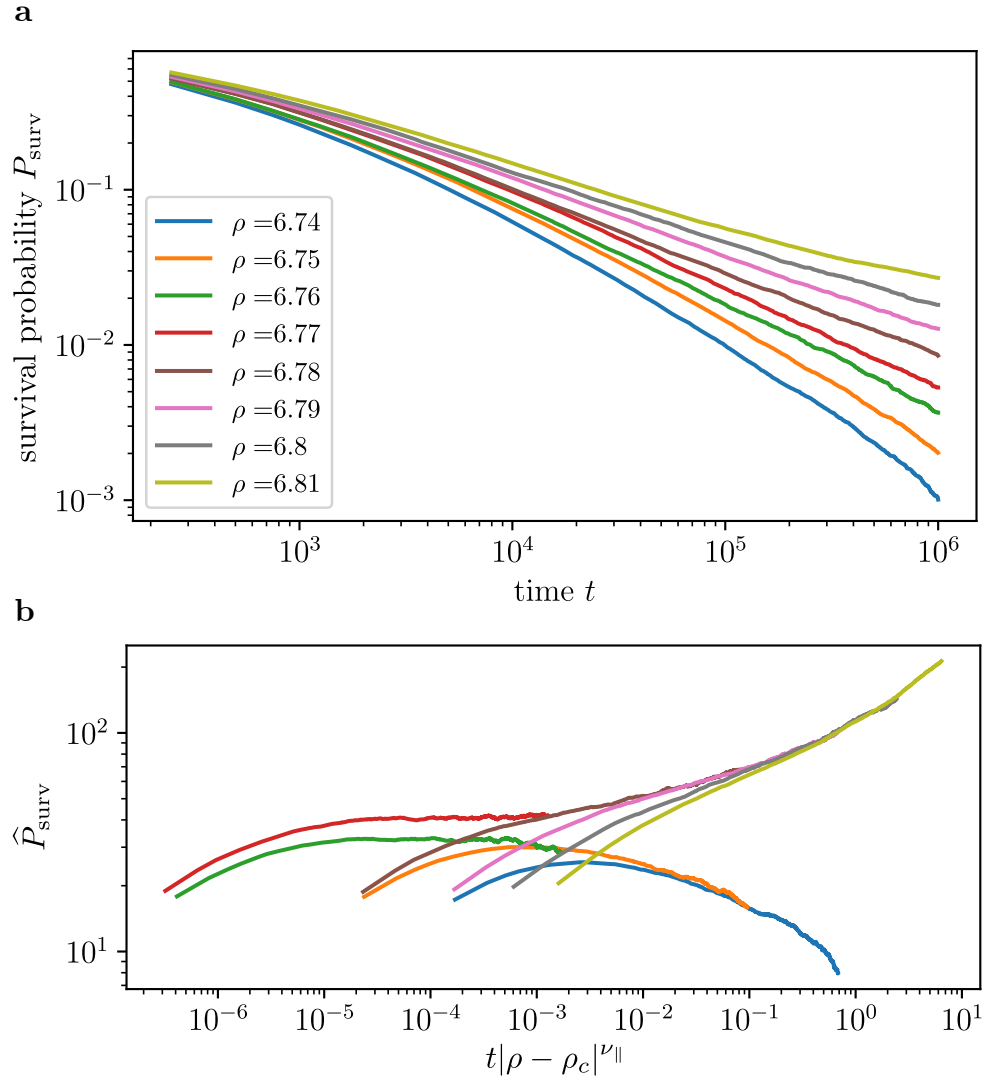


Figure 4.8: **Data collapse of the survival probability  $P_{\text{surv}}$  for  $D_A = 2D_B$  starting from a cluster of infected particles.** All curves can be collapsed successfully assuming  $\rho_c = 6.765$ ,  $\delta = 0.68$  and  $\nu_{\parallel} = 4$ . Long initial transients exist for all densities before the master curve is reached. [Parameters:  $\text{ens.} = 5 \times 10^4$ ,  $L = 8192$ ,  $D_A = 1$ ,  $\lambda = 0.2$ ,  $1/\tau = 1$ ]

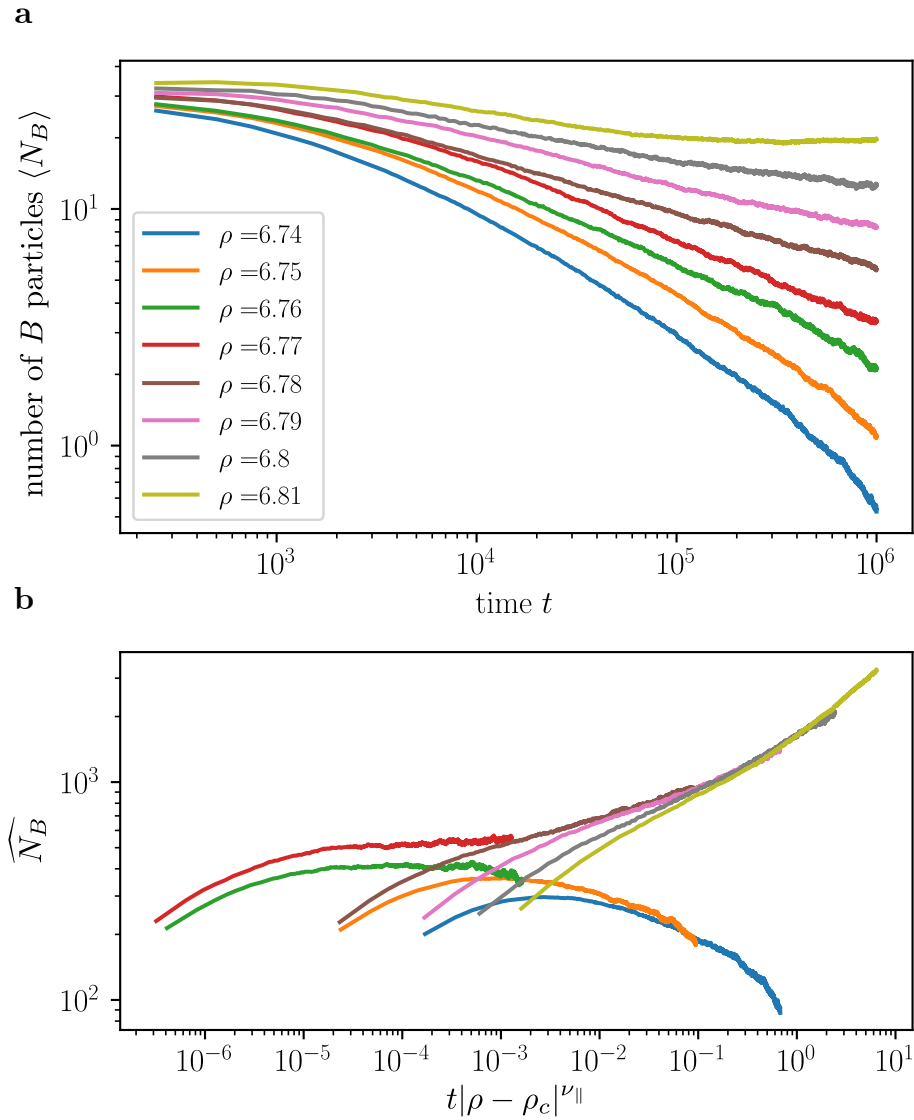


Figure 4.9: **Data collapse of the number of  $B$  particles  $N_B$  for  $D_A = 2D_B$  starting from a cluster of infected particles.** All curves can be collapsed assuming  $\rho_c = 6.765$ ,  $\theta = -0.38$  and  $\nu_{||} = 4$ . Long initial transients exist for all densities before the universal curve is reached. [Parameters:  $\text{ens.} = 5 \times 10^4$ ,  $L = 8192$ ,  $D_A = 1$ ,  $\lambda = 0.2$ ,  $1/\tau = 1$ ]

and predicts  $\theta \approx -0.86$  which is off by more than a factor two; But is unclear whether it has to hold in the first place. Since we did not make any approximations and all results were correct in the  $D_A = D_B$  case, we do not have any reason to doubt our findings which now show clear differences in comparison to other numerical studies. Most importantly, the value  $z \approx 3$  implies sub-diffusive spreading of the cluster which is in stark contrast to the diffusive behavior indicated by  $z = 2$  that was assumed previously [37, 41, 45]. This immediately raises the question, what the differences in the dynamic spreading behavior between the two cases  $D_A = D_B$  and  $D_A > D_B$  are and why they have not been observed before.

## 4.5 Spreading behavior for different diffusion ratios

The best way to investigate the origin of the sub-diffusive spreading at the phase transition indicated by the critical exponent  $z = 3$ , is to directly resolve the spatio-temporal evolution of the particle clusters and compare it to the  $D_A = D_B$  case. As it turns out, the quantity providing the most insight into the underlying mechanism is the total particle number  $n_i := n_i^A + n_i^B$ . For a system with identical diffusion rates  $D_A = D_B = D$  the dynamics of the system is described by

$$\begin{aligned}\frac{d}{dt}n_i^A &= D\Delta n_i^A + n_i^B/\tau - \lambda n_i^A n_i^B, \\ \frac{d}{dt}n_i^B &= D\Delta n_i^B - n_i^B/\tau + \lambda n_i^A n_i^B.\end{aligned}\tag{4.11}$$

Summing up both equations yields

$$\frac{d}{dt}n_i = D\Delta n_i.\tag{4.12}$$

Because of its conservation in combination with the identical diffusion rates, the total particle density  $m_i(t) = \langle n_i \rangle$  obeys a simple diffusion equation. Gradients originating from the initially placed particle cluster smoothen out over time and the spreading of the  $B$  particles takes place in a homogeneous environment (with respect to the total mass, not the individual species distributions). This intuitive arguing is confirmed by the stochastic simulations shown in Fig. 4.10.a.

For the case  $D_A = 2D_B$  a completely different phenomenology can be observed as presented in Fig. 4.10.b. The  $B$  particle cluster does not spread in a homogeneous environment but accumulates mass. By doing so, it depletes its surroundings and causes a *local* reduction in the total density below the average value. The cluster hinders its own expansion by reshaping the density distribution in the system<sup>6</sup>. As a result, the cluster sizes squared  $R^2$  grows slower, manifesting in the dynamical exponent  $z = 3$ .

<sup>6</sup>For completeness the time evolution of the individual densities is shown in Fig. C.6 in the Appendix. However, apart from the expected strong anti-correlations between the species no additional insight compared to the total particle density can be obtained.

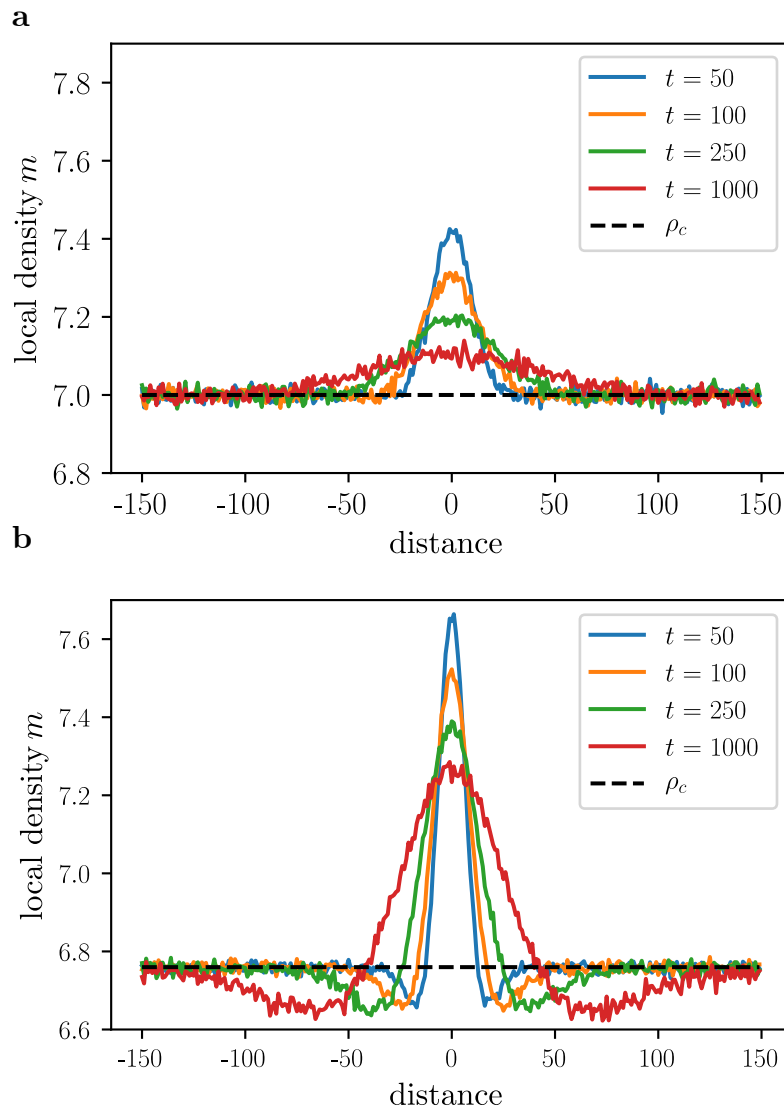


Figure 4.10: **Comparison of the activity spreading behavior.** (a) For identical diffusion constants  $D_A = D_B$ , the particle density of the initial particle cluster spreads diffusively until a flat profile is reached (This does not imply the extinction of the  $B$  species. The total particle density in the system just shows diffusive behavior as a whole.). (b) In contrast, for different diffusion rates  $D_A = 2D_B$  the cluster accumulates mass and hence depletes the surrounding area. [Parameters:  $L = 512$ ,  $D_A = 1$ ,  $\lambda = 0.2$ ,  $1/\tau = 1$ , (a) ens. = 50000,  $\rho = 7.0$ , (b) ens. =  $10^5$ ,  $\rho = 6.76$ ]

The intuitive explanation for the redistribution of mass lies in the heterogeneous initial  $B$  particle distribution. Since infected particles diffuse slower compared to the  $A$  particles present mainly outside the cluster, effectively, a gradient in the diffusion rate of the total particle density  $m$  exists. Movement into the cluster is faster than out of it, which cause a net particle flux towards the cluster. To phrase it differently, for  $D_A = 2D_B$  twice as many  $B$  particles are required to have the same probability for a hopping event. This idea can be expressed in the form

$$D_A \cdot a_i + D_B \cdot b_i = \text{const}, \quad (4.13)$$

which has to be fulfilled for no fluxes in the total density to occur. Accordingly, mass moves from lattice sites with high  $A$  density (outside the cluster) towards sites of higher  $B$  density (inside the cluster). Fig. C.7 in the Appendix shows the spatial distribution of the effective number of hopping events per unit time  $D_A a_i + D_B b_i$  which has indeed a minimum at the cluster's boundaries.

For the case  $D_A = 2D_B$ , Eq. 4.13 would require  $a_i = \rho_c - 0.5 \cdot b_i$  and hence contradicts a uniform particle distribution. For  $D_A = D_B$ , however, a uniform density distribution and Eq. 4.13 are identical. Fig. 4.11 compares the phase space distributions for both diffusion ratios. As can be seen in panel (a), the well-understood case of equal diffusion rates follows the expected behavior. For different diffusion rates in contrast, neither flux balance nor a constant density distribution is realized, as shown in panel (b). The actual subspace representing the states of lattice sites that can occur in the system follows a function which has a cusp when approaching the  $a$ -axis. Empirically we find  $a = 6.73 - 0.6 \cdot b^{0.53}$ . Similarly, as shown in Fig. C.8 of the Appendix, for  $D_B = 0.8$  a function of the form  $a = 6.92 - 0.81 \cdot b^{0.77}$  is measured. This suggests an analytic expression of the form

$$a = \rho_c - f \left( \frac{D_B}{D_A} \right) \cdot b^{\frac{D_B}{D_A}}, \quad (4.14)$$

to describe the phase behavior of the system (at least approximately). The shape of this function is at the heart of an analytic description of the phase transition of the diffusive epidemic process.

## 4.6 Conclusion

By measuring the dynamic spreading of activity, we managed to obtain reliable estimates for the critical exponents of the diffusive epidemic process. In case of identical diffusion rates  $D_A = D_B$ , which is the best understood of three existing parameter regimes, our findings agree with all previous results, and the expected symmetries and hyperscaling relations are fulfilled.

For different diffusion rates  $D_A > D_B$ , we observed significant deviations between our measurements and other studies. The differences are most evident in the form of the dynamical exponent  $z = 3$  that indicates sub-diffusive spreading instead of the diffusive spreading that was reported before. At this point the central question is why our results

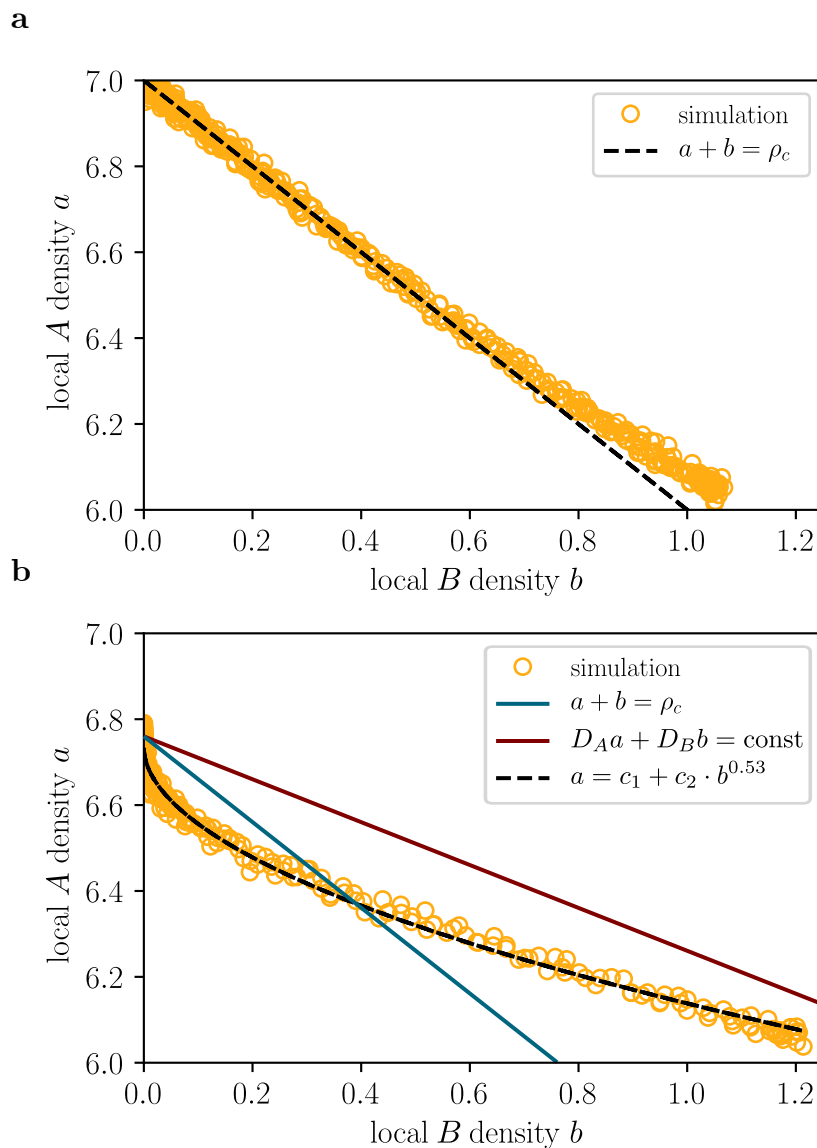


Figure 4.11: **Comparison of phase space distributions.** (a) In case of identical diffusion constants  $D_A = D_B$ , the flux balance condition  $D_A a + D_B b = \text{const.}$  is identical to the curve of homogeneous local density  $a + b = \rho_c$ . Apart from small deviations for large  $B$  particle densities caused by the non-homogeneous initial condition, all lattice sites adapt configurations on this line. (b) For different diffusion rates  $D_A = 2D_B$  configurations neither adapt to the line of balanced fluxes nor the line of constant local density. Instead a dependency showing a  $\sqrt{b}$  like shape is realized. [Parameters:  $L = 512$ ,  $t = 1000$ ,  $D_A = 1$ ,  $\lambda = 0.2$ ,  $1/\tau = 1$ , (a) ens. = 50000,  $\rho = 7.0$ , (b) ens. =  $10^5$ ,  $\rho = 6.76$ ,  $c_1 = 6.73$ ,  $c_2 = -0.6$ ]

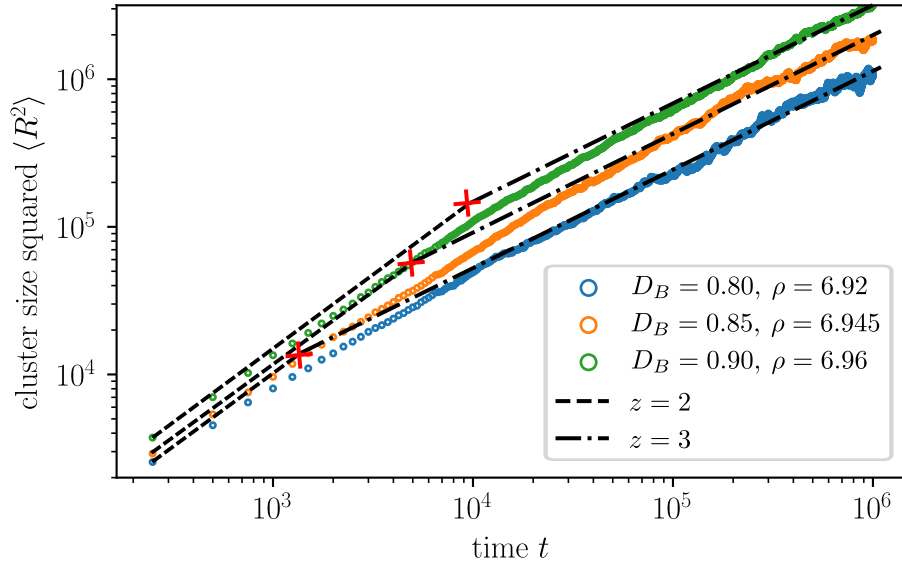


Figure 4.12: **Transition times between diffusive and sub-diffusive spreading close to the critical density.** For systems which have different diffusion constants, close to the critical density  $\rho_c$   $D_B < D_A$  a transition between transient diffusive behavior ( $z = 2$ ) and asymptotic sub-diffusive spreading ( $z = 3$ ) takes place. The transition time increases with the diffusion constant  $D_B$ . [Parameters:  $\text{ens.} = 25000$ ,  $L = 8192$ ,  $D_A = 1$ ,  $\lambda = 0.2$ ,  $1/\tau = 1$ ]

differ from other simulations which all hint at  $z = 2$ . Two aspects are relevant in this context. First, the mechanism explained in Sec. 4.5 is caused by local gradients in the number of  $A$  and  $B$  particles. For the dynamic spreading of activity this is naturally a dominating effect since strong differences in the distributions exist by construction. In contrast, in a homogeneous state it does not occur. Fluctuations would need to create spatial heterogeneities which are then amplified. The time required for the necessary events to take place and significantly affect the system is most likely far beyond any reasonable simulation scope. This directly relates to the second reason which is illustrated in Fig. 4.12. Depending on the difference between the two diffusion rates, the time and length scales required to resolve the deviations even using the dynamic spreading approach may increase drastically. Actually, the case of equal diffusion rates can be interpreted as the limit of infinite transient diffusive behavior for  $D_B \rightarrow D_A$ . For finite-size scaling methods which use smaller system sizes and simulation times the transition simply cannot be resolved. Previous numerical studies hence performed correct measurements, but either in an entirely different state or a transient configuration that may stretch out almost to eternity depending on the choice of parameters and initial conditions. With respect to the predictions based on perturbative renormalization group methods, our results suggest that indeed terms that can be neglected in higher dimensions play a fundamental role in one

dimension [39]. Based on our findings those should account for the accumulation of mass in the cluster caused by different diffusion rates.

Taking together, by providing the corresponding critical exponents and data collapses we succeeded in proving that the diffusive epidemic process exhibits a continuous phase transition in the notorious  $D_A > D_B$  regime. In this context, we found significant deviations compared to existing results but managed to provide a consistent picture of the underlying phenomenology. Mass is accumulated inside the  $B$  particle cluster because of the reduced diffusion speed inside. Since the number of healthy particles in the surroundings gets depleted, the cluster hampers its own spreading. As a consequence,  $A$  particle and  $B$  particle densities on identical lattice sites do not follow a simple linear relation that corresponds to a constant distribution of the total particle density. Instead a non-trivial function that exhibits a cusp is realized. Mass conservation and flux balance are two major determinants of the structure of this function but are by themselves not sufficient to explain the observed shape. Additional analytic research that mathematically formalizes our findings is needed to provide a detailed understanding of the mechanisms at work.

Finally, we take a step back and put our results into perspective with respect to the research goals of this thesis. In the same way as for the systems studied in Chapters 2 and 3, we analyzed a stochastic system that we cannot solve analytically. Employing a mean-field approximation a solution can be derived which is accurate in the macroscopic limit of high particle numbers but shows significant deviations at mesoscopic levels. Here, the reason for the crucial relevance of fluctuations was the existence of an absorbing state. In contrast to the other cases however, a refined analytic theory already existed as well as other numerical studies; These, however, presented an inconsistent picture.

The reference for our analysis this time was not a mean-field theory but the parameter choice  $D_A = D_B$  which is affected by fluctuations but is understood on the basis of renormalization group theory. In this sense, we had to go a step further than in the other projects. Nonetheless, in a similar way as before by comparing stochastic simulations with the predictions obtained using simplifying assumptions we identified the driving force of the observed deviations. For the diffusive epidemic process, it is the mass redistribution caused by the difference in diffusion rates. Hence, the diffusion parameter  $D_B$  plays a similar role as the number of lattice sites for the extended TASEP model or the number of species for the self-assembly model. In the next step, it has to be clarified whether a similar effect exists in two dimensions because the same doubts with respect to negligible terms in the DEP's action exist [39]. How this can be achieved efficiently and extended to other systems is the topic of the next chapter.

# Chapter 5

## Exact stochastic simulations of general reaction-diffusion systems

Chapters 2–4 deal with specific systems which all are affected by stochastic fluctuations in different ways. The deterministic approximation methods, however, are conceptually similar. They are based on using densities instead of particle numbers and neglecting correlations. For the deterministic part of the analysis standard approaches exist. This by no means implies that they are easy or straightforward to apply. There are just tools available which are known to be promising in this context — in particular in case of large enough particle numbers and length scales such that fluctuations become negligible. But for the systems studied in this thesis, they get insufficient at some point because exactly those stochastic fluctuations become a major determinant of the dynamics. The respective analytic tools have to be tailored to each problem individually. How this is done and which aspects necessarily must be included is a priori unclear. The only approach that can be employed in all cases that does not rely on any ad hoc assumptions are exact stochastic simulations. They are the reference against which all other methods can be tested. In addition, they provide a basic understanding of the systems phenomenology. However, just because stochastic simulations are a universal tool does not mean they can always be used in the same way. Limitations in time and hardware resources may result in simulations that solve an underlying problem in principle but are impossible to perform. Hence, simulations as well have to be optimized for a particular problem, to be useful. How this is done for the systems considered in this thesis is explained in detail in Appendix A.

The goal of the project discussed in this chapter is to provide means that can be employed to study stochastic effects for entire classes of systems instead of just the ones they were designed for. Using analytical methods, this is not feasible. As of today, it is not even clear if a unifying approach for systems far from thermal equilibrium exists not to speak of how it could look like. Overarching patterns between different systems have to be found to further this research. In the biochemical context of this thesis, reaction-diffusion systems constitute a very promising class of systems with broad applications that may serve as a starting point. Already at the deterministic level, approximated in terms of densities

without correlations instead of particle numbers a very rich phenomenology exists. But as was shown in Chapter 4, even a very simple system can be drastically affected by stochastic fluctuations.

As a first step towards a more general ansatz for the study of stochastic effects I created a simulation framework which allows for lattice-based exact stochastic simulations of arbitrary reaction-diffusion systems. It is constructed in a way such that it can be easily extended to include new features e.g., different geometries or modes of motion. In addition, a script language was implemented to make the creation of new simulations as intuitive and simple as possible. This was done having two kinds of users in mind. On the one hand, more experienced programmers can extend the code itself and use it to study systems beyond the provided geometries or even reaction-diffusion dynamics. On the other hand, researchers who are focused on descriptions based on non-linear dynamics can immediately check their results against simulation data and verify their approximation methods or find limitations, and hence possibly discover unknown effects. The primary goal of this project is to provide easy and fast means to perform exact stochastic simulations without prior time consuming or inefficient<sup>1</sup> implementation by the user. This chapter serves as an introduction to the framework and its structure as well as the usage of the script language to create and evaluate simulations.

## 5.1 Basics

Two central aspects of the framework exist: the script language which is used to create simulations and the program structure itself which can be modified to allow for new classes of simulations. As a start, this section gives some basic examples of the functionality and the work flow using the script language while treating the program itself as black box. Later sections built on this part to explain the program structure, its extension, general simulations and possible research applications.

Scripts written in .txt files serve as the input of the main program. A first minimalistic example which simulates the combination of hydrogen H and oxygen O to form water H<sub>2</sub>O, looks as follows.

```
2H + O -> H2O : 0.0001
H = 3000
O = 1000
SimulateWellMixed(0.05,0.00025,WaterReaction,42)
```

The initial line "2H + O -> H<sub>2</sub>O : 0.0001" defines a possible reaction<sup>2</sup>. In this context three key symbols exist. The rate at which a reaction takes place is written at the end of a line and is indicated by the ":". Products and educts of the reaction are separated by the

<sup>1</sup>A program specifically created for just a single system always admits more optimization potential. But the additional speed-up is significantly smaller than the one achieved for spatially extended system using optimized algorithms (see Appendix A.3).

<sup>2</sup>Expressions like H<sub>2</sub> are not supported by normal .txt files hence H2O is used.

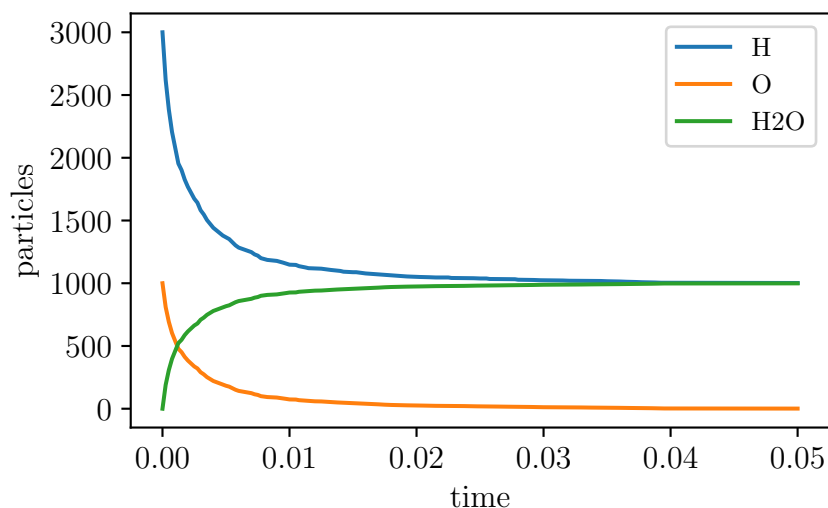


Figure 5.1: **Simulation of the minimal example script.** A stochastic version of the reaction  $2\text{H} + \text{O} \rightarrow \text{H}_2\text{O}$  was simulated and visualized using the simulation framework. Because of the large particle numbers all curves are comparably smooth.

reaction arrow " $\rightarrow$ ". Finally, individual components are distinguished via the "+" sign in between. The names of components are allowed to consist of letters and numbers, however, they are always assumed to start with letters such that an initial number e.g., 2 in "2H" is interpreted as two components of H being needed for the reaction. The next two lines "H = 3000" and "O = 1000" specify the initial particle numbers. They are characterized by a regular species name followed by an "=" sign and a *real* number. For a particle-based simulation of a well-mixed system of course only natural numbers<sup>3</sup> can be realized. In spatially extended systems however, the average density does not have this constraint (see Sec. 5.3). The last line of the script, "SimulateWellMixed(0.05,0.00025,WaterReaction,42)", states which kind of simulation should be performed for the above specified system. A list of all available functions is provided in Table 5.1 at the end of Sec. 5.3. In this case, a well-mixed system is simulated for 0.05 units of time. Information about the current state of the system is recorded every 0.00025 units of time and stored in the output-file by the name "WaterReaction". The last argument 42 specifies the initial seed for the random number generator<sup>4</sup>. The output of the resulting simulation is shown in Fig. 5.1.

As another basic example, the three-component cyclic suppression system given below introduces several additional features such as birth and death, reaction names, reaction inhibition and ensemble simulations.

```
U -> 0 : 0.3
V -> 0 : 0.3
```

<sup>3</sup>If no initial particle number is specified for a species it is assumed to be 0.

<sup>4</sup>In this form, the danger of reusing the seed and hence creating correlated simulations exists. Tools to avoid this problem are explained in later sections.

```
W -> 0 : 0.3
inhibU = 0 -> U : 10
inhibV = 0 -> V : 10
inhibW = 0 -> W : 10
U -| inhibV: 0.1
V -| inhibW: 0.2
W -| inhibU: 0.3
U = 25
EnsembleWellMixed(50,0.5,Oscillations,1337,5000)
```

The first 6 lines describe which reactions are possible. The "0" on either side of the reaction arrow indicates the absence of any component. Here they amount to birth and death events. In contrast to the first three reactions, names are assigned to the second three. A regular character sequence followed by "=" and a reaction, creates the reaction and assigns it to a variable which can later be referred to in inhibition relations indicated by the "-" symbol. Those consists of a species which performs the inhibition on the left side and a reference to the reaction which is inhibited on the right side of the spacer. As always, the corresponding rate is indicated by the ":". Negative numbers are interpreted as positive feedback. In this example, the different species suppress each other's production. At the current stage, both kinds of interactions are implemented as being exponential.

Because of the low numbers of particles specified, an ensemble of simulations has to be performed to obtain meaningful statistics which is achieved using the ensemble function. All arguments provided are identical to the single simulation request except for the additional integer 5000 which specifies the number of ensembles to simulate. The output of the execution of the script is shown in Fig. 5.2.

Both examples discussed so far, are most basic in the sense that no additional work beyond the creation of the respective scripts was necessary. All simulation set-ups and visualizations are automatically performed as illustrated in Fig. 5.3. Scripts are translated by a parser into the desired simulations which create standardized data output that can be processed via the visualization tools.

In case additional information about the system is needed all is contained in the time trajectories stored in the .hdf5 files. In this scenario, it is only necessary to extend the visualization tools e.g., to extract information like time correlations. This is the main use the project is intended for. The simulations of the script can be treated as a black box as far as usage is concerned.

To study reaction diffusion systems in general however, a lot of additional functionality is needed. In fact, so far diffusion was not even a part of the scripts because all systems were well mixed. The full functionality of the script language is discussed in Sec. 5.3 and Sec. 5.4. But before that, the next section explains the actual program structure to allow for a better understanding of how the respective simulations are implemented.

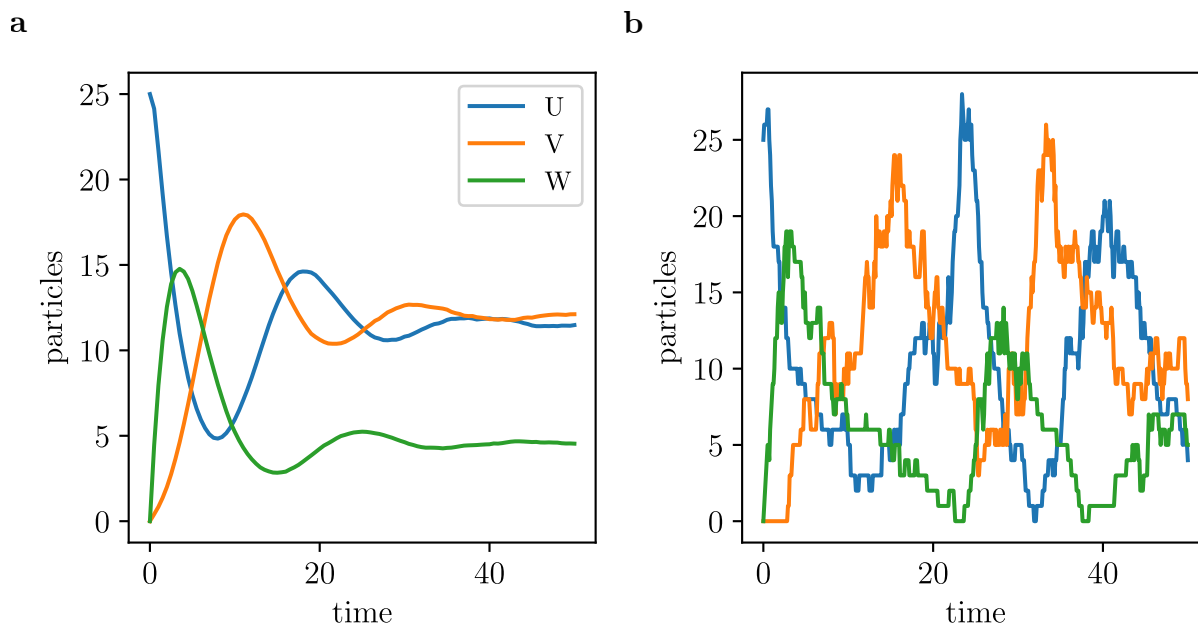


Figure 5.2: **Ensemble simulation example.** The three different species U, V and W cyclically suppress each other's production resulting in transient oscillations. Panel (a) shows the results for an average performed over 5000 ensembles. As a contrast, output from a single simulation is shown in panel (b). Both only differ by the *Ensemble* keyword in the simulation script.

## 5.2 Program structure

The program is implemented in C++ using the object-oriented programming paradigm. Employing inheritance and polymorphic programming, a modular structure that can easily be extended is achieved. An illustration of the code architecture is shown in Fig. 5.4.

For every simulation two major components exist. First, the *reaction network* that contains initial particle numbers, diffusion rates, inhibition relations and reactions. Those are themselves classes which are in turn composed of component objects and reaction rates. The reaction network defines the dynamics that is simulated but is itself independent from the algorithmic implementation and serves as a data container that only provides information. The second component is the *simulation class* which specifies the actual simulation type that is performed. This includes the algorithm used, the measurement times and the system's geometry. A simulation class in combination with a reaction network defines a simulation.

The execution of the simulation and the entire program is controlled by the parser. It reads the scripts provided by the user, performs error checks and creates the according reaction network and simulation class which are then executed. Each line is processed individually. First, regular expressions are used to identify the type of input e.g., reaction

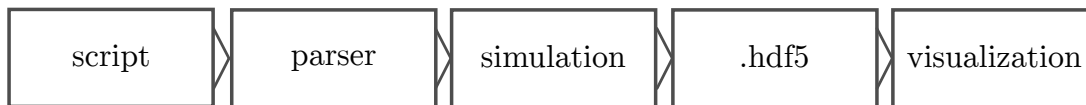


Figure 5.3: **Illustration of the simulation pipeline.** The user creates a script which specifies the desired dynamics, geometry and simulation type. The script serves as the input for the main program. A parser translates the human readable request into a stochastic simulation which is then executed. Depending on the specified parameters available results are stored in an hdf5 file. The unified data structure for all types of simulations allows for the use of general visualization tools.

or particle numbers. String operations are used to extract the information and translate them into the respective data objects which are then used to create reaction networks and simulation classes. If an *Ensemble* function is requested, the parser simply performs several simulations of the same system in parallel and takes care of the relevant statistics. The simulation classes which are at the heart of the actual execution are constructed in hierarchical order employing inheritance. The higher the class the more abstract are the functions it introduces. The *simulation base-class* only includes the general concepts of a stochastic algorithm such as iterations, time and random number generation. In principle, it can be applied to any system because no assumption about the actual type are made. Following classes add more specific functionality which, however, may still not define executable simulations but just the basis for a broader group of systems. The *system base-class* is used for the implementation of simulations of all actual systems. All examples discussed in the previous section were based on the *well-mixed system class* which is a direct offspring of the system base-class. It implements an efficient *Gillespie algorithm* by using dependency graphs to minimize computational effort. In contrast, spatially extended systems have one more layer of abstraction before actual simulations such as the one-dimensional system are realized. Everything that can be implemented as a rectangular lattice or a subset thereof can be created as an offspring of the *spatial base-class*. To account for large system sizes, in particular in higher dimensions, a modified version of the *next reaction method* [49] is employed for the corresponding simulations (for details see Appendix A.3).

An example for a stochastic simulation class that is not an offspring of the system class is the *connected systems* class. Instead of being an actual system itself it contains two of them and implements particle exchange and time consistency. The simulation of each compartment is based on its own algorithm to keep the structure as modular as possible.

At this point, the program structure may seem to be unnecessary complicated. There are almost as many abstract classes as simulation types and the 1d simulation could just be realized as a 2d system of width 1. However, the particular structure was not just chosen to achieve the provided functions in the fastest way. It was designed to make it easier to add further modules to the code that allow for additional functions without changing any aspects of the main program. An illustration of how different kinds of new systems can be included is shown in Fig. 5.5.

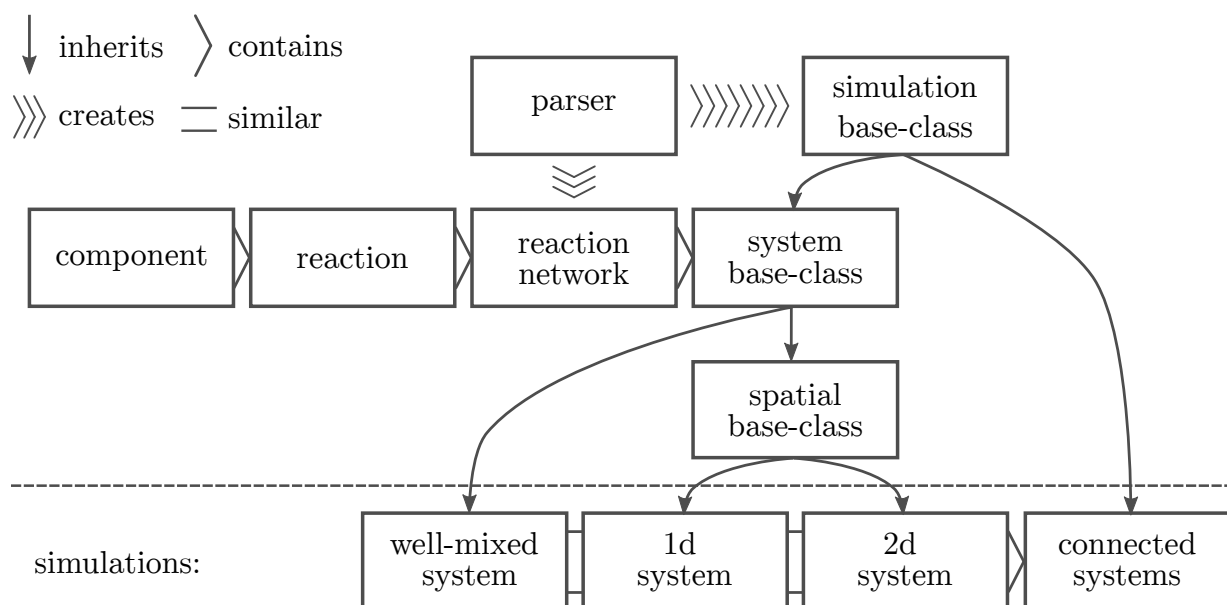


Figure 5.4: **Illustration of the program structure.** Object-oriented programming was used as the main paradigm. A hierarchical class structure is employed to create several simulation types which all possess the same functionalities. Systems contain a reaction network that is specified via the script provided to the parser (see Fig. 5.3). The networks are composed of reactions which are in turn composed of components. In the same way, a connected system simulation contains two basic systems for which it provides the interactions.

Depending on how different a new simulation type is from the existing ones it has to be an offspring of a more abstract class and needs to implement more execution aspects itself e.g., output formats. A class that allows for simulations of reaction-diffusion systems on a disk for example could simply be realized as a 2d system for which hopping to lattice sites with a certain distance from the center is prohibited. The effort is rather minimal. In contrast, the implementation of a simulation of reaction networks on graphs requires more work. The arrangement of nodes and edges and how they are stored in the output files have to be designed from scratch and cannot be adapted from any of the spatially extended systems. But because it still simulates a reaction network created by the parser, all functionality provided for the system base-class is readily available.

In this form, some additional coding may be needed if a user wants to simulate a specific type of system, but only a new module instead of an entirely new program is needed. This adds some advantages beyond just less effort. The unified format simplifies the transfer of simulations to other members of the research group. Furthermore, once a geometry is implemented it can not only be used for a particular system but for all types of reaction-diffusion system. To this end, a commented version is provided to our chair and may later be turned into an open source project.

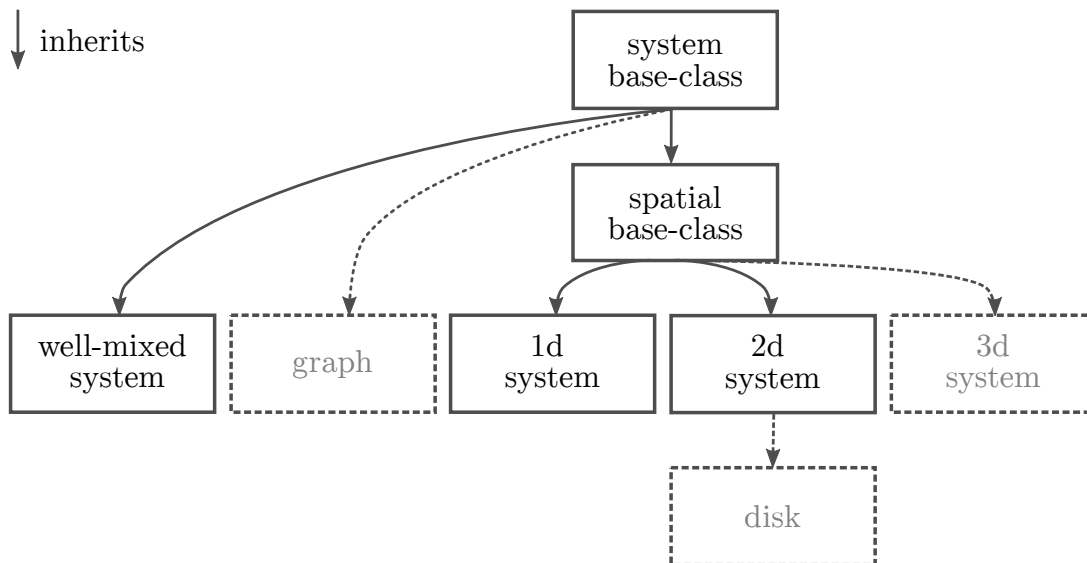


Figure 5.5: **Extension of the simulation framework.** Depending on how much a new simulation class differs from the existing ones it has to be added to a different level in the class hierarchy. The simulation of a disk can simply be included as a 2d system for which movement is restricted depending on the distance from the center. A 3d system includes a more complex modification because the arrangement of the lattice and hence the associated data structure differ from the other systems. The simulation of a graph structure finally requires its own type of dynamics, definitions of how nodes are connected and interact, and a completely different storage system for the representation. However, because of polymorphic programming most functionality can directly be adopted and even has to be.

### 5.3 Spatially extended systems

In this section, simulations of reaction-diffusion systems in different lattice-based geometries are explained. All of them make use the modified Gillespie algorithm which is discussed in Appendix A.3 to improve performance. As before, only the core framework shown in Fig. 5.3 is used to create the presented output. Beyond the provided scripts no additional work is required. The following script simulates a stochastic implementation of the famous Lotka-Volterra dynamics in one dimension [189, 190]. Fig. 5.6 shows the corresponding output.

```

prey -> 2prey : 1
2prey -> prey : 0.01
predator -> 0 : 1
prey + predator -> 2predator : 0.1
prey = 10.5
predator = 2.5
D: prey = 1
  
```

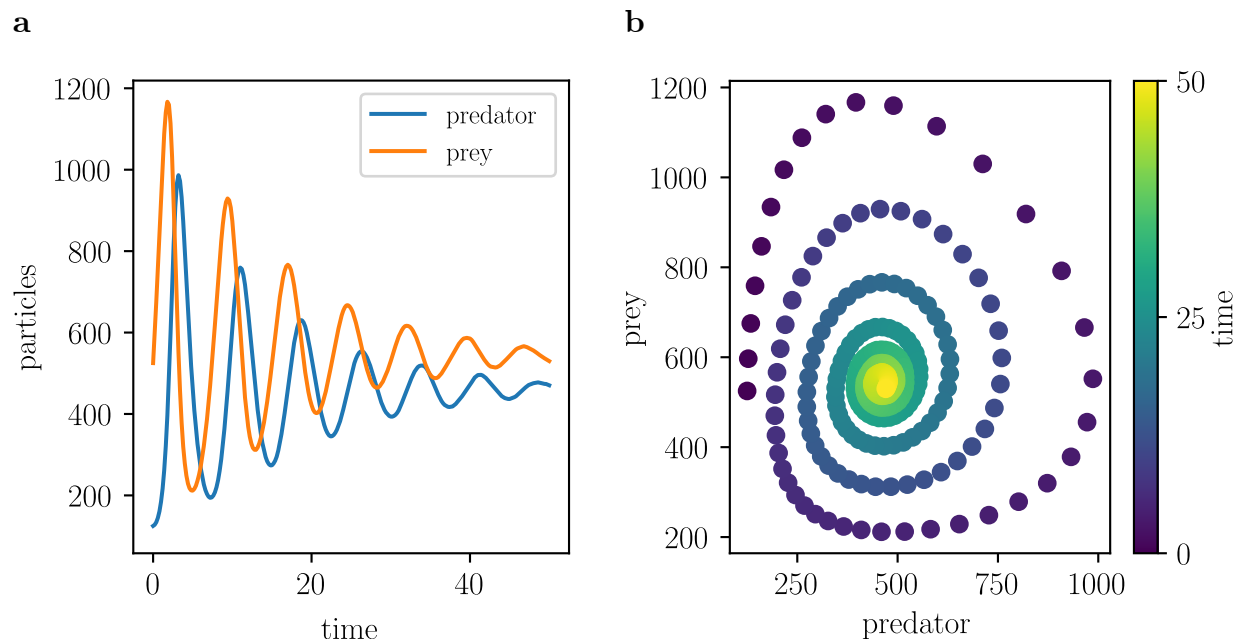


Figure 5.6: **Ensemble simulation of the one-dimensional Lotka-Volterra system.** The time evolution for both predator and prey is shown in panel (a). However, a phase space plot as depicted in panel (b) contains the same information but is better suited to illustrate the dynamics of the system.

```
D: predator = 0.3
Ensemble1D(50, 50, 0.2, True, LotkaVolterra1D, *1, 1000)
```

First, reactions and densities are defined. The initial state by default has a homogeneous particle distribution but since the system has more than a single lattice site non-integer values can be realized. For a density of 10.5 for example 10 prey elements are placed on each lattice site. Afterwards,  $0.5 \cdot 50 = 25$  additional particles are positioned at random in the system. The resolution of this method is limited to the inverse of the number of lattice sites (one additional particle shared among all lattice sites). To avoid correlation effects, additional particles are randomly distributed within the system. The hopping rates of the different species are defined in lines that start with "D:" followed by the species name and the respective value. For the one-dimensional ensemble simulation two more arguments exist in comparison to the well-mixed case: The size of the system 50 right at the beginning of the function and an additional boolean variable which has the value *True*. The boolean decides whether just the state of the system as a whole is recorded or the exact configurations. For large systems simulated for long times this may require a significant amount of memory. That is why the option can be turned off passing the value *False*. In case all spatial information is recorded it can readily be turned into movies or plots with spatial resolution as shown in Fig. 5.7. Note that for ensemble simulations the data represents the entire ensemble, not a single simulation. Finally, it is important to note that instead of a number the expression "*\*1*" was passed as a seed. It indicates a

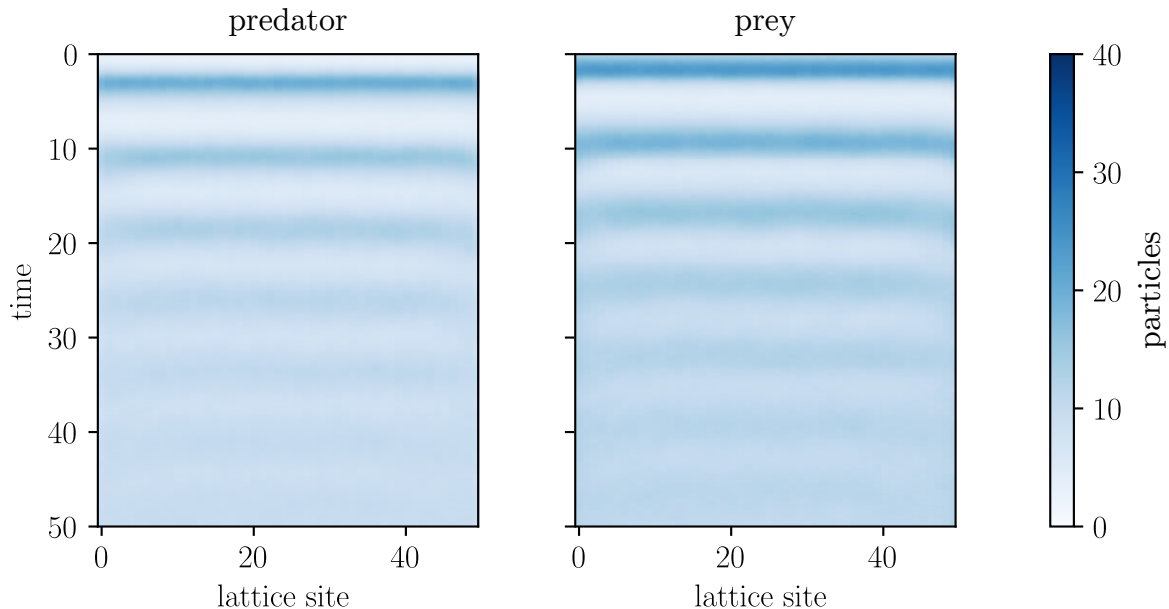


Figure 5.7: **Kymographs for the one-dimensional Lotka-Volterra system.** If requested, not only the time evolution of the system as a whole is recorded but the entire configurations. This allows for the immediate creation of movies and plots with spatial resolution.

variable that is not specified in the script but is passed as an argument to the program. `"*1"` refers to the first additional argument specified in the command line when the program is executed. Similarly, `"*2"` is substituted by the second variable and so on. This allows for systematic parameters sweeps without creating a new script each time. Furthermore, the unintended reuse of identical seeds is circumvented since it has to be specified separately when the script is executed.

The last example script illustrates the full extent of possible simulations. Two two-dimensional systems which exchange particles on one edge are simulated. One is referred to as the membrane the other as the bulk. These kinds of simulations were created having specifically biological systems like cells in mind [191]. The output created from this script is shown in Fig. 5.8.

```
#MEMBRANE
reproduction = predator -> 2predator : 1
predator -| reproduction: 0.02
predator = 5
Dext: predator = 0.7
Dint: predator = 1
#BULK
prey -> 2prey : 0.75
predator -> 0 : 1
prey + predator -> 2predator : 0.03
```

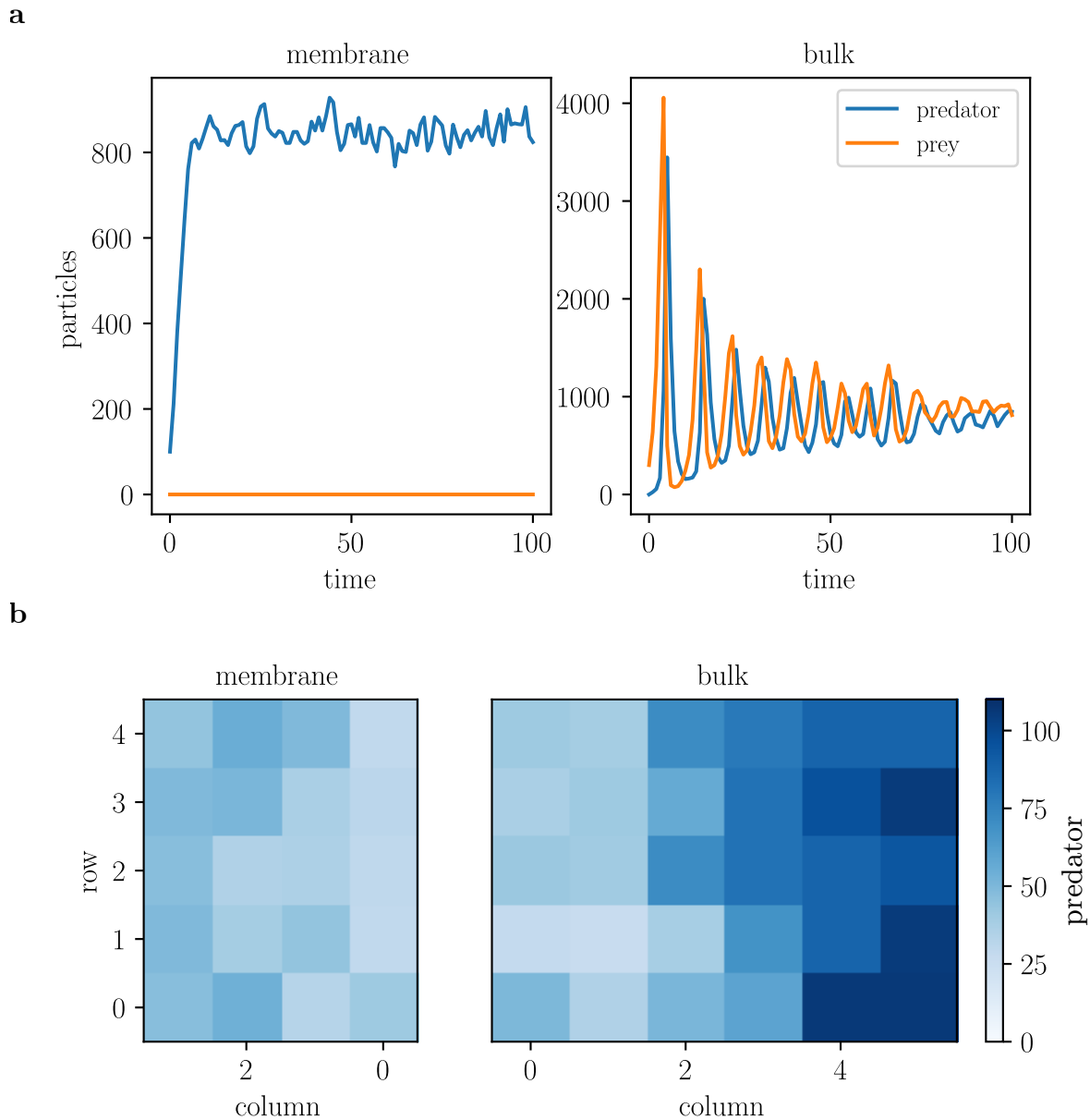


Figure 5.8: **Simulation of a two-dimensional membrane with bulk.** Both, membrane and bulk have to have the same height to be connected. Particles can switch between the compartments at the columns indicated as 0. The time evolution for each compartment is recorded individually. Depending on the recording options either only total particle numbers (**a**) or entire configurations (**b**) are recorded.

```

prey = 10
D: prey = 0.5
Dint: predator = 1
Simulate2DMembraneWithBulk(5,4,6,100,1,True,Invasion3,*1)

```

The keywords "#MEMBRANE" and "#BULK" indicate to which of the two compartments the following lines of script apply. Per default the membrane is assumed to be one-dimensional and the bulk two-dimensional. Here, the membrane is explicitly set differently in the *Simulate* function. In contrast to simulations of independent systems two types of hopping rates exist. One within the respective compartment called "Dint" and one out of it, "Dext". The external diffusion parameter is responsible for the particle flux between the two system parts. If only a general diffusion value "D" is supplied, "Dint" and "Dext" are assumed to be identical. The final simulation request has to specify the dimensions of each compartment. The height of both has to be identical such that only three independent variables exist.

The provided scripts exemplify all different groups of simulation types but not each individual one. Table 5.1 shows a complete overview of all simulation possibilities. Beyond the simulation functions the script language supports functions in general as well as optional arguments; For example, a print function exists. Furthermore, comments indicated by a "//" are possible, and reactions can be copied between the different compartments via the "#SAME" macro. All those additional features which emulate a normal script language have been excluded from the example scripts to make them more concise. Optional function arguments, however, provide additional functionality with research application discussed in the next section.

## 5.4 Measurement of critical exponents

The diffusive epidemic process studied in depth in Chapter 4 is a mass-conserving two component reaction-diffusion system. Combining efficient stochastic simulations with measurements of dynamic spreading of activity provided a new perspective one previously existing discrepancies between analytical methods and numerical investigations with respect to its phase transition. This, in fact, was the original motivation to create the simulation framework discussed in this chapter. Conceptually, the methods used can be readily applied to various systems to get a systematic understanding of when and how stochastic effects change phase behavior and cause approximation methods like perturbative renormalization to fail. The major limitation to the method is the computational effort to obtain good statistics close to a critical point or other extreme configurations that lead to strong fluctuations. For each system to study a new optimized simulation needs to be created. This significant time investment can now be dispensed with. In the following, an example of how the developed script language can be used to perform measurements of dynamic spreading of activity is presented.

We study the diffusive epidemic process in two dimensions as a possible application to current research. The necessary stochastic simulations can immediately be created using

<b>simulation type</b>	<b>arguments</b>
SimulateWellMixed	simulated time, measurement intervals, output name, seed
Simulate1D	system height, simulated time, measurement intervals, output name, seed
Simulate2D	system height, system width, simulated time, measurement intervals, output name, seed
SimulateMembraneWithBulk	joined height, membrane width, simulated time, measurement intervals, output name, seed
SimulateMembraneWith0DBulk	membrane height, simulated time, measurement intervals, output name, seed
SimulateMembraneWith1DBulk	joined height, simulated time, measurement intervals, output name, seed
Simulate2DMembraneWithBulk	membrane width, joined height, bulk width, simulated time, measurement intervals, output name, seed
Simulate2DMembraneWith0DBulk	membrane width, membrane height, simulated time, measurement intervals, output name, seed
SimulateConnected0DSystems	simulated time, measurement intervals, output name, seed
EnsembleWellMixed	simulated time, measurement intervals, output name, seed, ensemble size
Ensemble1D	system height, simulated time, measurement intervals, output name, seed, ensemble size, (seed species)
Ensemble2D	system height, system width, simulated time, measurement intervals, output name, seed, ensemble size, (seed species)

Table 5.1: **List of all currently supported simulation types.** Arguments—which have to be specified in the correct order—are listed on the right. The "(seed species)" represents an optional argument that is used to indicate a request to perform dynamic spreading measurements.

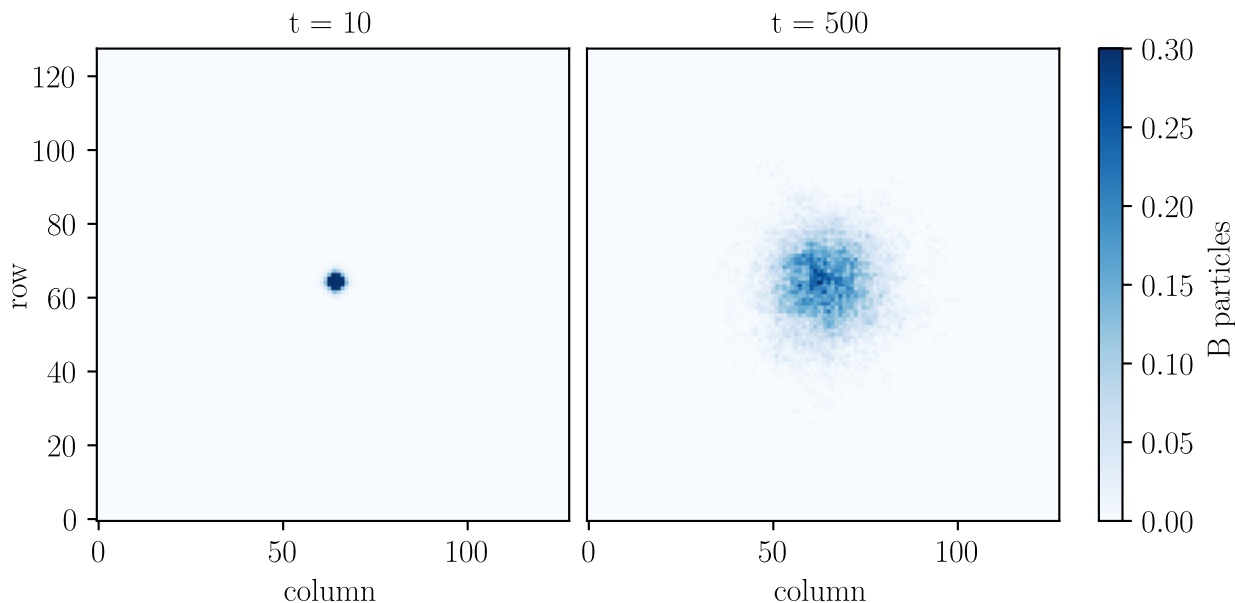


Figure 5.9: **Dynamic spreading simulation initiation.** All particles of the seed species are placed in the center of the system. All other species are homogeneously distributed. The ensemble average of the evolution of microscopic states only takes *surviving systems* into account.

the following short script.

```
A + B -> 2B: 0.2
B -> A : 1
A = *1
B = 10
D: A = 1
D: B = 0.1
Ensemble2D(128,128,1000,1,False,DEP_2D,*2,10000,B)
```

Here, a new type of optional argument was provided to the simulation function. A name of a species at the end of an ensemble function indicates that it is used for dynamic spreading measurements<sup>5</sup>. Instead of being homogeneously distributed, the respective particles are placed as a cluster in the middle of the system as illustrated in Fig. 5.9. The particle density "B = 10" is now interpreted as the number of particles in the initial cluster. For the A species the expression "\*1" is specified instead of an actual particle number. This indicates that the respective argument is replaced with the first command line input which allows for a systematic density sweep without creating a new script for each set of parameters.

Because of the large amount of memory, it would require to record all microscopic configurations, the recording variable is set to False. If set to True, only systems with a surviving seed species are considered for the state average in contrast to homogeneous

<sup>5</sup> A detailed discussion of the respective scaling relations is provided in Sec. 4.2 of the previous chapter.

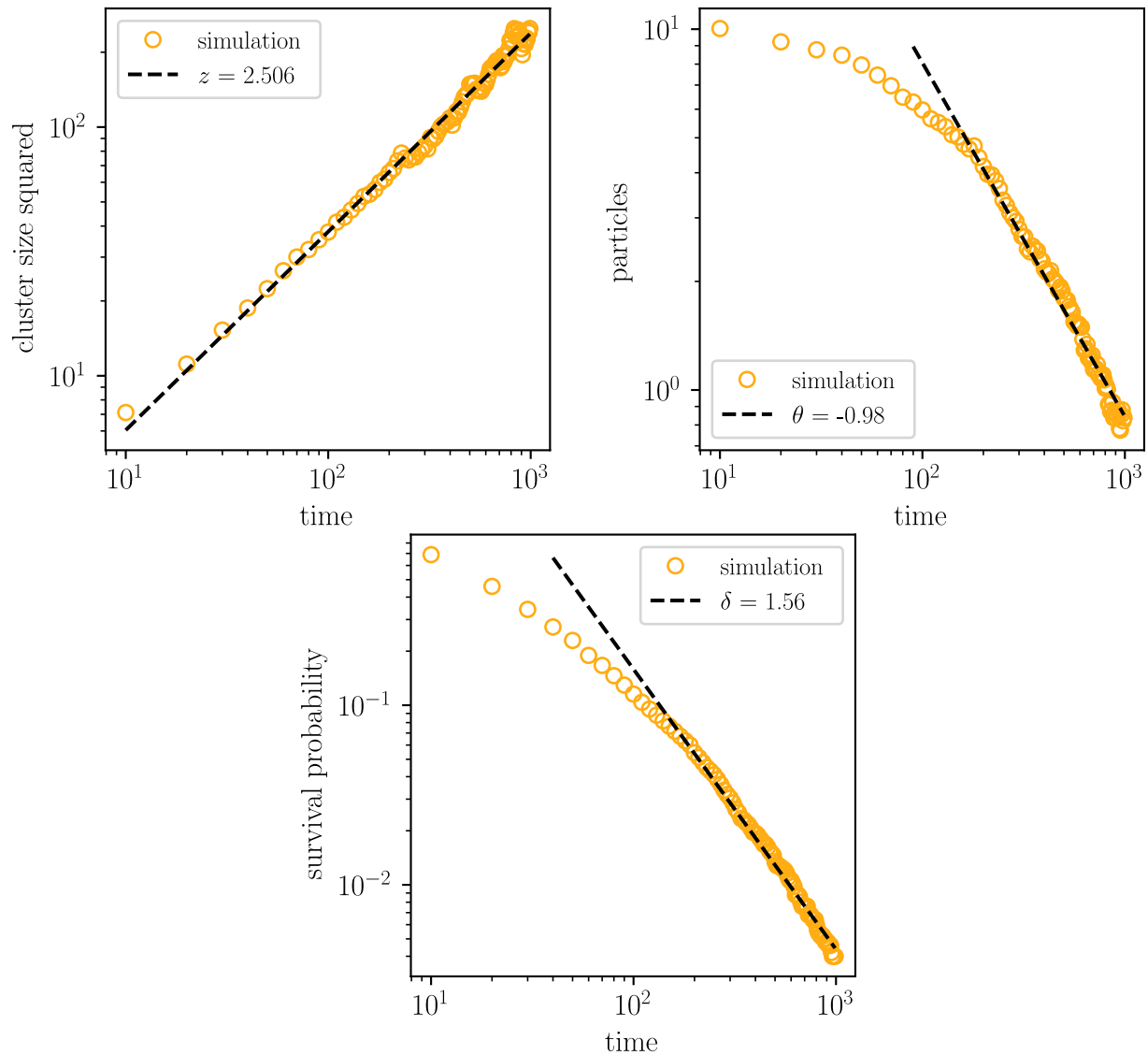


Figure 5.10: **Dynamic spreading measurements for the diffusive epidemic process in two dimensions.** Assuming the simulation was performed close to the critical point, the visualization tools automatically create estimates for the critical exponents based on least square fits. (In this example, the simulated time is too short to make reliable predictions about the asymptotic behavior.)

ensembles for which all runs are taken into account. To extract the critical exponents later on, the size of the clusters, the size squared<sup>6</sup> and their survival probabilities are automatically recorded in addition to the other macroscopic observables. In the current form the script is constructed to perform a parameter-sweep to find the critical density and the respective critical exponents for a B-particle diffusion rate  $D_B = 0.1$ . Fig. 5.10 shows the results of a single ensemble run. Estimates for the critical exponents are created automatically using least square linear fits based on the assumption the simulation was performed close to the critical point.

## 5.5 Conclusion

In this chapter, I gave an introduction to the newly created simulation framework. It is constructed in a modular fashion to allow for easy extension by other researchers. The program is controlled by a script language whose features were explained based on simple examples. Those ranged from the basic time evolution of well-mixed systems to deriving critical exponents in a spatially extended system using dynamic spreading of activity. Since the framework allows for the simulation of arbitrary reaction-diffusion systems, these methods can now directly be applied to an entire class of systems. In addition, several different types of simulation functions exist which are listed in Table 5.1 e.g., particle exchange between connected compartments.

The provided systematic approach to study not only the dynamics but also the critical behavior of new systems using exact stochastic simulations is the generalization of the work shown in Chapter 4 we were aiming for. Now, in principle, arbitrary extensions of diffusive epidemic process can be studied as well as general reaction-diffusion systems. The analytic methods may have to be adapted for each of them and it is unclear which approximations can be made. But at least for the numerical part a simple general solution is made available.

The commented code is provided to our chair, with the existing option to be made an *open source* project at some point to further increase its outreach and functionality.

---

<sup>6</sup>Because of correlations the expectation values of size and size squared may not simply be converted.

# Chapter 6

## Conclusion

In this thesis, I investigated the role of stochastic fluctuations in different biochemically motivated systems far from thermal equilibrium.

Chapter 2 focused on the influence of geometry and particle arrangement in the context of intracellular transport along microtubules. By creating an extended model based on the totally asymmetric simple exclusion process, together with Emanuel Reithmann and Erwin Frey, I showed how fluctuations strongly hinder transport when protofilaments are coupled via different motor species. This effect becomes most evident in the existence of the maximal density and the cramming density which a system realizes in the limits of vanishing and actually zero current. Both are significantly lower than one, meaning only a small fraction of the entire system may contribute to transport simultaneously. We managed to explain the origin of this behavior on a microscopic level, and provided a proof of our understanding in the form of an exact analytic solution for the cramming density in the two-lane case.

The variable defining the strength of the transport limitation was identified to be the number of lanes composing the cylindrical lattice. Counterintuitively, increasing the number of lanes leads to lower maximal densities even though one might expect to recover an uncoupled limit. So far, simulations suggest the paradoxical scenario of complete jamming on an empty lattice. Furthermore, in case the length of individual lanes and the number of lanes do not differ by a significant margin ( $\sim 100$ ), the system self-organizes into density patterns. Applying standard mean-field approximations which work well for the original TASEP none of the observed phenomena can be explained. To overcome this problem, we developed effective description methods to quantify and extrapolate the influence of stochastic fluctuations while giving an intuitive explanation of their origin. Finally, based on an extended model including Langmuir kinetics, we pointed out how even small fractions of a second motor species may modify the systems phenomenology in an experimentally observable way. In the context of the biological setup considered, the results of this project show that overcrowding phenomena might be far more relevant in intracellular transport than previously expected.

Continuing the research how stochastic fluctuations affect collective behavior on a cellular level, Chapter 3 deals with depletion traps in macromolecular self-assembly. In a col-

laboration with Florian Gartner, Isabella Graf, Philipp Geiger and Erwin Frey we showed that heterogeneous structures strongly differ from homogeneous ones when it comes to low subunit concentrations, despite being equivalent when described in terms of chemical rate equations. In fact, a homogeneous system always behaves as deterministically predicted irrespective of the total number of particles. In contrast, heterogeneous systems are very susceptible to fluctuations and hence show significant deviations. Most importantly, in a deterministic system, perfect yield can always be achieved if the nucleation of new structures is much slower compared to growth of existing ones. However, in the heterogeneous case, fluctuations create an upper bound for the maximum assembly yield, no matter how slow this process takes place. This can even cause the yield to be zero despite a deterministically expected value of one. Furthermore, those fluctuations may increase when the assembly speed is reduced, leading to a non-monotonic dependency on certain parameters caused by a transition from a deterministic to a stochasticity-dominated regime. This turns self-assembly into a fine-tuning problem compared to a simple "more is always better" scheme and has important implications for example in the field of artificial self-assembly.

As in Chapter 2, in Chapter 3 we explained and quantified the impact of stochastic fluctuations by comparing analytic calculations to exact stochastic simulations. Despite the differences of the biochemical systems themselves, our models for macromolecular self-assembly and intracellular transport show unexpected similarities on the mathematical level. The size of a polymer behaves similar to the position of a molecular motor and both can be approximated by an advection-diffusion equation. Accordingly, the number of different components assembling a structure and the number of lanes in the extended TASEP model play the same role. If they are set to one, no relevant fluctuations are present in the system, but when they are further increased stochastic effects start to dominate the entire dynamics.

The third system I investigated was the diffusive epidemic process (DEP) in Chapter 3. The research was performed in collaboration with Borislav Polovnikov and Erwin Frey. Applying exact stochastic simulations in combination with measurements of the dynamic spreading of activity, we managed to achieve a unified picture of the previously controversial absorbing-state phase transition. In particular, we discovered that in the regime of faster diffusion of healthy particles a cluster of infected particles spreads sub diffusively at the continuous phase transition; The effect manifests in the form of the critical exponent  $z = 3$ . By comparing the  $D_A > D_B$  regime to the better-behaved  $D_A = D_B$  case, we identified mass redistribution as the driving force. Since the  $B$  type particles, which are mainly present inside the cluster, diffuse slower compared to the  $A$  particles outside, a net flux into the cluster is created that depletes its surroundings. In this way, the cluster hinders its own expansion. Because the effect is based on heterogeneities in the distribution of the different species, simulations starting from a homogeneous initial state behave differently; It would take astronomical amounts of time for the necessary spatial fluctuations to occur. The mass redistribution probably also induces strong coupling which causes perturbative renormalization group methods to fail in one dimension. This explains the prediction of a discontinuous phase transition, in contrast to all numerical investigations indicating a continuous transition. Interestingly, despite the absorbing-state phase transition being a

stochasticity-focused phenomenon, the final mechanism we unraveled is rather deterministic. The exact values of the exponents, however, are still dependent on the underlying fluctuations.

Finally, based on the success of our approach presented in Chapter 4, I developed a general computational framework for exact stochastic simulations of reaction-diffusion systems which was discussed in Chapter 5. A script language built around chemical reaction equations provides an interface for easy interaction with the program. Furthermore, direct support for measurements of dynamic spreading of activity is included. This allows for the systematic study of critical behavior in stochastic reaction-diffusion systems in different dimensions which hopefully eases the way towards a general theoretical understanding.

Looking at all systems studied in this thesis, reoccurring themes exist despite all of them being vastly different with respect to their biological motivations. In all cases closely related systems exist for which a deterministic approach works perfectly well but one central modification causes their breakdown. For Chapter 2, it is the importance of particle arrangement compared to the TASEP, for Chapter 3 it is the non-trivial reaction path of the heterogeneous system compared to the homogeneous one. Finally, in Chapter 4, the absorbing unstable fixed point in contrast to many other mass-conserving two component reaction-diffusion systems leads to a significant relevance of fluctuations. In addition, the case of equal diffusion rates  $D_A = D_B$  served as a reference for the controversial regime  $D_A > D_B$ .

For the systems studied in Chapters 2 and 3, we find the introduction of combinatorics to be the central source of fluctuations. In the case of the diffusive epidemic process it is the irreversibility caused by the absorbing state which makes the otherwise negligible fluctuations so relevant. In the end, all three systems possess a combination of stochastic fluctuations and irreversibility. The TASEP and the homogeneous assembly model exhibit irreversibility from the start but only the modifications introduced relevant fluctuations. In contrast, the DEP combined an irreversible step with the existing fluctuations of two-component reaction-diffusion systems.

Taking another step back and focusing on the central features we used for the choices of our systems, namely being *far from thermal equilibrium* and describing a *cellular (mesoscopic)* system, we find that each of them accounts for one of the two aspects. Irreversibility directly links to not reaching thermal equilibrium and a mesoscopic scale leads to non-negligible fluctuations. To put it simply, a mesoscopic scale causes fluctuations and irreversibility makes them matter. Hence, only a combination of those creates non-trivial modifications. In our systems all modifications had a negative effect on performing the actual task they are meant for. This leads to the conclusion that either irreversibility or fluctuations should be avoided or at least suppressed.

In the context of understanding mechanisms that are important for collective phenomena on a cellular level, the findings of this thesis point out two central research questions; On the one hand which mechanisms can be used to suppress the detrimental effects discussed above and on the other hand whether cases exist for which they may be desired e.g., to favor a certain state that is irrelevant in thermal equilibrium. However, at this point, it seems most likely that such a mechanism is based on the reaction kinetics—which can

reliably be modified—while fluctuations have to be suppressed in order to ensure proper function.

Looking at our results from a physical and biological perspective, respectively, we draw different final conclusions. In terms of physics the combination of strong fluctuations and dynamics far from thermal equilibrium is the source of complex and interesting new phenomenology. Coming from the biological side of ensuring robust and reliable function, a combination of both should certainly be avoided.

# Appendix A

## Optimization methods

The main goal of this thesis is to investigate how stochasticity affects the phenomenology of biochemical systems far from thermal equilibrium. We do so by comparing the results of deterministic approximation methods with the actual stochastic behavior of different systems. However, because for none of those analytic solutions are feasible we have to rely on exact stochastic simulations. This adds a new problem layer. Often times we are specifically interested in extremal cases such as phase transitions and critical points which go along with strong fluctuations. As a result, a huge number of ensembles, large system sizes, or even both combined, have to be simulated to obtain meaningful statistics, causing simulation times and hardware resources to be one of the central limitations of our research.

All systems discussed in this thesis can be adapted into a *Gillespie algorithm* [47, 48] which serves as the basis for the methods described in the following. But extrapolating the runtime of direct or naive implementations to the extremal parameter configurations used in the main text, we find that those would take up to the order of years to complete. Hardware and programming language choice can only provide speed-ups up to several hundred percent, which remains insufficient. This means we have to use optimization methods to bring runtimes down to a manageable magnitude by reducing the time complexity per iteration of the respective algorithm<sup>1</sup>. In all cases discussed in the following, this can be achieved by trading runtime for memory but without increasing the memory complexity.

The more an algorithm is tailored to a specific problem the more optimization potential exists by using all information available. In this chapter I am going to discuss the central ideas and concepts I have used for the different simulation frameworks employed in this thesis, to enable easy reproduction and extension by other researchers<sup>2</sup>. At this point it is important to emphasize once more that, all methods used are based on existing algorithms [48, 49, 192] which are optimized for the respective problems using general knowledge about

---

<sup>1</sup>Naturally, the overall time complexity of a simulation is at least linear in the number of events per unit time. Each event causes one additional iteration. This is a limit set by physics not by the algorithms considered. For that reason, we focus on the time complexity per iteration as quality measure.

<sup>2</sup>The methods described have already been adapted by other chair members to improve their simulations.

data structures and programming language features. Code for crucial functions is provided in C++ to further the intent for this appendix to be an implementation guide<sup>3</sup>.

Finally, it is worth noting that, despite being created for one particular system all discussed methods can be extended to other or more general problems. Hence, this appendix chapter should be viewed as an introduction to possible methods for implementing efficient stochastic simulations rather than a guide for simulations of the systems themselves they were used for.

## A.1 TASEP-like systems

The central feature determining the algorithm time complexity for the totally asymmetric simple exclusion process and extensions thereof (e.g., Chapter 2), is the number of lattice sites  $N$ . At each site, depending on its current state and the respective next site, a hopping event may take place. Using a naive implementation of the Gillespie algorithm it is either necessary to iterate over all lattice sites or all possible events which can be mapped to the lattice sites.

In the first case, by iterating over all lattice sites a *vector* [193] with the indices of all sites with hopping events is created. Since the rate for all of them is one w.l.o.g. the total rate for any event to happen is just the size of the vector and the next hopping event can be determined by choosing a random position within the vector. However, one quickly realizes that this method has a lot of unnecessary overhead. Because of the strictly local interactions only a lattice site and its direct neighbors are affected by an event which makes checking the entire lattice again a huge over-investment. This leads directly to the second possibility of keeping a vector of all possible events and updating it according to the changes on the lattice. From the physics perspective the approach seems to have constant complexity. At most, events at three lattice sites have to be added or removed. In addition, one element from the vector is chosen at random. Unfortunately, this argument is not true for an actual algorithmic implementation. In case elements are added and removed from the container at random we lose track of their positions and to remove them we have to search for them amongst at most  $N$  other event-representing elements<sup>4</sup>. This again has time complexity  $N$ . To make thing worse, removing an element at the beginning of the container results in a shift of at most  $N$  elements in addition<sup>5</sup>.

In the end, both basic implementations amount to a time complexity of the order of

---

<sup>3</sup>The following naming conventions are used: functions start and are spaced by capital letter (MyFunction), variables are entirely lower case and spaced by underscores (my\_variable), and class members which are shared amongst all functions of a simulation are variables terminated by an underscore (my\_member\_). Furthermore, integer division (/) and modulo operations (%) are always avoided because of their high costs in general.

<sup>4</sup>For the TASEP it is actually  $N/2$  because the most hopping events occur if every second lattice site is occupied.

<sup>5</sup>This could be circumvented by using a list which allows for adding and removing elements with constant complexity. But such a container does not allow for random excess making the determination of the event a problem of complexity  $N$  instead of 1.

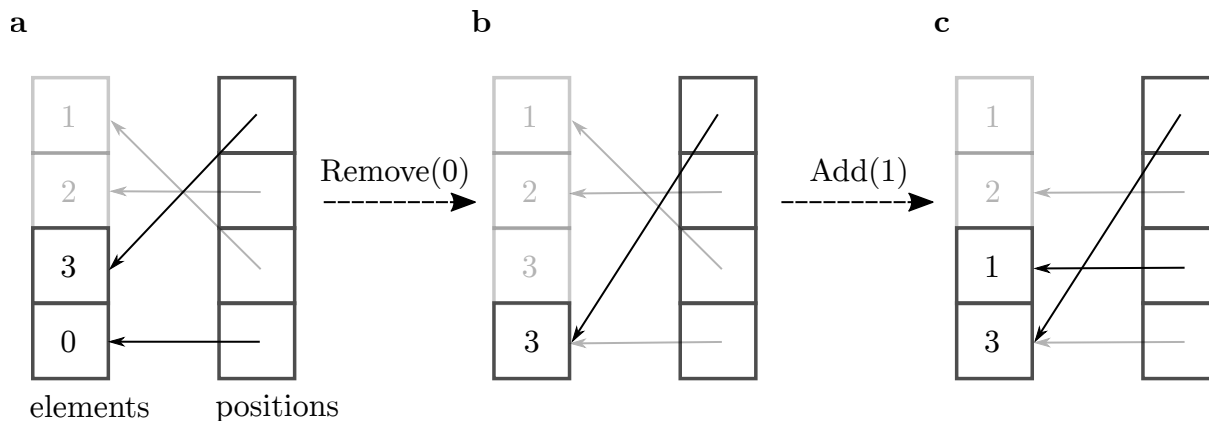


Figure A.1: **Illustration of the random-access container.** A number corresponds to a hopping event at the respective lattice site. (a) Initially the elements 0 and 3 are actively stored in the container. (b) After removing the 0 element only 3 is left. This is achieved by replacing 0 with 3 and updating the position of 3. (c) The 1 element is added to the container. It is inserted at the end and its location is updated. In all cases only positions stored for elements which are considered inside the container are meaningful.

$N$ . For the simulations of our extended model with two species on a lattice with 50 lanes and 16384 sites per lane performing  $10^{12}$  iterations as needed would cause at the very least  $8.2 \cdot 10^{17}$  processor operations. On a normal 3 GHz processor this would take more than 8 years to complete assuming ideal conditions. Even using any kind of parallelized computational method would not be of much use making algorithmic optimization the only option. The Gillespie algorithm is naturally sequential and splitting the system in parts handled by different processors requires synchronization and roll backs. As a consequence, the speed increases sub-linear with the number of processors and resources are wasted.

Looking again at the second method described above two weaknesses exist, namely finding an element and removing it without losing random access<sup>6</sup>. Both can be overcome by using the stochastic nature of the system and its well-defined binary lattice structure. Each event can or cannot happen on one particular site and it is always possible to find a mapping between events and consecutive natural numbers. This makes the system perfect to create a *hash map* [194] for the positions of the events<sup>7</sup>. Furthermore, because events are chosen at random the order of elements is irrelevant. Using the fact that only add and remove operations of elements which are (almost) identical to their key are needed, it is possible to create a minimalistic data container which is optimized for those specific tasks. An illustration of the functionality is shown in Fig. A.1. An implementation of the container only needs three components. First, the current size has to be known. In addition, two arrays are needed. One storing the actual elements and a second one storing

<sup>6</sup>Random access means any element in a data container can be accessed directly without traversing through memory.

<sup>7</sup>After each event the hash map needs to be updated.

the positions of those elements<sup>8</sup>.

```
long current_size_;
const std::unique_ptr<LatticePosition[] > elements_;
const std::unique_ptr<long[] > positions_;
```

Adding an element is fairly simple, in particular for the TASEP for which the references to lattice sites and hopping events are identical<sup>9</sup>. The new value is assigned to the position which is indexed by the current container size. And the position which is accessed via the lattice site becomes the current container size. Afterwards, the size is increased by one.

```
void Add(LatticeSite element){
    elements_[current_size_] =element;
    positions_[ElementToIndex(element)] =current_size_;
    ++current_size_;
}
```

For removing an element two cases have to be distinguished. If it was the last one the size only needs to be reduced to zero. Otherwise, the value of the last element has to be assigned to the position of the element that is removed and the hash map has to be updated<sup>10</sup>.

```
void Remove(LatticeSite element){
    --current_size_;
    if(current_size_ > 0){
        const long element_position =\
            positions_[ElementToIndex(element)];
        elements_[element_position] =elements_[current_size_];
        positions_[ElementToIndex(elements_[current_size_])] \
            =element_position;
    }
}
```

Having implemented the event selection as described above one measurement operation remains which may still be of linear time complexity and hence becomes critical. If the density at a lattice site is recorded by summing up each time interval it is occupied and dividing the final value by the total amount of (system) time, this procedure is again linear in  $N$ . The problem can be circumvented by trading additional memory against runtime. Instead of adding up time intervals the moment of initial occupation of a lattice site is stored.

```
density_counter_[species][row][column] =t_now_;
```

Only if the particle leaves the lattice site the total amount of time passed is recorded. By

<sup>8</sup>In this form, the largest index possible has to be known when the container is constructed. Dynamic versions can be constructed using a vector.

<sup>9</sup>Note that, in the current form the container does absolutely no error checking to increase performance.

<sup>10</sup>The position of the removed element does not need to be updated because accessing it would only be possible as a bug in the main program

giving each site its own timer, a constant complexity is achieved. Only before the first and after the last iteration the whole systems needs to be traversed to initiate and evaluate occupations.

```
density_[type][row][column]+=\  
t_now-density_counter_[type][row][column];
```

Applying the described methods to the actual simulations, runtime is reduced to the order of hours for very large simulations and normally just minutes, compared to several years if the basic implementations are used. The reason is the reduction of time complexity for an iteration step from linear in the number of lattice sites to constant. For extended models with different events one container is used for each type. The selection of the kind of event taking place is just a random choice weighted by the size of the containers times the respective rates. The key aspects for this method to work are local interactions and events that can be grouped because their rates do not differ between lattice sites.

## A.2 Heterogeneous self-assembly

In Chapter 3 we study different models for molecular self-assembly in a well-mixed environment. Since the focus is on results obtained for low particle numbers causing strong fluctuations large ensemble averages have to be performed to obtain good statistics. The time complexity of an iteration step is mainly determined by the number of particle species  $S$ . This is because instead of tracking each growing structure their respective number in each state is recorded. In case of the ring model this means the state of our system is described by an  $S \times L$  matrix of integer values which correspond to the number of structures with a given species on their left end and a certain size. In the following, the fully heterogeneous case  $L = S$  is discussed for simplicity in combination with the polymer-polymer binding model which can directly be simplified to simulate the main model<sup>11</sup>.

Considering a general binding event of two polymers, in principle  $S^4$  possibilities exist — $S$  for each end of each polymer. Since binding is only possible between two specific species the additional constraint reduces the complexity to  $S^3$ . For a system with  $S = 100$  species hence  $10^6$  events exist which all have to be considered individually each iteration. Fortunately, by breaking up the process of finding the next event into stages, as shown in Fig. A.2, the time complexity can be reduced to  $3S$  resulting in a speed-up of roughly  $S^2/3$  or 3000 for the example  $S = 100$ .

In the first stage of determining the event, only the binding ends are chosen. For convenience and memory efficiency, it is always the left end that is considered to bind to the right end. To allow for this step a vector of size  $S$  stores the accumulated binding

---

<sup>11</sup>Note that, this model does not work for the square system. The number of states roughly scales as  $2^S$  and hence becomes unfavorable for  $N < 2^{1+S}/S$  because more states than possible structures exist. For example, in case of  $S = 20$  this is fulfilled for particle numbers smaller than 100000.

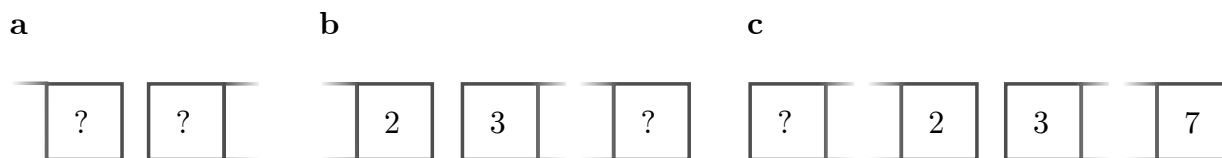


Figure A.2: **Illustration of the stages of polymer-polymer binding.** (a) Fixing the binding end of the first polymer also determines the complementary end of the second one. (b) In the next step, a random right end is chosen for the binding polymer (right one by definition). (c) Based on all constraints given by the binding polymer, the left end of the bound-to polymer (left one by definition) is chosen at random. To keep track of all rates needed to apply this scheme additional bookkeeping after each iteration step is performed. All affected rates as well as the accumulated rates are updated according to the changes caused by the last event.

rates<sup>12</sup> for each species irrespective of the polymer length<sup>13</sup>.

```

const int GetFirstReactingComponentLeftEnd() {
    int component=0;
    double random_number=\
std::uniform_real_distribution<double>\
(0,rates_.back())(rng_engine);
    while(rates_[component]<random_number){
        ++component;
    }
    return component;
}

```

In the next step, the right end of the binding polymer is chosen. To this end, all binding possibilities of a polymer in dependence of its right end have to be stored in an additional  $S \times S$  matrix. This is then used to give the appropriate stochastic weight to all conditioned events.

```

const int GetFirstReactingComponentRightEnd(const int left_end) {
    int right_end=0;
    long particle_index=std::uniform_int_distribution<long>\
(1,all_binding_combinations_of_species_[left_end])(rng_engine);
    long sum_of_binding_partners=possible_bindings_2D\
[left_end][right_end]*ring_structures_[left_end][right_end];
    while(sum_of_binding_partners<particle_index){
        ++right_end;
    }
}

```

<sup>12</sup>A larger vector is actually used to account for events other than binding e.g., activation or depolymerization. Left ends drawn in the first reaction step which are larger than  $S$  cause those to happen.

<sup>13</sup>This method relies on the assumption that it is the species that determines the binding rate. However, it is possible as well to use polymer sizes instead with the steps: 1. first size, 2. first left end (fixes right end and other left end), 3. other size.

```

        sum_of_binding_partners+=possible_bindings_2D_\
        [left_end][right_end]*ring_structures_[left_end][right_end];
    }
    return right_end;
}

```

Finally, the left end of the bound-to polymer is chosen. Since, this end does not interact with the other polymer, except for not being allowed to overlap<sup>14</sup>, each species is just weighted by the number of polymers that have the specified combination of left and right end. At this point, it is important to be careful which configurations create an overlap because of the periodic ring structure.

```

const int GetSecondReactingComponentLeftEnd(const int\
left_end_1, const int right_end_1, const int right_end_2){
    int left_end_2=0;
    long site_index=std::uniform_int_distribution<long>\
(1,possible_bindings_2D_[left_end_1][right_end_1])(rng_engine);
    long sum_of_binding_partners;
    if(right_end_1<right_end_2){
        left_end_2=right_end_1+1;
        sum_of_binding_partners=\
ring_structures_[left_end_2][right_end_2];
        while(sum_of_binding_partners<site_index){
            ++left_end_2;
            sum_of_binding_partners+=
ring_structures_[left_end_2][right_end_2];
        }
    }
    else{
        if(right_end_1+1==number_of_species){
            left_end_2=0;
        }
        else{
            left_end_2=right_end_1+1;
        }
        sum_of_binding_partners=\
ring_structures_[left_end_2][right_end_2];
        while(sum_of_binding_partners<site_index){
            ++left_end_2;
            if(left_end_2==number_of_species){
                left_end_2=0;
            }
        }
    }
}

```

<sup>14</sup>An additional binding with right end of the other polymer does not need to be considered because of the definition that it is always the left end which binds to the right end. This binding combination would simply be another route in the algorithm.

```

    }
    sum_of_binding_partners+=\
    ring_structures_[left_end_2][right_end_2];
  }
}
return left_end_2;
}

```

The described methods made it possible to perform series of ensemble simulations within less than a day that admit high enough accuracy such that errors of the mean could be completely neglected. And, even though a lot of additional management is added to the event execution<sup>15</sup>, making it significantly more error prone compared to the particle-based implementation, the simulation speed-up makes up for the additional time investment very fast.

### A.3 Reaction-diffusion systems on lattices

For spatially extended systems the time complexity per iteration step scales with the number of lattice sites  $N$  as well as reactions  $R$  and diffusion events  $D$ . In a normal setting each reaction and diffusion event may take place at any lattice site leading to a total of  $(R + D)N$  events<sup>16</sup>. For a basic Gillespie implementation this directly maps to the time complexity of the problem which is not very efficient for a system with purely local interactions. In principle, a method similar to the one used in Section A.1 could be employed which achieves constant time complexity. In practice however, because events at different lattice sites have different rates depending on the number of particles it is not a useful approach in general. Only for incredibly large systems containing very few particles or even obeying exclusion as the TASEP does it could be beneficial.

For the simulation of large numbers of different events the *Next Reaction Method* [49] was developed. Instead of using a single random number to determine the (in simulation) time that passes till the next event happens, for each reaction the absolute time at which it would take place under the current circumstances is used. Employing a *minimal heap* [194] structure, as illustrated in Fig. A.3, with respect to the event times the (wallclock) time complexity of a general reaction can be reduced to a logarithmic scaling. This is the lowest complexity apart from a completely constant value which was discussed above to be not feasible. If implemented as a normal Gillespie algorithm a simulation of 8192 lattice sites with just one event each would be roughly  $8192/\log 8192 \approx 600$  times slower causing simulations to take years instead of days. However, there is one important limitation. For each event which takes place a number of  $k$  other events whose rates have changed throughout have to be updated as well. In the case of a spatially extended reaction-diffusion

<sup>15</sup>Those implementations are not shown as they are not a direct part of the algorithm itself or necessary for the understanding of the overall concept.

<sup>16</sup>Note that  $D$  depends on the dimensionality of the system.

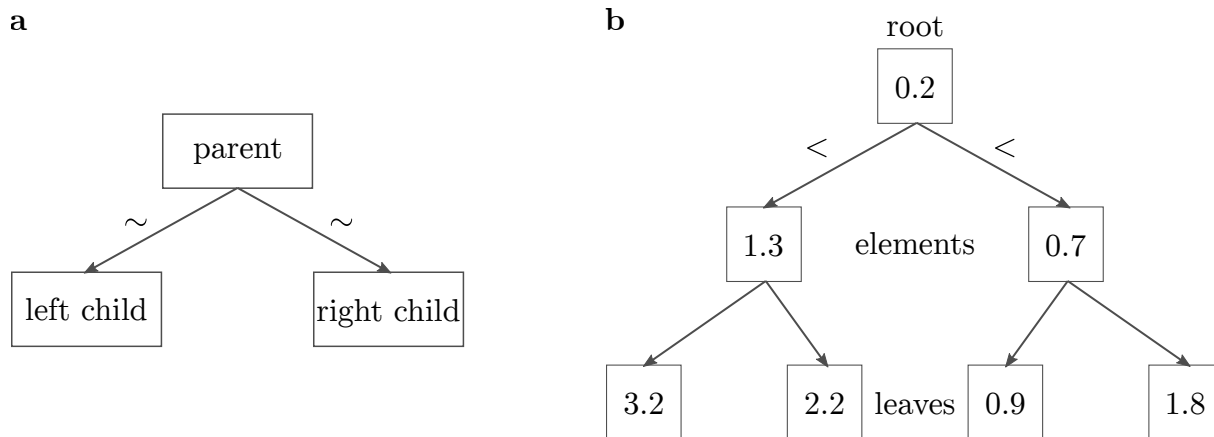


Figure A.3: **Illustration of a heap structure.** (a) The arrangement of heap elements is defined via a relation  $\sim$  (e.g.,  $\leq$  or  $\geq$ ). The two child nodes always fulfil this relation with respect to their parent node. (b) Each child node may itself be a parent of two other nodes. A node without children is called a leaf. There exists just one node, the root, which does not have a parent. The structure of a heap is not uniquely defined because it depends on the order in which elements are added (it is not a tree which can be traversed in order).

system the corresponding time complexity hence scales as  $k \log(r + d)N$ . Accordingly, this method works best if  $k$  is small corresponding to sparse reaction dependencies. Because the models at our chair mainly involve a smaller number of components which all interact with each other, leading to a large number of additional updates  $k$ , further room for improvement exists.

The central idea is to group events which are strongly dependent and sort these groups into a heap structure such that the number of updates caused by interactions is minimized. For a lattice with only local interactions the ideal choice is to group by sites.

```
struct HeapElement{
    double time;
    long lattice_site;
};
```

If a reaction takes place no other site is affected. In case of a diffusion event just one additional element has to be updated. Furthermore, as explained in Sec. A.1 a lattice can be directly translated into a hash map of unique elements making updating the heap most efficient. The corresponding data structure is illustrated in Fig. A.4. Accordingly, the time and lattice site of the next event are always stored as the first heap element.

```
const double GetMinTime() const{
    return elements_[0].time;
}
const long GetMinSite() const{
    return elements_[0].lattice_site;
```

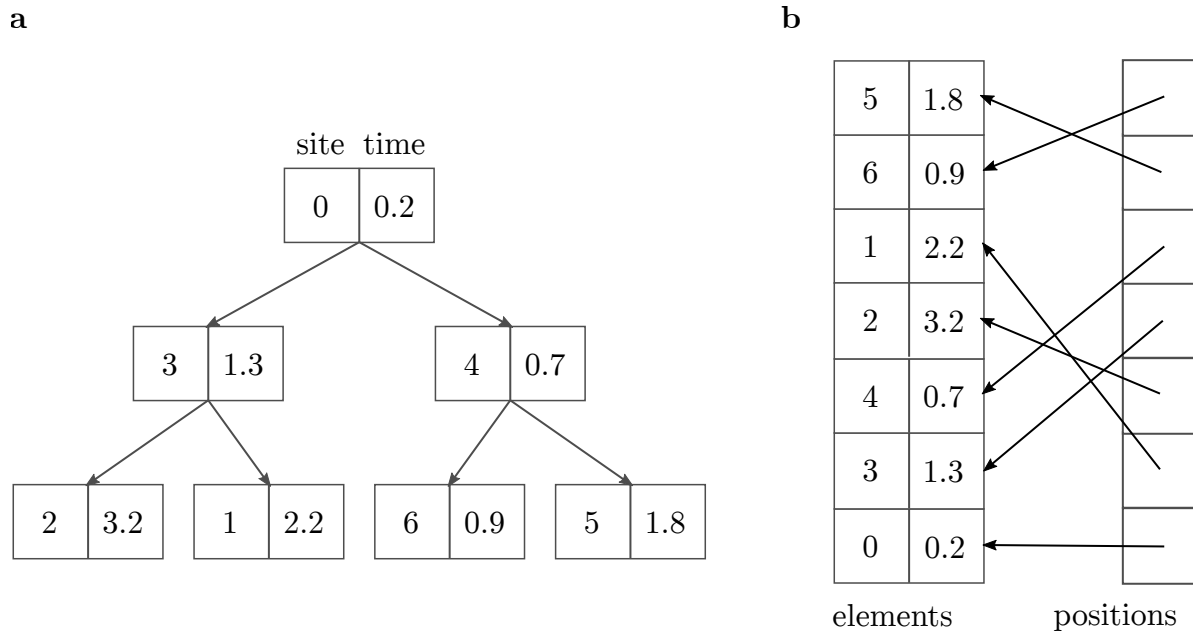


Figure A.4: **Illustration of the minimal heap implementation.** (a) Each element consists of a reference for an event and a random time at which the event takes place. The heap property is that the time of each child is larger than for the parent. This immediately implies that the root has the earliest time and hence corresponds to the next event. Because of the branching the depth of the heap is the logarithm to the power two of the number of elements. (b) In practice, the heap is stored as a one-dimensional array. The root has index 0. The children of the  $n$ -th element have the indices  $2n + 1$  and  $2n + 2$ . Since, other elements than the root need to be updated as well, a hash map is used to directly access all elements without searching.

```
}

```

This is an operation of constant time complexity. In the optimal case, only the element at the top of the heap that corresponds to the lattice site of the event has to be updated.

```
void UpdateMin(double new_value){
    elements_[0].time=new_value;
    Heapify(0);
}
```

The major computational effort has to be put only into maintaining the heap structure after performing an event which is done using a *Heapify* function [194]. Assuming that the heap property is fulfilled for all offspring of the considered element *Heapify* sorts the element into the correct position. Because a hash map has to be used to track the positions of all stored elements, the respective entries need to be updated in addition.

```
void Heapify(const long ID){
    for(long i=ID; i<Size>>1;){
```

```

const long left=2*i+1;
const long right=std::min(2*i+2,Size-1);
if(elements_[i].time>elements_[left].time){
    if(elements_[left].time>elements_[right].time){
        std::swap(elements_[right], elements_[i]);
        std::swap(positions_[elements_[right].lattice_site],\
positions_[elements_[i].lattice_site]);
        i=right;
    }
    else{
        std::swap(elements_[left], elements_[i]);
        std::swap(positions_[elements_[left].lattice_site],\
positions_[elements_[i].lattice_site]);
        i=left;
    }
}
else if(elements_[i].time>elements_[right].time){
    std::swap(elements_[right], elements_[i]);
    std::swap(positions_[elements_[right].lattice_site],\
positions_[elements_[i].lattice_site]);
    i=right;
}
else{
    return;
}
}
}

```

By iteratively applying the Heapify function starting from the final leaves upwards to the root, the initial heap is constructed.

```

void MakeHeap(){
    for(long i=(Size>>1)-1; -1<i; --i){
        Heapify(i);
    }
}

```

Since diffusion events lead to a coupling of lattice sites often times an additional element which is not the root has to be updated. Knowing that all elements but the one considered are compatible with the heap structure only minor changes are necessary to re-establish a fully functioning heap. If the new value is larger than the old one, a single application of Heapify is enough. The element travels down one branch and the relation of all other elements stays the same. If the new value is smaller than before the element climbs up the heap by being swapped with its parents until it has its correct position either as the new root element or having a parent node with smaller time value.

```

void Update(long site,double new_value){
    long i=positions_[site];
    if(elements_[i].time<new_value){
        elements_[i].time=new_value;
        Heapify(i);
        return;
    }
    elements_[i].time=new_value;
    while(0<i){
        const long parent=(i-1)>>1;
        if(elements_[parent].time>elements_[i].time){
            std::swap(elements_[parent], elements_[i]);
            std::swap(positions_[elements_[parent].lattice_site],\
positions_[elements_[i].lattice_site]);
            i=parent;
        }
        else{
            return;
        }
    }
}

```

At a chosen lattice site, the normal steps of the Gillespie algorithm are performed to decide on the actual event and the time update. In case of a diffusion event, at the site the particle diffuses to all rates have to be updated and a new event time has to be drawn. The corresponding time complexity hence scales as  $2a \log N + 2kb$  instead of  $ka \log N + ka \log(R + D)$  with  $a$  and  $b$  being empirical constants. The resulting speed-up is at least  $k/2$  because  $a$  can be expected to be larger than  $b$  due to the higher complexity of the underlying operations. For the minimalistic diffusive epidemic process studied in Chapter 4 for example simulations are on the order of three times faster compared to an implementation without grouping elements. In conclusion, the next reaction method applied to spatially extended systems results a significant speed-up on the order of  $N/\log N$  compared to the Gillespie algorithm. For a dense reaction network with several species that cause  $k$  updates of reactions and diffusion events per iteration an additional performance increase of at least  $k/2$  can be achieved<sup>17</sup> by grouping events by lattice sites and using the hybridized algorithm.

---

<sup>17</sup>This will always be larger than 1 since already for one species on a one-dimensional lattice there are 2 diffusion events which are dependent.

# Appendix B

## Supplementary calculations

This appendix chapter discusses calculations that generalize and extend results derived in the main text but do not add new methods or concepts by doing so. Despite being interesting, they do not further the respective segment in a way that makes up for the increase in technicality required. However, because the final generalizations obtained contribute significant value and are being used in the main text the respective derivations are provided in the following.

### B.1 Cramming density for arbitrary species ratios

In Chapter 2 an extension of the totally asymmetric simple exclusion process is discussed. It exhibits a phase transition at zero particle exit rate  $\beta = 0$  characterized by the cramming density  $\rho_{\text{cram}}$  that differs from the jamming density  $\rho_{\text{max}}$  realized for  $\beta \rightarrow 0$ . In sec. 2.6 the filling process that is defined via the limit of vanishing in rate  $\alpha \rightarrow 0$  and zero exit rate  $\beta = 0$  is introduced to calculate the cramming density for a two-lane system with symmetric species ratio  $\delta = 1/2$ . In the following the corresponding derivation is extended to arbitrary  $\delta$ .

Fig. B.1 shows the generalized version of the transition matrix Fig. 2.9.b in the main text. Because of its symmetries and the species exchange symmetry  $\delta \rightarrow 1 - \delta$  of the system itself the corresponding stationary state vector has to be of the form

$$P^{\text{st.}} = \begin{pmatrix} a[\delta] \\ b_0[\delta] \\ b_0[1 - \delta] \\ b_1[\delta] \\ b_1[1 - \delta] \\ \vdots \end{pmatrix}. \quad (\text{B.1})$$

To make it easier to distinguish between multiplication and  $\delta$  dependencies the latter ones are indicated by square brackets for the remainder of this section. Similar to the symmetric

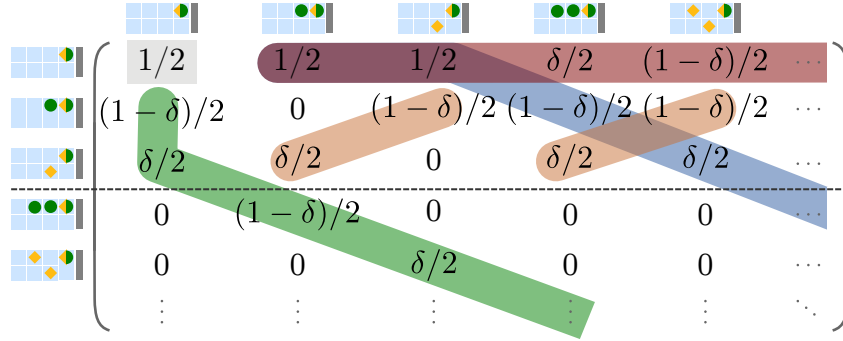


Figure B.1: **Generalized transition matrix.** The green line indicates particle sequence growth, the blue line shrinkage. Red and orange correspond to a double or single closing of the state as defined in the main text. The dashed line indicates the region in which the matrix becomes completely regular. Because the single particle state does not distinguish between the species it causes deviations from the regular matrix structure (grey and kinks in blue and green).

case, the probabilities of sequences are related by a recursion relation that now depends on the species ratio  $\delta$

$$b_n[\delta] = \frac{1-\delta}{2} (b_{n-1}[\delta] + b_{n+1}[\delta]), \quad n \geq 1. \quad (\text{B.2})$$

The corresponding normalizable solution which fulfils the initial condition is given by

$$b_n[\delta] = b_0[\delta] \left( \frac{1}{1-\delta} - \sqrt{\frac{1}{(1-\delta)^2} - 1} \right)^n. \quad (\text{B.3})$$

At this point, it is convenient to define the following two series

$$U[\delta] := \sum_{n=0}^{\infty} b_n[\delta] = \sum_{n=0}^{\infty} \left( \frac{1}{1-\delta} - \sqrt{\frac{1}{(1-\delta)^2} - 1} \right)^n = \frac{1-\delta}{(1-\delta) \sqrt{\frac{1}{(1-\delta)^2} - 1} - \delta}, \quad (\text{B.4})$$

$$V[\delta] := \sum_{n=0}^{\infty} n b_n[\delta] = \sum_{n=0}^{\infty} n \left( \frac{1}{1-\delta} - \sqrt{\frac{1}{(1-\delta)^2} - 1} \right)^n = \frac{1-\delta}{2\delta}.$$

This allows us to write the remaining equations which have to be solved to find the stationary state vector as

$$\begin{aligned} a[\delta] &\stackrel{!}{=} (1-\delta + \delta U[\delta]) b_0[\delta] + (\delta + (1-\delta)U[1-\delta]) b_0[1-\delta] \\ b_0[1-\delta] &\stackrel{!}{=} \frac{\delta}{2} (a[\delta] + b_0[\delta] U[\delta] + b_1[\delta]) \\ 1 &\stackrel{!}{=} a[\delta] + b_0[\delta] U[\delta] + b_0[1-\delta] U[1-\delta]. \end{aligned} \quad (\text{B.5})$$

initial state	following	rates	particles $p_l$	lattice sites $s_l$
		$\delta/2$	$l + 1$	$2l$
		$\delta/2$	$l - 1$	$2l - 2$
		$(1 - \delta)/2$	2	2
		$(1 - \delta)/2$	0	0

Figure B.2: **Contributions to the stationary state by transition type for  $T$  species particles.** Depending on the state a particle sequence transitions to, another sub-configuration of the stationary state is fixated. For each case four different scenarios exist. The transition rates depend on the species ratio  $\delta$ . The transitions for the  $S$  species can be obtained immediately via the  $\delta \rightarrow 1 - \delta$  symmetry.

The first two equations are obtained by applying the transition matrix to the vector Eq. B.1 and demanding that the first two lines are identical to the respective vector entries. The last equation reflects that the eigenvector has to be normalized to one. Solving the equations results in

$$\begin{aligned}
 a[\delta] &= 1 - \frac{1}{\delta} - \frac{1}{1 - \delta} + \sqrt{\frac{1}{(1 - \delta)^2} - 1} + \sqrt{\frac{1}{\delta^2} - 1}, \\
 b_0[\delta] &= \frac{\sqrt{\frac{1}{(1 - \delta)^2} - 1} + \delta \left( \delta - 3 - \delta \sqrt{\frac{1}{(1 - \delta)^2} - 1} \right)}{(1 - \delta)^2},
 \end{aligned} \tag{B.6}$$

which together with relation Eq. B.3 fully characterizes the eigenvector. To calculate the final cramming density, we further need the contributed particles and lattice sites for the different state transitions as explained in detail in the main text. However, because the species ratio  $\delta$  is not  $1/2$ , both species need to be treated separately. For the  $T$  species the contributions of the  $n$ -th sequence element to the total particle number  $N_n$  and number of lattice sites  $Z_n$  read

$$\begin{aligned}
 N_n[\delta] &= \delta n + 1 + \delta, \\
 Z_n[\delta] &= 2\delta n + 1 + 2\delta.
 \end{aligned} \tag{B.7}$$

Employing the species exchange symmetry  $\delta \rightarrow 1 - \delta$  it is unnecessary to additionally calculate those values for the  $S$  species. By construction they have to be  $N_n[1 - \delta]$  and  $Z_n[1 - \delta]$ . For the same reason, we know that  $a[\delta] = a[1 - \delta] = a[\delta]/2 + a[1 - \delta]/2$  has to hold. Using this symmetrized version of  $a$  we can define the symmetric total particle

contribution  $N[\delta]$  and lattice site contribution  $Z[\delta]$  of the  $T$  species

$$\begin{aligned} N[\delta] &= \frac{a[\delta]}{2} + \sum_{n=0}^{\infty} b_n[\delta] N_n[\delta] = \frac{a[\delta]}{2} + b_0[\delta] (\delta V[\delta] + (1 + \delta)U[\delta]), \\ Z[\delta] &= \frac{a[\delta]}{2} + \sum_{n=0}^{\infty} b_n[\delta] Z_n[\delta] = \frac{a[\delta]}{2} + b_0[\delta] (2\delta V[\delta] + (1 + 2\delta)U[\delta]). \end{aligned} \quad (\text{B.8})$$

In this form, the respective quantities for the  $S$  species are just the complements  $N[1 - \delta]$  and  $Z[1 - \delta]$ . Dividing the total number of particles by the number of lattice sites yields the cramming density as stated in the main text

$$\rho[\delta] = \frac{N[\delta] + N[1 - \delta]}{Z[\delta] + Z[1 - \delta]} = \frac{\sqrt{\frac{1}{(1 - \delta)^2} - 1} - 1 - 1 - \delta \left( \sqrt{\frac{1}{(1 - \delta)^2} - 1} + \sqrt{\frac{1}{\delta^2} - 1} - 2 \right)}{4\delta - 2}. \quad (\text{B.9})$$

The expression  $(N[\delta] + N[1 - \delta])/Z[\delta] + Z[1 - \delta]$  nicely illustrates the species exchange symmetry. As was shown in Fig. 2.11, the stochastic simulations are in perfect agreement. Interestingly, the general solution Eq. B.9 is not defined for the symmetric case  $\delta = 1/2$ . Hence, the solution derived in the main text is not a special case of Eq. B.9 but the value used to lift this gap.

## B.2 Derivatives of the hindrance function

In Section 2.7 of the main text we used the derivatives of the hindrance function for extremal densities to perform a series expansion. In the following, the origin of those are explained in detail. As the central physical quantity in the system, the current serves as the basis for our analysis. Taking the derivative with respect to the density we obtain

$$\frac{d}{d\rho} J(\rho) = 1 - H(\rho) - \rho H'(\rho) - 2\rho. \quad (\text{B.10})$$

This allows us to relate the derivative of the current, which can be understood using physical arguments, to the abstract derivative of the hindrance function. Assuming the species ratio  $\delta$  to be identical to the density ratios of both species—which holds exactly in the limit  $\rho \rightarrow 0$  but is in approximation otherwise—we can express the species specific densities as  $\rho^T = (1 - \delta)\rho$  and  $\rho^S = \delta\rho$ . This is interpreted as the chance of having an arbitrary lattice site occupied by the respective species.

Fig. B.3 illustrates the mean-field probabilities of the different states of a single lattice site in combination with all configurations relevant for the current in the system. For a hopping event to occur towards a certain lattice site, it has to be empty which is the case with probability  $1 - \rho$ . If this condition is met, three different scenarios exist. First, two particles of different species may target the same lattice site. This has a probability of  $\delta(1 - \delta)\rho^2$  to occur. Despite two particles targeting, the same lattice site the state

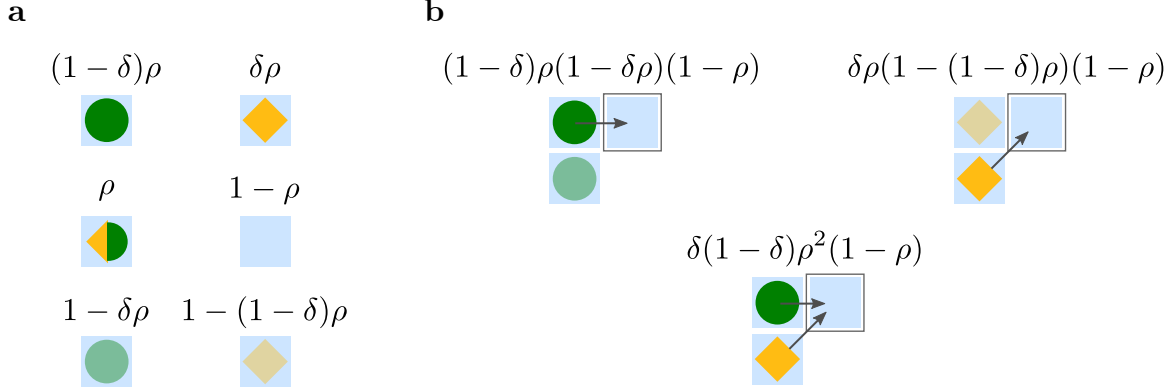


Figure B.3: **Illustration of the mean-field probabilities of different states.** Panel (a) shows the probabilities for different states of an individual lattice site given a fixed density  $\rho$  in the system. Panel (b) displays the configurations relevant for the refined mean-field theory in combination with their corresponding probabilities.

only contributes once to the total current. The reason is sequential hopping which cannot be understood in a notion purely based on densities. If one particle hops, the other is blocked. So, only one event may occur (to linear order or in the limit  $dt \rightarrow 0$ ). The other two relevant cases are one particle being able to hop without a particle of the respective other species being present on the neighboring lane. For an  $S$  particle the probability is given by  $\delta\rho(1 - (1 - \delta)\rho)$  and for a  $T$  particle is  $(1 - \delta)\rho(1 - \delta\rho)$  which amounts to a total *refined* mean-field current

$$J(\rho) = \left( (1 - \delta)\rho(1 - \delta\rho) + \delta\rho(1 - (1 - \delta)\rho) + \delta(1 - \delta)\rho^2 \right) (1 - \rho), \quad (\text{B.11})$$

which reduces to the derivative of the TASEP's current for  $\delta = 0$  and  $\delta = 1$ . While the result is exact in these cases, it is only an approximation in general as long as the density is finite. We can now use Eq. B.11 to calculate the change in current in response to an infinitesimal change in density  $d\rho$ :

$$dJ = J(\rho + d\rho) - J(\rho) = ((1 - 2\rho) + \delta(1 - \delta)(3\rho - 2)\rho) d\rho + \mathcal{O}(d\rho^2). \quad (\text{B.12})$$

Plugging the result into Eq. B.10 yields

$$\frac{dJ}{d\rho} = 1 - H(\rho) - \rho H'(\rho) - 2\rho \stackrel{!}{=} (1 - 2\rho) + \delta(1 - \delta)(3\rho - 2)\rho. \quad (\text{B.13})$$

Since,  $H(\rho)/\rho \rightarrow H'(0)$  for  $\rho \rightarrow 0$ , this results in

$$H'(0) = \delta(1 - \delta), \quad (\text{B.14})$$

the relation used in the main text. Because correlations vanish for an empty lattice as no interaction takes place, the mean-field approximation becomes exact in this limit.

We now apply the same line of thought to a completely jammed configuration  $\rho = \rho_{\max}$ . However, instead of adding density we calculate the effect of removing it. Since the system is assumed to be completely jammed, this will not reduce the current as there was no potential to contribute to begin with. But, because of its absence are other particles now able to move. As before the exact change depends on the species present on the neighboring lattice site. In complete analogy to the low-density case the change in current is given by

$$\begin{aligned} \frac{dJ}{d\rho} &= -\delta\rho_{\max}(1 - \rho_{\max}(1 - \delta)) - (1 - \delta)\rho_{\max}(1 - \delta\rho_{\max}) - \delta(1 - \delta)\rho_{\max}^2 \\ &= -\rho_{\max} + \delta(1 - \delta)\rho_{\max}^2. \end{aligned}$$

Combining the definition of the maximal density  $H(\rho_{\max}) = 1 - \rho_{\max}$  with Eq. B.10 yields the final result

$$H'(\rho_{\max}) = -\delta(1 - \delta)\rho_{\max}. \quad (\text{B.15})$$

It is important to note that, in contrast to the low-density case this is not an exact result; But it is not pure mean-field either. Knowledge about the existence of  $\rho_{\max}$  is part of the derivation. This can easily be seen by the fact that Eq. B.15 is not Eq. B.12 evaluated for  $\rho = \rho_{\max}$ .

### B.3 General low-density theory

In the main text we showed the derivation of the low-density theory for the totally symmetric case  $\delta = 1/2$ . In this appendix, we provide the derivation of the general case for arbitrary  $\alpha_T$  and  $\alpha_S$ . As before, we start from the assumption, that the current reduction due to the second species can be interpreted as an external field slowing down particle motion

$$\begin{aligned} \rho^T (1 - \rho^T - \rho^S) &= \rho^T (1 - \rho^T) \nu_T, \\ \rho^S (1 - \rho^T - \rho^S) &= \rho^S (1 - \rho^S) \nu_S. \end{aligned} \quad (\text{B.16})$$

Taking the interactions of the additional densities into account this yields the recursion relation

$$\begin{aligned} \nu_T^{N+1} &= \frac{1 - \rho^T(\alpha, \delta, \nu_T^N) - \rho^S(\alpha, \delta, \nu_S^N)}{1 - \rho^T(\alpha, \delta, \nu_T^N)}, \\ \nu_S^{N+1} &= \frac{1 - \rho^T(\alpha, \delta, \nu_T^N) - \rho^S(\alpha, \delta, \nu_S^N)}{1 - \rho^S(\alpha, \delta, \nu_S^N)}. \end{aligned} \quad (\text{B.17})$$

The final solution has to fulfil the self consistency conditions

$$\begin{aligned} \nu_T &= \frac{1 - \rho^T(\alpha, \delta, \nu_T) - \rho^S(\alpha, \delta, \nu_S)}{1 - \rho^T(\alpha, \delta, \nu_T)}, \\ \nu_S &= \frac{1 - \rho^T(\alpha, \delta, \nu_T) - \rho^S(\alpha, \delta, \nu_S)}{1 - \rho^S(\alpha, \delta, \nu_S)}. \end{aligned} \quad (\text{B.18})$$

Rescaling time for both species according to their slowdown can be used to derive the respective densities in dependence of the hopping rates

$$\begin{aligned}\rho^T(\alpha, \nu_T) &= \frac{\alpha_T}{\nu_T}, \\ \rho^S(\alpha, \nu_S) &= \frac{\alpha_S}{\nu_S}.\end{aligned}\tag{B.19}$$

Because in the low-density phase the in rates are assumed to be small and the hopping rates can be considered to be of similar order Eq. B.18 can be expanded to obtain a more concise solution later on

$$\nu_T = 1 - \frac{\alpha_S}{\nu_S - \alpha_T \frac{\nu_S}{\nu_T}} \approx 1 - \frac{\alpha_S}{\nu_S} \left(1 + \frac{\alpha_T}{\nu_T}\right)\tag{B.20}$$

$$\nu_S = 1 - \frac{\alpha_T}{\nu_T - \alpha_S \frac{\nu_T}{\nu_S}} \approx 1 - \frac{\alpha_T}{\nu_T} \left(1 + \frac{\alpha_S}{\nu_S}\right).\tag{B.21}$$

Defining  $\nu_T =: 1 - \gamma$  which makes  $\gamma$  small under the given assumptions, we can further simplify the first of the two equations

$$\gamma = \frac{\alpha_S}{\nu_S} \left(1 + \frac{\alpha_T}{1 - \gamma}\right) \approx \frac{\alpha_S}{\nu_S} (1 + \alpha_T(1 + \gamma)).\tag{B.22}$$

Solving for  $\nu_T$  we find

$$\nu_T \approx \frac{\frac{\nu_S}{\alpha_S} - 1}{\frac{\nu_S}{\alpha_S} + \alpha_T}.\tag{B.23}$$

This can be plugged into Eq. B.21 to obtain an approximate equation

$$\nu_S \approx 1 - \alpha_T \left(\frac{\nu_S}{\alpha_S} + \alpha_T\right) \frac{\frac{\nu_S}{\alpha_S} + 1}{\frac{\nu_S}{\alpha_S} - 1} \approx 1 - \alpha_T \frac{\frac{\nu_S}{\alpha_S} + 1}{\frac{\nu_S}{\alpha_S} - 1},$$

which admits a short analytic solution of the form

$$\nu_S \approx \frac{1}{2} \left(1 - \alpha_T + \alpha_S + \sqrt{1 - 2\alpha_T + \alpha_T^2 - 2\alpha_S - 6\alpha_T\alpha_S + \alpha_S^2}\right).\tag{B.24}$$

Now, instead of solving the original equation for  $\nu_T$  which would result in a lengthy expression, we simply employ the species exchange symmetry. It tells us that, if Eq. B.24 is a valid solution for the  $S$  species, in the same way

$$\nu_T \approx \frac{1}{2} \left(1 - \alpha_S + \alpha_T + \sqrt{1 - 2\alpha_S + \alpha_S^2 - 2\alpha_T - 6\alpha_S\alpha_T + \alpha_T^2}\right),\tag{B.25}$$

has to be the solution for the  $T$  species.

Having derived expression for the effective hopping rates all physical observables directly follow using Eq. B.19. An implication of our general low-density has is that in rates of one

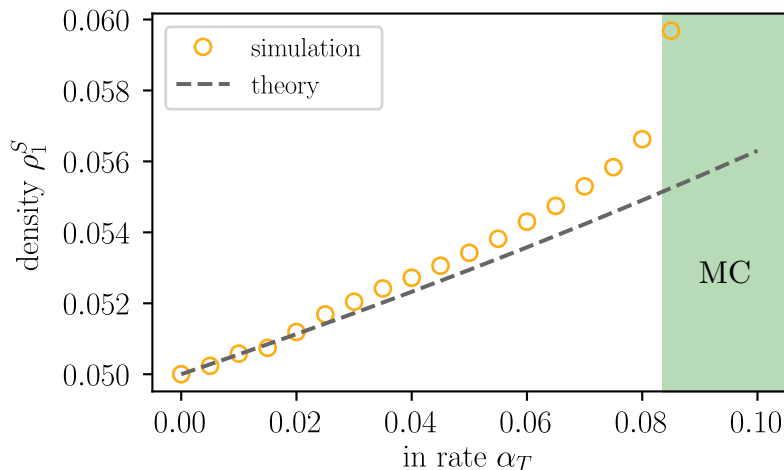


Figure B.4:  $S$  species density plotted against the  $T$  species in rate  $\alpha_T$ . In contrast to the mean-field scenario, in rates affect the density of other species. This confirms the prediction made by the extended low-density theory. Simulations (symbols) agree well with the theory (dashed line) for low in rates  $\alpha_T$ . For higher values stronger deviations occur. This is to be expected since  $\alpha_T \ll 1$  was assumed during the derivation. [Parameters:  $W = 2$ ,  $L = 16384$ ,  $\alpha_S = 0.05$ ,  $\beta = 0.8$  ]

species affect the density of the other. This is never the case for the TASEP. We can test this prediction by measuring the density of the  $S$  species while changing the in rate  $\alpha_T$  of the  $T$  species. The results are shown in Fig. B.4 and confirm our prediction. Slight deviations between simulation and theory can be observed which is however not surprising taking the approximations into account which have been made during the derivation. Actually, an exact analytic solution to Eq. B.18 exists. But because of its highly convoluted structure, no additional insight with regard to the system's mechanisms can be obtained. For that reason, only the approximate solution is presented in this thesis.

# Appendix C

## Supplementary figures

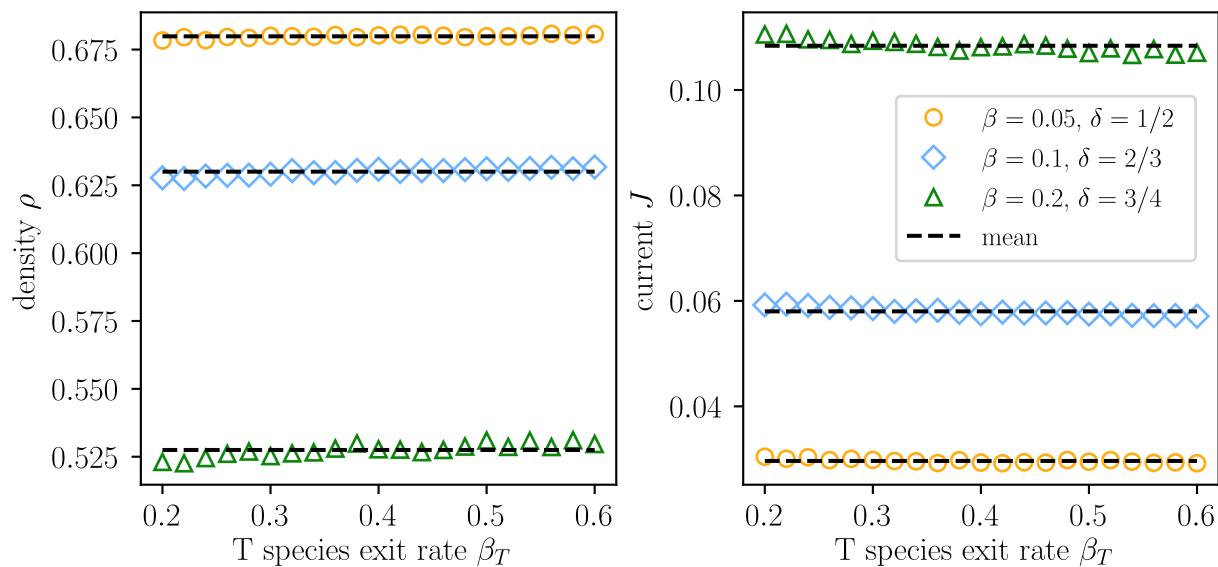


Figure C.1: **Illustration of the correspondents between different exit rate configurations.** The  $S$  species exit rate  $\beta_S$  is adapted in dependence on the  $T$  exit rate  $\beta_T$  to keep the effective exit rate  $\beta$  constant. In agreement with the theoretical predictions, current and density remain unchanged. [Parameters:  $W = 2$ ,  $L = 16384$ ,  $\alpha = 0.4$ ]

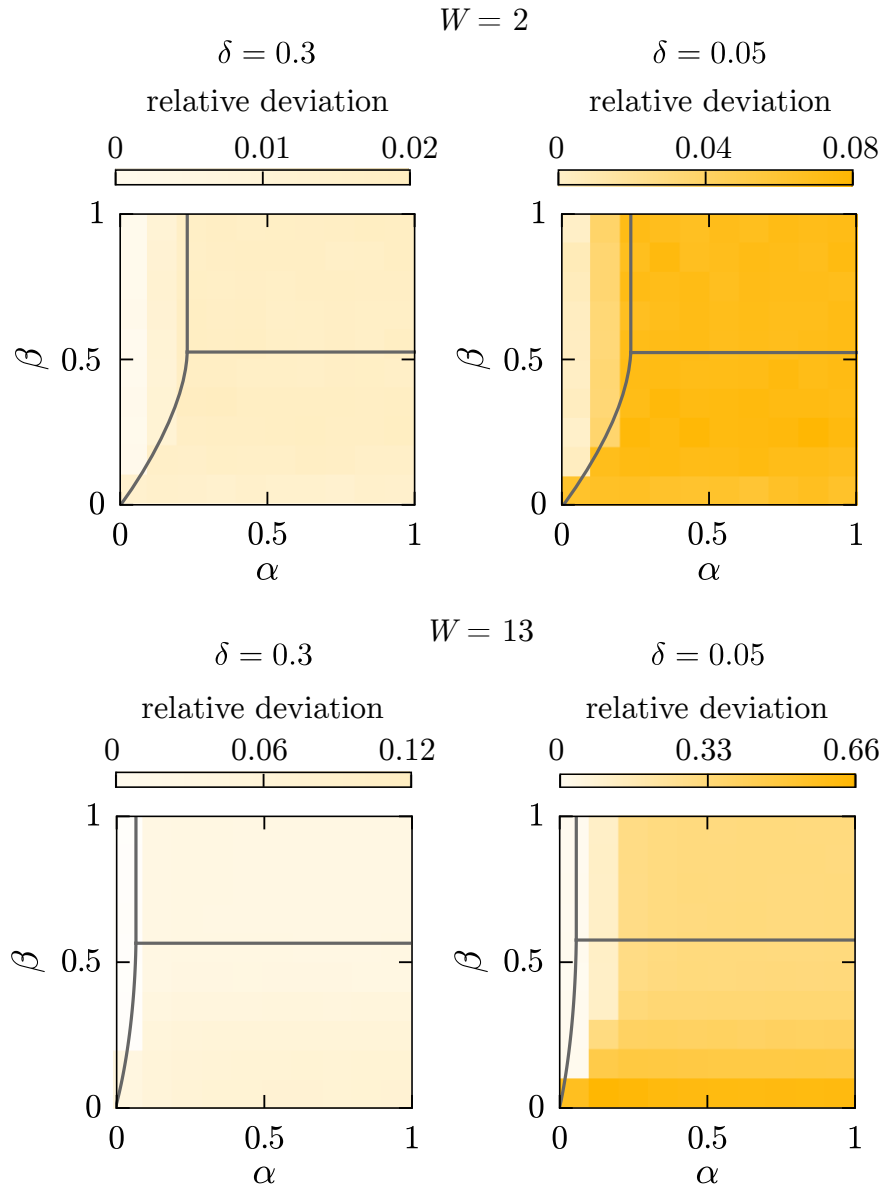


Figure C.2: **Deviations between density ratio and species ratio  $\delta$ .** In the low-density phase in general and for low numbers of lanes the ratios between the particle densities is close to the species ratio  $\delta$ . For high numbers of lanes and very asymmetric species ratios  $0 < \delta \ll 1/2$  significant deviations occur underlining the relevance of strong fluctuations in those regimes. The color scales for systems with the same number of lanes  $W$  are identical. [Adapted from [53]]

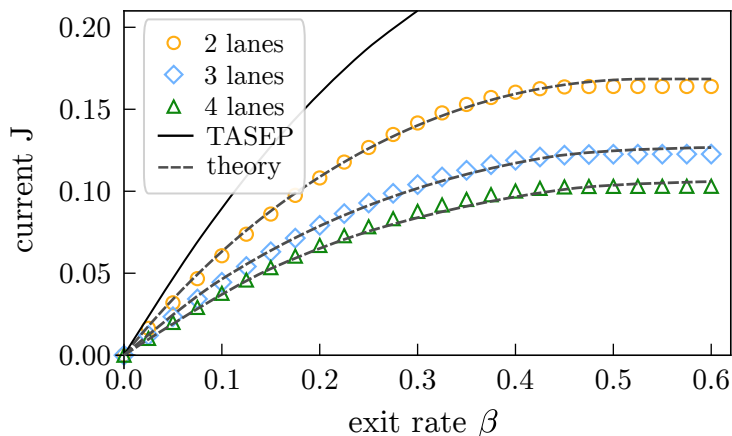


Figure C.3: **Comparison between high-density theory and stochastic simulations.** In the high-density phase the exit rate  $\beta$  controls the particle current. The dependency differs from the TASEP because of arrangement driven fluctuations. The derived theory (dashed line) and stochastic simulations (symbols) are in good agreement. [Parameters:  $W = 2$ ,  $L = 16384$ ,  $\alpha = 0.4$ ,  $\delta = 1/2$ ; adapted from [53]]

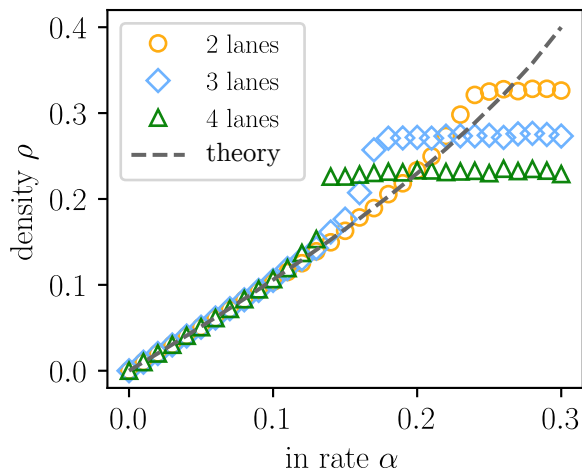


Figure C.4: **Comparison of the low-density theory with stochastic simulations for the bulk density.** Up to the transition to the maximal current phase simulations (symbols) and theory (dashed line) are in good agreement. A lane dependency only enters because the maximal current decreases with the number of lanes and hence the phase transition is triggered at a lower densities. [Parameters:  $L = 16384$ ,  $\delta = 1/2$ ,  $\beta = 0.8$ ]

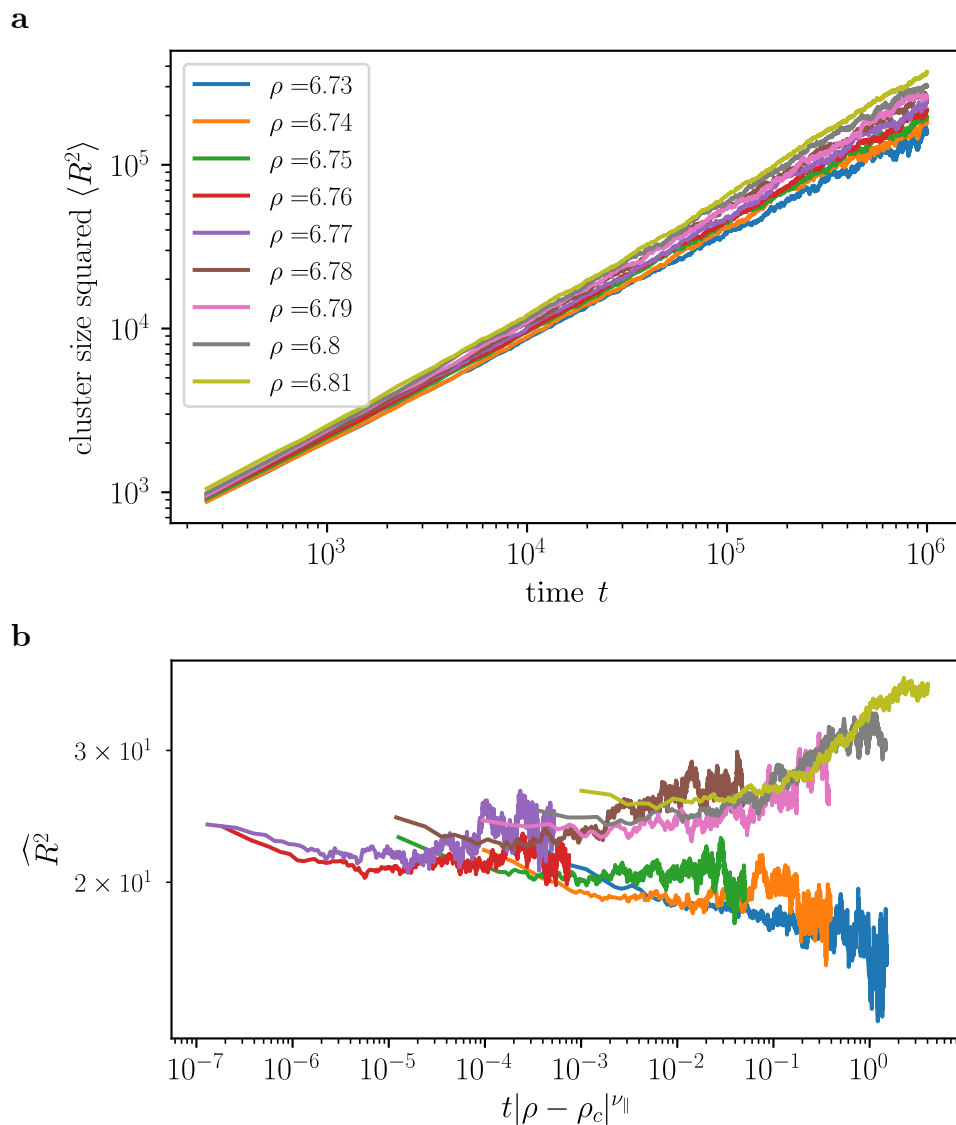


Figure C.5: **Data collapse of the cluster size squared for  $D_A = 2D_B$ .** Assuming  $\rho_c = 6.765$ ,  $\nu_{\parallel} = 4$  and  $z = 3$  a data collapse can be achieved. However, because of the reduction of the effective ensemble size when only considering surviving clusters, strong fluctuations occur. [Parameters: ens. =  $5 \times 10^4$ ,  $L = 8192$ ,  $D_A = 1$ ,  $\lambda = 0.2$ ,  $1/\tau = 1$ ]

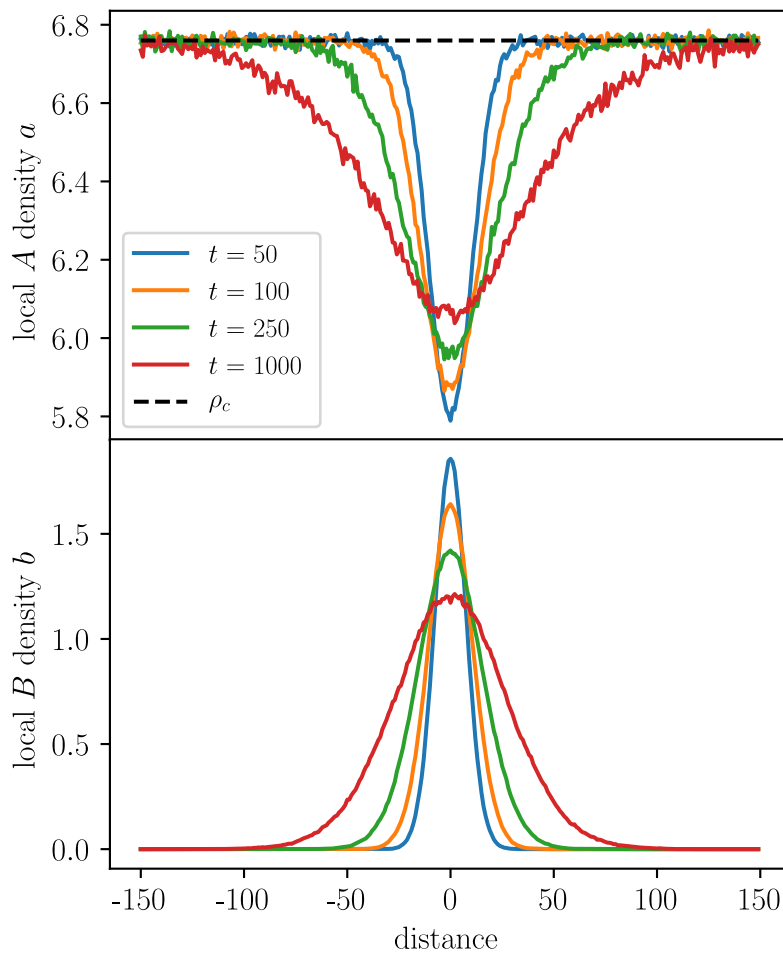


Figure C.6: **Spatial distribution of the local particle densities for  $D_A = 2D_B$ .** A clear anti-correlation between  $A$  and  $B$  particles can be observed. However, the reduction in  $A$  particles extends further than the  $B$  particle cluster. [Parameters:  $\text{ens.} = 10^5$ ,  $L = 512$ ,  $D_A = 1$ ,  $\lambda = 0.2$ ,  $1/\tau = 1$ ,  $\rho = 6.76$ ]

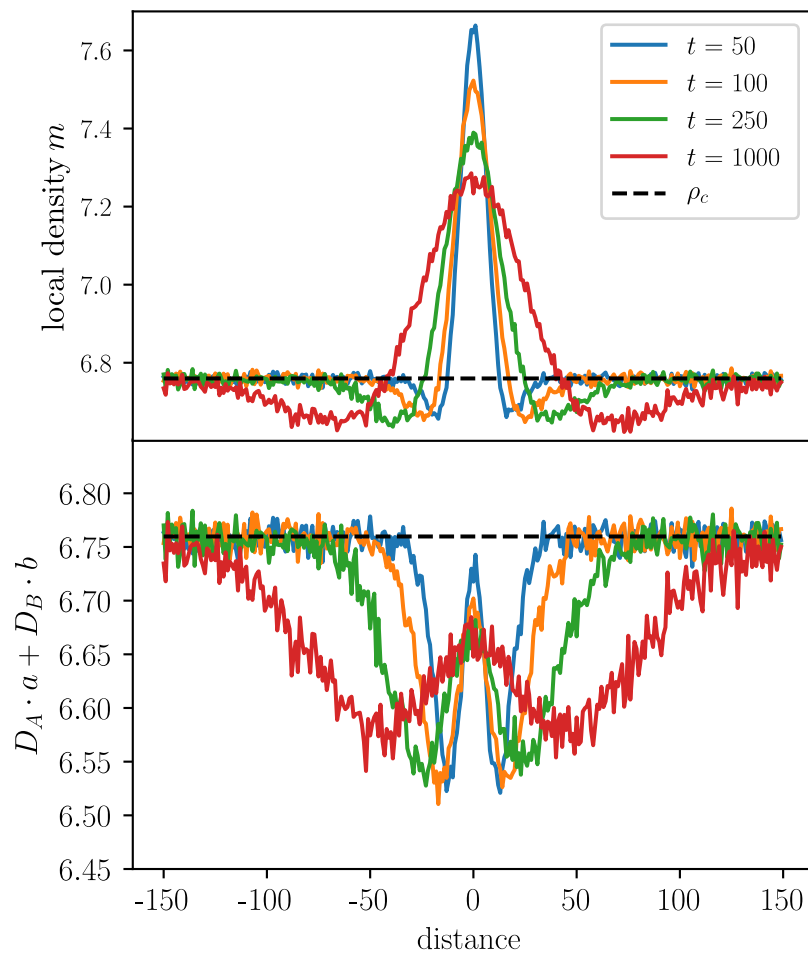


Figure C.7: **Spatial distribution of the effective number of hopping events for  $D_A = 2D_B$ .** Because particles of the  $B$  species diffuse slower, the effective number of hopping events  $D_A \cdot a + D_B \cdot b$  is lower close to the cluster. This causes a net particle flux towards the center. The additional particles which are present in the center of the system in the initial state create a local maximum which decreases over time. [Parameters:  $\text{ens.} = 10^5$ ,  $L = 512$ ,  $D_A = 1$ ,  $\lambda = 0.2$ ,  $1/\tau = 1$ ,  $\rho = 6.76$ ]

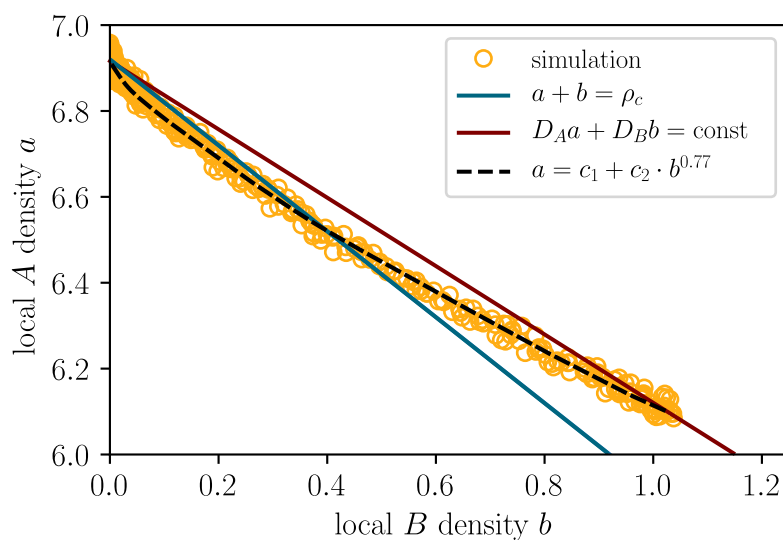


Figure C.8: **Phase space plot for  $4D_A = 5D_B$ .** For different diffusion rates  $4D_A = 5D_B$  configurations neither adapt to the line of balanced fluxes nor the line of constant local density. Instead a  $b^{0.77}$  dependency is realized. The exponent is approximately equal to the ratio of the diffusion rates. At the tip (which corresponds to the center of the cluster), the curve touches the line that indicates the balance of fluxes. [Parameters:  $\text{ens.} = 10^5$ ,  $L = 512$ ,  $D_A = 1$ ,  $\lambda = 0.2$ ,  $1/\tau = 1$ ,  $\rho = 6.92$ ,  $c_1 = 6.92$ ,  $c_2 = -0.81$ ]



# Appendix D

## Reprint: Supplementary information for stochastic yield catastrophes and robustness in self-assembly

This chapter is a publication reprint of the *supplementary information* of the manuscript *Stochastic Yield Catastrophes and Robustness in Self-Assembly* published in **eLife**, 9:e51020 (2020) under the Creative Commons Attribution License. The layout and labelling have been adapted to fit this thesis. No further changes to the content originally submitted to the journal have been made.

Chapter 3 of the main text focuses on the comparison between deterministic theory and stochastic effects to give an intuitive understanding of the underlying phenomenology and central determinants. Aspects that were part of the supplementary information of the published paper were not discussed in detail. To still provide a complete picture by including the more technical results and simulations, the respective content is reprinted in the following.



---

## Supplementary Information for 'Stochastic Yield Catastrophes and Robustness in Self-Assembly'

Florian M Gartner<sup>†</sup>, Isabella R Graf<sup>†</sup>, Patrick Wilke<sup>†</sup>, Philipp M Geiger, Erwin Frey\*

*Arnold Sommerfeld Center for Theoretical Physics and Center for NanoScience,  
Department of Physics, Ludwig-Maximilians-Universität München,  
Theresienstraße 37, D-80333 München, Germany*

<sup>†</sup> These authors contributed equally to this work

\* For correspondence: frey@lmu.de

©Gartner, Graf, Wilke et al. This article is distributed under the terms of the  
Creative Commons Attribution License  
and was published in **eLife**, 9:e51020 (2020)  
DOI: <https://doi.org/10.7554/eLife.51020>



## D.1 Chemical reaction equations and the equivalence of models with different numbers of species

In this section we derive the chemical rate equations (deterministic equations) for the self-assembly process as described in the main text. Furthermore, we show that for general  $S$  in the deterministic limit the model is equivalent to a set of  $S$  independent assembly processes with only one species.

### Homogeneous structures

First, we consider the homogeneous model ( $S = 1$ ). By  $c_\ell(t)$  we denote the concentration of complexes of length  $\ell$  ( $\ell \geq 2$ ) at time  $t$ ,  $c_1(t)$  is the concentration of active monomers and  $c_0(t)$  the concentration of inactive monomers at time  $t$ . In the following we will usually skip the time argument for better readability. We denote the reaction rate for binding of a monomer to a polymer of size  $\ell$  by  $\nu_\ell$ . The model from the main text is recovered by setting  $\nu_\ell := \mu_\ell$  if  $\ell < L_{\text{nuc}}$ , and  $\nu_\ell := \nu$  otherwise. The ensuing set of ordinary differential equations then reads:

$$\frac{d}{dt}c_0 = -\alpha c_0, \tag{D.1a}$$

$$\frac{d}{dt}c_1 = \alpha c_0 - 2c_1 \sum_{\ell=1}^{L-1} \nu_\ell c_\ell + \sum_{\ell=2}^{L_{\text{nuc}}-1} l \delta_\ell c_\ell, \tag{D.1b}$$

$$\frac{d}{dt}c_2 = \nu_1 c_1^2 - 2\nu_2 c_1 c_2 - \delta_2 c_2 \mathbf{1}_{\{2 < L_{\text{nuc}}\}}, \tag{D.1c}$$

$$\frac{d}{dt}c_\ell = 2\nu_{\ell-1} c_1 c_{\ell-1} - 2\nu_\ell c_1 c_\ell - \delta_\ell c_\ell \mathbf{1}_{\{\ell < L_{\text{nuc}}\}}, \quad \text{for } 3 \leq \ell < L, \tag{D.1d}$$

$$\frac{d}{dt}c_L = 2\nu_{L-1} c_1 c_{L-1}. \tag{D.1e}$$

The indicator function  $\mathbf{1}_{\{x < L_{\text{nuc}}\}}$  equals 1 if the condition  $x < L_{\text{nuc}}$  is satisfied and 0 otherwise. The first equation describes loss of inactive particles due to activation at rate  $\alpha$ . The equation is uncoupled from the remainder of the equations and is solved by  $c_0(t) = C e^{-\alpha t}$ , with  $C$  denoting the initial concentration of inactive monomers. The temporal change of the active monomers is governed by the following processes (Eq. (D.1b)): activation of inactive monomers at rate  $\alpha$ , binding of active monomers to existing structures at rate  $\nu_\ell$  (polymerization), and decay of below-critical polymers into monomers at rate  $\delta_\ell$  (disassembly). All binding rates appear with a factor of 2 because a monomer can attach to a polymer on its left or on its right end.

Note that there is a subtlety with the dimerization term “ $2\nu_1 c_1^2$ ”: the dimerization term as well bears a factor of 2 because two identical monomers  $A$  and  $B$  can form a dimer in two possible ways, either as  $AB$  or  $BA$ . Additionally, there is a stoichiometric factor

of 2 for this reaction. However, one factor of 2 is cancelled again because, assuming there are  $n$  monomers, the number of ordered pairs of monomers that describe possible reaction partners is  $\frac{1}{2}n(n-1) \approx n^2/2$  (if  $n$  is large) rather than  $n^2$  (the number of reaction partners when two different species react). This leaves us with a single factor of 2 like for all the other binding reactions.

Equations (D.1c) and (D.1d) describe the dynamics of dimers and larger polymers of size  $3 \leq \ell < L$ , respectively. The terms account for reactions of polymers with active monomers (polymerization) as well as decay in the case of below-critical polymers (disassembly). The dimerization term in the equation for  $\partial_t c_2$  lacks the factor of 2 because the stoichiometric factor is missing as compared with the dimerization term in the line above. Finally, polymers of length  $L$  – the complete ring structures – form an absorbing state and therefore only include a reactive gain term (Eq. (D.1e)).

## Heterogeneous structures

Next we consider systems with more than one particle species ( $S > 1$ ). The heterogeneous system can be described by dynamical equations equivalent to the homogeneous system. We show this starting from a full description that distinguishes both monomers and polymers into a set of different species  $1, \dots, S$ . In order to formulate the dynamic equations and to see the equivalence to a one-species model, we distinguish both monomers and polymers into a set of different species  $1, \dots, S$ . The species of a polymer is defined by the species of the respective monomer at its left end. As polymers assemble in consecutive order of species, a polymer is uniquely determined by its length and species (i.e. species of leftmost monomer). In that sense,  $c_\ell^s$  with  $0 \leq \ell < L$  and  $1 \leq s \leq S$  denotes the concentration of a polymer of length  $\ell$  and species  $s$  ( $c_0^s$  and  $c_1^s$  again denote inactive and active monomers of species  $s$ , respectively). For example,  $c_4^5$  denotes the concentration of polymers [5678] if  $S \geq 8$ , or of polymers [5612] if  $S = 6$ . Upper indices are always assumed to be taken modulo  $S$  whenever they lie outside the range  $[1, S]$ . Therefore, the dynamics of the concentrations  $c_\ell^s$  with  $3 \leq \ell < L$  is given by

$$\frac{d}{dt}c_\ell^s = \nu_{\ell-1} c_{\ell-1}^s c_1^{\ell+s-1} + \nu_{\ell-1} c_{\ell-1}^{s+1} c_1^s - \nu_\ell c_\ell^s c_1^{s+\ell} - \nu_\ell c_\ell^s c_1^{s-1} - \delta c_\ell^s \mathbf{1}_{\{\ell < L_{\text{nuc}}\}}. \quad (\text{D.2})$$

The terms on the right-hand side account for the influx due to binding of the respective polymers of length  $\ell - 1$  with a monomer either on the right or on the left (first and second term), and for the outflux due to reactions of a polymer of length  $\ell$  and species  $s$  (third and fourth term), as well as for decay into monomers for  $\ell < L_{\text{nuc}}$  (last term). For the dynamics of the dimers, however, there is only one gain term arising from dimerization:

$$\frac{d}{dt}c_2^s = \nu_1 c_1^s c_1^{s+1} - \nu_2 c_2^s c_1^{s+2} - \nu_2 c_2^s c_1^{s-1} - \delta_2 c_2^s \mathbf{1}_{\{2 < L_{\text{nuc}}\}}. \quad (\text{D.3})$$

Equivalently, for the active monomers we find:

$$\frac{d}{dt}c_1^s = \alpha C e^{-\alpha t} - c_1^s \sum_{\ell=1}^{L-1} \nu_\ell (c_\ell^{s+1} + c_\ell^{s-\ell}) + \sum_{\ell=2}^{L_{\text{nuc}}-1} \sum_{k=s+1-\ell}^{k=s} \delta_\ell c_\ell^k. \quad (\text{D.4})$$

Now we exploit the symmetry of the system with respect to the species index, that is, the upper index in  $\{c_\ell^s\}$ : Since all species in the system are equivalent, the dynamic equations are invariant under relabelling of the upper indices. Consequently, it must hold that:

$$c_\ell^s(t) = c_\ell^k(t), \quad \text{for any } s, k \leq S \text{ at any time } t. \quad (\text{D.5})$$

In other words, the upper index is irrelevant and can also be discarded. The variable  $c_\ell$  then denotes the concentration of *any* one polymer species of length  $\ell$ . Taking advantage of this symmetry for the equations of the heterogeneous system, (Eq. (D.2), Eq. (D.3) and Eq. (D.4)), and collecting equal terms leads to a set of equations fully identical to those for the homogeneous system (Eq. (D.1)). We show the equivalence to the homogeneous model exemplarily for the dynamics of the polymers with size  $\ell \geq 3$  in Eq. (D.2). Applying  $c_\ell^s(t) = c_\ell(t)$  to Eq. (D.2) yields for the dynamics of the concentration of an arbitrary polymer species of size  $\ell$ :

$$\begin{aligned} \frac{d}{dt}c_\ell &= \nu_{\ell-1} c_{\ell-1} c_1 + \nu_{\ell-1} c_{\ell-1} c_1 - \nu_\ell c_\ell c_1 - \nu_\ell c_\ell c_1 - \delta c_\ell \mathbf{1}_{\{\ell < L_{\text{nuc}}\}}. \\ &= 2\nu_{\ell-1} c_{\ell-1} c_1 - 2\nu_\ell c_\ell c_1 - \delta c_\ell \mathbf{1}_{\{\ell < L_{\text{nuc}}\}}, \end{aligned}$$

which is identical to the respective dynamic equation (D.1d) for the homogeneous model. The other equations for the heterogeneous system reduce to those for the homogeneous system in an analogous manner.

Summarizing, we have shown that the (deterministic) heterogeneous assembly process decouples into a set of  $S$  identical and independent homogeneous processes. In particular, yield, which is given by the quotient of the number of completely assembled rings and the maximal possible number of complete rings, becomes independent of  $S$ :

$$\text{yield}(t) = \frac{S c_L(t)}{S N L^{-1}} = \frac{c_L(t) L}{N}. \quad (\text{D.6})$$

## **D.2 Effective description of the evolution of the polymer size distribution as an advection-diffusion equation**

The dynamical properties of the evolution of the polymer size distribution become evident if the set of ODEs (D.1) is rewritten as a partial differential equation. This approach

was previously described in the context of virus capsid assembly<sup>9,45</sup> but we will restate the essential steps here for the convenience of the reader. To this end we interpret the length index of the polymer  $\ell \in \{2, 3, \dots, L\}$  as a continuous variable that we rename  $x \in [2, L]$ . With such a continuous description in view we write  $c(x = \ell) := c_\ell$  to denote the concentration of polymers of size  $\ell$ .

Since the active monomers play a special role, we denote their concentration in the following by  $A$ . For simplicity we restrict our discussion to the case  $L_{\text{nuc}} = 2$  and let  $\nu_1 = \mu$  and  $\nu_{\ell \geq 2} = \nu$ . Generalizations to  $L_{\text{nuc}} > 2$  can be done in a similar way. Then, for the polymers with  $\ell \geq 3$  we have:

$$\partial_t c(\ell) = 2\nu A [c(\ell - 1) - c(\ell)]. \quad (\text{D.7})$$

Formally, expanding the right-hand side in a Taylor series up to second order

$$c(\ell - 1) = c(\ell) - \partial_x c(\ell) + \frac{1}{2} \partial_x^2 c(\ell), \quad (\text{D.8})$$

we arrive at an advection-diffusion equation with both advection and diffusion coefficients depending on the concentration of active monomers  $A(t)$ ,

$$\partial_t c(x) = -2\nu A \partial_x c(x) + \nu A \partial_x^2 c(x). \quad (\text{D.9})$$

Equation (D.9) can be written in the form of a continuity equation  $\partial_t c(x) = -\partial_x J(x)$  with flux  $J = 2\nu A c - \nu A \partial_x c$ . The flux at the left boundary,  $x = 2$ , equals the influx of polymers due to dimerization of free monomers,  $J(2, t) = \mu A^2$ . This enforces a Robin boundary condition at  $x = 2$ ,

$$2\nu A c(2, t) - \nu A \partial_x c(2, t) = \mu A^2. \quad (\text{D.10})$$

At  $x = L$ , we have an absorbing boundary  $c(L, t) = 0$  so that completed structures are removed from the system. Furthermore, the time evolution of the concentration of active particles is given by

$$\partial_t A = \alpha C e^{-\alpha t} - 2\mu A^2 - 2\nu A \int_2^L c(x, t) dx. \quad (\text{D.11})$$

The terms on the right-hand side account for activation of inactive particles, dimerization, and binding of active particles to polymers (polymerization).

Qualitatively, Eq. (D.9) describes a profile that emerges at  $x = 2$  from the boundary condition, Eq. (D.10), moves to the right with time dependent velocity  $2\nu A(t)$  due to the advection term, and broadens with a time-dependent diffusion coefficient  $\nu A(t)$ . The concentration of active particles  $A$  determines both the influx of dimers at  $x = 2$ , as well as the speed and diffusion of the wave profile.

Next, we derive an expression that solves Eq. (D.9), assuming that we know  $A(t)$ . We start by solving Eq. (D.9) at the left boundary  $c(2, t)$ , and then translate the resulting expression to obtain a solution for  $c(x, t)$ . To obtain  $c(2, t)$  in dependence of  $a(t)$  we can solve  $\frac{d}{dt}c(2, t) = \mu A^2 - \nu A c(2, t)$  (see Eq. (D.1c)) by 'variation of the constants' as

$$c(2, t) = \int_0^t \mu A(\tilde{t})^2 \exp \left[ - \int_{\tilde{t}}^t \nu A(t') dt' \right] d\tilde{t}. \quad (\text{D.12})$$

With help of this expression we find  $c(x, t)$ : Given  $c(2, t)$ , the advective part of Eq. (D.9),

$$\partial_t \tilde{c}(x) = -2\nu A \partial_x \tilde{c}(x). \quad (\text{D.13})$$

is solved by

$$c_{\text{advec}}(x, t) = c(2, \tau(x, t)). \quad (\text{D.14})$$

Here,  $\tau(x, t)$  denotes the time that a particle at position  $x$  and time  $t$  was at  $x = 2$ . In other words, a particle at time  $t$  and position  $x$  has entered the system at  $x = 2$  at time  $\tau(x, t)$ . This ansatz solves the PDE (Eq. (D.13)) if and only if  $\tau(x, t)$  satisfies

$$\tau(x, t) = \tilde{A}^{-1} \left( \tilde{A}(t) - \frac{x-2}{2\nu} \right) \quad (\text{D.15})$$

with  $\tilde{A}$  being an arbitrary integral of  $A$  such that  $\partial_t \tilde{A}(t) = A(t)$  and  $\tilde{A}^{-1}$  denoting its inverse. More easily, we find this form of  $\tau$  by requiring that the integral over the velocity from time  $\tau$  to  $t$  equals the travelled distance  $x - 2$ :

$$\int_{\tau}^t 2\nu A(t') dt' = x - 2. \quad (\text{D.16})$$

To include the diffusive contribution in Eq. (D.13), we use the diffusion kernel,

$$k(x, y, t) = \left( 4\pi \int_{\tau(y,t)}^t D(t') dt' \right)^{-1/2} \exp \left( \frac{-x^2}{4 \int_{\tau(y,t)}^t D(t') dt'} \right), \quad (\text{D.17})$$

with the time dependent diffusion constant  $D(t) = \nu A(t)$ . The kernel  $k(x, y, t)$  accounts for the mass that has been diffusively transported from  $y$  a distance of  $x$ . Because the mass has entered the system at  $x = 2$  at time  $\tau(y, t)$ , it diffused for the time  $t - \tau(y, t)$ . The complete expression for  $c(x, t)$  is then obtained as the convolution of  $c_{\text{advec}}(x, t)$  (Eq. (D.14)), that is obtained from Eq. (D.12) and Eq. (D.15), and the diffusion kernel  $k(x, y, t)$  (Eq. (D.17)):

$$c(x, t) = \int c_{\text{advec}}(s, t) k(x - s, s, t) ds = \int c(2, \tau(s, t)) k(x - s, s, t) ds. \quad (\text{D.18})$$

Interpreting the terms in the equations and the general form of the solution, we are able to understand the qualitative behavior of the system. If both the activation and the

dimerization rate are large, the system produces zero yield: both advection and diffusion are driven by the concentration of active monomers  $A$ . If activation is fast, the concentration of active monomers  $A$  will become large initially since activation is faster than the reaction dynamics. Consequently, provided  $\mu \sim \nu$ , dimerization dominates over binding because it depends quadratically on  $A$ , see Eq. (D.11). The reservoir of free particles then depletes quickly and cannot sustain the motion of the wave for long enough to reach the absorbing boundary, resulting in a very low yield. Only if either the activation rate is low enough or if  $\mu \ll \nu$ , the motion of the wave can be sustained until it reaches the absorbing boundary.

### D.3 Threshold values for the activation and dimerization rate

Based on the analysis from the previous section, we will now determine the threshold activation rate and threshold dimerization rate which mark the onset of non-zero yield. Yield production starts as soon as the density wave reaches the absorbing boundary at  $x = L$ . Therefore, finite yield is obtained if and only if the sum of the advectively travelled distance  $d_{\text{adv}}$  and the diffusively travelled distance  $d_{\text{diff}}$  exceeds the system size  $L - 2$ :

$$d_{\text{adv}} + d_{\text{diff}} \geq L - 2. \quad (\text{D.19})$$

The condition for the onset of non-zero yield is obtained by assuming equality in this relation. The advectively travelled distance is obtained from Eq. (D.16) by setting the borders of the integral over the velocity to  $\tau = 0$  and  $t = \infty$ :

$$d_{\text{adv}} = \int_0^{\infty} 2\nu A(t') dt'. \quad (\text{D.20})$$

The diffusively travelled distance is approximately given by the standard deviation of the Gaussian diffusion kernel, Eq. (D.17), again with  $\tau = 0$  and  $t = \infty$ ,

$$d_{\text{diff}} = \sqrt{2\nu \int_0^{\infty} A(t) dt}. \quad (\text{D.21})$$

Taken together, we obtain a condition for the onset of finite yield:

$$2\nu \int_0^{\infty} A(t) dt + \sqrt{2\nu \int_0^{\infty} A(t) dt} = L - 2. \quad (\text{D.22})$$

Substituting  $y = \sqrt{2\nu \int A}$  and requiring that  $y$  is positive, we can solve the quadratic equation and find that Eq. (D.22) is equivalent to

$$2\nu \int_0^{\infty} A(t) dt = y^2 = \frac{1}{4} \left( \sqrt{1 + 4(L - 2)} - 1 \right)^2 \approx L - \sqrt{L}, \quad (\text{D.23})$$

where the last approximation is valid for large  $L$ .

We determine the threshold values for the activation rate  $\alpha$  and the dimerization rate  $\mu$  by finding solutions of the dynamical equation for the active particles  $A(t)$ , Eq. (D.11), such that the condition, Eq. (D.23), is fulfilled. Thus, we start by deriving the dependence of  $\int_0^\infty A(t)dt$  on  $\alpha$  and  $\mu$ .

The concentration  $c(x, t)$  appears in Eq. (D.11) only in terms of an integral  $\int_2^L c(x, t) dx$ , counting the total number of polymers in the system. As long as yield is zero there is no outflux of polymers at the absorbing boundary  $x = L$  and the total number of polymers in the system only increases due to the influx at the left boundary  $x = 2$ . As long as yield is zero we can therefore equivalently consider the limit  $L \rightarrow \infty$ . We denote the total number of polymers in Eq. (D.11) by  $B(t) := \int c(x, t) dx$  for which the dynamics is determined from the boundary condition, Eq. (D.10):

$$\frac{d}{dt}B = \int_2^\infty \partial_t c(x, t) dx = \int_2^\infty -\partial_x J(x, t) dx = -\underbrace{J(\infty, t)}_{=0} + J(2, t) = \mu A(t)^2. \quad (\text{D.24})$$

Hence, as long as yield is zero, the total number of polymers increases with the rate of the dimerization events. The system then simplifies to a set of two coupled ordinary differential equations for  $A$  and  $B$ :

$$\frac{d}{dt}A = \alpha C e^{-\alpha t} - 2\mu A^2 - 2\nu A B, \quad (\text{D.25a})$$

$$\frac{d}{dt}B = \mu A^2. \quad (\text{D.25b})$$

The dynamics of  $A$  and  $B$  is equivalent to a two-state activator-inhibitor system, where  $A$  dimerizes into  $B$  at rate  $\mu$ , and  $B$  degrades (inhibits)  $A$  at rate  $2\nu$ . Note that Eq. (D.25a) describes the exact dynamics of the active monomers  $A$  and total number of polymers  $B$  in the deterministic system as long as yield is zero. The system has therefore been greatly reduced from originally  $SN$  coupled ODEs to now only 2 coupled ODEs.

For the further analysis it is useful to non-dimensionalize Eq. (D.25a) by measuring  $A$  and  $B$  in units of the initial concentration of inactive monomers  $C$  and time in units of  $(\nu C)^{-1}$ :

$$\frac{d}{dt}A = \omega e^{-\omega t} - 2\eta A^2 - 2A B, \quad (\text{D.26a})$$

$$\frac{d}{dt}B = \eta A^2, \quad (\text{D.26b})$$

with the remaining dimensionless parameters  $\omega = \frac{\alpha}{\nu C}$  and  $\eta = \frac{\mu}{\nu}$ . We are interested in the integral over  $A(t)$  as a function of  $\omega$  and  $\eta$ ,

$$\int_0^\infty A_{\omega, \eta}(t) dt := g(\omega, \eta), \quad (\text{D.27})$$

which relates to the totally travelled distance of the wave. Note that, in case of zero yield,  $2g(\omega, \eta)$  is the total advectively travelled distance of the wave (cf. Eq. (D.20)) and the square of the diffusively travelled distance (cf. Eq. (D.21)).

### Analysis of the dimerization scenario

The dimerization scenario is characterized by fast activation  $\alpha \gg C\nu$  and slow dimerization  $\mu \ll \nu$ . For the dimensionless parameters these assumptions translate to  $\eta \ll 1$  and  $\eta \ll \omega$ . Because for small  $\eta \ll 1$  nucleation is much slower than growth we neglect the dimerization term in Eq. (D.26a) against the growth term. Furthermore, because  $\eta \ll \omega$  activation happens on a fast time scale compared with nucleation and we may therefore integrate out the fast time scale assuming that all particles are activated instantaneously at the beginning. The system Eq. (D.26) then reduces to

$$\frac{d}{dt}A = -2A B, \quad (\text{D.28a})$$

$$\frac{d}{dt}B = \eta A^2, \quad (\text{D.28b})$$

with the initial condition  $A(0) = 1$  and  $B(0) = 0$ . We divide the first equation by the second one (formally applying the chain rule and the inverse function theorem) to obtain a single equation for the dynamics of  $A(B)$ :

$$\frac{dA}{dB} = -\frac{2B}{\eta A}, \quad (\text{D.29})$$

where  $A(B=0) = 1$ . This first order ODE can be solved by separation of variables and subsequent integration, yielding

$$A(B) = \sqrt{1 - \frac{2}{\eta}B^2}. \quad (\text{D.30})$$

Because the number of active monomers  $A(t)$  must vanish for  $t \rightarrow \infty$ , the final value of  $B$  is

$$B_\infty := B(t=\infty) = \sqrt{\frac{\eta}{2}}. \quad (\text{D.31})$$

Thereby, we calculate the function  $g(\eta)$  via variable substitution  $dt = \frac{dB}{\eta A^2}$ :

$$g(\eta) = \int_0^\infty A(t)dt = \int_0^{B_\infty} A(B) \frac{dB}{\eta A(B)^2} = \frac{1}{\eta} \int_0^{B_\infty} \frac{dB}{\sqrt{1 - \frac{2}{\eta}B^2}} = \frac{\pi}{2\sqrt{2}} \eta^{-\frac{1}{2}}. \quad (\text{D.32})$$

So, the dependence of the travelled distance of the wave on  $\eta$  obeys a power law with exponent  $-\frac{1}{2}$ , confirming the previous result<sup>9</sup>. For the coefficient we find  $\frac{\pi}{2\sqrt{2}} \approx 1.1107$ .

Additionally, we can determine the time dependent solutions  $A(t)$  and  $B(t)$ . Using the solution for  $A(B)$  from Eq. (D.30) in Eq. (D.28b) we obtain  $B(t)$  as

$$B(t) = \sqrt{\frac{\eta}{2}} \tanh(\sqrt{2\eta t}). \quad (\text{D.33})$$

We use this expression for  $B(t)$  in Eq. (D.28a) to obtain  $A(t)$ . The resulting ODEs can again be solved by separation of variables as

$$A(t) = \frac{1}{\cosh(\sqrt{2\eta t})}. \quad (\text{D.34})$$

### Analysis of the activation scenario

In the activation scenario,  $\alpha \ll C\nu$ , such that  $\omega \ll 1$  and  $\omega \ll \eta$ . As we know already that decreasing  $\omega$  will slow down nucleation relative to growth we can again neglect the dimerization term in Eq. (D.26a). In contrast to the dimerization scenario, however, we have to keep the activation term. Transforming time via  $\tau := 1 - e^{-\omega t}$  such that  $\tau \in [0, 1]$  and writing  $a(\tau) = a(1 - e^{-\omega t}) := A(t)$  and  $b(\tau) = b(1 - e^{-\omega t}) := B(t)$  the system in Eq. (D.26) becomes:

$$\frac{d}{d\tau} a = 1 - \frac{2}{\omega(1-\tau)} ab, \quad (\text{D.35a})$$

$$\frac{d}{d\tau} b = \frac{\eta}{\omega(1-\tau)} a^2, \quad (\text{D.35b})$$

with the initial condition  $a(0) = b(0) = 0$ . The function  $g(\omega, \eta)$  transforms as

$$g(\omega, \eta) = \int_0^\infty A(t) dt = \frac{1}{\omega} \int_0^1 \frac{a(\tau)}{1-\tau} d\tau. \quad (\text{D.36})$$

In the following we derive the asymptotic solution for  $a(\tau)$  in the limit of small  $\omega$  in order to evaluate the integral in Eq. (D.36). In the limit  $\tau \rightarrow 1$  ( $\Leftrightarrow t \rightarrow \infty$ ) both  $a(\tau)$  and  $\frac{d}{d\tau} a(\tau)$  will become small whereas  $b(\tau)$  increases monotonically. The reaction term in Eq. (D.35a) is furthermore weighted by a factor  $\frac{1}{\omega}$  which will become large if  $\omega \ll 1$ . We therefore postulate that for sufficiently large  $\tau$  the derivative  $\frac{d}{d\tau} a(\tau)$  is much smaller than the two terms on the right-hand side of Eq. (D.35a) and hence negligible. This assumption has to be justified *a posteriori* with the obtained solution. Neglecting the derivative term  $\frac{d}{d\tau} a$  in (D.35a) reduces the equation to an algebraic equation and we find

$$a = \frac{\omega(1-\tau)}{2b}. \quad (\text{D.37})$$

Using this result in Eq. (D.35b) we can solve for  $b$  by separation of variables and subsequent integration:

$$b(\tau) = (\omega\eta)^{\frac{1}{3}} \cdot \left( \frac{3}{4}\tau - \frac{3}{8}\tau^2 \right)^{\frac{1}{3}}. \quad (\text{D.38})$$

From Eq. (D.37) we immediately obtain  $a(\tau)$ :

$$a(\tau) = \frac{\omega^{\frac{2}{3}}}{\eta^{\frac{1}{3}}} \cdot \frac{1 - \tau}{(6\tau - 3\tau^2)^{\frac{1}{3}}} := \frac{\omega^{\frac{2}{3}}}{\eta^{\frac{1}{3}}} h(\tau), \quad (\text{D.39})$$

where by  $h(\tau)$  we denote the part of the solution that depends only on  $\tau$ . Hence, we find that  $a$  and hence also  $\frac{d}{d\tau}a$  scale like  $\sim \omega^{\frac{2}{3}}$ , and will thus become small if  $\omega \ll 1$  and  $\tau$  is large enough. Therefore the solution is consistent<sup>1</sup> and justifies the approximation in which we neglected the derivative term in the limit of small  $\omega$  and sufficiently large  $\tau$ .

In the limit  $\tau \rightarrow 0$ , however, the expression for  $a(\tau)$  in Eq. (D.39) diverges and consistency is violated. Hence, the obtained solution is valid only for sufficiently large  $\tau$ .

We fix some small  $\epsilon > 0$  such that the approximation can be assumed to be sufficiently good if  $\frac{d}{d\tau}a < \epsilon$ . Furthermore, we define  $\tau_\epsilon$  such that  $\frac{d}{d\tau}a < \epsilon$  for all  $\tau > \tau_\epsilon$ . Using Eq. (D.39) we can write this as  $\frac{d}{d\tau}h < \epsilon\eta^{\frac{1}{3}}/\omega^{\frac{2}{3}}$  for all  $\tau > \tau_\epsilon$ , where the left-hand side,  $\frac{d}{d\tau}h$ , depends only on  $\tau$ . Hence, by decreasing  $\omega$  we can make  $\tau_\epsilon$  arbitrarily small:  $\lim_{\omega \rightarrow 0} \tau_\epsilon = 0$ . In order to calculate  $g(\omega, \eta)$  the integral in Eq. (D.36) can be separated in a domain where the approximation  $a(\tau)$  is accurate and a domain where the correct solution  $\tilde{a}(\tau)$  deviates

---

<sup>1</sup>Consistency of the solution with the approximation is a sufficient criterion for the validity of the approximation: We can solve the system for  $A$  and  $B$  in Eq. (D.35) iteratively by defining

$$\begin{aligned} \frac{d}{d\tau}a_{i-1} &= 1 - \frac{2}{\omega(1-\tau)}a_i b_i, \\ \frac{d}{d\tau}b_i &= \frac{\eta}{\omega(1-\tau)}a_i^2. \end{aligned}$$

Assuming that for  $i \rightarrow \infty$ ,  $a_i$  and  $b_i$  converge to the correct solutions  $a(\tau)$  and  $b(\tau)$  when starting with  $a_0 = 0$ , we obtain  $a_1$  and  $b_1$  as given by Eq. (D.39) and Eq. (D.38) and can iteratively refine the approximation. The next iteration step then reads:  $\frac{d}{d\tau}a_1 = 1 - \frac{2}{\omega(1-\tau)}a_2 b_2$ . As  $a_1 \sim \omega^{\frac{2}{3}}$  we know that the left-hand side will be small and  $a_1$  and  $b_1$  solve the system if the left-hand side equals 0. Writing  $a_2 = a_1 + \tilde{a}_2$  and  $b_2 = b_1 + \tilde{b}_2$  this gives:

$$\frac{d}{d\tau}a_1 = 1 - \frac{2}{\omega(1-\tau)}(a_1 + \tilde{a}_2)(b_1 + \tilde{b}_2) \approx \frac{2}{\omega(1-\tau)}(a_1 \tilde{b}_2 + b_1 \tilde{a}_2). \quad (\text{D.40})$$

From dimensional analysis it follows that the correction terms  $\tilde{a}_2$  and  $\tilde{b}_2$  must scale like  $\tilde{a}_2 \sim \omega^{\frac{4}{3}}$  and  $\tilde{b}_2 \sim \omega$  and are hence much smaller than the first order approximations  $a_1$  and  $b_1$ . Higher order corrections will give even smaller contributions showing that if  $\frac{d}{d\tau}a_1 \ll 1$ ,  $a_1$  is indeed a very good approximation.

strongly from  $a(\tau)$ :

$$g(\omega, \eta) = \frac{1}{\omega} \int_0^{\tau_\epsilon} \frac{\tilde{a}(\tau)}{1-\tau} d\tau + \frac{1}{\omega} \int_{\tau_\epsilon}^1 \frac{a(\tau)}{1-\tau} d\tau. \quad (\text{D.41})$$

We see from Eq. (D.35a) that  $\frac{d}{d\tau}\tilde{a} = 1$  describes an upper bound to  $\tilde{a}$  showing that  $\tilde{a}(\tau) \leq \tau$ . Therefore we can bound the contribution of the first integral as  $\int_0^{\tau_\epsilon} \frac{\tilde{a}(\tau)}{1-\tau} d\tau \leq \int_0^{\tau_\epsilon} \frac{\tau}{1-\tau_\epsilon} d\tau = \frac{1}{2} \frac{\tau_\epsilon^2}{1-\tau_\epsilon}$ . Because this upper bound for the integral goes to 0 if  $\omega$  and hence  $\tau_\epsilon$  become small the first integral will become negligible against the second one. Asymptotically, we therefore only need to consider the second integral with the solution for  $a(\tau)$  as given by Eq. (D.39):

$$\begin{aligned} g(\omega, \eta) &= (\omega\eta)^{-\frac{1}{3}} \int_0^1 (6t - 3t^2)^{-\frac{1}{3}} dt = (\omega\eta)^{-\frac{1}{3}} \int_0^3 \frac{dz}{6z^{\frac{1}{3}} \sqrt{1 - \frac{z}{3}}} = \\ &= \frac{3^{\frac{2}{3}} \sqrt{\pi} \Gamma(\frac{2}{3})}{6 \Gamma(\frac{7}{6})} (\omega\eta)^{-\frac{1}{3}} \approx 0.8969 \cdot (\omega\eta)^{-\frac{1}{3}}, \end{aligned} \quad (\text{D.42})$$

where we used the substitution  $t = 1 - \sqrt{1 - z/3}$  and  $\Gamma(x)$  is the (Euler) Gamma function. So, in the limit of small  $\omega$ ,  $g$  scales with  $\omega$  and  $\eta$  with identical exponent  $-\frac{1}{3}$ . This contrasts the dimerization scenario where  $g$  as well as  $A$  and  $B$  depend only on  $\eta$  and are independent of  $\omega$  (cf. Eq. (D.32), (D.33) and (D.34)).

## Numerical analysis and the threshold values for the rate constants

In order to confirm the results of the last two paragraphs and to see how  $g(\omega, \eta)$  behaves in the intermediate regime where  $\omega$  and  $\eta$  are of the same order of magnitude we also investigate the function  $g(\omega, \eta)$  numerically. For that purpose we numerically integrate the ODE-system for  $A(t)$  and  $B(t)$  in Eq. (D.26) for different values of  $\omega$  and  $\eta$  with a semi-implicit method. Subsequently, we integrate the solution  $A(t)$  using an adaptive recursive Simpson's rule. Plotting  $g$  in dependence of  $\omega$  for fixed  $\eta$  on a double-logarithmic scale reveals a rather simple bipartite form of  $g$ , see Fig. SD.1a:

$$g(\omega, \eta) = \begin{cases} g_1(\eta) \omega^{-\frac{1}{3}} & \omega \ll 1 \\ g_2(\eta) & \omega \gg 1. \end{cases} \quad (\text{D.43})$$

The transition between these two regimes is rather sharp so that  $g$  is best described in a piecewise fashion

$$g(\omega, \eta) = \max(g_1(\eta) \omega^{-\frac{1}{3}}, g_2(\eta)). \quad (\text{D.44})$$

Next, we plot the coefficients  $g_1(\eta)$  and  $g_2(\eta)$  against  $\eta$ . Here we find that  $g_1(\eta) = a\eta^{-\frac{1}{3}}$  with  $a = \text{const} \approx 0.90$  and  $g_2(\eta)$  is again bipartite with a sharp kink in between (Fig. SD.1b):

$$g_2(\eta) = \min(b\eta^{-\frac{1}{2}}, b'\eta^{-0.85}), \quad (\text{D.45})$$

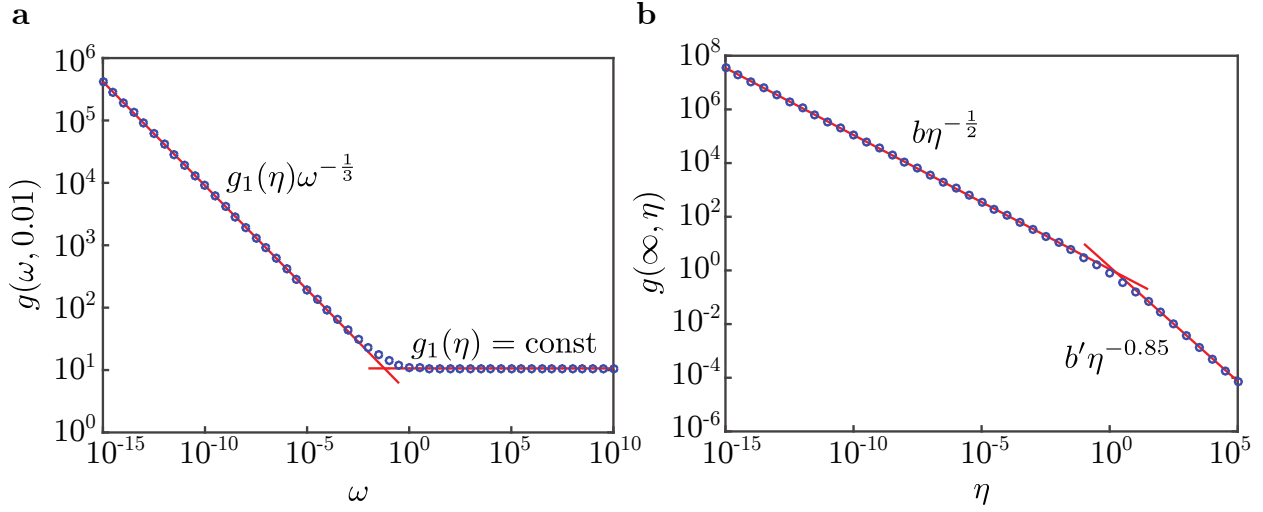


Figure D.1: **Fit of  $g(\omega, \eta)$  on log-log scale.** The function  $g(\omega, \eta) = \int_0^\infty A_{\omega, \eta}(t) dt$  describes (half) the travelled distance of the profile of the polymer size distribution in dependence of  $\omega = \frac{\alpha}{\nu C}$  and  $\eta = \frac{\mu}{\nu}$ . Marker points show solutions for  $g(\omega, \eta)$  as obtained numerically from integration of Eq.(D.26). Red lines are linear fits on log-log scale. In **(a)** we plot  $g(\omega, \eta)$  for fixed  $\eta$  (here exemplarily for  $\eta = 0.01$ ) over 25 orders of magnitude in  $\omega$  and find a markedly bipartite behavior: For small  $\omega$  the dependence on  $\omega$  is perfectly matched by a power law with exponent  $-\frac{1}{3}$  and  $\eta$ -dependent coefficient  $g_1(\eta)$ , whereas for large  $\omega$  it is a constant  $g_2(\eta)$ . **(b)** Plotting  $g_2(\eta) = g(\omega = \infty, \eta)$  in dependence of  $\eta$  reveals again strictly bipartite behavior. Here, however, only the brach for small  $\eta$  is realistically relevant. With the coefficient  $g_1(\eta)$  that can be determined in a similar way this leads to the final form of  $g(\omega, \eta)$  as given by Eq. (D.46).

where  $b \approx 1.11$  and  $b' \approx 1.37$ . The transition between both regimes is at  $\eta \approx 1.82$ . The second regime is not relevant for self-assembly since it refers to both large  $\omega$  and large  $\eta$ , hence the travelled distance  $2g$  is too small to give finite yield in this regime. Therefore, we discard the second regime and obtain as final result

$$g(\omega, \eta) = \max(a(\eta\omega)^{-\frac{1}{3}}, b\eta^{-\frac{1}{2}}), \quad (\text{D.46})$$

with  $a \approx 0.90$  and  $b \approx 1.11$ . This confirms perfectly the exponents as well as the coefficients found in the last two paragraphs. It is, however, surprising that there is such a sharp transition between both regimes, which allows to define  $g(\omega, \eta)$  in a piecewise fashion. This behavior must be the result of a series of lower order terms in  $g(\omega, \eta)$  which are unimportant in the limits  $\omega \ll \eta$  and  $\eta \ll \omega$  but cause the sharp transition when  $\omega$  and  $\eta$  are of the same order of magnitude.

Finally, we return to our original task of finding the threshold values of the activation and dimerization rate for the onset of yield. Using our result for  $g(\omega, \eta)$  in Eq. (D.23) we

find as necessary and sufficient condition to obtain finite yield in the deterministic system:

$$2 \max(a(\eta\omega)^{-\frac{1}{3}}, b\eta^{-\frac{1}{2}}) \geq L - \sqrt{L}. \quad (\text{D.47})$$

Alternatively, we can state this result as two separate conditions out of which at least one must be fulfilled to obtain finite yield:

$$2a(\eta\omega)^{-\frac{1}{3}} \geq L - \sqrt{L} \quad \Rightarrow \quad \alpha < \alpha_{\text{th}} := P_\alpha \frac{\nu}{\mu} \frac{\nu C}{(L - \sqrt{L})^3} \quad (\text{D.48})$$

$$\text{or} \quad 2b\eta^{-\frac{1}{2}} \geq L - \sqrt{L} \quad \Rightarrow \quad \mu < \mu_{\text{th}} := P_\mu \frac{\nu}{(L - \sqrt{L})^2} \quad (\text{D.49})$$

where  $P_\alpha = 8a^3 \approx 5.77$  and  $P_\mu = 4b^2 \approx 4.93$ . This verifies Eq. (1) in the main text.

## D.4 Impact of the implementation of sub-nucleation reactions

In the main text we focused our discussion on irreversible binding  $L_{\text{nuc}} = 2$ . In this section we investigate the effect of different implementations of the sub-nucleation reactions.

In general, perfect yield is trivially achieved if the complete ring is the only stable structure. However, yield can be maximal already for smaller nucleation sizes  $L_{\text{nuc}}$  depending on the explicit decay rate  $\delta$ . In the deterministic limit without the dimerization and activation mechanisms ( $\mu = \nu$ ,  $\alpha \rightarrow \infty$ ) a rapid transition from zero yield to perfect yield occurs in dependence of the critical nucleation size (see Fig. SD.2). The threshold value in this case is approximately half the ring size and is weakly affected by the decay rate  $\delta$ . In order to obtain finite yield for small nucleation sizes, an extremely high decay rate would be necessary. Hence, maximizing the yield solely by increasing the nucleation size is not very feasible.

In our model, the subcritical reaction rates  $\mu_i$  may take different values. Here, we want to restrict our discussion to two scenarios. First, all rates have an identical value  $\mu_i = \mu$  and second, the rates increase linearly up to the super-nucleation reaction rate:  $\mu_i = \mu + (\nu - \mu) \frac{i-1}{L_{\text{nuc}}-1}$ .

In the deterministic limit, both implementations show the same qualitative behavior as the dimerization mechanism with  $L_{\text{nuc}} = 2$  in the main text (see Fig. SD.3). The only relevant aspect for the final yield is the extend to which nucleation is slowed down in total. In the constant scenario all reaction steps contribute equally. As a results there is a strong dependence on the number of such reaction steps, i.e. on the critical nucleation size. If however, the reaction rates increase linearly with the size of the polymers, the dimerization rate dominates. Only in the case  $\mu \ll \nu$  finite yield is observed at all. In this limit the dimerization rate is much smaller than the subsequent growth rates. The explicit form of

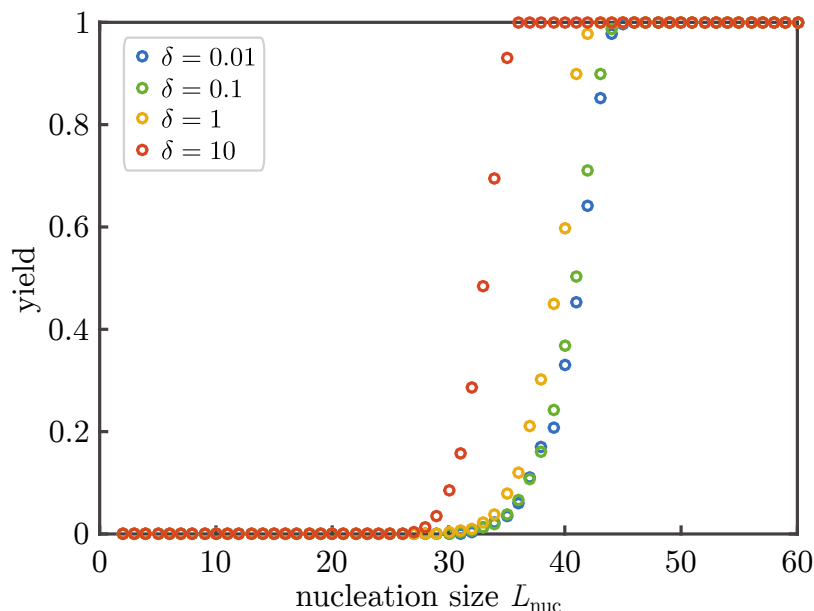


Figure D.2: **Yield maximization due to increased nucleation size.** Without activation and dimerization mechanism ( $\alpha \rightarrow \infty, \mu = \nu$ ) the yield can still be optimized by increasing the critical nucleation size  $L_{nuc}$ . However, a significant improvement is only achieved for critical sizes larger than half the ring size. Above, a rapid transition to perfect yield takes place. Below no effect is observed at all. Increasing  $\delta$  shifts the onset of yield to slightly smaller critical nucleation sizes. Other parameters:  $L = 60, N = 10000$ .

the different  $\mu_i$  is not of major importance for the yield. The total slowdown of nucleation is the central feature. Structure decay does not play any role for intermediate nucleation sizes.

The last question we want to address is how the combination of activation and dimerization mechanism and the corresponding non-monotonic behavior is affected by the nucleation size. Again, we compare constant sub-nucleation growth with a linearly increasing growth rate (see Fig. SD.4). In the deterministic regime both implementations behave qualitatively similar as the dimerization mechanism discussed in the main text. However, in both cases the stochastic yield catastrophe is less pronounced. For the constant growth rates a saturation of the maximal yield is observed for sufficiently low  $\mu$ . If the profile is linear this effect is weaker as compared to the constant case and a dependency on the explicit value of  $\mu$  is still observed. The saturation value is not reached for these reactions rates.

Taking all our results for the sub-nucleation behavior together we draw the following conclusions: First, structure decay by itself it not very efficient in order to maximize yield. Second, the explicit choice of the sub-nucleation rates is of minor importance for

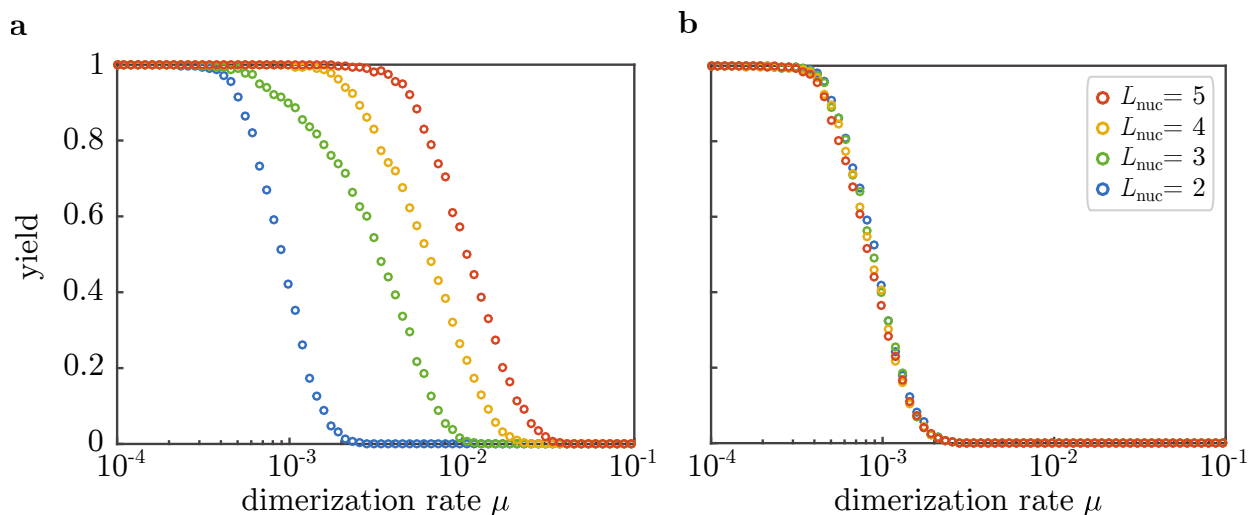


Figure D.3: **Yield for the dimerization mechanism ( $\alpha \rightarrow \infty$ ) with different nucleation sizes (colors).** (a) If all sub-nucleation growth rates are identical ( $\mu_i = \mu$ ) increasing the nucleation size increases the threshold value  $\mu_{th}$ . The slow down of nucleation due to the individual sub-nucleation steps in total determines the yield. (b) If the sub-nucleation growth rates increase linear ( $\mu_i = \mu + (\nu - \mu) \frac{i-1}{L_{nuc}-1}$ ) no dependence on the nucleation size is observed. The dimerization rate  $\mu_1 = \mu$  (which is the most limiting step) dominates entirely. Other parameters:  $L = 60$ ,  $N = 10000$ ,  $\delta = 1$ .

the qualitative behavior. The system behaves similarly to the case  $L_{nuc} = 2$ . Third, larger nucleation sizes mitigate the stochastic yield catastrophe in general.

## D.5 Time evolution of the yield in the activation and dimerization scenario

In the main text we focus on the final yield, which represents the maximal yield that can be obtained in the assembly reaction for  $t \rightarrow \infty$ . Here, we briefly discuss the temporal evolution of the yield in the two scenarios. Figure SD.5 shows the yield as a function of time for the dimerization scenario (blue) and the activation scenario (red) for the corresponding parameters indicated in the plot. Drawn lines show the evolution of the yield in the stochastic simulation whereas dashed lines represent its deterministic evolution obtained by integrating the corresponding mean-field rate equations (only shown for the activation scenario).

In both scenarios, yield production sets in after a short lag time<sup>16</sup>. The emergence of a lag time can be understood in terms of the interpretation of the assembly process as the progression of a travelling wave (see Sec. D.2). The travelling wave thereby describes the

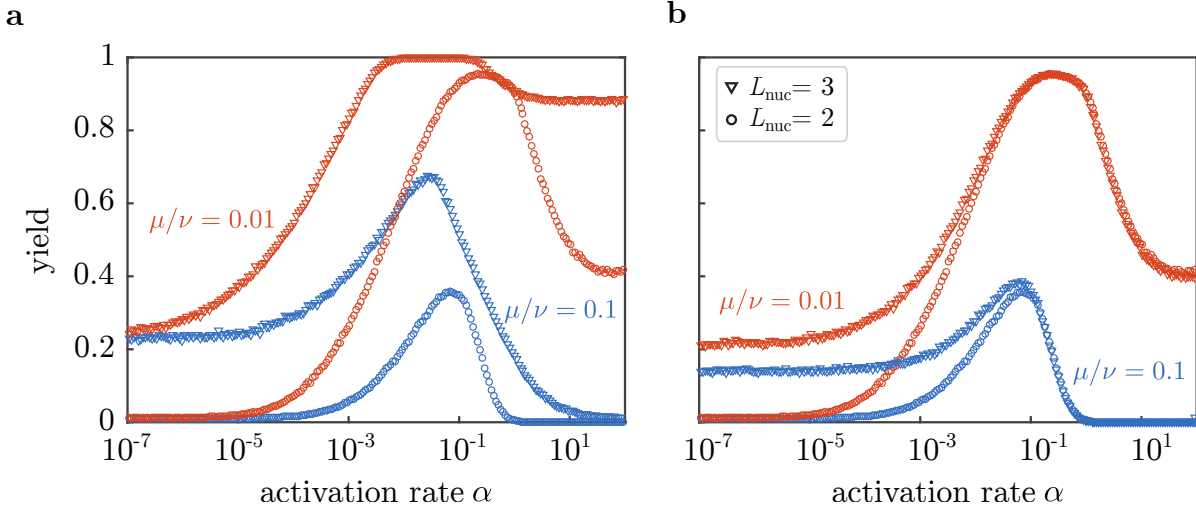


Figure D.4: **Combined mechanisms for different nucleation sizes (symbols) and dimerization rates (color).** (a) If the sub-nucleation growth rates are identical ( $\mu_i = \mu$ ) The stochastic yield catastrophe is weakened but still has a drastic impact. The qualitative behavior remains unchanged. (b) For a linearly increasing sub-nucleation growth rate ( $\mu_i = \mu + (\nu - \mu) \frac{i-1}{L_{nuc}-1}$ ) in the deterministic regime no changes are observed at all. The effect of the stochastic yield catastrophe is less pronounced. This improvement is mainly caused by structure decay which mitigates stochastic fluctuations. However, a slight dependency of the saturation value on the rate  $\mu$  is observed. Other parameters:  $L = 60$ ,  $S = L$ ,  $N = 100$ ,  $\delta = 0.1$ .

polymer size distribution and the time that is needed for the wave to reach the absorbing boundary equals the lag time for yield production observed in Fig. SD.5. After the lag time, the yield increases very abruptly in the dimerization scenario and a bit more continually in the activation scenario. Since monomers are provided gradually in the activation scenario, the emerging wave is flatter and extends over a larger range (in polymer size space) as compared to the dimerization scenario. Consequently, yield production is more gradual in the activation scenario than in the dimerization scenario. For the same reason, the dimerization scenario is generally “faster” or more time efficient than the activation scenario. For a detailed analysis of the time efficiency of these and other self-assembly scenarios we refer the reader to [10].

In all depicted situations, the yield increases monotonically with time. This is, of course, generally true since the completed ring structures define an absorbing state in our system. The final yield, which is indicated in the right bar, therefore represents the upper limit for the yield that can be achieved in the assembly reaction. Figure SD.5 shows that the temporal yield curves initially are rather steep and quickly reach a value that lies within 10% of the final yield (“quickly” thereby refers to the respective time scale), before the

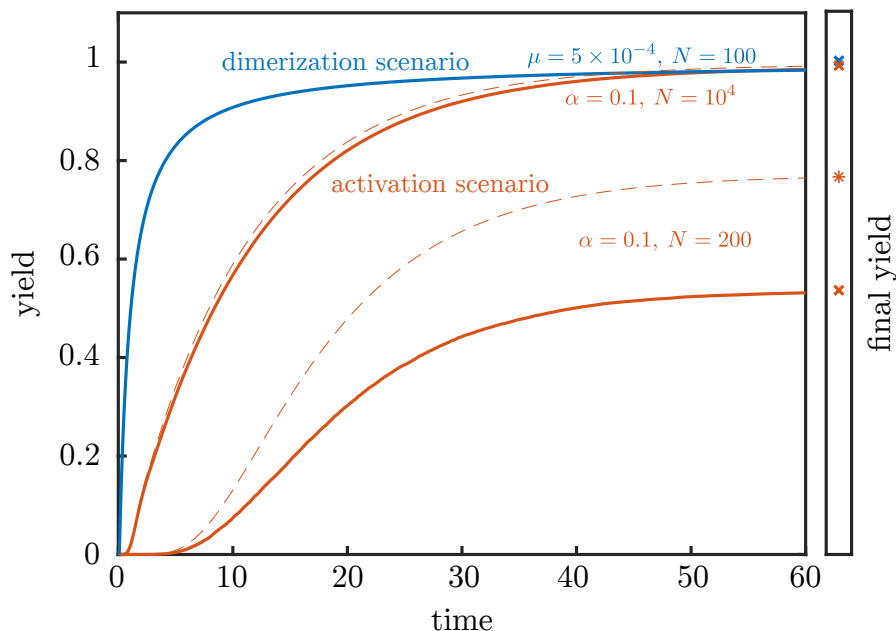


Figure D.5: **Time evolution of the yield in the activation and dimerization scenario.** The time dependence of the yield is depicted for a dimerization scenario (blue) with  $\mu = 5 \times 10^{-4}$  and  $N = 100$  and for two activation scenarios (red) with  $\alpha = 0.1$  and  $N = 10^2$  and  $N = 10^4$ , respectively, for target structures of size  $L = 20$ . Drawn lines show the time evolution of the stochastic systems while dashed lines describe the time evolution in the corresponding deterministic systems (where the final yield may be higher in the activation scenario). In all cases the yield increases monotonically with time. The final yield, that is indicated in right bar, represents the upper limit of the yield at any time. Yield production in the activation scenario is generally more gradual than in the dimerization scenario. Therefore, the dimerization scenario is, in general, more time efficient than the activation scenario.

curves flatten and increase more slowly. This underlines that the final yield is a meaningful observable that not only describes the upper limit for the yield but also approximates the typical yield of the assembly reaction under appropriate time constraints that are not too restrictive (on the time scale set by the respective lag time).

## D.6 Standard deviation of the yield

In the main text, the analysis focuses on the average yield. A priori it is, however, not apparent that this average quantity is informative, in particular due to the strong effect of stochasticity in the system. Here, we thus take a step forward to complement this picture by additionally considering a simple measure for the fluctuations of the yield, its standard

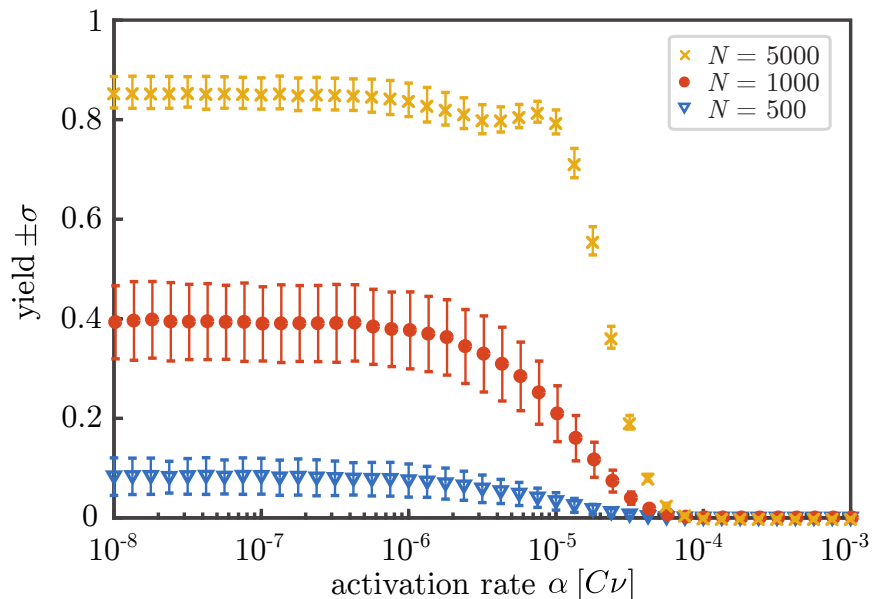


Figure D.6: **Average yield and its sample standard deviation.** For average yield close to 0 or close to 1, the standard deviation has to be small due to the boundedness of the yield to the interval  $[0, 1]$ . For intermediate values, the standard deviation is highest. Its value is, however, still considerably smaller than the average yield. The parameters are  $L = 60$ ,  $S = L$ ,  $\mu = \nu = 1$  and different particle numbers  $N$  (colors/symbols). To obtain the average yield, the yield has been averaged over 1000 simulations. The standard deviation corresponds to the unbiased sample standard deviation.

deviation. Fig. SD.6 is an extension of Fig. 3.a in the main text, showing the dependence of the average yield and its sample standard deviation on the activation rate. Since yield is always positive, the standard deviation of the yield has to be small if the average yield is close to 0 ( $N = 500$  in Fig. SD.6). The same holds true for average yield close to 1 as the yield is bounded by 1 from above ( $N = 5000$  in Fig. SD.6). For intermediate values of the average yield, the standard deviation is highest but still small compared to the average yield ( $N = 1000$  in Fig. SD.6). The average yield is, thus, meaningful. Naturally the ratio of the standard deviation compared to the average yield also depends on the number of particles per species  $N$  and on the number of species  $S$ . Generally speaking, for higher  $N$  and  $S$ , this ratio decreases (see Fig. SD.7 for the dependency on  $S$ ).

## D.7 Influence of the heterogeneity of the target structure for fixed number of particles per species

Fig. 3(d) in the main text shows how the maximal yield  $y_{\max}$  depends on the number of species  $S$  if the ring size  $L$  and the number of possible ring structures  $NS/L$  is fixed. This comparison for fixed  $NS$  is motivated by the question which role the heterogeneity of a structure plays for assembly efficiency if a certain number of structures should be realized. Fig. 3(d) illustrates that a higher number of species  $S$  (more heterogeneous structures) leads to a lower maximally possible yield, suggesting that it is beneficial to build structures with as few different species as possible. However, this situation does not correspond to the deterministically equivalent case<sup>2</sup> of fixed number of particles per species  $N$ . Instead, for higher number of species  $S$ , the number of particles per species  $N \propto 1/S$  decreases. How does the heterogeneity of the structures  $S$  alter the maximally possible yield if  $L$  and  $N$  (instead of  $L$  and  $NS$ ) are fixed? Fig. SD.7 shows how the maximal yield  $y_{\max}$  and its standard deviation (obtained as average yield and sample standard deviation for  $\alpha = 10^{-8}$  when the yield has well saturated and the dynamics (except for the timescale) get independent of the exact value of the rate-limiting activation rate) depend on the number of species  $S$ . For homogeneous structures  $S = 1$  yield is always perfect since in this case there can be no fluctuations between species. As a result, the average yield is 1 and the standard deviation is 0. For increasing  $S$ , the average yield decreases until it levels off for  $S \gg 1$ . This behavior indicates that indeed the decreasing number of particles per species  $N$  for larger  $S$  is essential for the decrease of the maximal yield with  $S$  in Fig. 3(d). As mentioned above, the standard deviation is largest for small  $S > 1$  and decreases with  $S$ .

---

<sup>2</sup>Note, though, that in the deterministic case the maximally possible yield is always 1, namely for  $\alpha \rightarrow 0$ .

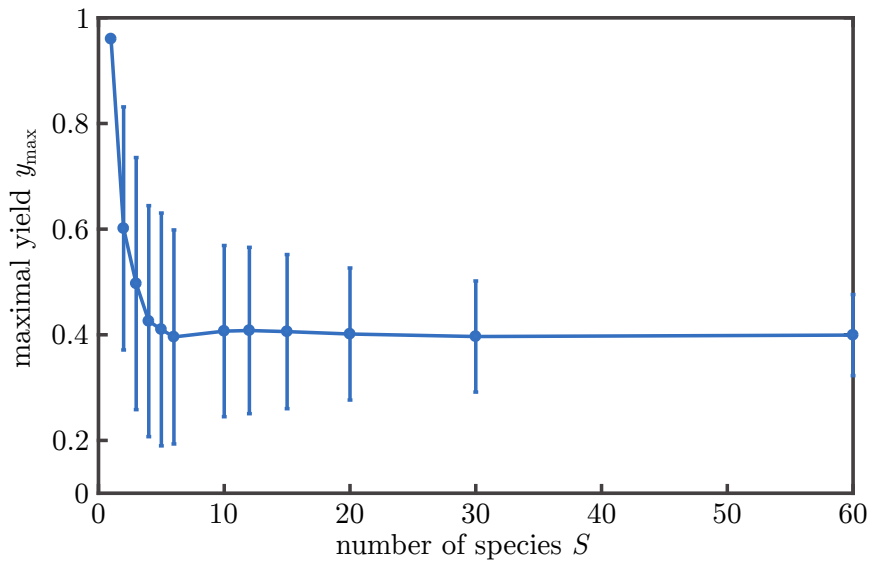


Figure D.7: **Influence of the heterogeneity of the target structure on the yield for fixed number of particles per species  $N$ .** The maximal yield and its standard deviation (obtained as average yield and sample standard deviation for  $\alpha = 10^{-8}$ ) are plotted against the number of species  $S$  making up the structure of size  $L = 60$ . The number of particles per species  $N = 1000$  is fixed. Yield drops from a perfect value of 1 for  $S = 1$  to a smaller value and levels off for  $S \gg 1$ . The standard deviation is largest for small  $S$  (except for  $S = 1$  where the yield is always perfect) and decreases with increasing number of species.

## D.8 Dependence of the maximal yield $y_{\max}$ in the activation scenario on $N$ and $L$

Fig. 3(c) in the main text characterizes the dependence of the maximal yield  $y_{\max}$  in the activation scenario as a “phase diagram” distinguishing different regimes of  $y_{\max}$  in dependence of the particle number  $N$  and target size  $L$ . Supplementing this figure in the main text, Fig. SD.8 shows the maximum yield that is obtained in the activation scenario in the limit  $\alpha \rightarrow 0$  for fixed  $L$  in dependence of  $N$  (Fig. SD.8a) as well as for fixed  $N$  in dependence of  $L$  (Fig. SD.8b). For larger particle number  $N$ , the maximal yield exhibits a transition from 0 to 1 over roughly three orders of magnitude. Increasing  $L$  shifts the transition to larger  $N$ . The threshold particle number where the transition starts is characterised by  $N_{\text{th}}^{>0}(L)$  (see main text). Approximately, for  $L \leq 600$ , we find  $N_{\text{th}}^{>0}(L) \sim L^{2.8}$  (cf. main text, Fig. 3(c)).

Similarly, decreasing the target size  $L$  for fixed  $N$ , the maximal yield exhibits a transition from 0 to 1 over roughly one order of magnitude in  $L$ . The corresponding threshold value  $L_{\text{th}}^{>0}$  as a function of  $N$  is obtained as the inverse function of  $N_{\text{th}}^{>0}(L)$ . Hence, at least for  $N \leq 10^5$ , approximately it holds  $L_{\text{th}}^{>0}(N) \sim N^{0.36}$ .

Since  $y_{\max}$  is largely independent of the number of species  $S$  for fixed  $N$  and  $L$  (see Sec. D.7), the maximal yield in the activation scenario (for  $L_{\text{nuc}} = 2$ ) can be fully characterized as a function  $y_{\max}(N, L)$  of  $N$  and  $L$ . Hence,  $y_{\max}$  can roughly be expressed in terms of the threshold particle number  $N_{\text{th}}^{>0}(L)$  as

$$y_{\max}(N, L) \begin{cases} \approx 1 & \text{if } N > 10^3 N_{\text{th}}^{>0}(L) \\ < 1 & \text{if } N_{\text{th}}^{>0}(L) < N < 10^3 N_{\text{th}}^{>0}(L) \\ = 0 & \text{if } N < N_{\text{th}}^{>0}(L) \end{cases} \quad (\text{D.50})$$

As can be seen from Fig. 3(c) in the main text, the transition line between zero and nonzero yield slightly flattens with increasing  $L$ . Hence, the power law  $N_{\text{th}}^{>0}(L) \sim L^{2.8}$  (and similarly for  $L_{\text{th}}^{>0}$ ) only holds approximately and for a restricted range in  $L$  and  $N$ . The asymptotic behavior of  $N_{\text{th}}^{>0}$  in the limit  $L \rightarrow \infty$  remains elusive.

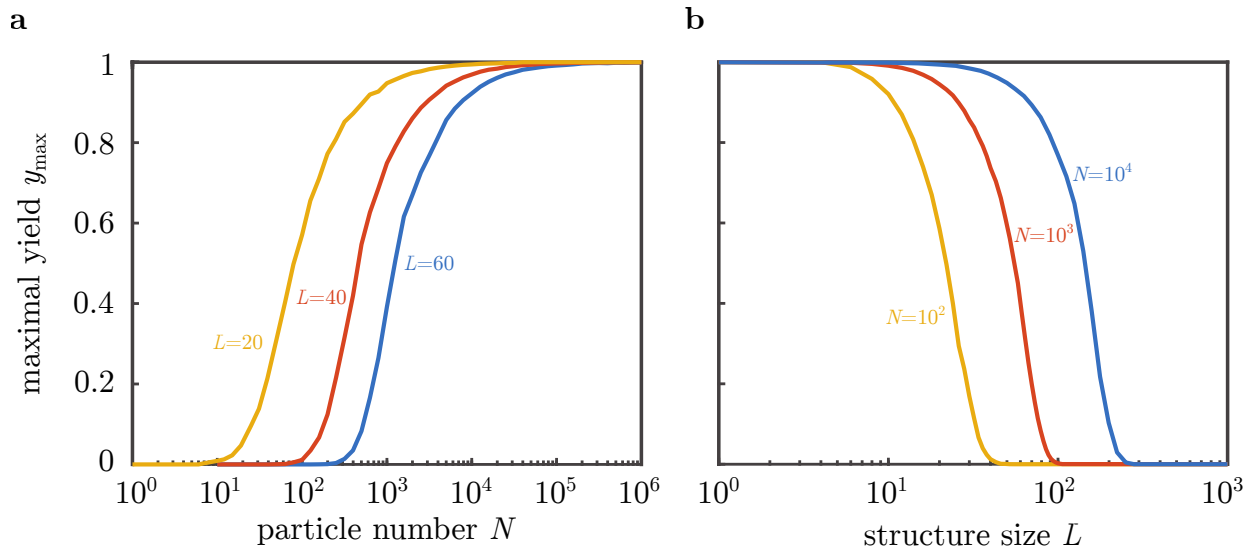


Figure D.8: **Dependence of the maximal yield  $y_{\max}$  in the activation scenario on  $N$  and  $L$ .** For each data point,  $y_{\max}$  was determined as the average yield of 100 independent stochastic simulations of the activation scenario with  $\alpha = 10^{-12}$ . (a) Variation of the particle number  $N$  for different target sizes  $L$ . The maximal yield increases from 0 to 1 over roughly three order of magnitude in  $N$ . The onset of the transition depends on  $L$ . (b) Variation of the target size  $L$  for different particle numbers  $N$ . Increasing the target size  $L$  with  $N$  being fixed causes the maximal yield to drop to 0. The transition from 1 to 0 spans roughly one order of magnitude in  $L$  and its position is determined by  $N$ .

# Bibliography

- [1] F. Schwabl, *Statistische Mechanik*, vol. 3. Springer Verlag, 2006.
- [2] R. P. Feynman, R. B. Leighton, and M. Sands, *The Feynman lectures on physics, Vol. I: The new millennium edition: mainly mechanics, radiation, and heat*, vol. 1. Basic books, 2011.
- [3] T. Chou, K. Mallick, and R. K. P. Zia, “Non-equilibrium statistical mechanics: from a paradigmatic model to biological transport,” *Rep. Prog. Phys.*, vol. 74, no. 11, p. 116601, 2011.
- [4] E. Schrödinger, “What is life? the physical aspect of the living cell and mind.,” 1944.
- [5] F. Gnesotto, F. Mura, J. Gladrow, and C. Broedersz, “Broken detailed balance and non-equilibrium dynamics in living systems: a review,” *Reports on Progress in Physics*, vol. 81, no. 6, p. 066601, 2018.
- [6] P. C. Bressloff, *Stochastic processes in cell biology*, vol. 41. Springer, 2014.
- [7] S. Katz, J. L. Lebowitz, and H. Spohn, “Phase transitions in stationary nonequilibrium states of model lattice systems,” *Phys. Rev. B*, vol. 28, no. 3, pp. 1655–1658, 1983.
- [8] T. Chou, “How Fast Do Fluids Squeeze through Microscopic Single-File Pores?,” *Phys. Rev. Lett.*, vol. 80, no. 1, p. 85, 1998.
- [9] T. Reichenbach, T. Franosch, and E. Frey, “Exclusion Processes with Internal States,” *Phys. Rev. Lett.*, vol. 97, p. 050603, aug 2006.
- [10] T. Reichenbach, E. Frey, and T. Franosch, “Traffic jams induced by rare switching events in two-lane transport,” *New J. Phys.*, vol. 9, p. 159, 2007.
- [11] A. Schadschneider, D. Chowdhury, and K. Nishinari, *Stochastic Transport in Complex Systems*. Elsevier, Amsterdam, 2011.
- [12] T. Chou and G. Lakatos, “Clustered Bottlenecks in mRNA Translation and Protein Synthesis,” *Phys. Rev. Lett.*, vol. 93, pp. 198101–1, nov 2004.

- [13] J. Krug, “Boundary-Induced Phase Transitions in Driven Diffusive Systems,” *Phys. Rev. Lett.*, vol. 67, no. 14, p. 1882, 1991.
- [14] A. Parmeggiani, T. Franosch, and E. Frey, “Phase coexistence in driven one-dimensional transport,” *Phys. Rev. Lett.*, vol. 90, no. February, p. 086601, 2003.
- [15] A. Parmeggiani, T. Franosch, and E. Frey, “Totally asymmetric simple exclusion process with langmuir kinetics,” *Phys. Rev. E*, vol. 70, no. 4, p. 046101, 2004.
- [16] C. Leduc, K. Padberg-Gehle, V. Varga, D. Helbing, S. Diez, and J. Howard, “Molecular crowding creates traffic jams of kinesin motors on microtubules,” *Proc. Natl. Acad. Sci. U.S.A.*, vol. 109, p. 6100, 2012.
- [17] A. I. Curatolo, M. R. Evans, Y. Kafri, and J. Tailleur, “Multilane driven diffusive systems,” *J. Phys. A-Math. Theor.*, vol. 49, no. 9, p. 095601, 2016.
- [18] V. Bormuth, B. Nitzsche, F. Ruhnöw, A. Mitra, M. Storch, B. Rammner, J. Howard, and S. Diez, “The highly processive kinesin-8, Kip3, switches microtubule protofilaments with a bias toward the left,” *Biophys. J.*, vol. 103, no. 1, pp. L4–L6, 2012.
- [19] M. Bugiel, E. Böhl, and E. Schäffer, “The kinesin-8 Kip3 switches protofilaments in a sideward random walk asymmetrically biased by force,” *Biophys. J.*, vol. 108, no. 8, pp. 2019–2027, 2015.
- [20] M. Brunnbauer, R. Dombi, T. Ho, M. Schliwa, M. Rief, and Z. Ökten, “Torque generation of kinesin motors is governed by the stability of the neck domain,” *Mol. Cell*, vol. 46, pp. 147–58, apr 2012.
- [21] A. Zlotnick, J. M. Johnson, P. W. Wingfield, S. J. Stahl, and D. Endres, “A theoretical model successfully identifies features of hepatitis b virus capsid assembly,” *Biochemistry*, vol. 38, no. 44, pp. 14644–14652, 1999.
- [22] Y. Ke, L. L. Ong, W. M. Shih, and P. Yin, “Three-dimensional structures self-assembled from dna bricks,” *Science*, vol. 338, no. 6111, pp. 1177–1183, 2012.
- [23] B. Wei, M. Dai, and P. Yin, “Complex shapes self-assembled from single-stranded dna tiles,” *Nature*, vol. 485, no. 7400, p. 623, 2012.
- [24] A. Reinhardt and D. Frenkel, “Numerical evidence for nucleated self-assembly of dna brick structures,” *Phys. Rev. Lett.*, vol. 112, no. 23, p. 238103, 2014.
- [25] W. M. Jacobs, A. Reinhardt, and D. Frenkel, “Rational design of self-assembly pathways for complex multicomponent structures,” *Proceedings of the National Academy of Sciences*, vol. 112, no. 20, pp. 6313–6318, 2015.
- [26] M. F. Hagan and O. M. Elrad, “Understanding the concentration dependence of viral capsid assembly kinetics - the origin of the lag time and identifying the critical nucleus size,” *Biophysical journal*, vol. 98, no. 6, pp. 1065–1074, 2010.

- [27] K. F. Wagenbauer, C. Sigl, and H. Dietz, “Gigadalton-scale shape-programmable dna assemblies,” *Nature*, vol. 552, no. 7683, pp. 78–83, 2017.
- [28] F. Praetorius and H. Dietz, “Self-assembly of genetically encoded dna-protein hybrid nanoscale shapes,” *Science*, vol. 355, no. 6331, p. eaam5488, 2017.
- [29] K. V. Gothelf, “Lego-like dna structures,” *science*, vol. 338, no. 6111, pp. 1159–1160, 2012.
- [30] F. H. Crick and J. D. Watson, “Structure of small viruses,” *Nature*, vol. 177, no. 4506, pp. 473–475, 1956.
- [31] D. L. Caspar and A. Klug, “Physical principles in the construction of regular viruses,” in *Cold Spring Harbor symposia on quantitative biology*, vol. 27, pp. 1–24, Cold Spring Harbor Laboratory Press, 1962.
- [32] C. Chen, C. C. Kao, and B. Dragnea, “Self-assembly of brome mosaic virus capsids: insights from shorter time-scale experiments,” *The Journal of Physical Chemistry A*, vol. 112, no. 39, pp. 9405–9412, 2008.
- [33] D. Endres and A. Zlotnick, “Model-based analysis of assembly kinetics for virus capsids or other spherical polymers,” *Biophysical journal*, vol. 83, no. 2, pp. 1217–1230, 2002.
- [34] A. Zlotnick, “Are weak protein–protein interactions the general rule in capsid assembly?,” *Virology*, vol. 315, no. 2, pp. 269–274, 2003.
- [35] R. Kree, B. Schaub, and B. Schmittmann, “Effects of pollution on critical population dynamics,” *Physical Review A*, vol. 39, no. 4, p. 2214, 1989.
- [36] F. Van Wijland, K. Oerding, and H. Hilhorst, “Wilson renormalization of a reaction–diffusion process,” *Physica A: Statistical Mechanics and its Applications*, vol. 251, no. 1-2, pp. 179–201, 1998.
- [37] D. S. Maia and R. Dickman, “Diffusive epidemic process: theory and simulation,” *Journal of Physics: Condensed Matter*, vol. 19, no. 6, p. 065143, 2007.
- [38] H. Hinrichsen, “Non-equilibrium critical phenomena and phase transitions into absorbing states,” *Advances in physics*, vol. 49, no. 7, pp. 815–958, 2000.
- [39] M. Tarpin, F. Benitez, L. Canet, and N. Wschebor, “Nonperturbative renormalization group for the diffusive epidemic process,” *Physical Review E*, vol. 96, no. 2, p. 022137, 2017.
- [40] J. De Freitas, L. Lucena, L. Da Silva, and H. Hilhorst, “Critical behavior of a two-species reaction-diffusion problem,” *Physical Review E*, vol. 61, no. 6, p. 6330, 2000.

- [41] U. Fulco, D. Messias, and M. Lyra, “Critical behavior of a one-dimensional diffusive epidemic process,” *Physical Review E*, vol. 63, no. 6, p. 066118, 2001.
- [42] E. Perlsman and S. Havlin, “Method to estimate critical exponents using numerical studies,” *EPL (Europhysics Letters)*, vol. 58, no. 2, p. 176, 2002.
- [43] D. Bertrand, Y. Siqueira, M. Lyra, I. Gleria, and C. Argolo, “Critical behavior of a two-species reaction–diffusion problem in 2d,” *Physica A: Statistical Mechanics and its Applications*, vol. 386, no. 2, pp. 748–751, 2007.
- [44] D. S. Maia and R. Dickman, “The nature of the absorbing-state phase transition in the diffusive epidemic process,” *Journal of Physics A: Mathematical and Theoretical*, vol. 41, p. 405002, 2008.
- [45] G. Corso, M. Lyra, U. Fulco, *et al.*, “Critical properties of the diffusive epidemic process obtained via an automatic search technique,” *Journal of Statistical Mechanics: Theory and Experiment*, vol. 2010, no. 04, p. P04027, 2010.
- [46] C. Argolo, V. Tenório, and M. Lyra, “Stationary and dynamical critical behavior of the three-dimensional diffusive epidemic process,” *Physica A: Statistical Mechanics and its Applications*, vol. 517, pp. 422–430, 2019.
- [47] D. T. Gillespie, “Exact stochastic simulation of coupled chemical reactions,” *J. Phys. Chem-US*, vol. 93555, no. 1, pp. 2340–2361, 1977.
- [48] D. T. Gillespie, “Stochastic Simulation of Chemical Kinetics,” *Annu. Rev. Phys. Chem.*, vol. 58, no. 1, pp. 35–55, 2007.
- [49] M. A. Gibson and J. Bruck, “Efficient exact stochastic simulation of chemical systems with many species and many channels,” *The journal of physical chemistry A*, vol. 104, no. 9, pp. 1876–1889, 2000.
- [50] P. Grassberger and A. de la Torre, “Reggeon field theory (schlögl’s first model) on a lattice: Monte carlo calculations of critical behaviour,” *Annals of Physics*, vol. 122, no. 2, pp. 373 – 396, 1979.
- [51] S. Lübeck, “Universal scaling behavior of non-equilibrium phase transitions,” *International Journal of Modern Physics B*, vol. 18, no. 31n32, pp. 3977–4118, 2004.
- [52] M. Henkel, H. Hinrichsen, S. Lübeck, and M. Pleimling, *Non-equilibrium phase transitions*, vol. 1. Springer, 2008.
- [53] P. Wilke, E. Reithmann, and E. Frey, “Two-species active transport along cylindrical biofilaments is limited by emergent topological hindrance,” *Physical Review X*, vol. 8, no. 3, p. 031063, 2018.

- [54] E. J. Reithmann, *On the role of nonequilibrium processes in intracellular organization*. PhD thesis, Ludwig–Maximilians–Universität München, 2 2019.
- [55] D. A. Fletcher and R. D. Mullins, “Cell mechanics and the cytoskeleton,” *Nature*, vol. 463, no. 7280, pp. 485–492, 2010.
- [56] T. Vignaud, L. Blanchoin, and M. Théry, “Directed cytoskeleton self-organization,” *Trends in cell biology*, vol. 22, no. 12, pp. 671–682, 2012.
- [57] T. D. Pollard and R. D. Goldman, “Overview of the cytoskeleton from an evolutionary perspective,” *Cold Spring Harbor perspectives in biology*, vol. 10, no. 7, p. a030288, 2018.
- [58] S. L. Rogers and V. I. Gelfand, “Membrane trafficking, organelle transport, and the cytoskeleton,” *Current opinion in cell biology*, vol. 12, no. 1, pp. 57–62, 2000.
- [59] F. Huber, A. Boire, M. P. López, and G. H. Koenderink, “Cytoskeletal crosstalk: when three different personalities team up,” *Current opinion in cell biology*, vol. 32, pp. 39–47, 2015.
- [60] K. H. Downing and E. Nogales, “Tubulin and microtubule structure,” *Current opinion in cell biology*, vol. 10, no. 1, pp. 16–22, 1998.
- [61] J. Howard, “Molecular motors: structural adaptations to cellular functions,” *Nature*, vol. 389, no. 6651, pp. 561–567, 1997.
- [62] A. B. Kolomeisky, *Motor proteins and molecular motors*. CRC press, 2015.
- [63] R. D. Vale and R. J. Fletterick, “The design plan of kinesin motors,” *Annual review of cell and developmental biology*, vol. 13, no. 1, pp. 745–777, 1997.
- [64] J. Howard, *Mechanics of Motor Proteins and the Cytoskeleton*. Sinauer Associates, Sunderland, 2001.
- [65] A. J. Roberts, T. Kon, P. J. Knight, K. Sutoh, and S. A. Burgess, “Functions and mechanics of dynein motor proteins,” *Nature reviews Molecular cell biology*, vol. 14, no. 11, pp. 713–726, 2013.
- [66] G. Woehlke and M. Schliwa, “Walking on two heads: the many talents of kinesin,” *Nature Reviews Molecular Cell Biology*, vol. 1, no. 1, pp. 50–58, 2000.
- [67] A. Gennerich and R. D. Vale, “Walking the walk: how kinesin and dynein coordinate their steps,” *Current opinion in cell biology*, vol. 21, no. 1, pp. 59–67, 2009.
- [68] A. Yildiz, R. D. Tomishige, Michio and, and P. R. Selvin, “Kinesin walks hand-over-hand,” *Science*, vol. 303, no. 5658, pp. 676–678, 2004.

- [69] A. Yildiz and P. R. Selvin, “Kinesin: walking, crawling or sliding along?,” *Trends in cell biology*, vol. 15, no. 2, pp. 112–120, 2005.
- [70] R. A. Cross, “The kinetic mechanism of kinesin,” *Trends in biochemical sciences*, vol. 29, no. 6, pp. 301–309, 2004.
- [71] S. M. Block, L. S. Goldstein, and B. J. Schnapp, “Bead movement by single kinesin molecules studied with optical tweezers,” *Nature*, vol. 348, no. 6299, pp. 348–352, 1990.
- [72] J. Howard, A. Hudspeth, and R. Vale, “Movement of microtubules by single kinesin molecules,” *Nature*, vol. 342, no. 6246, pp. 154–158, 1989.
- [73] S. Ray, E. Meyhöfer, R. A. Milligan, and J. Howard, “Kinesin follows the microtubule’s protofilament axis,” *J. Cell. Biol.*, vol. 121, no. 5, pp. 1083–1093, 1993.
- [74] C. T. MacDonald, J. H. Gibbs, and A. C. Pipkin, “Kinetics of biopolymerization on nucleic acid templates,” *Biopolymers: Original Research on Biomolecules*, vol. 6, no. 1, pp. 1–25, 1968.
- [75] B. Derrida, E. Domany, and D. Mukamel, “An Exact Solution of a One-Dimensional Asymmetric Exclusion Model with Open Boundaries,” *J. Stat. Phys.*, vol. 69, pp. 667–687, 1992.
- [76] B. Derrida, M. R. Evans, V. Hakim, and V. Pasquier, “Exact solution of a 1D asymmetric exclusion model using a matrix formulation,” *J. Phys. A-Math. Gen.*, vol. 26, no. 7, pp. 1493–1517, 1993.
- [77] G. M. Schütz and E. Domany, “Phase transitions in an exactly soluble one-dimensional exclusion process,” *J. Stat. Phys.*, vol. 72, no. 1-2, pp. 277–296, 1993.
- [78] G. M. Schütz, *1-Exactly Solvable Models for Many-Body Systems Far from Equilibrium*, vol. 19. Academic Press, London, 2001.
- [79] M. Gorissen, A. Lazarescu, K. Mallick, and C. Vanderzande, “Exact current statistics of the asymmetric simple exclusion process with open boundaries,” *Phys. Rev. Lett.*, vol. 109, no. 17, pp. 1–5, 2012.
- [80] M. Mabilia, T. Reichenbach, H. Hirsch, T. Franosch, and E. Frey, *Generic principles of active transport*. Polish Academy of Science, Warsaw, 2008.
- [81] M. J. Lighthill and G. B. Whitham, “On Kinematic Waves. II. A Theory of Traffic Flow on Long Crowded Roads,” *P. Roy. Soc. A-Math. Phys.*, vol. 229, no. 1178, pp. 317–345, 1955.
- [82] V. Popkov and G. M. Schütz, “Steady-state selection in driven diffusive systems with open boundaries,” *Europhys. Lett.*, vol. 48, no. 3, p. 257, 2000.

- [83] R. A. Blythe and M. R. Evans, “Nonequilibrium Steady States of Matrix Product Form: A Solver’s Guide,” *J. Phys. A-Math. Theor.*, vol. 40, no. 46, p. R333, 2007.
- [84] J. Hager, J. Krug, V. Popkov, and G. Schütz, “Minimal current phase and universal boundary layers in driven diffusive systems,” *Phys. Rev. E*, vol. 63, p. 056110, apr 2001.
- [85] M. R. Evans, Y. Kafri, K. E. P. Sugden, and J. Tailleur, “Phase diagram of two-lane driven diffusive systems,” *J. Stat. Mech-Theory E*, p. P06009, 2011.
- [86] M. R. Evans, D. P. Foster, C. Godrèche, and D. Mukamel, “Asymmetric exclusion model with two species: Spontaneous symmetry breaking,” *J. Stat. Phys.*, vol. 80, no. 1-2, pp. 69–102, 1995.
- [87] G. M. Schütz, “Critical phenomena and universal dynamics in one-dimensional driven diffusive systems with two species of particles,” *J. Phys. A-Math. Gen.*, vol. 36, p. 339, 2003.
- [88] S. Klumpp and R. Lipowsky, “Phase transitions in systems with two species of molecular motors,” *Europhys. Lett.*, vol. 66, pp. 90–96, apr 2004.
- [89] R. Juhász, “Weakly coupled, antiparallel, totally asymmetric simple exclusion processes,” *Phys. Rev. E*, vol. 76, no. 2, pp. 1–13, 2007.
- [90] S. Prolhac, M. R. Evans, and K. Mallick, “The matrix product solution of the multispecies partially asymmetric exclusion process,” *J. Phys. A-Math. Theor.*, vol. 42, p. 165004, apr 2009.
- [91] D. Johann, D. Goswami, and K. Kruse, “Segregation of diffusible and directionally moving particles on a polar filament,” *Phys. Rev. E*, vol. 89, no. 4, pp. 1–6, 2014.
- [92] V. Popkov and G. M. Schütz, “Shocks and Excitation Dynamics in a Driven Diffusive Two-Channel System,” *J. Stat. Phys.*, vol. 112, no. 3-4, pp. 523–540, 2003.
- [93] E. Pronina and A. B. Kolomeisky, “Two-channel totally asymmetric simple exclusion processes,” *J. Phys. A-Math. Gen.*, vol. 37, no. 42, pp. 9907–9918, 2004.
- [94] J. Brankov, N. Pesheva, and N. Bunzarova, “Totally asymmetric exclusion process on chains with a double-chain section in the middle: Computer simulations and a simple theory,” *Phys. Rev. E*, vol. 69, no. 6 2, pp. 1–13, 2004.
- [95] E. Pronina and A. B. Kolomeisky, “Theoretical investigation of totally asymmetric exclusion processes on lattices with junctions,” *J. Stat. Mech-Theory E*, vol. 2005, pp. P07010–P07010, jul 2005.
- [96] R. Wang, M. Liu, and R. Jiang, “Theoretical investigation of synchronous totally asymmetric exclusion processes on lattices with multiple-input-single-output junctions,” *Phys. Rev. E*, vol. 77, no. 5, pp. 1–8, 2008.

- [97] M. Liu and R. Wang, “Asymmetric exclusion processes on m-input n-output junctions with parallel update,” *Physica A*, vol. 388, no. 19, pp. 4068–4074, 2009.
- [98] B. Embley, A. Parmeggiani, and N. Kern, “Understanding totally asymmetric simple-exclusion-process transport on networks: Generic analysis via effective rates and explicit vertices,” *Phys. Rev. E*, vol. 80, no. 4, pp. 1–22, 2009.
- [99] H. J. Hilhorst and C. Appert-Rolland, “A multi-lane TASEP model for crossing pedestrian traffic flows,” *J. Stat. Mech-Theory E*, vol. 2012, no. 06, p. P06009, 2012.
- [100] Z. J. Ding, R. Jiang, and B. H. Wang, “Traffic flow in the Biham-Middleton-Levine model with random update rule,” *Phys. Rev. E*, vol. 83, no. 4, pp. 2–5, 2011.
- [101] S. Klumpp, T. M. Nieuwenhuizen, and R. Lipowsky, “Self-Organized Density Patterns of Molecular Motors in Arrays of Cytoskeletal Filaments,” *Biophys. J.*, vol. 88, no. 5, pp. 3118–3132, 2005.
- [102] B. Embley, A. Parmeggiani, and N. Kern, “HEX-TASEP: dynamics of pinned domains for TASEP transport on a periodic lattice of hexagonal topology,” *J. Phys-Condens. Mat.*, vol. 20, p. 295213, 2008.
- [103] I. Neri, N. Kern, and A. Parmeggiani, “Totally Asymmetric Simple Exclusion Process on Networks,” *Phys. Rev. Lett.*, vol. 107, p. 068702, aug 2011.
- [104] T. Ezaki and K. Nishinari, “A balance network for the asymmetric simple exclusion process,” *J. Stat. Mech-Theory E*, vol. 2012, no. 11, p. P11002, 2012.
- [105] I. Neri, N. Kern, and A. Parmeggiani, “Modeling cytoskeletal traffic: An Interplay between passive diffusion and active transport,” *Phys. Rev. Lett.*, vol. 110, no. 9, pp. 1–5, 2013.
- [106] G. Lakatos and T. Chou, “Totally asymmetric exclusion processes with particles of arbitrary size,” *Journal of Physics A: Mathematical and General*, vol. 36, no. 8, p. 2027, 2003.
- [107] M. Rank, A. Mitra, L. Reese, S. Diez, and E. Frey, “Limited resources induce bistability in microtubule length regulation,” *Physical review letters*, vol. 120, no. 14, p. 148101, 2018.
- [108] I. R. Graf and E. Frey, “Generic Transport Mechanisms for Molecular Traffic in Cellular Protrusions,” *Phys. Rev. Lett.*, vol. 118, no. 12, pp. 6–11, 2017.
- [109] A. Melbinger, L. Reese, and E. Frey, “Microtubule Length-Regulation by Molecular Motors,” *Phys. Rev. Lett.*, vol. 108, no. 25, p. 258104, 2012.
- [110] E. Reithmann, L. Reese, and E. Frey, “Nonequilibrium Diffusion and Capture Mechanism Ensures Tip Localization of Regulating Proteins on Dynamic Filaments,” *Phys. Rev. Lett.*, vol. 117, no. 7, p. 078102, 2016.

- [111] J. Yajima and R. A. Cross, “A torque component in the kinesin-1 power stroke,” *Nat. Chem. Biol.*, vol. 1, no. 6, pp. 338–341, 2005.
- [112] R. A. Walker, E. D. Salmon, and S. A. Endow, “The *Drosophila* claret segregation protein is a minus-end directed motor molecule,” *Nature*, vol. 347, no. 6295, pp. 780–782, 1990.
- [113] X. Pan, S. Acar, and J. M. Scholey, “Torque generation by one of the motor subunits of heterotrimeric kinesin-2,” *Biochem. Biophys. Res. Co.*, vol. 401, no. 1, pp. 53–57, 2010.
- [114] J. Yajima, K. Mizutani, and T. Nishizaka, “A torque component present in mitotic kinesin Eg5 revealed by three-dimensional tracking,” *Nat. Struct. Mol. Biol.*, vol. 15, no. 10, pp. 1119–1121, 2008.
- [115] R. D. Vale and Y. Yano Toyoshima, “Rotation and translocation of microtubules in vitro induced by dyneins from *Tetrahymena* cilia,” *Cell*, vol. 52, no. 3, pp. 459–469, 1988.
- [116] T. Nishizaka, T. Yagi, Y. Tanaka, and S. Ishiwata, “Right-handed rotation of an actin filament in an in vitro motile system,” *Nature*, vol. 361, no. 6409, pp. 269–271, 1993.
- [117] T. Liggett, *Continuous Time Markov Processes: An Introduction*. American Mathematical Society, 2010.
- [118] O. Biham, A. A. Middleton, and D. Levine, “Self-organization and a dynamical transition in traffic-flow models,” *Phys. Rev. A*, vol. 46, no. 10, pp. 6124–6127, 1992.
- [119] P. Winkler, *Mathematical Puzzles: A Connoisseur’s Collection*. AK Peters, Natick, 2004.
- [120] P. Winkler, *Mathematical mind-benders*. CRC Press, Boca Raton, 2007.
- [121] O. Angel and J. B. Martin, “The jammed phase of the Biham-Middleton- Levine Traffic Model,” *Electron. Commun. Probab.*, vol. 10, pp. 167–178, 2005.
- [122] F. M. Gartner, I. R. Graf, P. Wilke, P. M. Geiger, and E. Frey, “Stochastic yield catastrophes and robustness in self-assembly,” *Elife*, vol. 9, p. e51020, 2020.
- [123] I. Graf, *Principles of self-organization and self-assembly in biologically inspired non-equilibrium systems*. PhD thesis, Ludwig-Maximilians-Universität München, 12 2019.
- [124] M. Jucker and L. C. Walker, “Self-propagation of pathogenic protein aggregates in neurodegenerative diseases,” *Nature*, vol. 501, no. 7465, pp. 45–51, 2013.

- [125] D. A. Drummond and C. O. Wilke, "The evolutionary consequences of erroneous protein synthesis," *Nature Reviews Genetics*, vol. 10, no. 10, pp. 715–724, 2009.
- [126] J. D. Perlmutter and M. F. Hagan, "Mechanisms of virus assembly," *Annual review of physical chemistry*, vol. 66, pp. 217–239, 2015.
- [127] V. L. Morton, P. G. Stockley, N. J. Stonehouse, and A. E. Ashcroft, "Insights into virus capsid assembly from non-covalent mass spectrometry," *Mass spectrometry reviews*, vol. 27, no. 6, pp. 575–595, 2008.
- [128] H. C. Berg, "The rotary motor of bacterial flagella," *Annual review of biochemistry*, vol. 72, 2003.
- [129] T. Minamino and K. Imada, "The bacterial flagellar motor and its structural diversity," *Trends in microbiology*, vol. 23, no. 5, pp. 267–274, 2015.
- [130] A. Fatica and D. Tollervey, "Making ribosomes," *Current opinion in cell biology*, vol. 14, no. 3, pp. 313–318, 2002.
- [131] S. Klinge and J. L. Woolford, "Ribosome assembly coming into focus," *Nature Reviews Molecular Cell Biology*, vol. 20, no. 2, pp. 116–131, 2019.
- [132] D. Kressler, E. Hurt, and J. Baßler, "Driving ribosome assembly," *Biochimica Et Biophysica Acta (BBA)-Molecular Cell Research*, vol. 1803, no. 6, pp. 673–683, 2010.
- [133] F. C. Simmel, "Dna-based assembly lines and nanofactories," *Current opinion in biotechnology*, vol. 23, no. 4, pp. 516–521, 2012.
- [134] S. Zhang, "Fabrication of novel biomaterials through molecular self-assembly," *Nature Biotechnology*, vol. 21, no. 10, pp. 1171–1178, 2003.
- [135] I. Saaem and T. H. LaBean, "Overview of dna origami for molecular self-assembly," *Wiley Interdisciplinary Reviews: Nanomedicine and Nanobiotechnology*, vol. 5, no. 2, pp. 150–162, 2013.
- [136] X. S. Chen, R. L. Garcea, I. Goldberg, G. Casini, and S. C. Harrison, "Structure of small virus-like particles assembled from the l1 protein of human papillomavirus 16," *Molecular cell*, vol. 5, no. 3, pp. 557–567, 2000.
- [137] P. G. Leiman, F. Arisaka, M. J. Van Raaij, V. A. Kostyuchenko, A. A. Aksyuk, S. Kanamaru, and M. G. Rossmann, "Morphogenesis of the t4 tail and tail fibers," *Virology journal*, vol. 7, no. 1, p. 355, 2010.
- [138] D. Arslan, M. Legendre, V. Seltzer, C. Abergel, and J.-M. Claverie, "Distant mimivirus relative with a larger genome highlights the fundamental features of megaviridae," *Proceedings of the National Academy of Sciences*, vol. 108, no. 42, pp. 17486–17491, 2011.

- [139] A. Zlotnick, “To build a virus capsid: an equilibrium model of the self assembly of polyhedral protein complexes,” *Journal of molecular biology*, vol. 241, no. 1, pp. 59–67, 1994.
- [140] A. Y. Morozov, R. F. Bruinsma, and J. Rudnick, “Assembly of viruses and the pseudo-law of mass action,” *The Journal of chemical physics*, vol. 131, no. 15, p. 10B607, 2009.
- [141] D. Rapaport, J. Johnson, and J. Skolnick, “Supramolecular self-assembly: molecular dynamics modeling of polyhedral shell formation,” *Computer physics communications*, vol. 121, pp. 231–235, 1999.
- [142] H. D. Nguyen, V. S. Reddy, and C. L. Brooks, “Deciphering the kinetic mechanism of spontaneous self-assembly of icosahedral capsids,” *Nano Letters*, vol. 7, no. 2, pp. 338–344, 2007.
- [143] V. Linko and H. Dietz, “The enabled state of dna nanotechnology,” *Current opinion in biotechnology*, vol. 24, no. 4, pp. 555–561, 2013.
- [144] N. C. Seeman, “Nucleic acid junctions and lattices,” *Journal of theoretical biology*, vol. 99, no. 2, pp. 237–247, 1982.
- [145] P. W. Rothemund, “Folding dna to create nanoscale shapes and patterns,” *Nature*, vol. 440, no. 7082, pp. 297–302, 2006.
- [146] P. Wang, T. A. Meyer, V. Pan, P. K. Dutta, and Y. Ke, “The beauty and utility of dna origami,” *Chem*, vol. 2, no. 3, pp. 359–382, 2017.
- [147] S. M. Douglas, H. Dietz, T. Liedl, B. Högberg, F. Graf, and W. M. Shih, “Self-assembly of dna into nanoscale three-dimensional shapes,” *Nature*, vol. 459, no. 7245, pp. 414–418, 2009.
- [148] J. Zheng, J. J. Birktoft, Y. Chen, T. Wang, R. Sha, P. E. Constantinou, S. L. Ginell, C. Mao, and N. C. Seeman, “From molecular to macroscopic via the rational design of a self-assembled 3d dna crystal,” *Nature*, vol. 461, no. 7260, pp. 74–77, 2009.
- [149] S. Whitelam, “Hierarchical assembly may be a way to make large information-rich structures,” *Soft Matter*, vol. 11, no. 42, pp. 8225–8235, 2015.
- [150] W. M. Jacobs and D. Frenkel, “Self-assembly of structures with addressable complexity,” *Journal of the American Chemical Society*, vol. 138, no. 8, pp. 2457–2467, 2016.
- [151] A. Murugan, J. Zou, and M. P. Brenner, “Undesired usage and the robust self-assembly of heterogeneous structures,” *Nature Communications*, vol. 6, p. 6203, 2015.

- [152] B. Alberts, A. Johnson, J. Lewis, D. Morgan, M. Raff, K. Roberts, P. Walter, J. Wilson, and T. Hunt, *Molecular Biology of the Cell*. Garland Science, 2015.
- [153] W. M. Jacobs and D. Frenkel, “Self-assembly protocol design for periodic multicomponent structures,” *Soft Matter*, vol. 11, no. 46, pp. 8930–8938, 2015.
- [154] R. P. Sear, “Nucleation: theory and applications to protein solutions and colloidal suspensions,” *Journal of Physics: Condensed Matter*, vol. 19, no. 3, p. 033101, 2007.
- [155] G. R. Lazaro and M. F. Hagan, “Allosteric control of icosahedral capsid assembly,” *The Journal of Physical Chemistry B*, vol. 120, no. 26, pp. 6306–6318, 2016.
- [156] M. F. Hagan, O. M. Elrad, and R. L. Jack, “Mechanisms of kinetic trapping in self-assembly and phase transformation,” *The Journal of chemical physics*, vol. 135, no. 10, p. 104115, 2011.
- [157] J. Grant, R. L. Jack, and S. Whitelam, “Analyzing mechanisms and microscopic reversibility of self-assembly,” *The Journal of chemical physics*, vol. 135, no. 21, p. 214505, 2011.
- [158] T. C. Michaels, A. J. Dear, J. B. Kirkegaard, K. L. Saar, D. A. Weitz, and T. P. Knowles, “Fluctuations in the kinetics of linear protein self-assembly,” *Phys. Rev. Lett.*, vol. 116, no. 25, p. 258103, 2016.
- [159] T. C. Michaels, M. M. Bellaiche, M. F. Hagan, and T. P. Knowles, “Kinetic constraints on self-assembly into closed supramolecular structures,” *Scientific Reports*, vol. 7, no. 1, p. 12295, 2017.
- [160] M. D’Orsogna, G. Lakatos, and T. Chou, “Stochastic self-assembly of incommensurate clusters,” *The Journal of chemical physics*, vol. 136, no. 8, p. 084110, 2012.
- [161] L. O. Hedges, R. V. Mannige, and S. Whitelam, “Growth of equilibrium structures built from a large number of distinct component types,” *Soft Matter*, vol. 10, no. 34, pp. 6404–6416, 2014.
- [162] M. R. D’Orsogna, B. Zhao, B. Berenji, and T. Chou, “Combinatoric analysis of heterogeneous stochastic self-assembly,” *The Journal of chemical physics*, vol. 139, no. 12, p. 121918, 2013.
- [163] C. Pena, E. Hurt, and V. G. Panse, “Eukaryotic ribosome assembly, transport and quality control,” *Nature structural & molecular biology*, vol. 24, no. 9, p. 689, 2017.
- [164] F. F. Chevance and K. T. Hughes, “Coordinating assembly of a bacterial macromolecular machine,” *Nature Reviews Microbiology*, vol. 6, no. 6, p. 455, 2008.
- [165] T. K. Haxton and S. Whitelam, “Do hierarchical structures assemble best via hierarchical pathways?,” *Soft Matter*, vol. 9, no. 29, pp. 6851–6861, 2013.

- [166] F. Gartner, I. Graf, and E. Frey, “Controlling fidelity and time-efficiency in self-assembly,” *in preparation*, 2020.
- [167] R. Becker and W. Döring, “Kinetische behandlung der keimbildung in übersättigten dämpfen,” *Annalen der Physik*, vol. 416, no. 8, pp. 719–752, 1935.
- [168] I. Graf, F. Gartner, and E. Frey, “Understanding and guiding robust self-assembly of heterogeneous structures,” *in preparation*, 2020.
- [169] B. Polovnikov, P. Wilke, and E. Frey, “Strong coupling behavior in the diffusive epidemic process,” *in preparation*, 2020.
- [170] B. Polovnikov, “Fluctuations and criticality in reaction-diffusion systems,” Master’s thesis, Ludwig-Maximilians-Universität München, 10 2019.
- [171] S. J. Altschuler, S. B. Angenent, Y. Wang, and L. F. Wu, “On the spontaneous emergence of cell polarity,” *Nature*, vol. 454, no. 7206, pp. 886–889, 2008.
- [172] U. C. Täuber, M. Howard, and B. P. Vollmayr-Lee, “Applications of field-theoretic renormalization group methods to reaction–diffusion problems,” *Journal of Physics A: Mathematical and General*, vol. 38, pp. R79–R131, apr 2005.
- [173] K. J. Wiese, “Coherent-state path integral versus coarse-grained effective stochastic equation of motion: From reaction diffusion to stochastic sandpiles,” *Physical Review E*, vol. 93, no. 4, p. 042117, 2016.
- [174] M. F. Weber and E. Frey, “Master equations and the theory of stochastic path integrals,” *Reports on Progress in Physics*, vol. 80, no. 4, p. 046601, 2017.
- [175] P. C. Hohenberg and B. I. Halperin, “Theory of dynamic critical phenomena,” *Rev. Mod. Phys.*, vol. 49, pp. 435–479, Jul 1977.
- [176] K. Oerding, F. Van Wijland, J.-P. Leroy, and H. J. Hilhorst, “Fluctuation-induced first-order transition in a nonequilibrium steady state,” *Journal of Statistical Physics*, vol. 99, no. 5-6, pp. 1365–1395, 2000.
- [177] H.-K. Janssen, “Comment on “critical behavior of a two-species reaction-diffusion problem”,” *Physical Review E*, vol. 64, no. 5, p. 058101, 2001.
- [178] J. De Freitas, L. Lucena, L. da Silva, and H. Hilhorst, “Reply to “comment on ‘critical behavior of a two-species reaction-diffusion problem’”,” *Physical Review E*, vol. 64, no. 5, p. 058102, 2001.
- [179] P. Grassberger, “Directed percolation in  $2 + 1$  dimensions,” *Journal of Physics A: Mathematical and General*, vol. 22, pp. 3673–3679, sep 1989.
- [180] R. Dickman, “Nonequilibrium critical behavior of the triplet annihilation model,” *Phys. Rev. A*, vol. 42, pp. 6985–6990, Dec 1990.

- [181] I. Jensen, H. C. Fogedby, and R. Dickman, “Critical exponents for an irreversible surface reaction model,” *Phys. Rev. A*, vol. 41, pp. 3411–3414, Mar 1990.
- [182] I. Jensen, “Universality class of a one-dimensional cellular automaton,” *Phys. Rev. A*, vol. 43, pp. 3187–3189, Mar 1991.
- [183] I. Jensen, “Critical behavior of the three-dimensional contact process,” *Phys. Rev. A*, vol. 45, pp. R563–R566, Jan 1992.
- [184] I. Jensen, “Critical exponents for branching annihilating random walks with an even number of offspring,” *Phys. Rev. E*, vol. 50, pp. 3623–3633, Nov 1994.
- [185] P. Grassberger and Y.-C. Zhang, ““self-organized” formulation of standard percolation phenomena,” *Physica A: Statistical Mechanics and its Applications*, vol. 224, no. 1, pp. 169 – 179, 1996. *Dynamics of Complex Systems*.
- [186] C. A. Voigt and R. M. Ziff, “Epidemic analysis of the second-order transition in the ziff-gulari-barshad surface-reaction model,” *Phys. Rev. E*, vol. 56, pp. R6241–R6244, Dec 1997.
- [187] J. D. Noh and H. Park, “Universality class of absorbing transitions with continuously varying critical exponents,” *Phys. Rev. E*, vol. 69, p. 016122, Jan 2004.
- [188] H.-K. Janssen, “Survival and percolation probabilities in the field theory of growth models,” *Journal of Physics: Condensed Matter*, vol. 17, no. 20, p. S1973, 2005.
- [189] V. Volterra, “Variations and fluctuations of the number of individuals in animal species living together,” *ICES Journal of Marine Science*, vol. 3, no. 1, pp. 3–51, 1928.
- [190] A. Lotka, “Zur theorie der periodischen reaktionen,” *Zeitschrift für physikalische Chemie*, vol. 72, no. 1, pp. 508–511, 1910.
- [191] J. Halatek, F. Brauns, and E. Frey, “Self-organization principles of intracellular pattern formation,” *Philosophical Transactions of the Royal Society B: Biological Sciences*, vol. 373, no. 1747, p. 20170107, 2018.
- [192] D. T. Gillespie, “A general method for numerically simulating the stochastic time evolution of coupled chemical reactions,” *J. Comput. Phys.*, vol. 22, no. 4, pp. 403–434, 1976.
- [193] B. Stroustrup, *The C++ programming language*. Pearson Education, 2013.
- [194] T. H. Cormen, C. E. Leiserson, R. L. Rivest, and C. Stein, *Introduction to algorithms*. MIT press, 2009.

# Acknowledgments

Completing a PhD is not limited to writing a thesis. It is a process in which a large number of people are involved to make it possible. In the following I would like to express my heartfelt gratitude to them.

First and foremost, I want to thank Erwin Frey, who supervised my thesis and made it possible for me to be part of this wonderful research group. His trust in my work and full support in my projects were the best environment anyone could hope for. Also, beyond the research, the time spent together was a great personal gain I will always like to remember. For example, the visit to an Izakaya as part of a joint research stay in Tokyo remains unforgettable.

Special thanks also go to my second assessor Ulrich Schollwöck, who without any hesitation agreed to take over this task.

During my time at our chair, I was lucky enough to work with many talented other PhD students. The person who embodies this experience like no other is Emanuel Reithmann. I wrote my first paper with him and spent countless hours in exciting discussions. From this time a significant friendship has emerged together with countless great memories.

Also, a group of people I will never forget is our “assembly team”. The working time together with Florian Gartner, Philipp Geiger and Isabella Graf always felt like a happy meeting with friends that ultimately resulted in a successful publication. I have rarely laughed as much in my life as during our sessions.

I would also like to thank Borislav Polovnikov, with whom I not only shared an office, but also worked together on a publication. Our daily conversations were an integral part of my everyday university life.

Special thanks also go to Laeschkir Würthner, with whom I shared the position of chair administrator for many years. In our time together, we averted some disasters and fought our way through as many.

I would also like to express my gratitude to everyone who proofread this thesis and gave me valuable feedback: Philipp Geiger, Isabella Graf, David Muramatsu, Borislav Polovnikov, Emanuel Reithmann, and Moritz Striebel.

For an outstanding time and a valuable friendship, I want to thank my office mate David Muramatsu. Learning the Japanese language together as well as our trips to Japan are among the best and happiest memories of my PhD.

Last but not least, I would also like to thank my two flat mates and good friends Philipp Geiger and Andreas Bluhm. We never needed a lot of words to have good communication.

This work was created under special circumstances at a time when a pandemic was isolating people from each other. The fact that I still managed to complete my thesis without falling into madness is only thanks to my wonderful partner Annika Kaiser. You are the one person who can replace all other social contacts. Your love and care have brought me through this time and will do so through all future challenges. I am so lucky to have you in my life.

Die letzten Worte dieser Arbeit gebühren meiner Familie. Meine ältere Schwester Melanie hat mich mein ganzes Leben lang begleitet und war jederzeit für mich da, wenn ich sie brauchte. Meine Eltern Gabriele und Axel haben immer alles in ihrer Macht Stehende getan, um mich bei allem so gut es nur menschenmöglich ist zu unterstützen. Ich bin jeden Tag dankbar so liebevolle und fürsorgliche Menschen in meinem Leben zu haben. Ohne euch wäre nichts hiervon möglich gewesen.